Control study of two-particle correlations in heavy ion collisions at RHIC-PHENIX

Eric Vazquez

Submitted in partial fulfillment of the
requirements for the degree
of Doctor of Philosophy
in the Graduate School of Arts and Sciences

COLUMBIA UNIVERSITY
2013

Abstract

Control study of two-particle correlations in heavy ion collisions at RHIC-PHENIX

Eric Vazquez

Measurements at the Relativistic Heavy Ion Collider (RHIC) have provided indirect measurements of jets in a heavy ion environment using the two-particle correlation method in the presence of a high-p_T particle. These measurements have offered insight into the formation of a new state of dense nuclear matter called the *Quark-Gluon Plasma* (QGP) through the observation of *jet quenching*. However, the two-particle methodology has also shown to be biased towards di-jet production near the surface of the medium being created. Here, a detailed study using the PHENIX detector is provided, in an attempt to measure a more accurate jet-induced two-particle correlation measurement than previously published and to reduce the bias observed in two-particle correlation measurements. The reduction in surface bias emission is performed via the requirement of *two* antipodal high-p_T particles (a.k.a. "2+1" correlation) in an attempt to control the production point of the di-jet. The measurements made in Au+Au collisions when compared to p+p collisions show that the method provides additional sensitivity to the jet quenching previously observed in two-particle correlation method.

Contents

List of Figures

List of Tables

Acknowledgements

In my road to attaining my doctoral degree, there are many individuals that have played a role in making this possible, some whom I will briefly mention.

First I would like to thank my adviser Bill Zajc for taking me under his wing while at the same time being an extremely patient person during my tenure at Columbia University. Bill's tremendous knowledge in the field and experience with the PHENIX detector helped me overcome many obstacles that I ran into along the way. Without his mentorship the work accomplished in this thesis would have not been possible.

This definitely wouldn't have been possible without the helpful discussions from my good friend and collaborator Yue Shi Lai whose suggestions helped me look at my analysis in a different way. Without his incredible physics intuition, it's not clear how much longer it would have taken me to finish my thesis.

I also owe deep gratitude to the Columbia group members that engaged with me in many interesting discussion and helped me along the way. Honorable mentions are Brian Cole for his useful insight during group meetings, Dave Winter for hammering in proper C++ coding skills into my skull, Aaron Veicht who over the last couple of years provided coffee, humor, and interesting discussions to my "stupid" questions. Other group members that I will quickly mention are Dennis Perepelitsa, Aaron Angerami, and Nathan Grau.

I should mention the individuals at San Diego State University who were

integral into my career in physics and pushing me to further pursue a graduate degree. Professor Terrance Frey allowed me to conduct research in his biophysics laboratory and provided moral support throughout my years there. Professor Douglas B. Grotjahn allowed me to conduct research in his chemistry laboratory. Professor Ray Menegus unknowingly steered me away from medical school with his enthusiasm in his Mathematical Methods in Physics course which eventually persuaded me to change my major to physics - one of the best decisions of my life. The MARC and MBRS program at SDSU whose excellent program provided support to myself and many other individuals who otherwise would have found it difficult to conduct research, and much less, pursue a higher education degree.

I must also thank my friends who throughout the years have provided much support. Back at home, my childhood "homies": Adrian Robles and Gerardo "Jerry" Lopez. Friends from undergrad: Phillip Poon, Peter Betts, Aleksander Simic, Genaro Hernandez, and many others. Also my friends at Columbia: William Horowitz, Christopher Kelly, Matthew Lightman, Guillaume Plante, Mina Fazlollahi, Gary Steinberg, Jeremy Carlo, Jiamin Jin, Simon Wicks, Azfar Adil, Tatia Engelmore, Yujiao Chen, and many others who are too numerous to mention.

I would like to thank Ciara Daniels for being a great friend and partner. Her kindness, love, and support made the last year of graduate school go much smoother than it otherwise would have gone.

Finally, I must thank my family. My godparents, Martha and Beto Huezo, for their encouragment, support, and fun times we had together. My father for providing support through my early years in life and who I hope can one day get his life back on track. My sister, Lupita Zambrano, who not only provided the love and care that younger brother could only wish for, but also paved the way by becoming the first person in our family to graduate from college. Without her mentorship and connections at SDSU my academic

path would have undoubtedly not been the same. And last but not least, I owe my deepest gratitude to my mother, who has been my biggest supporter throughout my life. Especially for having the courage to arrive in a strange country at a young age, in search for a better life, and having the will to provide the opportunities for her children when all odds were against her. My achievements in life reflect her achievements as a parent. Thank you.

Dedicated to my mother

Chapter 1

Introduction

Experimental science, and in particular physics, has offered an unprecedented understanding of the universe we live in. Observations and measurements made prior to the 20th century gave way to elegant theories on the electromagnetic and gravitational interaction of matter that could capture our every day experience of the natural world in a relatively intuitive manner [1] [2]. However the 20th century, with the formulation of Quantum theory and General Relativity, experienced a scientific revolution that led to deep, and often bizarre, consequences that have resulted in a huge departure from our intuitive understanding of the universe. All of this has culminated into nature revealing itself in the form of three fundamental interactions: gravity, electroweak, and strong interaction.

Much of what we now understand with regards to sub-atomic physics can be attributed to the development of high-energy colliders. A great deal has been explored with regards to the discovery of fundamental particles such as the $W^{\pm}$, Z, Higgs, etc... However, much less attention has been given to other fundamental aspects of the interactions of sub-atomic particles. In particular, the prospects of forming a new state of matter, i.e. the Quark-Gluon Plasma, at high temperatures from the collisions of heavy ions have

provided increased interest due to its implications to various fields in physics.

A study is provided in collaboration with the Relativistic Heavy Ion Collider (RHIC), into the exploration of signatures that will shed light into the creation and characterization of the Quark-Gluon Plasma.

1.1 For the skeptics: motivation for high-energy nuclear physics

The ever-pressing need to build larger, more complex, and thus more expensive experiments has, at times, called into question the relevance of high-energy nuclear physics. To put into perspective the importance of high energy nuclear physics it is useful to use atomic physics as an anology. With the development of quantum mechanics in the early half of the 20th century, the detailed physical structure of the hydrogen atom became apparent and along with it the description of many physical effects that could only be explained by the quantum theory of matter. From a reductionists point of view, this became the pinnacle achievement of atomic physics. However, the macroscopic properties of matter, the *collective behavior* of atoms, often does not lend it self to the tools that are used in atomic physics due to the difficulty in describing a N-body problem, and at times new phenomena emerge from this collective behavior that require a different approach to be taken (e.g. superconductivity) [3]. This difficulty often opens the door for experimentalists in the field to pave the way for new discoveries. In consequence, the fields of chemistry and condensed matter have devoted their time to the study of this collective behavior of atoms and currently represent much of the excitement in material science (e.g. nanotechonology, high-temperature superconductors).

In a very similar way, the Standard Model, and more specifically Quantum

Chromodynamics (QCD), has revealed and predicted the inner most workings of nuclear matter (e.g. quarks, gluons). Because of the non-Abelian nature of QCD, and therefore the approximations that need to be made such as a perturbative approach (pQCD) in order to make predictions, much of the measurements performed have been left to high-energy colliders for verification. Yet progress has been slow in the study of collective behavior in nuclear matter and its consequences to our understanding of the early cosmos. Many of the early theoretical developments led to the prediction of an asymptotically free state of nuclear matter, the Quark Gluon Plasma (QGP), beyond a critical temperature. Since then, many of the new developments can be attributed to the collision of dense nuclear matter at high energies and the unexpected new phenomena that has emerged from the creation of dense nuclear matter that require a different approach to explain the observed phenomena (e.g. hydrodynamics, "perfect liquid", AdS/CFT correspondence).

Just as in condensed matter, recent measurements in high-energy physics have provided new wonders regarding the collective behavior of matter that lack a rigorous explanation to date. The next chapter will go into detail of the current state of both experimental and theoretical high-energy nuclear physics, but first a brief description of QCD is in store.

Chapter 2

High-energy nuclear physics

2.1 Quantum Chromodynamics

One can probably trace the beginnings of the strong interaction, QCD, to James Chadwick's 1932 discovery of the neutron [4]. Up until that moment, the lack of a satisfactory model to describe the attributes of the nucleus eluded physicists. The neutron, not only provided the quanta needed to explain the discrepancy between atomic mass, A, and atomic number, Z, but provided a possible insight into the interaction of nucleons.

Given the striking similarity of the proton and the neutron, Werner Heisenberg was inspired to propose the first theory of nuclear matter: the theory of hadronic isospin [5]. The proposal was that in the absence of the electromagnetic interaction (i.e. charge), the neutron and proton were an internal degree of freedom for the strong interaction and represented the basic quanta of the theory. Although hadronic isospin, in retrospect, is clearly an approximation, it provided an important stepping stone in the development of a theory for the strong interaction. In fact, in 1953 it was hadronic isospin that led Chen Nin Yang and Robert Mills, in an effort to impose local gauge invariance to a system of $SU(2)$ symmetry, that led them to discover local

gauge invariance for non-Abelian groups which would later be used to describe the local symmetry, i.e. $SU(3)$, of the strong interaction [6]. There was much speculation in the high-energy community on approaches other than a field theory, until the SLAC experiments revealed *scaling* in deep-inelastic experiments that would eventually play a crucial role in elucidating the structure of the hadrons [7]. The scaling behavior indicated the presence of a non-interacting field theory at high energies. Eventually, the development on renormalizable non-Abelian gauge theories along with *asymptotic freedom*, the vanishing of the effective coupling at short distances, led to the most successful description of the strong interaction to date: Quantum Chromodynamics [8] [9] [10] [11] [12]. The QCD Lagrangian is given by,

$$\mathcal{L}_{\mathrm{QCD}} = -\frac{1}{4} G^{\alpha}_{\mu\nu} G^{\mu\nu}_{\alpha} - \sum_{n} \overline{\psi}_n \gamma^{\mu} [\partial_{\mu} - i g A^{\alpha}_{\mu} t_{\alpha}] \psi_n - \sum_{n} m_n \overline{\psi}_n \psi_n \tag{2.1}$$

$$G^{\alpha}_{\mu\nu} = \partial_{\mu} A^{\alpha}_{\nu} - \partial_{\nu} A^{\alpha}_{\mu} - g f^{\alpha}_{\beta\gamma} A^{\beta}_{\mu} A^{\gamma}_{\nu} \tag{2.2}$$

where ψ_n are the quark fields, A^{α}_{μ} the gluon fields, $G^{\alpha}_{\mu\nu}$ is the gluon field tensor, $f^{\alpha}_{\beta\gamma}$ are the $SU(3)$ structure constants, t_{α} are the generators in the fundamental representation, and g is the coupling strength. One of the major consequences of QCD is the *confinement* of quarks in the vacuum, the postulate that individual quarks cannot be observed as a final state particle [13], has been in experimental agreement to date. However, as will be described, the behavior of nuclear matter, i.e. quarks and gluons, at high temperatures is predicted to make a phase transition to *deconfined* nuclear matter which might give some insight into the evolution of the universe in the first few microseconds.

2.2 Collective behavior of strongly interacting particles

As is often the case, the curiosity of taking matter to extreme conditions is often one which is initially of theoretical interest which hopefully becomes experimentally feasible. In the 1950's there was some early theoretical exploration into the consequences of nuclear matter at high temperature [14] [15], but it wasn't until 1974 that T.D. Lee and G.C. Wick started looking at metastable excited vacuum states [16] and relating it to a finite volume, such as a heavy ion nucleus, was there a realization that a phase transition for nuclear matter was possible. Further studies and calculations performed by *lattice QCD* revealed a better picture of the expected phase transition for QCD (see Figure 2.1).

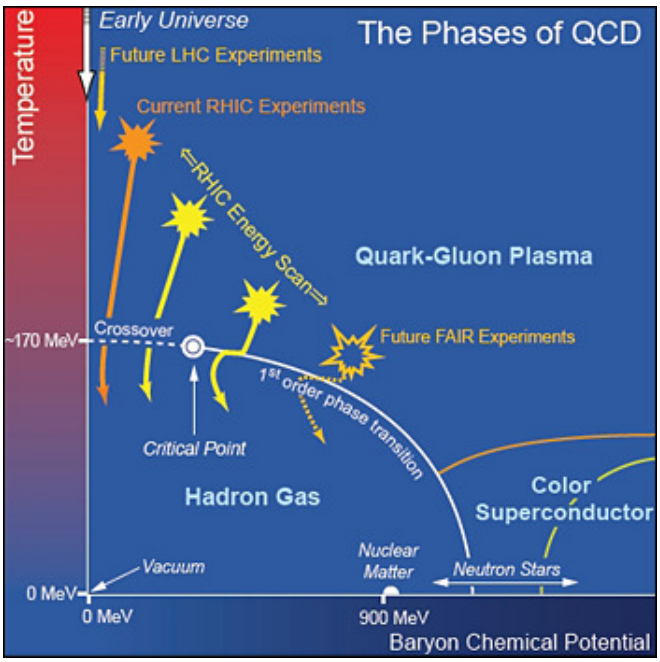

Figure 2.1: T vs. μ phase diagram of nuclear matter.

It has thus been left to heavy ion collision experiments to determine if a deconfined state of nuclear matter can be observed. However, before any evidence is put forward for the production of the QGP, a description of the measurement of *impact parameter* will explained which is central to the characterization of heavy ion collisions.

2.2.1 Centrality: an indirect measure of impact parameter b

The measurement of impact parameter, b, between collisions, which is in the order $\sim 10^{-15}$ m, is not directly measurable given the resolution of the current experiments ($\sim 10^{-5}$ m). Therefore alternative model dependent methods have been developed to statistically measure the impact parameter of a collision. The most widely used method relies on the Glauber model which relates the total particle production of an event to the nucleon-nucleon *inelastic* cross section [17].

To define the probability of finding a nucleon in a nucleus in the Glauber model, there are a few assumptions that are needed. The first assumption is that nucleon density takes the following form:

$$\rho(r) = \rho_0 \cdot \frac{1 + w(r/R)^2}{1 + \exp\left(\frac{r-R}{a}\right)} \tag{2.3}$$

where ρ_0 is the nucleon density at the center of the nucleus, R is the radius of the nucleus, a is the *skin depth* at the edge of the nucleus, and $w(r/R)$ is the deviation from uniform density. The second is use of the experimentally determined *inelastic* cross-section, $\sigma_{\text{inel}}^{\text{NN}}$ which for RHIC at $\sqrt{s_{NN}} = 200$ GeV is in the neighborhood of 42 mb.

To determine the *probability per unit transverse area* of finding a nucleon at a given position, the probability per unit volume, $\hat{\rho}_A(\mathbf{s}, z_A)$ is integrated

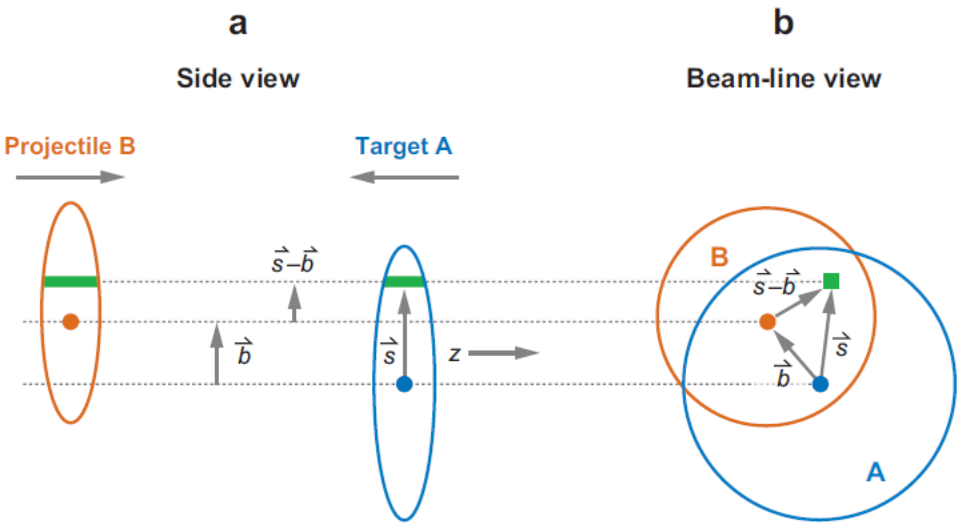

Figure 2.2: Illustration of two incoming nuclei along in the longitudinal and transverse direction.

in the longitudinal direction.

$$\hat{T}_A(\mathbf{s}) = \int \hat{\rho}_A(\mathbf{s}, z_A) dz_A \tag{2.4}$$

From this point, two different approaches can be taken: the *optical limit* or the Monte Carlo approach. The optical limit takes the approach of convoluting nucleon probability distributions $\hat{T}_A(\mathbf{s})$ and $\hat{T}_B(\mathbf{s}-\mathbf{b})$ of incoming nuclei A and B,

$$\hat{T}_{AB}(\mathbf{b}) = \int \hat{T}_A(\mathbf{s})\hat{T}_B(\mathbf{s}-\mathbf{b}) d^2s \tag{2.5}$$

to give the effective overlap area with which nucleus A can interact with nucleus B. From $\hat{T}_{AB}(\mathbf{b})$ the total number of collisions, $N_{\text{coll}}(b)$, and the number of interacting nucleons, $N_{\text{part}}(b)$, can be calculated. However, the shortcomings of the optical limit lie in the fact that for an incoming nucleon it sees the target as a smooth density. For this reason, the granular Monte Carlo

(MC) approach is preferred since it can describe local density fluctuations event-by-event.

The Glauber MC, in the simplest approach, assumes that there will be an interaction if the transverse distance d between any two nucleons is less than predetermined value:

$$d \leq \sqrt{\sigma_{\text{inel}}^{\text{NN}}/\pi} \tag{2.6}$$

Other implementations use Gaussian overlap functions to determine if an interaction takes place. Figure 2.3 illustrates the granularity of the nucleus

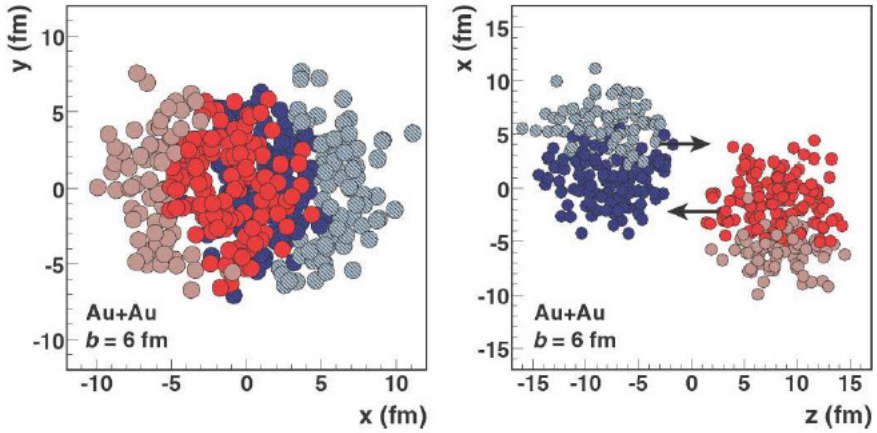

Figure 2.3: Illustration of Glauber Monte Carlo event. Darker colored nucleons represent participating nucleons (N_{part})

when using the Monte Carlo method. As a result, the total cross-section is better represented by,

$$\begin{aligned}\sigma_{AB} \;=\; & \int d^2b \int d^2s_1^A \cdots d^2s_A^A d^2s_1^B \cdots d^2s_B^B \times \\ & \hat{T}_A(\mathbf{s_1^A}) \cdots \hat{T}_A(\mathbf{s_A^A}) \hat{T}_B(\mathbf{s_1^B}) \cdots \hat{T}_B(\mathbf{s_B^B}) \times \\ & \left\{ 1 - \prod_{j=1}^{B} \prod_{i=1}^{A} [1 - \hat{\sigma}(\mathbf{b} - \mathbf{s_i^A} + \mathbf{s_j^B})] \right\}\end{aligned} \tag{2.7}$$

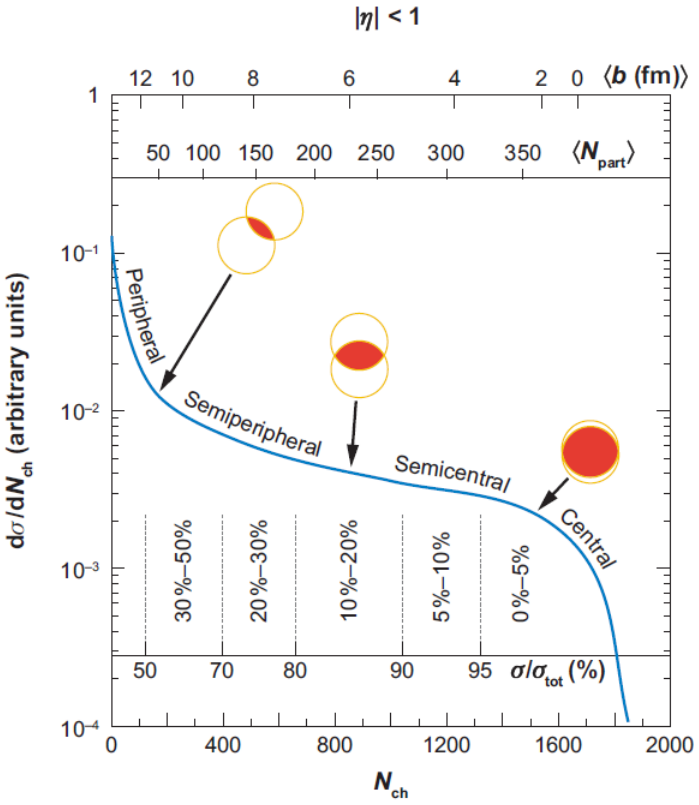

Figure 2.4: $dN_{\rm evt}/dN_{\rm ch}$ distributions demonstrating division of *centrality classes*.

and,

$$\int d^2s\ \hat{\sigma}(\mathbf{s}) = \sigma_{\rm inel}^{\rm NN} \tag{2.8}$$

As has been measured in recent experiments [18] [19], the event-by-event fluctuations can become significant in certain phase space regions.

In order to relate the Glauber MC collision parameters to an experiment, the measured multiplicity distributions, $dN_{\rm evt}/dN_{\rm ch}$, are mapped to those generated by Glauber MC distributions. These mapping procedures can differ between collision systems and experiments. One basic assumption is

that the impact parameter, b, monotonically decreases with respect to event particle multiplicity. Once the particle multiplicity distributions have been measured, which are well described by a negative binomial distribution, the distribution is binned in *centrality* classes where centrality is defined by (see Figure 2.4),

$$100 \times \frac{\int_{0}^{N_{\text{cent}}} dN_{\text{ch}}\, dN_{\text{evt}}/dN_{\text{ch}}}{\int_{0}^{\infty} dN_{\text{ch}}\, dN_{\text{evt}}/dN_{\text{ch}}} = \text{Centrality} \tag{2.9}$$

In particular, for a given centrality bin (e.g. 10-20%), it is up to the experiment to determine N_{cent} for the lower (10%) and the upper (20%) limit for that particular bin. One of the obstacles encountered when determining centrality bins is the efficiency of accepting inelastic collisions by the minimum bias triggers in a given experiment (see Section 4.1) which will typically limit the acceptance of peripheral collisions. Care must be taken to also use detectors that are minimally sensitive to hard scattering interactions (large Q^2) in a given event since the multiplicty of hard scattering events tends to be larger than minimum bias events.

2.2.2 A first look: Nuclear Modification Factor R_{AA}

One of the first measurements performed at RHIC to determine if the heavy ion collision high temperature environment differed from p+p was the comparison of particle species production per nucleon pair. By scaling the heavy ion collision particle production, dN^{AA}/dp_T by the nuclear overlap function, $\langle T_{AA} \rangle$, determined through the Glauber Monte Carlo to get the particle production per nucleon pair, one can measure the deviation of particle production with respect to p+p :

$$R_{AA}(p_T) = \frac{dN^{AA}/dp_T}{\langle T_{AA} \rangle \times dN^{pp}/dp_T} \tag{2.10}$$

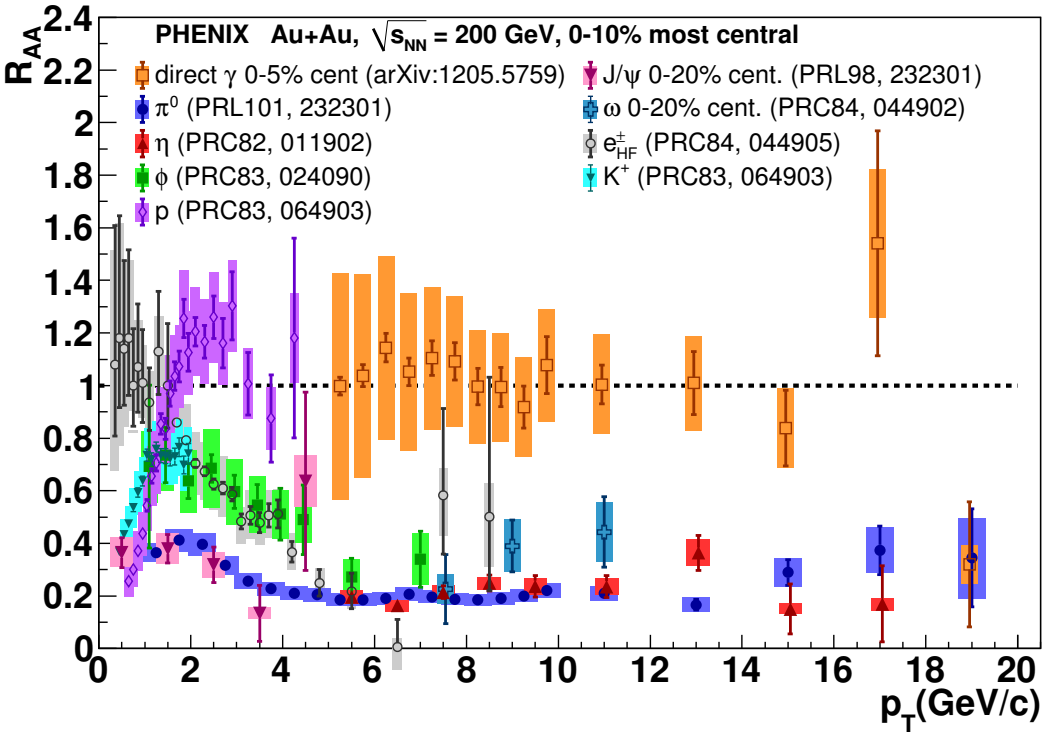

Figure 2.5: R_{AA} vs p_T measurements at PHENIX for selected particle species at various centralities.

The very first measurements that came out of RHIC displayed a strong suppression of high-p_T tracks which hinted at the formation of a dense strongly interacting medium [20] [21]. Figure 2.5 demonstrates the p_T dependence of R_{AA} for selected particle species in the most recent measurements at PHENIX. The direct photons, which are not expected to interact with a colored medium, provide a systematic check on the scaling of the cross-section. From the figure, which currently represents the most recent data, the direct photon production is observed to be consistent with an $R_{AA} \sim 1$ and provides confidence in the experiment's systematics. Except for protons, all particle species display a large suppresion that seems to plateau at $R_{AA} \sim 0.2$ for

$p_T > 5$ GeV.

Various explanations have attempted to describe the observed R_{AA}, each with its own assumptions, but there is yet to be a well agreed upon mechanism for this effect. There has even been some criticisms as to how well R_{AA} is able to constrain the different mechanisms that are expected to have a significant effect on the particle spectra. As a result alternative methods for probing the particle production in heavy ion collisions have been pursued.

2.3 Phase transition at T_c

It is natural to ask, given that arguments that have been made regarding a phase transition occuring, whether a critical temperature, T_c, can be predicted and measured. One of the very first estimations of T_c was due to James D. Bjorken in which a Landau hydrodynamic model and a longitudinal medium expansion resulting from heavy ion collisions was imposed [22]. The resultant estimate was attributed to collisional energy loss, ΔE_{coll} and thus predicted the phase transition to occur at temperatures $\gtrsim 200 - 300$ MeV. Nevertheless, it is instructive to lay out some of the key features of this prediction. If one assumes the dense nuclear matter to be an ideal gas of quanta with g degrees of freedom, one can derive an equation of state in accordance with the Stefan-Boltzmann law.

$$P = g \cdot \frac{\pi^2}{90} T^4 \tag{2.11}$$

At low temperatures, one can assume the degrees of freedom to take the form of pions ($\pi^{\pm}$, π^0), where $g = 3$. At high temperatures, the degrees of freedom are assumed to take the form of quarks and gluons including their corresponding internal degrees of freedom (e.g. spin, flavor, color, particle-

antiparticle, and statistics),

$$g = \left\{(2 \text{ spin} \times N_g) + \frac{7}{8}(2 \text{ spin} \times N_c \times N_f \times 2)\right\} \tag{2.12}$$

$$= 37 \tag{2.13}$$

where it the number of flavors and colors was set to $N_f = 2$ and $N_c = 3$. In addition, for the quark-gluon gas there is an added *bag pressure*, B, exerted by the vacuum on the medium. The resultant equation of state becomes,

$$P_{\text{QGP}} = 37 \cdot \frac{\pi^2}{90} T^4 - B \tag{2.14}$$

These represent the two extreme forms of matter below and above the critical temperature. However at T_c, the pressure from the two equation of states are expected to be equal to each other and one can use this to estimate the temperature at which the phase transition occurs.

$$3 \cdot \frac{\pi^2}{90} T_c^4 = 37 \cdot \frac{\pi^2}{90} T_c^4 - B \tag{2.15}$$

$$\implies T_c = \left(\frac{45}{17\pi^2}\right)^{1/4} B^{1/4} \tag{2.16}$$

From hadronic spectroscopy, the bag pressure is taken to be in the order of 200 MeV which therefore puts the critical temperature at around $T_c \sim 150$ MeV. As will be discussed, this is not too far from the most recent calculations of the critical temperature.

2.3.1 Lattice QCD

Near the critical temperature, where the running coupling is expected to be strong ($\alpha_s > 1$), non-perturbative techniques need to be employed so that the critical temperature can be estimated. Luckily, there is a systematic

method to calculate the low energy structure of QCD provided by lattice gauge theory. By descretizing QCD in Euclidian space-time, then the path integral formulation is equivalent to the Boltzmann distribution where the Boltzmann weights are given by the discretized action [23].

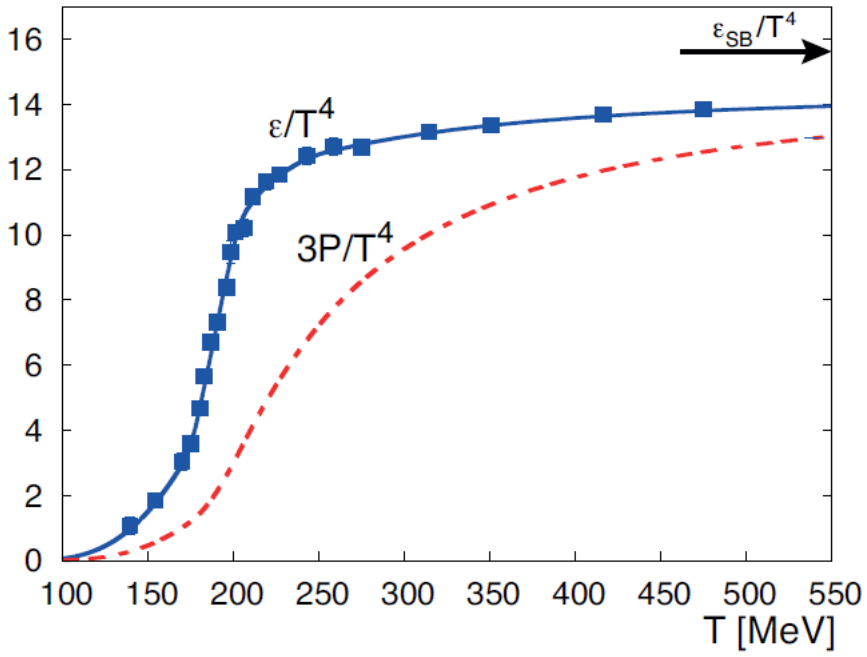

Figure 2.6: The Lattice QCD calculation of energy density (ε/T^4) and pressure ($3P/T^4$) dependence on temperature [24]. Arrow shows the energy density Stefan-Boltzmann limit.

It has been lattice QCD which has provided the most reliable estimate of the critical temperature for the QGP phase transition. Figure 2.6 demonstrates the most recent 2+1 flavor Monte-Carlo calculation [24] which puts the critical temperature in the range of $180 \lesssim T_c \lesssim 200$ MeV. In addition, lattice QCD provides an estimate of the equation of state of the thermalized system which can be used as input to hydrodynamic models (see Sec-

tion 2.4.1).

2.4 Thermalization of the medium

The application of thermodynamics to a system is always of interest to a multiparticle system such as the one encountered in heavy ion collisions [25]. However, in order for thermodynamics to be valid, the system has to reach thermal equilibrium quickly so that properties such as pressure, temperature, and entropy can be well defined. The most notable use of this assumption has been the application of *hydrodynamics* to the data that has come out of RHIC. Some of the implementations of hydrodynamics in heavy ion collisions will be briefly described.

2.4.1 Hydrodynamics

Hydrodynamics, in general, requires only one assumption: local thermodynamic equilibrium. Therefore the validity of a macroscopic description of heavy ion collisions using hydrodynamics requires that sufficiently large momentum transfer rates occur at the microscopic scale. Such an assumption requires a fast *relaxation time*, τ, to local thermal equilibrium when compared to the macroscopic scale. For this to be possible at RHIC, relaxation times need to be no larger than 1-2 fm/c, which were initially thought to be unattainable. However, application of hydrodynamics to measurements at RHIC using Au+Au at $\sqrt{s_{NN}} = 200$ GeV have provided astonishing agreement with the spectra for low-p_T particles.

If local thermal equilibrium is reached, then the hydrodynamics of a fluid with no dissipation, an *ideal fluid*, is described by the energy-momentum tensor,

$$T^{\mu\nu}(x) = (\varepsilon(x) + p(x))\, u^{\mu}(x) u^{\nu}(x) - p(x) g^{\mu\nu} \tag{2.17}$$

where $\varepsilon(x)$ is the energy density, $p(x)$ the pressure, and $u^{\mu}(x)$ is the Lorentz invariant four-velocity of the fluid ($u^{\mu}u_{\mu} = 1$). The local conservation of energy implies the following:

$$\partial_{\mu}T^{\mu\nu}(x) = 0 \tag{2.18}$$

It should be emphasized that hydrodynamics is only valid during a finite interval of time, i.e. the thermalized stage. Therefore the evolution of thermalization is dependent on the *initial conditions* of the collision prior to thermalization. Assumptions need to be made with regards to the initial conditions which have led to distinctive approaches, each with its own assumptions, that in turn have led to various degrees of agreement (e.g. three fluid dynamics, Glauber model, kinetic theory using transport models such as parton cascades).

As the medium evolves and expands, there comes a time where thermal equilibrium starts breaks down due to decreasing thermalization rates, i.e. *freeze-out*. The traditional way to describe the *freeze-out* stage is to use the Cooper-Frye formalism. The Cooper-Frye formalism defines a kinetic freeze-out criterion and then determines a hypersurface $\Sigma(x)$ at which this criterion occurs to compute the final spectrum of particles of a given type. One of the criticisms of this approach is the lack of p_T dependence which should be significant for high-p_T particles since they require a larger number of rescattering to reach thermal equilibrium. This might account for some of the deviations observed when comparing hydrodynamic models to RHIC data at high-p_T. Other shortcomings include possibility of space-like normal surface vector $d^3\sigma$ to $\Sigma(x)$ that leads to a counting of negative flux particles into the thermalized medium. More proper treatements of the Cooper-Frye formalism include the use of transport theory to "soften" the transition surface to describe a more realistic gradual transition from thermalized fluid to

freeze-out.

2.4.2 Elliptic flow

The p_T dependence of v_2 has been widely considered as evidence that the $\sqrt{s_{NN}} = 200$ GeV Au+Au collisions at RHIC reach thermal equilibrium [26]. Here, a "bare bones" description of hydrodynamics is outlined to display the essential features that describe the elliptic flow data.

If the radial expansion of the fluid is assumed to be in thermal equilibrium throughout most of its expansion, the momentum distribution of the final state particles can be assumed to be the same as in the fluid and be given by Boltzmann statistics. Furthermore, since the energy of the particles in the fluid rest frame, E^*, is invariant and can by represented in the laboratory frame by the particle velocity (p^μ) and fluid velocity (u^μ),

$$E^* = p^\mu u_\mu \tag{2.19}$$

given that $p^\mu u_\mu$ is a Lorentz scalar and it reduces to p^0 in if the fluid velocity is zero. If one assumes that the fluid velocity and particle velocity are parallel then the energy can be represented by,

$$E^* = m_T u^0 - p_T |\vec{u}| \tag{2.20}$$

where $m_T = \sqrt{p_T^2 + m^2}$ is the transverse mass. Substituting this energy into the Boltzmann factor gives the *isotropic* distribution of particles.

$$\frac{dN}{p_T dp_T dp_z d\phi} \propto \exp\left(-\frac{E^*}{T}\right) \tag{2.21}$$

$$\propto \exp\left(\frac{-m_T u_0 + p_T |\vec{u}|}{T}\right) \tag{2.22}$$

Because pressure gradients are expected to develop in the expansion of the

medium, especially in mid-central events, the velocities can be parametrized to depend on the azimuthal angle, ϕ, relative to the reaction plane Ψ_{RP} (see Figure 2.7).

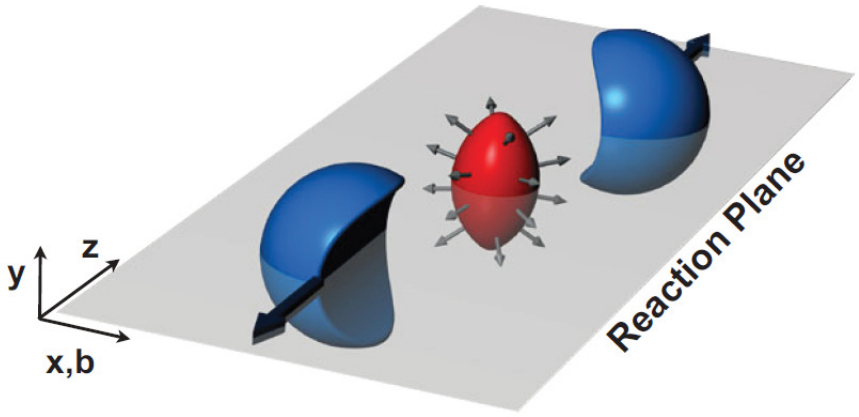

Figure 2.7: Mid-central heavy ion collision defining the reaction plane Ψ_{RP}.

$$\vec{u}(\phi) = \langle \vec{u} \rangle + 2\alpha \cos(2[\phi - \Psi_{RP}]) \tag{2.23}$$

In the previous equation α is a coefficient characterizing the elliptic flow. From $u^0 = \sqrt{u^2 + 1}$, expanding to leading order in α, the u^0 component can be approximated to be,

$$u^0(\phi) = \langle u^0 \rangle + 2v\alpha \cos(2[\phi - \Psi_{RP}]) \tag{2.24}$$

where $v = |\vec{u}|/u_0$. Substitute the azimuthal dependent velocities into the Boltzmann factor and expand with respect to α:

$$\begin{aligned} \exp\left(\frac{-m_T u_0(\phi) + p_T|\vec{u}(\phi)|}{T}\right) &\simeq 1 + \left(\frac{-m_T u_0(\phi) + p_T|\vec{u}(\phi)|}{T}\right) \\ &= 1 + \frac{1}{T}\left(-m_T\langle u^0\rangle + p_T\langle \vec{u}\rangle + \right. \end{aligned}$$

$$2\alpha(p_T - vm_T)\cos(2[\phi - \Psi_{RP}]))$$

Making the connection to the Fourier expansion coefficients, it is immedi-

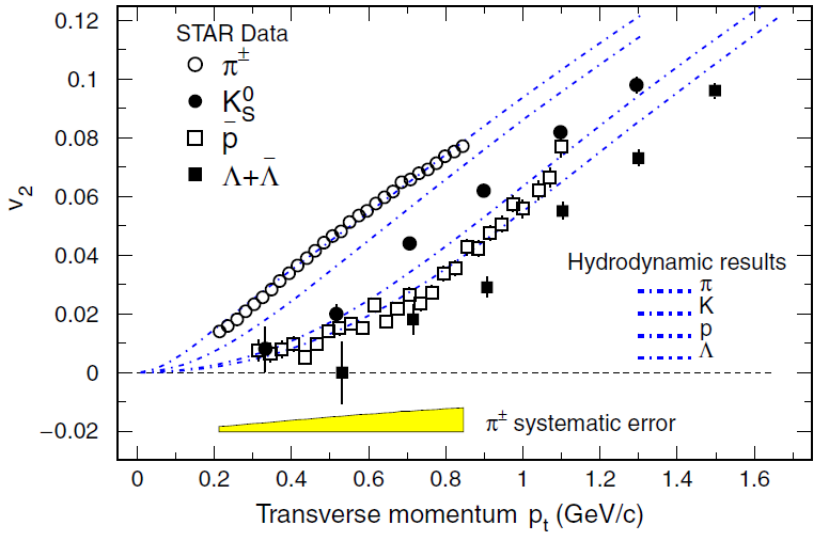

Figure 2.8: Identified particle v_2 vs. p_T [26]. Dashed lines represent hydrodynamic calculations for a given particle species.

ately observed the m_T and p_T dependence of v_2.

$$v_2 = \frac{\alpha}{T}(p_T - vm_T) \tag{2.25}$$

One of the key features of these equations is the mass dependence via m_T of the v_2 coefficient which suggests that heavier particles will result in a lower v_2 coefficient. Figure 2.8 displays measured v_2 vs. p_T spectra and exemplifies the mass dependence predicted by hydrodynamics. It really is astonishing the agreement with which hydrodynamics agrees with the data for $p_T < 2$ GeV using the simple assumptions stated above. At a p_T above 2 GeV/c, the agreement with hydrodynamics starts to break down and as a result there is a wide belief that dissipative (transport) contributions need to be included

in the models in order to better describe the data.

2.5 Jet quenching

Particles resulting from the fragmentation process of a hard scattered parton were some of the features of QCD that allowed for the calculation of many QCD processes in the high-energy regime. Much of this development can be attributed to the *factorization theorem* which states that there can be a separation of short-distance and long-distance behavior and as a result a systematic approach can be used to predict high-energy cross-sections using pertubation theory [27]. So it is no surprise that hard probes are of increased theoretical and experimental interest in heavy ion collisions since they might provide predictions on the properties of the medium and the behavior of hard partons as they propagate through the medium.

There are a number of models that attempt to describe energy-loss phenomena for hard-scattering partons observed in heavy ion collisions. Since energy loss ($-dE/dx$) is very well understood in QED, many of the approaches use the formalisms developed in QED and apply it to QCD (i.e. Bethe-Heitler and Landau-Pomeranchuk-Migdal(LPM)). Furthermore, since these models take a perturbative approach, all of the predictions lie in the high-p_T regime. Many different assumptions are made in the most popular models in order to make the calculations tractable. A description is shortly outlined here.

- **BDMPS:** In this approach the energy-loss, ΔE, is determined by assuming that a parton traveling through the medium radiates multiple soft gluons by scattering of static centers. By assuming a *static* medium where the formation time for radiation is smaller than the mean-free path length, λ_g, of the radiated gluon, an expression can be derived using the QED solution by identifying the emission angle of photons with

the transverse momentum, $p_\perp$, of the gluon [28]. In such a scenario the radiation spectrum is given by,

$$\omega \frac{d^2I}{d\omega dz} = \frac{6\alpha_s C_R}{\pi L} \ln \left| \frac{\sin(\omega_0 \tau_0)}{\omega_0 \tau_0} \right| \tag{2.26}$$

It is straight forward to determine the energy loss of a parton traversing the medium:

$$-\frac{dE}{dz} = \int \omega \frac{d^2I}{d\omega dz} d\omega \tag{2.27}$$

$$= \frac{\alpha_s C_R}{8} \frac{\mu^2}{\lambda_g} L \ln\left(\frac{L}{\lambda_g}\right) \tag{2.28}$$

or,

$$-\Delta E = \frac{\alpha_s C_R}{8} \frac{\mu^2}{\lambda_g} L^2 \ln\left(\frac{L}{\lambda_g}\right) \tag{2.29}$$

Different expressions can be obtained depending on the assumptions (e.g. expanding medium), yet the relevant information extracted from this approach is the prediction that $\Delta E \propto L^2$ as partons propagate through the medium.

- **GLV:** This formalism uses the Reactive operator approach to hard partons having multiple interactions in the medium. By solving this formalism order by order through the mean number of scatterings (i.e. opacity expansion), the contributions to the partonic cross section are obtained [29]. The radiation spectrum is represented by a recursive approach where the starting point is the *single-hard* radiation spectrum [30]:

$$\omega \frac{dI^{(1)}}{d\omega dk_\perp^2} = \omega \frac{dI^{(0)}}{d\omega dk_\perp^2} \frac{L}{\lambda_g} \int_0^{q_{\max}^2} d^2q_\perp \frac{\mu^2}{\pi \left(q_\perp^2 + \mu^2\right)^2} \frac{2k_\perp \cdot q_\perp \left(k - q_\perp\right)^2 L^2}{16\omega^2 + (k-q)_\perp^4 L^2} \tag{2.30}$$

where μ is the color-screened mass, q is the momentum transferred to the parton, and k is the momentum of the radiated gluon. The resulting energy loss relation is given by,

$$\Delta E = \frac{C_R \alpha_s}{4} \frac{L^2 \mu^2}{\lambda_g} \log \frac{E}{\mu} \tag{2.31}$$

which contains the same L^2 dependence found in the BDMPS formalism. However, the logarithmic factor in the GLV is due to the broad logarithmic integration over gluon energies while in BDMPS it is due to small impact parameters.

- **AMY:** This diagrammatic method determines the leading-order photon emmission via LPM formalism through the heirarchy of *scales* ($T \gg gT \gg g^2T$) as a parton propagates through a static scattering centers of a thermalized medium at temperature T [31]. Once a leading-

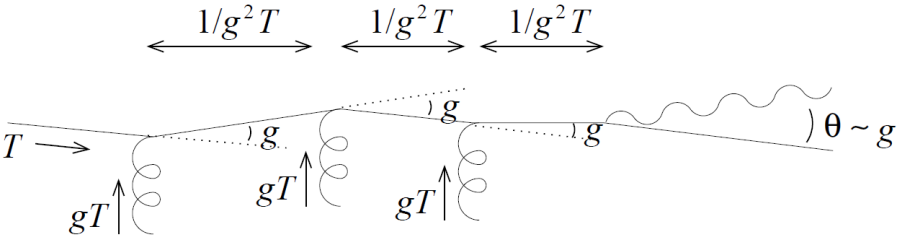

Figure 2.9: Orders of magnitude of various momentum, distance, and angular scales associated with bremsstrahlung of a photon with momentum of order T. The coupling strength is denoted by g.

order photon emission spectrum equation is derived, the expression is extended to derive an expression for gluon emission spectrum. The key difference in making the extension is that the gluon carries *color* charge. Thus the time evolution amplitude will include, unlike the pho-

ton emission spectrum, contributions of the emitted gluon interacting with the colored background field and, in addition, the color matrix T^A_{ab} will contribute to the hard particle vertex.

- **Higher-Twist:** This approach studies the parton energy-loss through deep inelastic scattering of nuclei. In particular, this is accomplished by expressing the energy-loss in terms of modified fragmentation functions.

2.5.1 Two-particle correlations

Some of the first methods to study hard scattering interactions came from the ISR at CERN. It had been proposed that the study of high-p_T final state particles [32], and in particular correlations among these particles [33], would reveal the topology of *jets* in hadron collisions. Eventually these were superceded by the development of jet reconstruction algorithms in e^+e^- and p+p collision systems which provided more details into the hard scattering processes.

At RHIC a similar approach has been taken due to the initial difficulties encountered in attempting to use jet reconstruction algorithms. To validate the measurement of jets using this method at RHIC energies, the first study performed at PHENIX was using p+p collisions at $\sqrt{s} = 200$ GeV [34]. Azimuthal correlations among particle pairs were shown to display jet-induced correlations expected from di-jet production (see Figure 2.10). The relative kinematics were studied to measure the jet transverse fragmentation momentum, $\sqrt{\langle j_T^2 \rangle}$, and the *intrinsic* partonic transverse momentum, $\sqrt{\langle k_T^2 \rangle}$ (see Figure 2.11 for definitions). The $\sqrt{\langle j_T^2 \rangle}$ and $\sqrt{\langle k_T^2 \rangle}$ were compared to previous measurements at similar $\sqrt{s}$ and were found to be comparable. In addition, *near-side* and *away-side* correlation widths were measured and compared to PYTHIA simulations using a $\vec{k}_T$ value in the range of that measured and were found to be in good agreement. These results provided

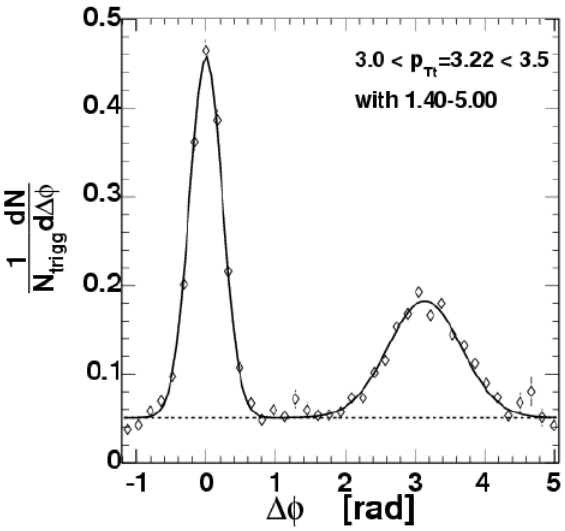

Figure 2.10: Two-particle correlation for $3 < p_{T\mathrm{t}} < 3.5$ GeV/c and associated particle $1.4 < p_{T\mathrm{a}} < 5.0$ GeV/c. The correlation is normalized to the number of π^0 triggers measured [34].

confidence in the method of two-particle correlations as a way to indirectly measure jet properties.

The first *heavy ion* two-particle correlation measurements to come out of RHIC provided the first glimpse into jet quenching for high-p_T triggers [35]. Later studies displayed a more refined study using a broader range of momenta which showed the evolution of the two-particle azimuthal distributions over a broad range of momenta [36](see Figure 2.12). In all studies using the most central Au+Au collisions at $\sqrt{s_{NN}} = 200$ GeV, the most notable effect was the dissappearance of the away-side correlation ($\Delta\phi > \pi/2$) relative to the near-side correlation above a *trigger* $p_T^a \gtrsim 4$ GeV and partner $p_T^b \gtrsim 3$ GeV[1]. This disappearance was the one of the first pieces of evidence that a

[1]There exists no consistent nomenclature and notation on the labeling of trigger and partner (a.k.a. associated) particles. Typical notation for trigger particle p_T includes p_T^a, $p_{T,t}$, p_T^t and for associated includes p_T^b, $p_{T,a}$, p_T^a. An attempt will be made to keep the

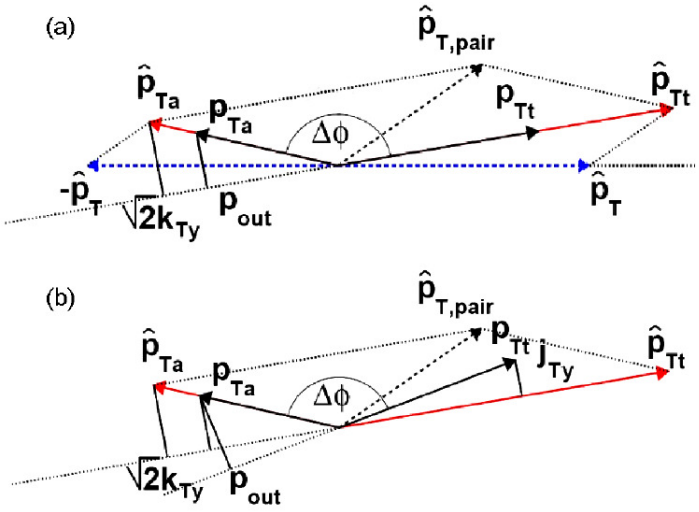

Figure 2.11: Particle kinematics in the tranverse plane to the beam. In a) the final state hard scattering partons are defined as $\hat{p}_T$ in the center-of-mass frame (blue) and are seen in the laboratory frame as $\hat{p}_{Tt}$ and $\hat{p}_{Ta}$ (red). The final state particles detected coming from the jet fragmentation process are labeled p_{Tt} and p_{Ta} which are also labeled as *trigger* and *associated*, respectively. The vector sum of partons $\hat{p}_{Tt}$ and $\hat{p}_{Ta}$ are represented by $\hat{p}_{T,pair}$ and also corresponds the sum of the $\vec{k}_T$-vector. In b) a similar schematic is drawn to measure the jet transverse fragmentation momentum, j_T.

jet-quenching mechanism was being observed. The fact that minimal reduction in the near-side jet was interpreted as an indicator that the requirement of a high-p_T particle biased the hard scattering production point to a region close to the surface of the hot dense medium. Such an interpretation would allow for one of the hard-scattered partons to travel a minimum path length, L, along the medium while allowing the other parton to travel the remaining length of the medium, hence the observed effect.

notation consistent when possible, but might change with no prior indication. Consider yourself warned.

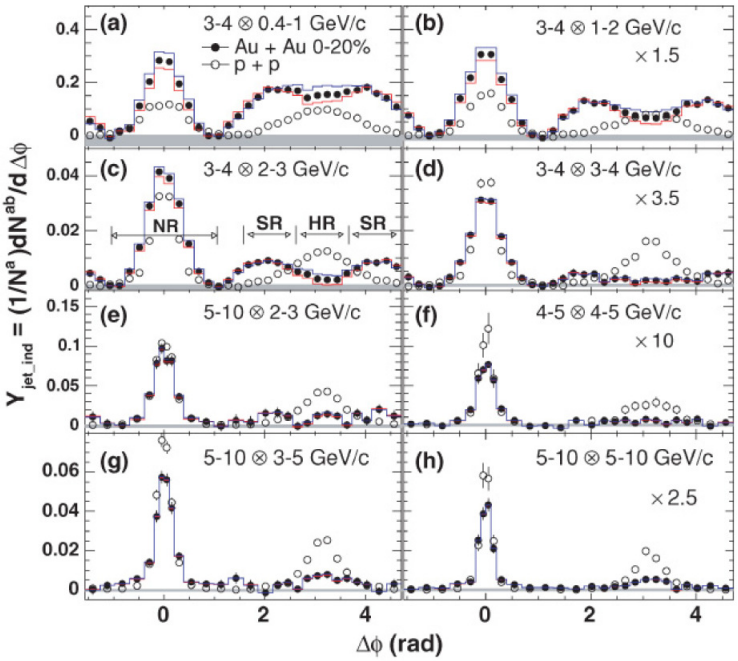

Figure 2.12: Comparison of two-particle azimuthal distributions per *trigger* in central Au+Au (0-20%) and p+p collisions. Each panel represents different particle p_T selection ($p_T^a \otimes p_T^b$). The *near-side* (NR) and *away-side* regions are depicted by in panel (c). The away-side is broken up into two regions: shoulder (SR) and head (HR) region

However, as the p_T of the particles selected starts to be reduced (associated $p_T < 2$ GeV) a much different structure was discovered. The appearance of two peaks centered around $|\Delta\phi - \pi| \sim \pm 1.1$ led to the speculation, prior to 2010, that fast partons from the hard scattering process were producing a mach cone like or gluon Čerenkov production. In addition to the away-side peaks, large $\Delta\eta$ seperation correlations around $\Delta\phi \sim 0$ were also being observed (a.k.a *the ridge*) [37]. Given the low-p_T of these effects it could only be said that it was highly probable that the effects were either originating from the bulk medium or were a result of the fast partons interacting with the

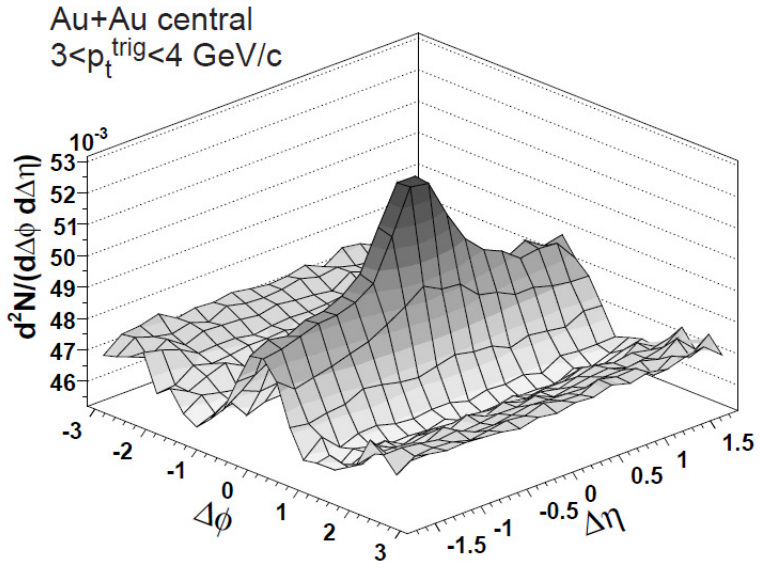

Figure 2.13: Two-dimensional two-particle correlations measured by STAR collaboration in 0-12% central Au+Au at $\sqrt{s_{NN}} = 200$ GeV [37]. Trigger p_T selection is given by $3 < p_{T\mathrm{t}} < 4$ GeV and associated p_T is given by 2 GeV/$c < p_{T\mathrm{a}} < p_{T\mathrm{t}}$. Long range correlation ("the ridge") can be observed in the $\Delta\eta$ direction around $\Delta\phi \sim 0$.

medium. However, since 2010, a widely supported alternative explanation has been brought forward which attributes both of these effects to fluctuations in collision event plane due to the granularity of the nucleus. These fluctuations would result in asymmetric fluctuations that could be measured through the v_3 Fourier coefficient. The v_3 coefficent, which was previously ignored in the subtraction of the correlated background, would explain the observed away-side peaks at $|\Delta\phi - \pi| \sim \pm 1.1$ and can account for a significant contribution to the long $\Delta\eta$ correlations seen in the near-side. Yet, as will be shown in this analysis, the away-side contribution for low-p_T associated hadrons cannot be fully accounted for through inclusion of the odd

anisotropy v_n coefficients.

Calibrated probes

In an effort to control the bias in path length, L, traveled by a hard scattered partons produced in the medium as described above, there are a few measurements that have gained increase interest over the years. Two of the leading candidate measurements that show promise in providing the path length dependence of partons are direct photon-hadron correlations (a.k.a. γ-$h^{\pm}$, γ-jet) and jet-reconstruction algorithms.

The γ-$h^{\pm}$ correlations, which has been coined as the "golden channel", has generated increased interest over time as prospects of reducing the asymmetrical effects observed on the near and away side in hadron two-particle correlations have diminished. Since the direct photons produced in the medium are, in principle, unaffected by the colored parton medium, they are expected to be minimally influenced by the QGP (aside from Compton scattering and NLO corrections which single particle measurements have shown to be negligible). The feasibility of measuring direct photons, which itself represents a product from the leading order $2 \rightarrow 2$ process, in comparison to measuring jets on a per-event basis has also contributed to its popularity. It provides a calibration of the away-side jet energy that is not possible with hadron-hadron two-particle correlations. Recent measurements in heavy ion collisions have shown a significant modification to the fragmentation process to the away side jet [38] [39].

2.5.2 2+1 correlations

In order to reduce the surface bias observed in two-particle correlations, it was proposed that an alternative to γ-hadron correlations, a reduction in surface bias could be achieved by the requirement in each event of two high-

p_T particles in opposite direction to one another and the subsequent measure of the azimuthal distribution of a third lower p_T particle relative to one of the high-p_T particles [40]. It was the hope that such a condition imposed on an event would reveal the di-jet structure in 2+1 correlations and at the same time provide a way to control the path length, L, traveled by both partons in the medium.

Ensuing measurements by the STAR collaboration showed no significant modification in the azimuthal distribution of particle pairs relative to p+p and d+Au [41] [42]. It is the purpose of this thesis to measure the 2+1 measurement using the PHENIX detector to confirm agreement (or disagreement) with previous measurements and extend the analysis to higher p_T.

2.5.3 Jet reconstruction

In the last five years there have been new and exciting developments in the study of jets using jet reconstruction algorithms. Recent measurements have been able to verify the jet quenching measurements performed via two-particle measurements [43] [44] [45]. Further measurements should be able to put a better constraint on the energy loss mechanisms experienced by hard partons.

2.6 Cold nuclear matter

Although up until now, the discussion of modified observables (e.g. R_{AA}) in a heavy ion collision environment has been in comparison to a p+p collision system, one must ask to what extent the effects observed are due to initial-state parton densities of the nucleus. These effects, called *cold nuclear matter effects*, need to be measured in order to determine their contribution to heavy ion collisions.

Measurements of cold nuclear matter have shown no significant suppresion from p+p to indicate they are responsible for the large suppresion observed in heavy ion collisions. In fact, the single particle particle observables (e.g. R_{AA}) have indicated an *enhancement* rather than a suppression. In addition, di-hadron azimuthal correlation measurements have not shown any significant difference with respect to p+p collision system at midrapidity [46].

Chapter 3

The Relativistic Heavy Ion Collider

Over the last 60 years, accelerators have provided the most feasible way to gain access to the subatomic structure of the nucleus. The higher the momentum one can transfer in a collision, which is achieved by increasing the center-of-mass collision energy, the more information it provides with regards to subatomic interactions. Although there have been a wealth of experiments that have explored the fundamental QCD interactions of partons, there have been relatively fewer experiments that have attempted to probe the consequences of high density nuclear matter. Some of the first experiments to search for high density nuclear matter were the BEVALAC, Super Proton Synchotron (SPS), and the Alternating Gradient Synchotron (AGS). Eventually, with the increased interest in high energy nuclear physics, there have been other experiments that have devoted some of their time to heavy ion collisions (e.g. LHC). However, to date RHIC is the only accelerator that has been designed with the main goal of measuring the QGP.

The proposal to build a dedicated facility, the Relativistic Heavy Ion Collider, at Brookhaven National Laboratory dates back to 1983. It wasn't

until June of 2000 that this proposal finally came to fruition with the collision of Au ions at 28 GeV/nucleon [47]. The RHIC accelerator consists of two quasi-circular concentric superconducting rings in an existing tunnel of 3.8 km in circumference. Each ring is injected independently (two Van de

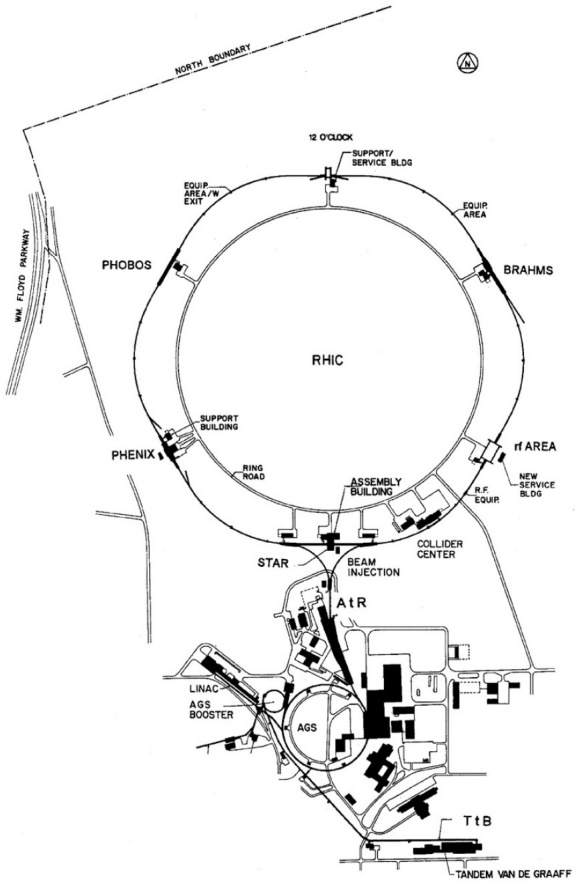

Figure 3.1: The RHIC facility

Graffs or a Van de Graff and a proton linac) which gives RHIC the ability to collide asymmetric ion species (e.g. *d*-Au). In order to inject ion species into the main accelerator ring (i.e. RHIC), there are three different supporting machines that prepare the ion species prior to injection into RHIC [47].

3.1 Tandem Van de Graaff accelerator and Linac

The initial operational step in preparing an ion species depends on the choice of ion species. For heavy ions (e.g. Au) the Tandem Van de Graff accelerator is used to generate the heavy ion beam for injection into the AGS Booster. Two of the most critical developments when designing the heavy ion source for the AGS, and subsequently the RHIC accelerator, was the development of the *pulsed* Tandem Van de Graff and the Mark VII sputter ion source [48]. The Mark VII sputter ion source technology, which increased particle currents by at least two orders of magnitude, provided sufficiently high particle currents needed to make heavy ion research viable using a synchotron accelerator. This process is done by using a voltage source to impinge the target source (typically Au for RHIC due to it being the heaviest electronegative element) with Cesium ions and leaving them in a negatively charged state (most commonly -1). These newly formed ions are then extracted by accelerating them towards to positive high voltage terminal (hence the name "sputter") using the same voltage source (Figure 3.2). Once the ion beam exits the MarkVII sputter ion source it enters the first acceleration stage inside the drift tube of the Tandem Van de Graff accelerator. There is an energy gain toward the high-voltage terminal setting at which, once it's reached, a *stripping target* is placed for the purpose of the initial stripping process of the ion beam. Depending on the ion source, different materials will be used to optimize the stripping electrons from the ions (e.g. gas for light ions, solid materials for heavier elements). After the initial stripping, the ions find themselves in a positively charged state, Q_T, and are subsequently accelerated once more as the move away from the high voltage terminal. In the case of Au and U atoms, there is second stripping process that occurs at the end of the drift tube which puts the ion in higher positively charged state, Q_F (

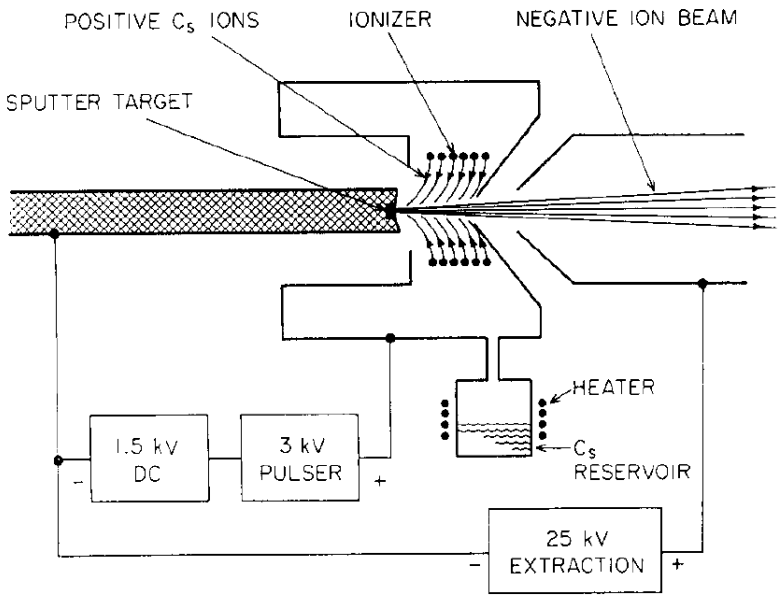

Figure 3.2: MarkVII sputter ion source used at RHIC

$Q_F = +32$ for Au) [49].

Prior to the implementation of the *pulsed* Tandem Van de Graff, continuous (dc) low-energy ion beams were used for acceleration. However, at higher energies, one of the major limitations was caused by the beam loading of the high-voltage terminal. The effect could be compensated by a recharging of the significant drop in voltage, but nevertheless is limited by the rate of recharging. The solution used for the AGS was to pulse the beam to match the rate of the circular accelerator which allowed for an injection of a much larger current [49] [50]. It should be noted that, in addition to what was described above, the small emittance and small energy spread of the beam is crucial for efficient injection of the beam into the Booster so that high particle density is achieved.

If the beam ion species chosen is proton, then the radio frequency quadrupole

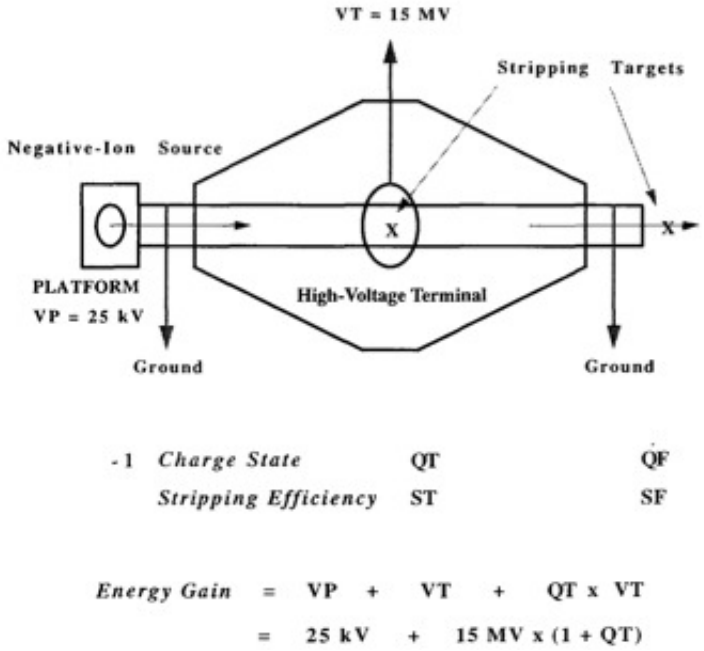

Figure 3.3: Tandem Van de Graff operation schematic.

(RFQ) and 200 MHz linear accelerator (LINAC) are used to accelerate H^- ions to 200 MeV. The H^- ions are then stripped of their electrons prior to injection into the Booster.

3.2 The Booster and the Alternating Gradient Synchotron (AGS)

Once the ions have left the Tandem Van de Graff accelerator (or the LINAC), the goal is to accelerate these ion beams up to the desired energy. One might ask: Is it possible to accelerate a beam to the energies required by the RHIC program using a *single* synchotron? Or, in other words, why are there multiple synchotrons used to accelerate the beam to full energy? Central to

answering this question is understanding *Lousville's theorem* which is very nicely stated by Edmund Wilson [51]:

> *"In the vicinity of a particle, the particle density in phase space is constant if the particles move in an external magnetic field or in a general field in which the forces do not depend upon velocity"*

Although *Louiville's theorem* is not strictly followed in beam dynamics due to small dissipative forces present in any realistic description, it must be emphasized that it's one of the guiding principles in the design and understanding of accelerators. And because it's one of the guiding principles, it tell us that the area inside a contour in phase space stays constant [52]:

$$A = \oint p\, dq = constant \tag{3.1}$$

where p and q are the canonical coordinates used in Hamilton's mechanics. Although many of the consequences of *Louiville's theorem* are beyond the scope of this thesis, it suffices to say that it provides for us some parameters which stay invariant through the acceleration process. One of these being the *normalized emittance*(ε^*) which is related to the *emittance*(ε), which is the quantity that is measured in the lab, through the following equation:

$$\varepsilon^* = (\beta\gamma)\varepsilon \ (\pi \,\mathrm{mm\,mrad}) \tag{3.2}$$

Choosing one of the transverse coordinates to the beam, y, the beam direction to be z, and the momentum p_0 in the direction of motion, one can show the relation of the emittance to the energy of the beam:

$$A = \oint p_y dy = p_0 \oint \frac{dy}{dz} dy = p_0(\mathrm{Area}) = p_0 \pi \varepsilon \tag{3.3}$$

This result tells us that the emittance is proportional to $1/p_0$ which therefore means that the beam dimensions shrink as $1/p_0^{1/2}$, a phenomenon called *adiabatic damping*. Because of this and the engineering requirements required to construct today's accelerators, it is economical to use a chain of accelerators where the smaller (lower energy) synchotrons have larger apertures and the larger (higher energy) synchotrons have smaller apertures.

Now, given that the AGS preceded the RHIC program, the AGS facility was initially designed in the 1960's using the innovative concept of *strong-focusing principle* in order to achieve the highest collision energies seen at that time. So it's no surprise that the technical specifications taken into consideration were not optimized to meet those needs of a heavy ion beam. Most important were the limitations of the aperture, which given the space-charge requirements and beam size, as described above, of a low-energy heavy ion beam were not sufficient for injection directly from the Tandem Van de Graff accelerator. The consequences were that the AGS was able to collide smaller ion species, such as Si, but in order to collide large ions, such as Au, the Booster was a necessary accelerator needed to prepare the beam for injection into the AGS.

The construction of the AGS Booster was concluded in 1991 in preperation for the heavy ion program [53] [54]. The 600 μs pulses from the Tandem Van de Graff are injected in 45 turns and then travel 201.78 m around the circumference of the synchotron accelerator. The beams are stacked vertically and horizontally in betatron space by adding linear coupling to the lattice. Once the beam has been injected, the beams are carefully captured into 6 bunches and then accelereated to 95 MeV/u. As the bunches exit the Booster and make their way into the AGS, the ions are further stripped of their electrons, which in the case for Au ions, leaves only two K-shell electrons bound to the Au nucleus (Q=+77). The AGS is filled in four Booster cycles depositing a total of 24 bunches into the AGS. These 24 bunches are

Table 3.1: Performance design specifications for RHIC [47]

	For Au+Au	For p+p
Beam energy	100→30 GeV/u	250→30 GeV/u
Luminosity	2×10^{26}cm^{-2}s^{-1}	1.4×10^{31}cm^{-2}s^{-1}
Number of bunches/ring	60 (→ 120)	60 (→ 120)
Luminosity lifetime	10 h	> 10 h
β^* at collision points	10 m → 2 m (1 m?)	10 m → 2 m (1 m?)

subsequently debunched and rebunched again into four bunches leaving each bunch to contain the number of ions in one Booster cycle. Finally, the beam is accelerated up to an energy of 8.86 GeV/u, then exits the AGS, is stripped of its remaining electrons, and transported to the AGS-to-RHIC transfer line (AtR) at which point the beam will be injected into the RHIC storage rings.

3.3 RHIC

The RHIC accelerator is a synchotron of 3.8km circumference that uses two counter rotating beams for collision at six intersection points. The magnet system is set up to provide a magnetic rigidity of $B\rho$=81 T-m at injection to a maximum of 840 T-m at top collision energy. From the magnetic rigidity and the mass-to-charge ratio, A/Z, one can determine the ion species that are allowed to collide at RHIC top energies. Table 3.1 shows a few of the basic RHIC parameters. Some of the unique design features of RHIC will be briefly reviewed [55].

Design features

The adopted design for RHIC is two independent magnetic rings which allows for asymmetric heavy ion collisions and also gives it the capability of colliding within a large energy range, in constrast to most colliders that collide only at

top design energy. At the interaction point (IP), final quadrupole magnets used to focus the beams are placed beyond the common DX dipole magnets for each beam, which deviates from the standard design where they are placed close to the IP and are common to both beams. This is done to accomodate different magnetic rigidities ($B\rho$) when colliding asymmetric ion species. The consequences are that it puts a limit on lowest beta and therefore luminosity achievable.

Another particular obstacle encountered when accelerating ions at RHIC, with the exception of proton collision setup, is the γ_T *crossing* region which becomes problematic due to a relatively slow acceleration rate ($d\gamma/dt = 1.6s^{-1}$). This represents an unstable acceleration region that can lead to significant emittance growth, beam losses, and loss of chromaticity if not handled properly. At RHIC, all ion species are injected at $\gamma = 10.5$ and encounter the *transition energy* at $\gamma_T = 22.89$. The solution employed at RHIC was to increase the acceleration rate by roughly an order of magnitude. By performing a γ_T jump of 0.8 units in a span of 60 ms any significant particle loss or bunch growth is avoided.

Injection, acceleration, and collisions

Injection into RHIC is done through 14 AGS cycles bringing a total of 56 bunches (14 cycles×4 bunches/cycle) to each ring. Given that a 100 GeV/c beam takes roughly 12.8 μs (78.125 KHz) to travel around the ring, then it's necessary to select a RF-system that is compatible with this frequency. Since the bunch length from the AGS at injection is ∼20 ns, the chosen operation of the acceleration RF-system was to use a harmonic number $h = 360$ (28.17 MHz) in order to reduce bunch dilution by matching the bucket shape to the bunch shape delivered by the AGS RF system [55]. Once the beam has been accelerated to its target energy, the beam bunches are transferred over to the

storage RF-system of 197 MHz in order to limit bunch length growth due to intrabeam scattering (<30 cm rms) and limiting the collision diamond rms length (< 20 cm ~ 30 cm$/\sqrt{2}$).

At the start of the RHIC program, four experiments, each one located at an intersection point, were commissioned to take collision data. The experiments BRAHMS, PHENIX, PHOBOS, and STAR all have different capabilities and philosophies on how to achieve their physics goals which influenced the specific design of each detector. The data used in this thesis was analyzed using the PHENIX detector which will be described in detail next.

Chapter 4

The PHENIX detector

The Pioneering High Energy Nuclear Interaction eXperiment (PHENIX) was designed with the goal of searching for the existence of nuclear matter in a deconfined state (i.e. QGP). By having superb energy and momentum resolution coupled with the ability to identify photons, electrons, hadrons and muons, it is optimized to measure predicted signatures of the QGP. The PHENIX detector consists of four magnetic spectrometers. A pair of Central Spectrometers situated at midrapidity and two forward spectrometers for the muon detector arms (see Figure 4.1). Although the muon arms are an integral part of the PHENIX program they were not used in this analysis and will not be discussed further (see reference [56]).

For analysis purposes, the reconstruction of each event can be separated into two categories: global characterization of the event and track reconstruction. Below in detail is the 2007 description of the different subsystems installed that allowed for the reconstruction and classification of events. Although the descriptions below are in the context of Au+Au and p+p collisions, the detectors can have different functionalities depending on collision species (e.g. d+Au)

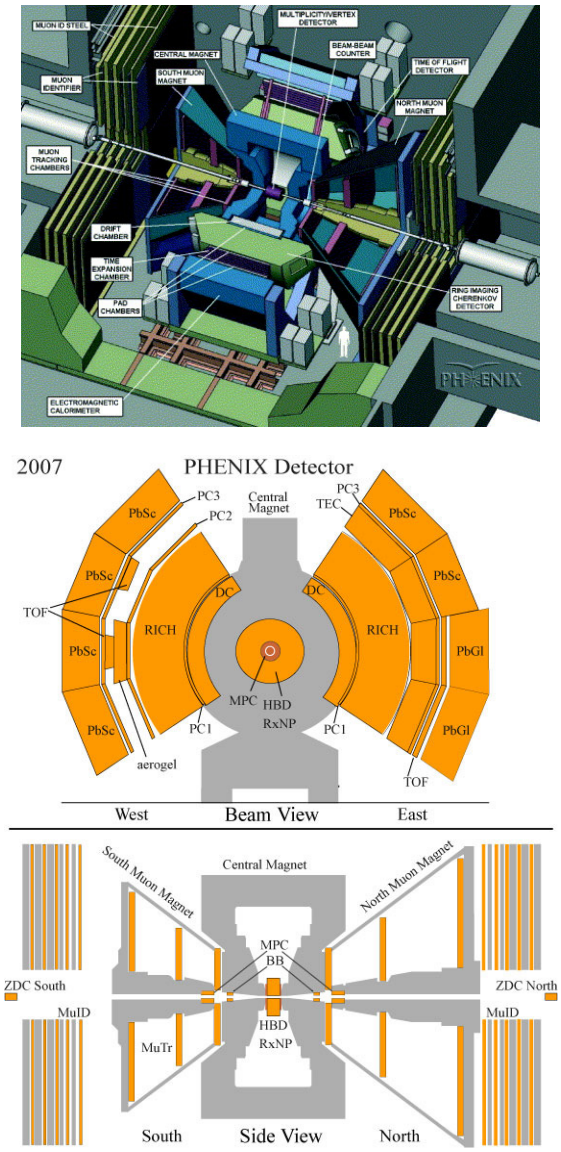

Figure 4.1: Cross-sectional view of the PHENIX experiment.

4.1 Global detectors

The following detectors allow for the measurement of the event vertex, centrality, and the collision event plane which are important parameters in the classification of events.

Beam-beam counters (BBC)

The main purpose of the BBC is to provide the following:

1) An event vertex measurement along the beam axis.

2) A precise beam-beam collision timing reference, t_o, needed for the Time-of-Flight (TOF) detector in order to make particle separation feasible (e.g. pion-kaon separation).

3) Provide a centrality determination from the integral charge sum measurements in the BBC's.

4) Provide a triggering condition (Local Level 1) for the data acquisition system.

The Beam-beam counters basic element consists of 1-inch mesh-dynode photomultiplier tubes (PMT) equipped with 3 cm quartz on the head of the PMT as a Čerenkov radiator [57]. Each BBC contains an array of 64 PMT's as shown in Figure 4.2. Both are situated 144 cm from the center of the interaction diamond along the beam pipe which corresponds to a pseudorapidity range of $3.0 < |\eta| < 3.9$.

The timing resolution of a single BBC element, after calibration and corrections, is 52±2 ps (rms). From the timing, the vertex position (Z_{vtx}) and the collision timing (t_o) can be calculated:

$$Z_{vtx} = c \times \frac{t_S - t_N}{2} \tag{4.1}$$

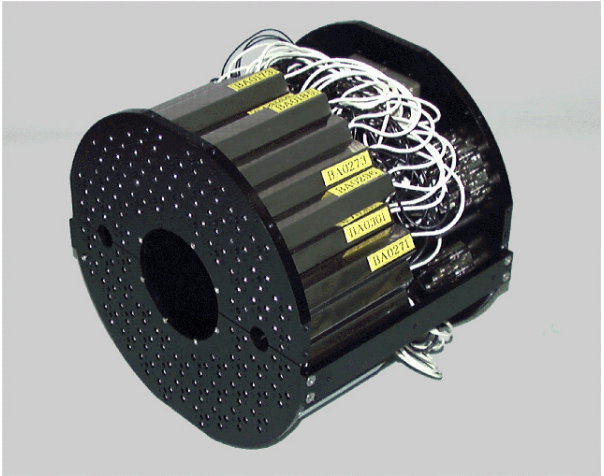

Figure 4.2: Example of Beam-beam counter (BBC).

$$t_o = \frac{t_S + t_N - 2L/c}{2} \tag{4.2}$$

where c is the speed of light, t_N (t_S) is the time measured in the BBCN (BBCS), and L is the distance of the BBC's (144 cm) from the nominal vertex position.

The method of *centrality* determination is based on the fact that the measured integrated charge sum in the BBC's is monotonically correlated to the collision centrality [58]. Since centrality is not a parameter that we can measure directly, there are a few assumptions that need to be made in order to ascertain it. The first assumption is that each participant produces hits in the BBC independently from any other participant. Each one of those participants will produce a number of hits (N_{hits}) in the BBC obeying a Negative Binomial distribution (NBD). To simulate the observed particle multiplicity, the $N_{\rm part}$ distribution from the Monte Carlo Glauber model was

convoluted with the negative binomial distribution.

$$P(N_{hits}) = \sum_{N_{\rm part}} \mathrm{NBD}(\mu N_{\rm part}, kN_{\rm part}) \times \mathrm{MCG}(N_{\rm part}) \tag{4.3}$$

From this information one can relate centrality ranges as those defined in the Glauber model (see Section 2.2.1).

In addition, in an attempt to detect all heavy ion collisions occuring at PHENIX, the BBC's serve as part of a Level 1 trigger for Minimum Bias event selection which is efficient for accepting inelastic Au+Au collisions in the centrality ranges of 0-92%. Trigger configurations change depending on various factors during the data taking period. However, typical configurations include the requirement of one PMT hit in either or both BBC's.

Zero Degree Calorimeter

The ZDC is a *sampling* hadronic calorimeter that focuses on detecting neutral beam fragments downstream from the collision vertex [59] [60]. Given the narrow region of acceptance in the forward direction (see Figure 4.3) of $\theta \leq 4$ mrad, produced particles and secondaries deposit negligible energy when compared to beam fragmented neutrons. Since it sits behind the DX dipole magnets, any charged beam fragments are swept away and don't contribute significant energy deposition.

The ZDC's choice of design was based on optimization of uniform response, energy resolution, and compactness given the space constraints [59]. It consistes of Tungsten (W) *absorber* plates and PMMA *sampling* fiber layers (see Figure 4.4). The Tungsten $5 \times 100 \times 150$ mm^3 plates provide six interaction lengths (Λ_I) of calorimeter depth and an energy resolution of $\sigma_E/E \sim 10\%$ for neutrons at $E_n = 100$ GeV. The energy resolution was determined by the need to resolve the single neutron peak in *peripheral* nuclear

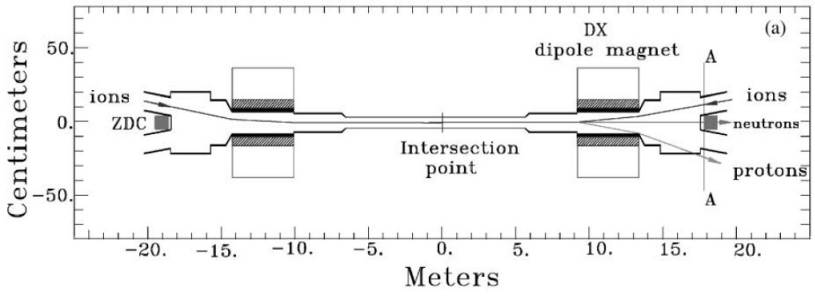

Figure 4.3: View of the collision region. Schematic shows location of ZDC relative to beam trajectories and DX dipole magnets.

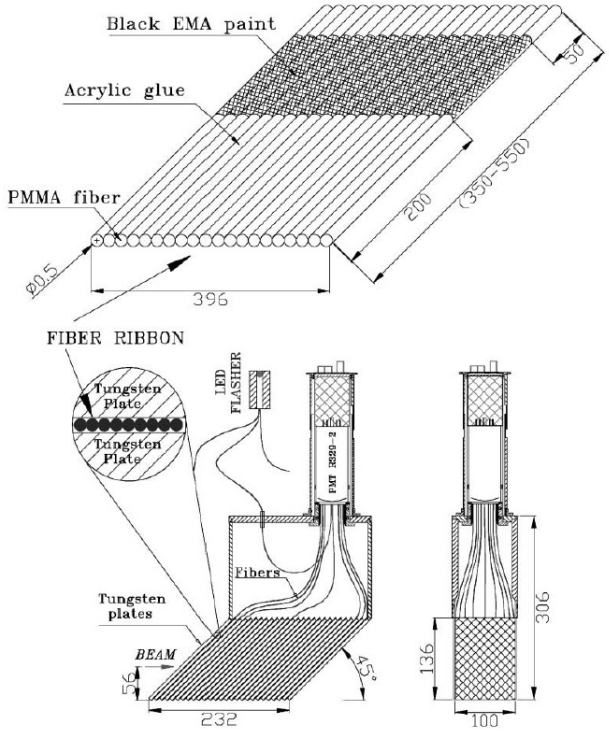

Figure 4.4: Mechanical design of production tungsten modules. Dimensions shown are in mm.

collisions. The sampling is performed by PMMA fibers (0.5 mm diameter), which are optimized to capture the Čerenkov radiation produced by charged shower secondaries, are oriented 45° relative to the incident beam which roughly coincides with $\beta = 1$ particles. The radiation traveling through the PMMA fibers is subsequently read out by 2" PMT's. In addition, the fast signal formation in the ZDC provides a time-of-flight measurement with a resolution of approximately 150 ps which can be used to measure the collision interaction point with roughly a 3 cm resolution. Other functionalities of the ZDC is as a coincidence trigger system for the selection of Minimum Bias events and as a luminosity monitor.

Although in the fist few years of running the ZDC was used in conjunction with the BBC to determine centrality it has been superceded by the method of using only the BBC.

Reaction Plane detector

The Reaction Plane Detector (RXNP) was an 2007 upgrade placed to improve the resolution of the *event plane* (Ψ_n) previously measured by the BBC's [61]. Due the RXNP's larger rapidity coverage ($1.0< |\eta| <2.8$), it provides the ability to measure higher multiplicities which results in an increase in the event-plane resolution ($\langle \cos(2[\Psi_2 - \Psi_R]) \rangle \sim 0.75$) by roughly a factor of 2 when compared to the BBC's.

The RXNP detector is composed of Lead-Scintillator paddles (see Figure). The RXNP detectors are placed at ± 40 cm from the nominal vertex position in order to minimize interference with existing detector subsystems (e.g. central arms). Each detector is segmented into 24 detector elements, 2 radial rings (inner and outer) and 12 segments in azimuth, bringing a total of 24 elements per detector (see Figure 4.5). For each element a 2 cm thick scintillator, made of EJ-200 material from Eljent Technology, was placed to

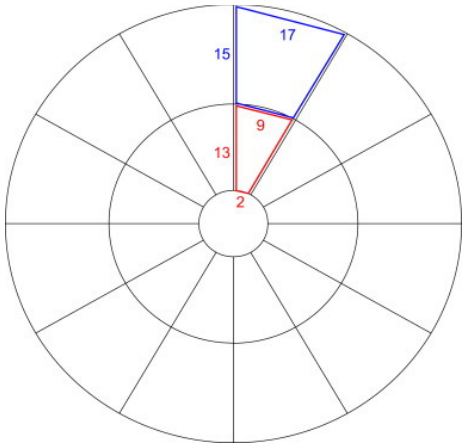

Figure 4.5: Reaction Plane Detector geometry illustrating the inner(red) and outer(blue) scintillator detector elements. The length of each scintillator is shown in centimeters.

capture primary charged particles. A 2 cm thick converter (98% Pb + 2% Antimony) was placed in front of the scintillator to improve the flow signal coming from photon, π^0, and η decays into secondary particle and reduce the low energy background. Wavelength shifting fiber light guides are embedded on one end to the surface of the scintillator every 0.5 cm and running its entire length. At the other end, the fibers run radially outward, leaving the region of RXNP acceptance and are connected to Hamamatsu R5543 3 inch fine mesh PMT's.

The signal measured in each element was converted into 12-bit ADC values that were subsequently used to measure the event plane for each event. See Section 5.6 for further details.

4.2 Tracking subsystems

One of the major shortcomings of the PHENIX central spectrometer design is the inability to provide full azimuthal coverage, as shown in Figure 4.1,

which only provide π coverage. Although this is sufficient for most single particle analysis, the problem manifests itself most profoundly in analysis that require the measurement of two or more correlated tracks where the efficiency of measuring correlated tracks drops as their relative angle, $\Delta\phi$, between two tracks approaches $\pi/2$. Since the measurement of J/ψ decays was one of the primary goals of the PHENIX experiment, it became crucial to optimize the *overall* acceptance for these decays. In order to circumvent this problem, the solution adopted was to slightly *kink* the arms such that they're shifted in azimuth from being antipodal. More specifically, the arms have a gap of 67.5° at the top (instead of 90°) and 112.5° at the bottom.

The tracking subsystems at PHENIX are used for the main purpose of determining momentum (p_T) and direction of the charged tracks produced during collisions. These subsystems also contribute to the association of tracks with other subsystems (e.g. RICH and EMCal). There are two major subsystems used in providing tracking information: the *drift chambers* and the *pad chambers*. From the information provided by these two subsystems, the PHENIX track reconstruction software is able to reconstruct parameters that are useful in physics analysis using the central arms.

Drift Chambers

The Drift Chamber is an example of a techonology that belongs to the multi-wire chamber technology developed in the late 1960's and at PHENIX is the most significant subsystem in providing momentum information for charged particles. It is the first subsystem encountered by a track in a region where the magnetic field from the central magnets has reduced significantly (roughly $B \sim$0.6kG at inner face of Drift Chamber).

The basic working principles of the Drift Chamber are based on the measurement of track position through drifting electrons that are produced by

the tracks ionization of gas molecules (e.g. Argon). The production of these electrons will cause the ionization of other atoms and therefore an avalanche of electrons that can be measured by an anode wire. Critical to making drift chambers reliable with regard to coordinate measurement is the ability to provide predictable *drift velocities*, v_D, for these electrons [62]. In the presence of an electric field, E, the key to producing a constant drift velocity lies in the ability of the gas to provide fractional energy loss λ_ε to compensate for the electrons acceleration in the electric field so that an equlibrium is reached,

$$qEv_D\tau = \lambda_\varepsilon\varepsilon \tag{4.4}$$

where τ is the mean time between collisions and q is the electric charge of the electron. It can be shown that the drift velocity to be approximately given by the following formula [63],

$$v_D \sim \left[\sqrt{\frac{\Delta\varepsilon}{2}}\frac{qE}{m}\lambda_e\right]^{1/2} \tag{4.5}$$

where λ_e is the mean-free path of the electron and m is the mass of the electron. In reality, the drift velocity is not calculated but measured from the drift times as shown in Figure 4.6. From the drift times, the minimum and maximum drift times, t_0 and t_1 respectively, can be extracted from the distribution and used to calculate the drift velocity knowing the maximum drift length d.

$$v_D = \frac{d}{t_1 - t_0} \tag{4.6}$$

Once a reliably constant drift velocity has been established the position measurement can be obtained from the measurement time, Δt, to determine the position of ionization from the traversing particle.

$$x(\Delta t) = v_D\Delta t \tag{4.7}$$

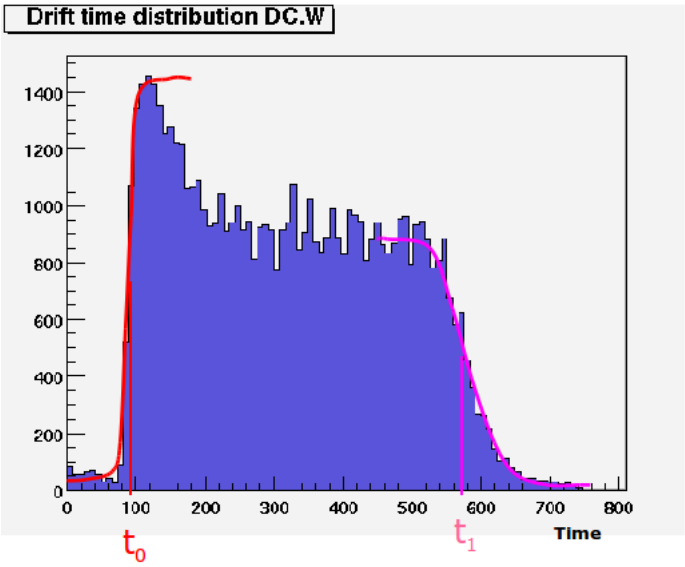

Figure 4.6: Example of measured drift times in PHENIX drift chamber. A Fermi function is fitted to the leading and trailing edge to determine drift times t_0 and t_1.

It must be noted that one of the main sources of false signals can come from photons produced during excitation of atoms or recombination of positive ions with electrons. These photons can produce, by way of Compton scattering, avalanches of their own and result in unwanted pulses. Therefore, to reduce this effect, a *quencher gas* with a relatively large absorption cross-section must be added, typically an organic molecule like methane or ethane, to reduce the range of avalanches coming from photon production.

The PHENIX Drift Chamber is located at a distance of about 2 m radially outward from the beamline with a solid angle coverage of π in azimuth (ϕ) and ± 0.35 units in pseudorapidity (η) for both arms combined (East and West) [64]. Each arm represents an independent composite gas mixture volume composed of 49% argon + 49% ethane + 1% ethanol and is supported by a cylindrical titanium frame. The volume is further segmented into 20

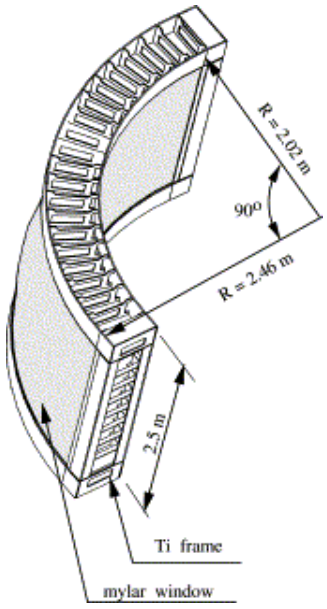

Figure 4.7: PHENIX Drift Chamber titanium frame.

identical sectors (a.k.a. keystones), each covering 4.5°. In each sector contains 4 sense(anode) and 4 cathode planes that are used to create six regions, each with a specific type of wire (X1,U1,V1,X2,U2,V2) for that region (see Figure 4.8). The U and V wires, set at a 6° stereo angle relative to the X wires, were initially intended to provide a z-coordinate measurement to the reconstruction software. That angle was selected to match the z-coordinate resolution of the *pad chambers* and in doing so, would minimize track ambiguities during reconstruction. However, the current reconstruction software version does not provide the z-coordinate measurement, presumably due to its poorer than expected resolution and/or problems in the pattern recognition.

The anode wire configuration is illustrated in Figure 4.8 where the Potential(P), Gate(G), and Back(B) wires are demonstrated. The focusing geometry eliminates the left-right ambiguity while at the same time reducing

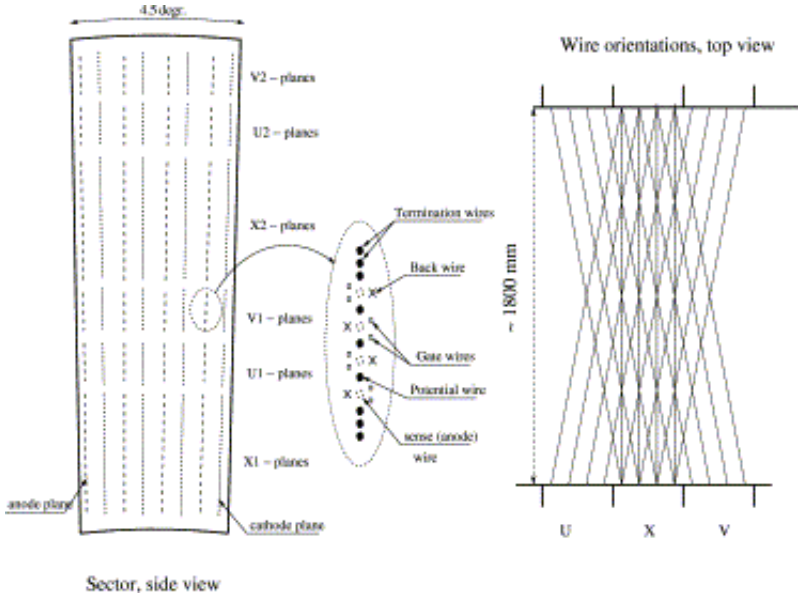

Figure 4.8: Cross sectional layout (left) of wire position in the radial direction. Positioning of X, U, and V wires relative to each other (right). U and V wire are positioned 6° relative to the X wires.

the number of tracks seen by each wire.

A typical drift chamber cell is maintained at an average electric field strength of $E \simeq 1.2$ kV/cm which allows for a maximum drift time of 400 ns. The single wire efficiency of 95-96% was achieved which allowed for a mean width pulse of 35 ns. Such a pulse width allows for double track resolution of better than 2mm. The single wire resolution was found to be approximately 165 μm. The reconstruction algorithm (see Section 4.5) which used the drift chamber hits to create track candidates provides the following momentum resolution

$$\frac{\delta p}{p} \simeq 0.7\% \oplus 0.1p \text{ (GeV/}c\text{)} \tag{4.8}$$

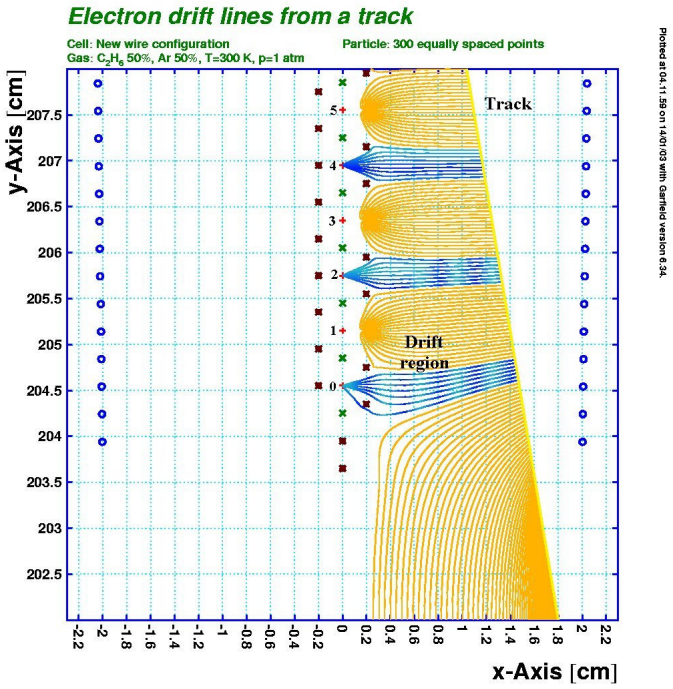

Figure 4.9: Drift chamber anode wire performance simulation. Illustration shows electrostatic field lines of due to Gates(G) and Back(B) wires.

Pad Chambers

With regards to design specifications, one of the major goals of PHENIX was to have a hadron to electron rejection rate of roughly 10^4 over a wide momentum range. This strict requirement suggests that there could be little tolerance for error when correlating momentum measurements coming from the drift chamber with particle identification subsystems (e.g. EMCal, RICH) [65]. To meet these demands the three *pad chamber* subsystems in Central Spectrometers were designed to provide support to the pattern recognition by providing space points to overcome projective ambiguities in the drift chambers, especially at high multiplicities, as charged tracks travel

through various detector subsystems. This in turn determines the requirements on the pad chamber position resolution, i.e., its effective pixels must be small enough to keep double hit probability very low even in the most central events. Each pad chamber is a multiwire proportional chamber meant to provide the increased coordinate resolution needed and behave as a complimentary detector to other subsystems.

The three pad chambers are situated at three different radial distances from the beam. The PC1 is located at a radius of 2.5 m in the region between the drift chamber an the RICH. Aside from providing a more accurate z-coordinate measurement, the PC1 in conjunction with the drift chamber serves as an auxilliary subsystem to the RICH in order to associate Čerenkov radiation with the appropriate track. The PC2 and PC3 are located at 4.2 m and 4.9 m respectively, the PC2 placed behind the RICH detector and the PC3 in front of the EMCal. Both PC2 and PC3 serve to resolve ambiguities in the outer detectors by providing an entry or exit coordinate of the track for these subsystems. They also facilitate the identification of particles such as secondaries, decays, and low-p_T tracks that bend around the acceptance of drift chamber and PC1 subsystems and deposit energy into the electromagnetic calorimeter (30% of electromagnetic clusters come from such particles).

All three of the pad chambers were constructed in order to have comparable angular resolution. Some of the design parameters are tabulated in Table 4.1. The two-dimensional readout of the pad chambers is made through the etching of the copper cathodes into pixels. In order to increase efficiency, a strict requirement of a track hit is defined as a triple coincidence of three adjacent pixels, which are needed in order to prevent false hits created by electronic noise. Each one of these three adjacent pixels is called a *cell* (8.4×8.4 mm^2). However, having such high pixelization in the pad chambers is very costly in terms of channels and therefore a very clever readout

Table 4.1: Pad chambers design parameters

Parameter	PC1	PC2	PC3
Gas gap (mm)	6.0	10.0	12.0
Number of wires	58	116	116
Wire pitch (mm)	8.4	13.6	16.0
Lenght (cells)	212	106	106
Cell pitch (mm)	8.45	14.2	16.7
Dimensions L × W × H (cm)	198 × 50 × 6.0	151 × 157 × 7.2	177 × 185 × 9.0
Radiation thicknes (% X_0)	1.2	2.38	2.37

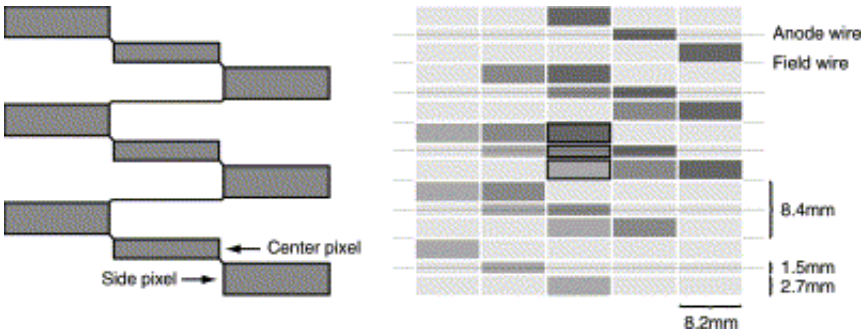

Figure 4.10: The pixel geometry (left) for a single pad in the pad chambers. Illustration of a *cell* at the center of the right figure. The variation in gray scale identifies the three pads contributing to the cell.

design was implemented such that pixels were ganged together while at the same time retaining the position resolution. Figure 4.10 demonstrates how a single pad contributes to nine cells and a single cell receives contribution from three pads. It also emphasizes three pads contributing to the cell are *unique*. This design reduces the channel consumption by a factor of 3 and results in 172,800 channels (1 bit per channel). The chamber is filled with 50/50 mixture of Argon+ethane.

The position resolution along the wire (z-coordinate) of PC1, PC2, and PC3 were 1.7 mm, 3.1 mm, and 3.2 mm respectively. The resolution perpendicular to the wire can be determined from the wire spacing, w, in Ta-

ble 4.1 and assuming a rectangular distrubution from the cathode pixels ($\sigma = w/\sqrt{12}$)

The hit information from PC1 is used in conjunction with the drift chamber to produce a *quality* variable which determines hit associated from these subsystems with a given track (see Section 4.5).

In addition, the reconstruction algorithm projects reconstructed track information from track candidates to the PC2 and PC3 subsytems. The projections are associated to the nearest PC2 and PC3 hit and the distance to the nearest hit is calculated (e.g. $\Delta\phi$, Δz) to aid in the identification of charged tracks (a.k.a. PC2 and PC3 *matching cuts*). The profile of these distance distributions are plotted and the width of the distribution (s) extracted to calculate a dimensionless normalized distance (σ) to the width:

$$\sigma_\phi = \frac{\Delta\phi}{s_\phi} \tag{4.9}$$

$$\sigma_z = \frac{\Delta z}{s_z} \tag{4.10}$$

For this analysis a radial distance was calculated to reduce the number of parameters used:

$$\sigma_{PC2} = \sqrt{\sigma^2_{\phi,PC2} + \sigma^2_{z,PC2}} \tag{4.11}$$

$$\sigma_{PC3} = \sqrt{\sigma^2_{\phi,PC3} + \sigma^2_{z,PC3}} \tag{4.12}$$

4.3 Particle Identification

The particle identifications subsystems present at PHENIX are the Ring Imaging Čerenkov detector (RICH), time-of-flight (TOF), and the electromagnetic calorimeter (EMCal).

Ring Imaging Čerenkov detector

As mentioned previously, one of the goals at PHENIX was to have an electron to hadron rejection factor of roughly 10^4 in order to have the ability perform measurements that require the identification of electrons. As a result the RICH was designed to measure Čerenkov radiation coming from charged particles traversing the volume with the main purpose of efficiently segregating electrons from pions below the pion Čerenkov threshold [66].

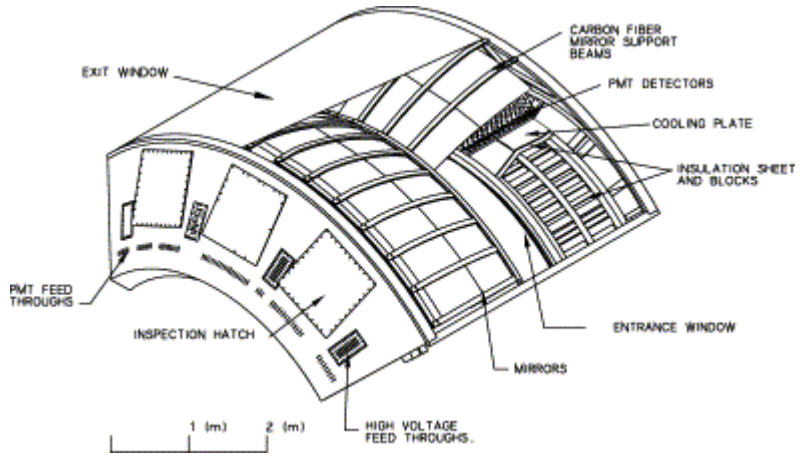

Figure 4.11: Cutaway view of the RICH subsystem.

The basic underlying principles of RICH detectors as particle identification detectors relies on the ability of particles to emit Čerenkov radiation. This effect is solely dependent on the particles speed v (or β) exceeding the speed of light in the medium ($v_{ph} = c/n$) which can be defined by the index of refraction, n. In the case where a particle exceeds the speed of light in the medium ,the Čerenkov radiation angle (θ_c) is related to the speed of the particle and the index of refraction through the following relation [67]:

$$\cos(\theta_c) = \frac{1}{n\beta} \tag{4.13}$$

In order for this to be useful for particle identification, the threshold energy (or momentum) at which a particle species will start to radiate should be determined, namely when $\beta = c/n$.

$$E_{th} = \gamma_{th} m_o c^2 \tag{4.14}$$

Given the velocity constraint, $\beta = c/n$, the Lorentz factor at threshold can be reformulated to depend only on the index of refraction.

$$\gamma_{th} = \frac{n}{\sqrt{n^2 - 1}} \tag{4.15}$$

Using the relativistic energy-momentum relation ($E^2 = p^2c^2 + m_o^2c^4$) one can obtain an equation of threshold radiation for each type of particle.

$$p = \frac{m_o c}{\sqrt{n^2 - 1}} \tag{4.16}$$

At PHENIX, where the RICH detectors sit at midrapidity ($|\eta| < 0.35$), the total momentum is approximately equal to the transverse momentum ($p \sim p_T$). Given that the RICH detector is filled with CO_2, as we'll see, this all translates into Čerenkov radiation thresholds of 0.017 GeV/c and 4.7 GeV/c for electrons and pions, respectively.

To determine the number of photons produced, the intensity distribution due to diffraction around the Čerenkov angle θ_c is given by,

$$\frac{dN}{d\lambda} = \frac{2\pi\alpha}{\lambda^2} L \sin^2\theta_c \tag{4.17}$$

for a radiator of length L and wavelength λ. Since a given PMT is sensitive in a narrow wavlength region, the distribution can be integrated within that

region to obtain the number of photons N emitted.

$$N = 2\pi\alpha L \int_{\lambda_2}^{\lambda_1} \frac{\sin^2\theta_c}{\lambda^2} d\lambda \tag{4.18}$$

For a PMT sensitive in the visible region, $\lambda_1 = 400$ nm to $\lambda_2 = 700$ nm, the number of photons per centimeter is given by:

$$\frac{N}{L} = 490 \sin^2\theta_c \tag{4.19}$$

Each RICH detector occupies 48 m^3 of volume beyond the PC1 detector. It consists of 48 composite mirror panels forming two intersecting spherical surfaces that results in 20 m^2 of reflecting area. The mirrors are designed to reflect and focus Čerenkov light onto an array of Hamamatsu H3171S UV photomultiplier tubes (PMT's) placed on either side of the RICH entrance window (see Figure 4.11). The PMT's on each side of the entrance window are grouped into 40 *supermodules*, each supermodule consisting of two rows of sixteen PMT's. Although, through simulations, the best performing radiation gas determined for e/π separation was ethane due its good compromise between photon statistics and the pion Čerenkov threshold, the radiation gas used in operation is CO_2 due to its non-flammable nature. Because the RICH is essentially an electron detector, the material in between the interaction region and the RICH is of great concern regarding the rate of photon conversions. For this reasons, the final design called for minimal material which resulted in 2% total radiation length.

In order to obtain efficient e/π discrimination, three factors must be taken into consideration; π Čerenkov threshold, statistical fluctuations in the number of photoelectrons detected, and background counting rates. The threshold and statistical fluctuations are influenced by the gas used during operation. For the background counting rates *dark current* noise was investigated

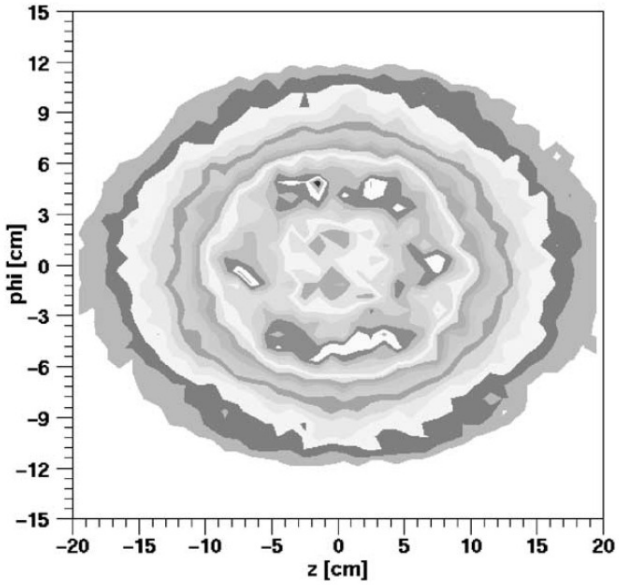

Figure 4.12: The distribution of hit PMTs around the projected ray from a reconstructed track in zero-field runs after the geometry calibration.

to ascertain its contribution to the background. It was determined that *dark current* noise produces roughly 0.5 hits per RICH per event. Therefore the background noise is dominated by electrons produced by photon conversions. Discussion on how to identify conversions shall be diverted to Section 5.3.

The PHENIX track reconstruction software provides variables of tracks projected onto the RICH aid in the identification of electrons and pions. This is done by ray tracing a track projection and reflecting it from the mirrors onto the PMT's. If the projection falls in the center of a ring of Čerenkov light, as in Figure 4.12, then the track is associated with Čerenkov light [68]. During test beam studies the efficiency for electron identification was established to be nearly 100%. However, in most central Au+Au events the effeciency drops to 80% and the pion rejection factor to the order of several hundreds. Table 4.2 defines some of the most commonly used variables. Using

Table 4.2: Commonly used RICH reconstruction variables

RICH variable	Definition
n0	Number of PMT's fired in a *ring* of inner radius 3.4 cm and outer radius of 8.4 cm around the projection point of the the track onto the PMT plane.
n1	Number of PMT's fired in a *disk* of radius 11 cm around the projection point of the track onto the PMT plane.

these variables along with information from other subsystems (e.g. p_T, E/p, etc...) one can, in principle, improve pion rejection factor(see Section 5.2).

4.4 Electromagnetic calorimeter

One of the primary, if not the main, goal for the PHENIX Central Spectrometers was to provide the ability to measure rare events with high transverse momentum photons and electrons. To this end the electromagnetic calorimeter (EMCal) was designed to measure the energies and positions of photons and electrons produced in heavy ion collisions [69]. Both arms are covered by eight sectors of calorimetry (see Figure 4.1), six of the sectors comprised of *sampling* calorimeters and the other two consisting of *homogenous* calorimeters. This choice of technology was done deliberately since both have different strenght and weaknesses which can also serve as a means to cross-check measurements in the same experiment. Both calorimeters are located beyond a radial distance of 5 m from the collision point.

Pb-Scintillator calorimeter

The sampling calorimeter which encompasses six sectors of the EMCal is composed of a commonly used Pb-Scintillator (PbSc) technology. Figure 4.13

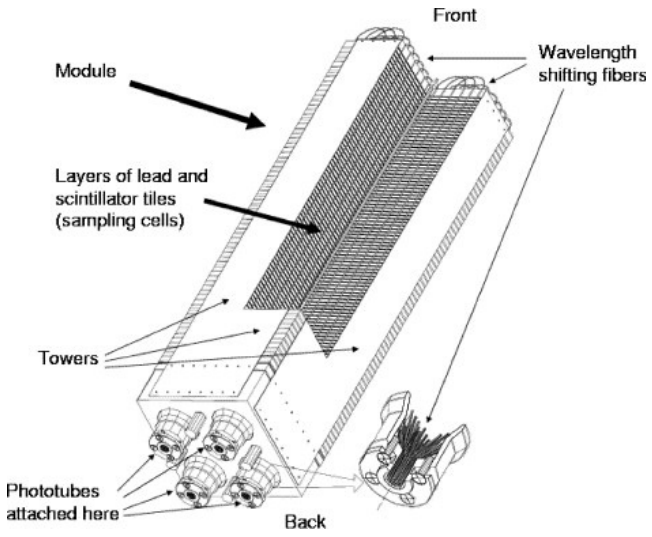

Figure 4.13: Design of Pb-Scinitillator calorimeter module (4 towers) illustrating alternating lead and scintillation tiles, wavelength shifting fibers, and phototubes.

demonstrates the design of a single PbSc calorimeter module. The basic detector calorimeter unit is a *tower* with dimensions of 5.535×5.535 cm^2 in lateral segmentation and 37.5 cm of active depth. Each tower consists of 66 cells of alternating Pb absorber and organic scintillation tiles which result in $18X_0$ (or 0.85 nuclear interaction lengths). Each cell is penetrated by 36 wavelength shifting fibers for light collection which are then read out at the back end of each tower by a 30mm FEU115M phototube. Every four towers are grouped together into another structure entity called a *module*, every 36 modules into a *supermodule*, and every 18 supermodules into a *sector*.

The PbSc calorimeter has a high light yield of photons, approximately 12,500 photons/GeV for an electromagnetic probe. Figure 4.14 shows ex-

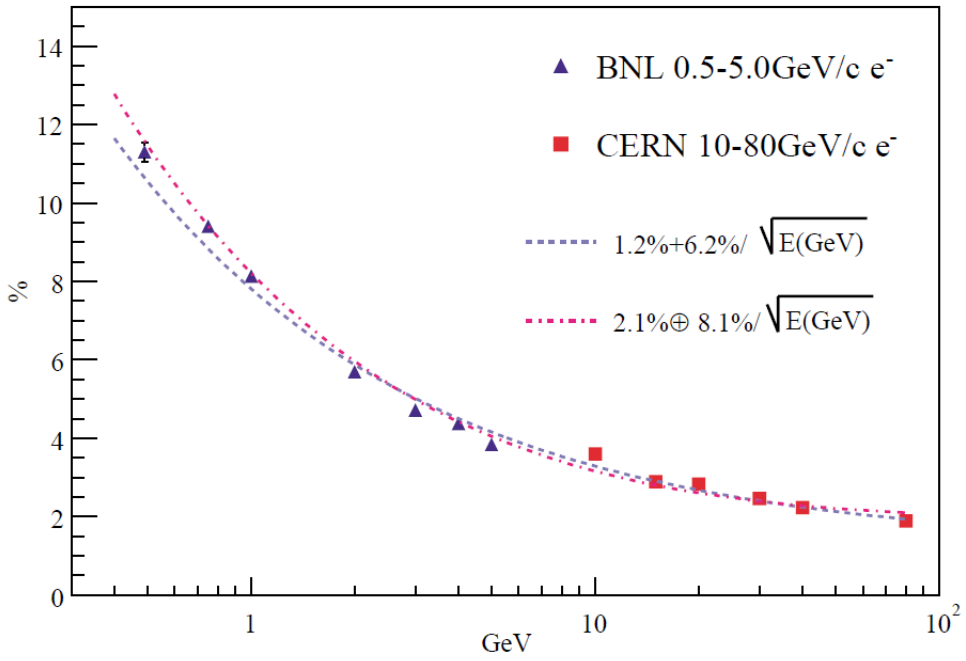

Figure 4.14: The PbSc energy resolution obtained from beam tests at BNL and CERN. The dashed line shows a fit to $\sigma(E)/E = 1.2\% \oplus 6.2\%/\sqrt{E(GeV)}$. The dash-dotted line shows the fit to the quadratic formula $\sigma(E)/E = 2.1\% \oplus 8.1\%/\sqrt{E(GeV)}$.

tensive beam test studies done at various energies performed at BNL and CERN. The best estimate for energy resolution was determined to be,

$$\frac{\sigma(E)_{\mathrm{PbSc}}}{E} = \frac{8.1\%}{\sqrt{E}} \oplus 2.1\% \tag{4.20}$$

The 8.1% stochastic term is very close to that determined from GEANT simulations while the relatively large 2.1% constant term was mostly due to particles hitting the corners of the towers which resulted in an 8% loss in calorimeter response. This results in a reconstructed π^0 mass resolution of 15 MeV.

Since the calorimeter does not have a projective geometry, the deposited shower can enter the face of the calorimeter at different incidence angles. The position resolution at normal incidence was measured to be,

$$\sigma_0(E) = 1.55 \oplus \frac{5.7}{\sqrt{E}}(\text{mm}) \tag{4.21}$$

where the spread is due mainly due to longitudinal shower fluctuations. However, in cases where the incident angle is not normal to the face of the calorimeter, the shower shape becomes skewed which results in position resolution. In such cases, the resolution becomes dependent on the angle of incidence.

$$\sigma_x(E, \theta) = \sigma_0(E) \oplus \Delta \sin(\theta) \tag{4.22}$$

The *time-of-flight* is another feature of the PbSc that allows for segregation of overlapping showers and particle identification. For energy depositions of greater than 0.5 GeV, the timing resolution is 120 ps for electrons and protons while 270 ps for pions.

Further particle identification can be accomplished by a shower analytical parametrization of the energy sharing and its fluctuations based upon measurements of identified electrons. By measuring the total energy deposited in a cluster of towers ($\sum E_i^{meas}$) and predicting the individual energy for each tower (E_i^{pred}) from the analytical parametrization, one can use this information to compute the χ^2 to determine the probablity that the shower is electromagnetic.

$$\chi^2 = \sum \frac{(E_i^{pred} - E_i^{meas})^2}{\sigma_i} \tag{4.23}$$

Figure 4.15 illustrates the χ^2 distributions for 2 GeV electrons and pions.

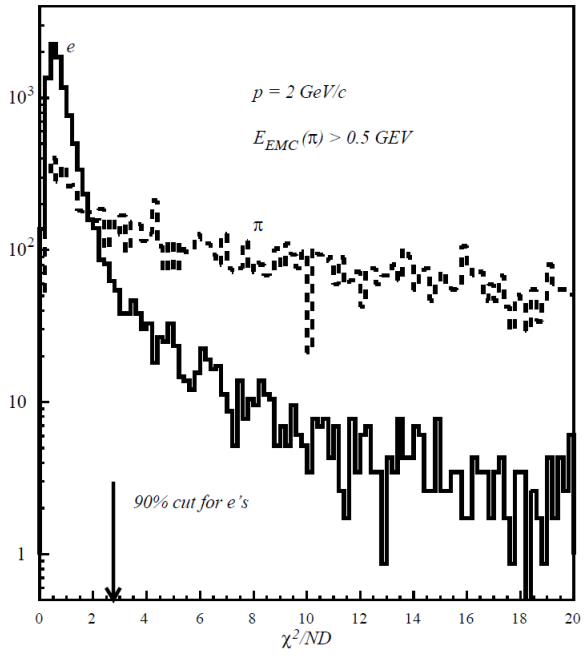

Figure 4.15: PbSc χ^2 distribution for 2 GeV electrons and pions.

Pb-Glass calorimeter

The remaining two sectors of the EMCal are occupied by the homogenous calorimeter. This calorimeter uses Pb-Glass technology which is a non-scintillating Čerenkov radiator. The basic detector unit for the Pb-Glass is a 40 mm × 40 mm × 400 mm module. The size of a Pb-Glass module results in $14.4X_0$ radiation lengths (or 1.05 nuclear interaction lengths). Figure 4.16 shows an example of a *supermodule* which consists of an array of 4 × 6 modules. Each sector is comprised of 192 supermodules. Each one of the Pb-Glass modules is read out by a FEU-84 phototube.

As with the PbSc, the Pb-Glass calorimeter was extensively studied using test beams at BNL and CERN to determine its energy and position resolution. Figure 4.17 shows the data and fit to extract the energy resolution.

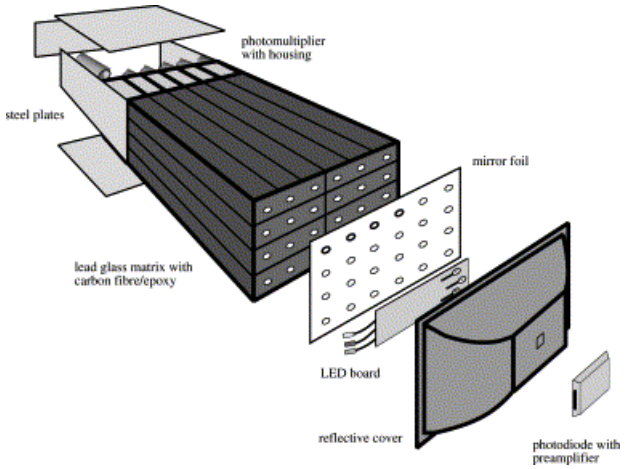

Figure 4.16: An illustration of a Pb-Glass supermodule.

The extracted resolution from Figure 4.17 was measured to be

$$\frac{\sigma(E)}{E} = \frac{[5.9 \pm 0.1]\%}{\sqrt{E/GeV}} \oplus [0.8 \pm 0.1\%] \tag{4.24}$$

The corresponding measured position resolution was determined to be:

$$\sigma_x(E) = \frac{[8.4 \pm 0.3]\text{mm}}{\sqrt{E/GeV}} \oplus [0.2 \pm 0.1]\text{mm} \tag{4.25}$$

Aside from particle identification via shower shape and time-of-flight measurements, the energy measured from the EMCal can also serve to further reject hadrons. Since hadrons typically deposit very little energy into the EMCal, using the momentum measurements from the drift chamber and calculating the E/p can further separate hadron from electrons measured in the central arms.

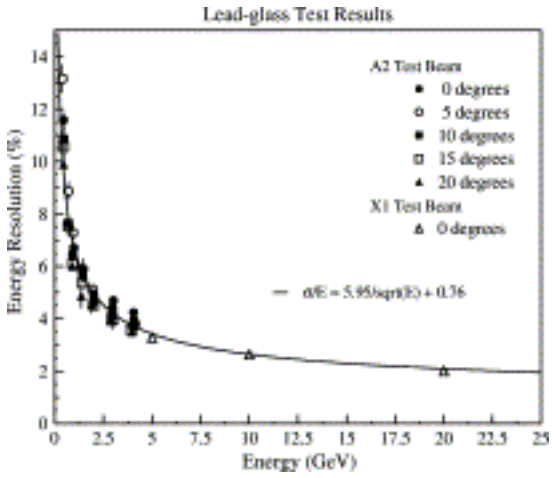

Figure 4.17: Energy resolution for Pb-Glass from test beam studies at BNL and CERN.

4.5 PHENIX track reconstruction software

Now that the all relevant detector subsystems have been described, a brief description of the track reconstruction is in store. The track reconstruction at PHENIX can, essentially, be broken up into two parts. The first being the construction of *track candidates* in the drift chamber using pattern recognition based on the Combinatorial Hough Transform (CHT) which was chosen mostly due to the gain in peak-to-background ratio in feature space [70] [71] [68]. The second being the projection of these track candidates onto outer detector subsystems to find hits associated with the track candidates.

The CHT is applied to *pair-wise* X1-X2 hits in the drift chamber. For every pair (indexed by j) the angle ϕ_j and local inclination angle, α_j,(see Figure 4.18) is determined at the reference radius of 220 cm:

$$\sin(\beta_j) = \frac{\rho_2 \sin(\Delta\phi_j)}{d} \tag{4.26}$$

$$\sin(\alpha_j) = \frac{\rho_1 \sin(\beta_j)}{\rho_{DC}} \quad (4.27)$$

$$\phi_j = \phi_1 - |\beta_j| + |\alpha_j| \quad (4.28)$$

where ρ_1 and ρ_2 are the cylindrical radii of the X1 and X2 layers respectively. The distance d is the distance from the X1 to the X2 hit. Each one of these pairs is discretized and filled into an array in ϕ-α space. Track candidates are

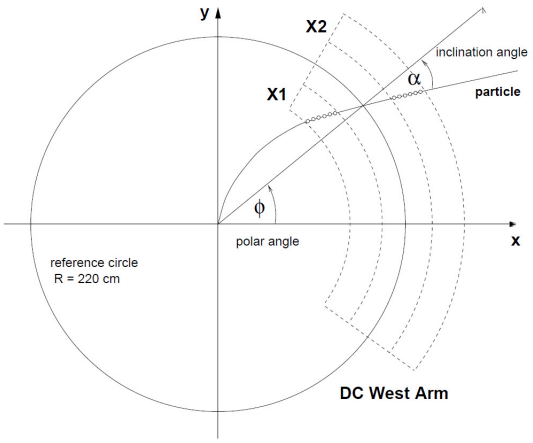

Figure 4.18: Track trajectory through the drift chamber. The azimuthal angle, ϕ, at the reference radius and the inclination angle, α, relative to ϕ are defined.

established by those bins in a 3×3 array that exceed a pre-defined threshold and a subsequent center-of-gravity calculation is prescribed to determine that candidates ϕ and α[1].

From here a track model is called to project the track to the outer detectors in order to associate information (e.g. PC hits, Čerenkov light, EMCal clusters, etc...), if any, with these track candidates and define roads from these projections. Once all the information have been associated with the

[1]The reconstructed parameter α is inversely related to $p_T \propto 1/\alpha$

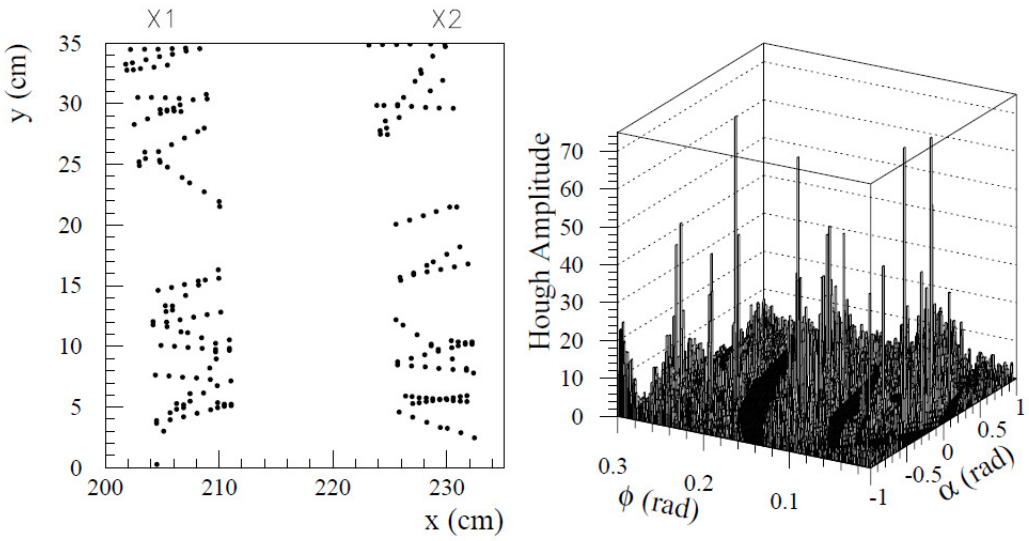

Figure 4.19: Left panel shows the drift chamber hits of a HIJING central Au+Au event. Right panel shows Hough transform ϕ-α space where track candidates can be indentified as peaks.

track candidates an iterative least squares fitting procedure is performed to best measure track parameters at the event vertex (e.g. ϕ_0, θ, p_T, etc...).

One of the parameters used to quantify the efficacy of the reconstruction procedure is the `quality` variable. The `quality` bitwise variable, defined in Table 4.3, provides information on to whether a track contains information from the drift chamber and PC1 subsystems. Typical usage of the `quality` variable is to keep tracks that have hits from all layers (that is, `quality =` 31 or 63) so that one can reduce the contamination of fake tracks due to occupancy effects which are prevalent in central heavy ion collisions.

Table 4.3: Description of bitwise `quality` variable

Bit	**Subsystem included**
0 (1)	Drift chamber X1 wire plane hits found
1 (2)	Drift chamber X2 wire plane hits found
2 (4)	Drift chamber UV wire plane hits found
3 (8)	Drift chamber UV wire plane hits found *and* unique
4 (16)	More than one PC1 hit found
5 (32)	A single PC1 hit found, but not necessarily unique to this track

Chapter 5

Analysis Method

In this chapter the method of measuring jet induced correlations via two-particle correlations at PHENIX will be outlined. The method of identifying hadrons will be described initially followed by the methodology for two-particle and 2+1 correlations. Since two-particle correlations in heavy ion collisions are contaminated by correlations due to the bulk flow, the methodology of measuring the Fourier flow coefficients, v_n, will be described. Finally, a model dependent approach will be used to subtract the correlated background in order to extract the jet-induced correlations.

5.1 Data

The data analyzed in this thesis are from the 2006 p+p and 2007 Au+Au data taking periods, both at $\sqrt{s_{NN}} = 200$ GeV unless otherwise noted. During these data taking periods PHENIX was able to collect a total integrated luminosity ($\int Ldt$) of 43.6 pb^{-1} and 3270 μb^{-1} for year 2006 and 2007 respectively [72]. The Au+Au luminosity can be translated into a *per binary collision* luminosity using calculated Glauber MC from Reference [73] which determines $\langle N_{\rm coll} \rangle \sim 257.8$ for 0-92% centrality. Using this $\langle N_{\rm coll} \rangle$ value one

estimates the per binary collision luminosity to be 12.7 pb^{-1}.

5.2 Hadron identification

Since the focus of this thesis is measuring *hadron* correlations, it becomes imperative to be able to segregate hadrons from electrons. We use many of the variables defined in Chapter 4 for various detector subsystems to identify hadrons on a *single* particle basis.

For all tracks in each event a selection is made by requiring that each track have hits in the X1, UV1, X2 layers of the Drift Chamber and a PC1 hit. This is achieved through the `quality` variable (see Section 4.5) by only keeping tracks that have a `quality` of either 31 or 63. This selection has little effect in p+p events where the multiplicity is low and the contamination due to fake tracks from combinatorics is minimal. However, in Au+Au events this `quality` selection greatly reduces the number of fake tracks that are reconstructed in each event.

To further improve the integrity of the track sample, an additional hit criterion is made by requiring each track to be used have a PC3 hit in the neighborhood of the track projection onto the PC3 subsystem. It is done using the normalized PC3 matching variable σ_{PC3} (see Section 4.2) and requiring that the track projection be within 2.5 standard deviations from the PC3 hit.

Once the integrity of the track sample has been established, a particle identification procedure is performed. For tracks below 5 GeV/c, any tracks projected onto the RICH that have Čerenkov light (fired PMT's) within a 11 cm radius are rejected. As explained in Section 4.3 Čerenkov light is a way to easily identify electron candidates below the pion p_T threshold of 4.7 GeV/c. Above the pion threshold, selection of hadrons becomes a bit more problematic since the RICH cannot be used to reliably segregate electrons

Table 5.1: Single track cuts

Variable	**Subsystem**	**Pass criterion**
`quality`	DC + PC1	`quality & 0x1f == 0x1f`
`n0`	RICH	`n0`< 0
σ_{PC3}	PC3	$\sigma_{PC3} < 2.5$
E/p	EMCal + DC	$p_T > 5$ GeV && $E/p > 0.2$

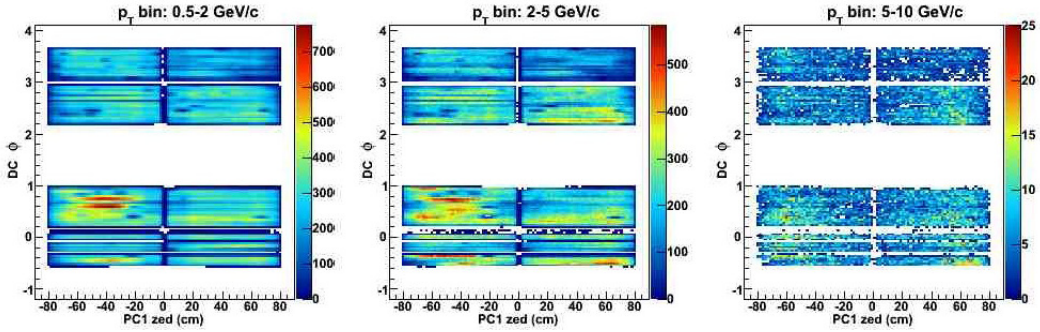

Figure 5.1: Drift chamber ϕ vs. PC1 z-coordinate distribution of tracks for various p_T bins.

from pions. In addition, there is a long tail background in the track p_T distribution that is believed to be coming from *soft* electrons that have badly reconstructed p_T. These electrons most likely originate from conversions and decays that are difficult to remove with the selection criterion previously mentioned. To remove these *soft* electrons, a semi measure is taken to reject tracks that have an $E/p < 0.2$ measured from the EMCal cluster energy and reconstructed momentum. The effect is that above 5 GeV/c there is significant reduction in statistics due to the E/p cut.

A review of the single track cuts used in this analysis is reviewed in Table 5.1. The final *single* particle selection made is to reject tracks that fall within the *fiducial cuts* of the central arms. These *fiducial cuts* remove single particle non-uniformities developed, including regions with low efficiency, in the central arms (i.e. edges and regions around broken drift chamber wires).

Figure 5.1 demonstrates how these non-uniformities manifest themselves in the 2007 Au+Au data.

Once all of these single particle cuts are applied to the track sample, the one major obstacle left to overcome is to remove correlated track artifacts that *do not* originate from any physical process of interest. These artifacts affect all charged track analyses that use the PHENIX tracking subsystems (i.e. drift chamber, pad chambers, RICH) and are typically from the tracking algorithm (e.g. hit sharing, track-splitting) or sources that contaminate the analysis of interest (e.g. $\gamma + X \longrightarrow X + e^+e^-$). These artifacts can, with good efficiency, be identified by analyzing *track pairs*.

5.3 Track pair cuts

The most common method at PHENIX to remove track pair artifacts (conversions, hit sharing, and track-splitting) is to correlate track pairs using variables defined at the drift chamber reference radius (e.g. $\phi_{\rm DC}$, $z_{\rm DC}$, α, etc...). By measuring the relative distances in $\Delta\phi_{\rm DC}$ vs. $\Delta z_{\rm DC}$ space, an *excess* of close proximity track pairs can be identified. To remove excess and deficiencies that are due to the detector, the distributions are usually divided by a *mixed-event* distribution to make a ratio distribution, which is a commonly used method at PHENIX and will be described in Section 5.4.1 (see Figure 5.2). This excess in the track pair distribution is usually removed on a track pair basis or, in other words, no removal of individual tracks from the sample. Although this reduces contamination of the "true" track pair distribution, this approach suffers from not adequately handling the removal or rejection of these artifacts due to the limited information provided in $\Delta\phi_{DC}$-Δz_{DC} space. In particular, Table 5.2 describes the effects contributing to these excesses and presents a strategy on how to best handle these artifacts.

As a result, a different approach is taken to identify and remove track

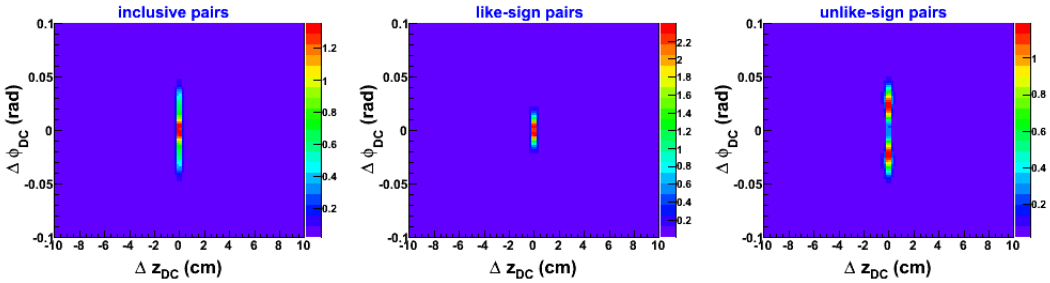

Figure 5.2: Ratio distributions (same-event pairs/mixed-event pairs) for $\Delta\phi_{DC}$ vs. Δz_{DC} in centrality 0-5% bin for inclusive, like-sign, and unlike-sign track pairs

Table 5.2: Track pair artifacts

Artifact	**Source**	**Procedure**
Conversions	Photons interacting with material to produce e^+e^- pairs.	Removal of both tracks from sample.
Track-splitting	Effect from track reconstruction algorithm producing *two* reconstructed tracks from *one* real track.	Keep best track and remove remaining track from sample.
Hit sharing	Result from two reconstructed tracks sharing pad chamber hit.	No removal of tracks from sample. Instead reject track pair.

pair artifacts than the traditional approach using additional information from drift chamber variables at the reference radius. The approach taken in this analysis is to construct 3-vectors from each track, assuming a straight line trajectory, and use them to calculate the distance-of-closest-approach (DCA) to all other tracks. Using the DCA, one is able to better identify ghosts, conversions, and pad chamber hit sharing tracks from data in order to handle them appropriately. It will be shown that for high-p_T tracks, this method is very efficent at removing this artifacts. However, there are effects at low ($p_T < 2.0$ GeV) that are yet to be fully understood.

Distance-of-closest-approach

The calculation of the DCA and cylindrical radial distance from the origin to the DCA (ρ_{DCA}) are both given in Appendix A while an illustration is given in Figure 5.3. Figure 5.4 illustrates how the DCA parameter space

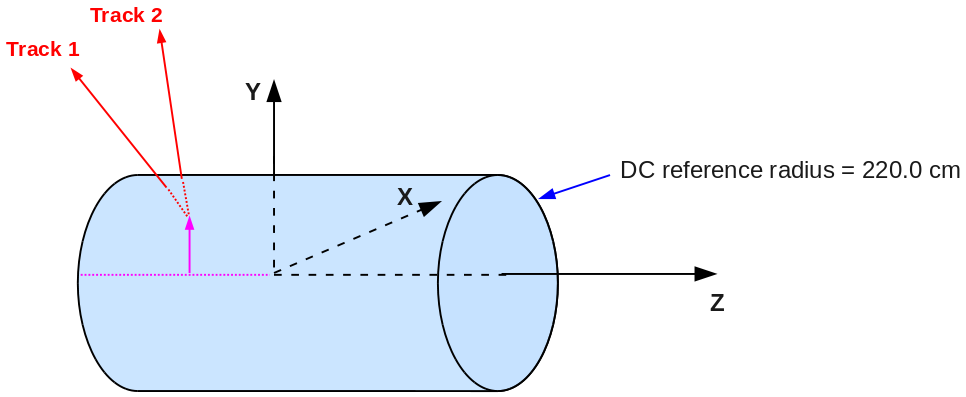

Figure 5.3: Illustration of the 3-vector approximation of two tracks and demonstration of geometrical interpretation of ρ_{DCA} (solid magenta arrow) and DCA (vertex of track pair). Cylinder represents drift chamber reference radius of 220 cm.

corresponds to each detector subsystem. Care must be taken how to interpret correlations below $\rho_{DCA} \sim 200$ cm since the magnetic field is at its maximum in this region and therefore the straight track approximation starts to break down. Regardless it will be demonstrated that, even below $\rho_{DCA} < 200$ cm, conversions originating from the Hadron Blind detector (HBD) can be identified.

Identification of conversions and PC hit sharing: ρ_{DCA} vs. DCA

From the ρ_{DCA} vs. DCA distribution one can identify to much better precision where the excess of track pairs originates from (Figure 5.5). Once again, the DCA provides information on how close the two tracks came to each

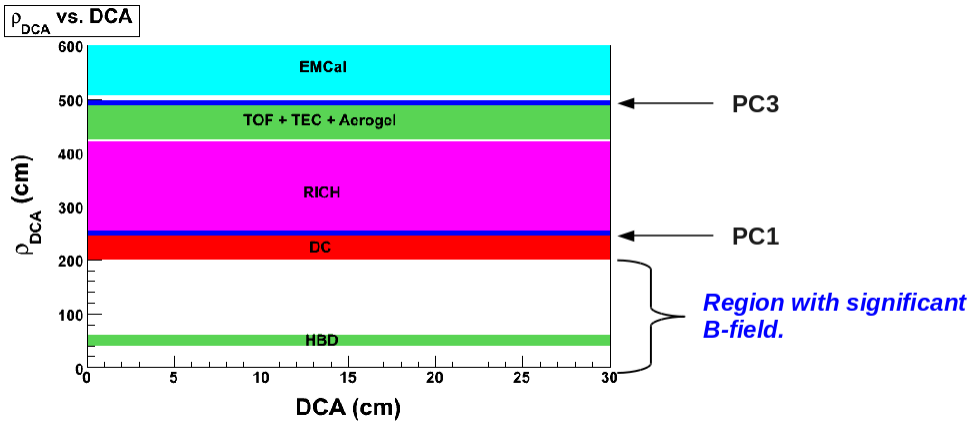

Figure 5.4: Figure shows the reconstruction of two tracks and what the ρ_{DCA} (solid magenta arrow) would geometrically represent.

other while the ρ_{DCA} measures where in the transverse direction the DCA was found for the track pair. It is striking that one can track most of the excess tracks to originate in the region around $\rho_{DCA} \sim 250$ cm. One can also see that there is a deficient region at a distance of $1.0 < DCA < 5.0$ cm. This region is precisely where the PC1 subsystem resides. One can bin the

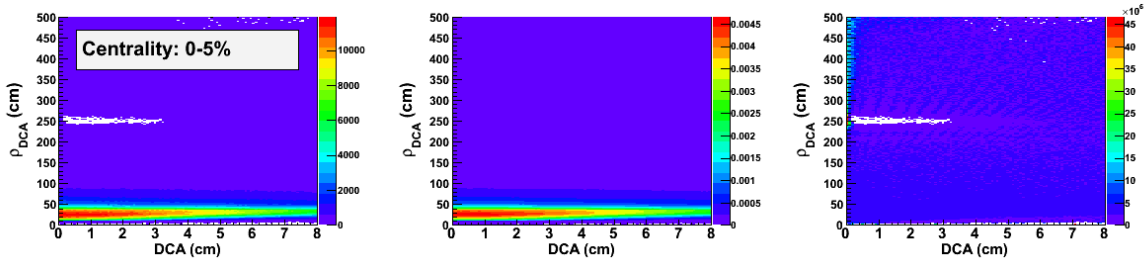

Figure 5.5: ρ_{DCA} vs. DCA for inclusive charged track pairs in central events (0-5%). Plotted are sequentially the foreground, mixed-event, and ratio distributions. Each track had a requirement of a PC3 match ($\sigma_{PC3} < 2.5$) and no RICH light associated with either track.

plots with respect to unlike-sign and like-sign track pairs to determine if this effect is having to do only with one type of pair species (i.e. unlike-sign or like-sign pairs). Figure 5.6 shows the result of binning track pairs in a bin of like-sign and unlike-sign pairs. One can see that there is a difference between both the like and unlike sign pairs. However, both samples do have the same strong correlation at the PC1 subsystem ($\rho_{DCA} \sim 250$ cm).

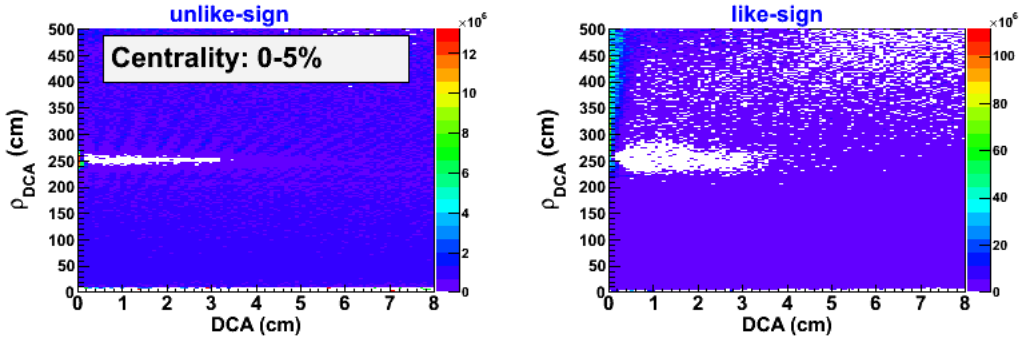

Figure 5.6: ρ_{DCA} vs. DCA for like-sign and unlike-sign track pair ratio (signal/mixed-event) distributions in central events (0-5%). Each of these tracks had a requirement of a PC3 match ($\sigma_{PC3} < 2.5$) and no RICH light associated with either track.

Furthermore, the *like-sign* distributions have an added correlation in the region of $0 < DCA < 1.0$ cm and $\rho_{DCA} > 200$ cm. This effect is due to *ghosting* (track-splitting). These are tracks that have been artificially created by the tracking algorithm and therefore share almost identical kinematic properties (e.g. p_T, η, etc...). As a result when calculating ρ_{DCA}, the distribution will lie randomly across a large range of values ($\rho_{DCA} > 200$ cm) and does not provide a reliable metric to identify and remove these track pairs. Instead these tracks can be efficiently identified by making a distribution of the *opening angle* (θ) vs. DCA. The opening angle is defined as:

$$\theta = \cos^{-1}(\hat{n}_1 \cdot \hat{n}_2) \tag{5.1}$$

where $\hat{n}$ is the direction of a given track at the drift chamber reference radius (these variables are all defined in Appendix A). However, since $\hat{n}_1$ and $\hat{n}_2$ are defined in the *local* coordinate system, then one has to further constrain this parameter with the DCA to make sure one is only selecting on tracks that are near each other and candidates of track-splitting. Figure 5.7 shows the

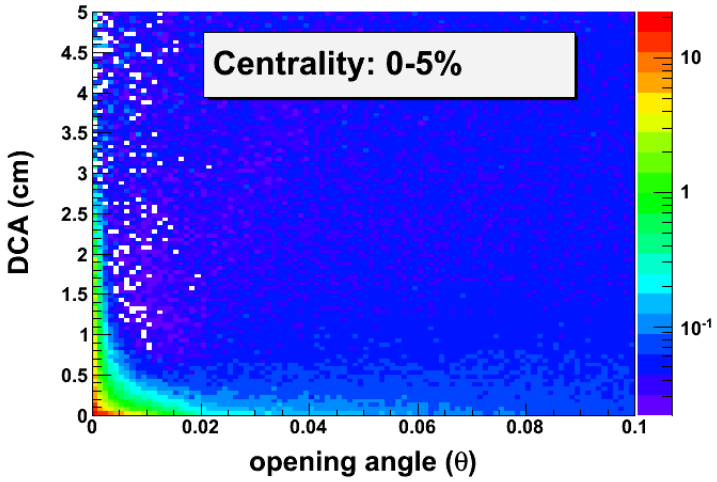

Figure 5.7: DCA vs. θ (opening angle) ratio distribution for *like-sign* track pairs for most central events (0-5%). Each of these tracks had a requirement of a PC3 match ($\sigma_{PC3} < 2.5$) and no RICH light associated with either track.

correlation and the excess of track pairs that appear when plotting DCA vs. θ.

5.4 Two-particle correlations

As mentioned in Section 2.5, jets are central to measuring the properties of the QGP. In the past decades, jet reconstruction algorithms have been developed to measure jets in low multiplicity environments such as p+p and

Table 5.3: Track pair cuts for 2006 p+p at $\sqrt{s_{NN}} = 200$ GeV

Parameter	**Cut**
DCA *unlike-sign* (−+,+−)	(115< ρ_{DCA} <140 cm) && (0< DCA <2 cm) HBD conversions (160< ρ_{DCA} <200 cm) && (0< DCA <1 cm) DC conversions (200< ρ_{DCA} <320 cm) && (0< DCA <12 cm) PC1 hit-sharing (320< ρ_{DCA} <400 cm) && (0< DCA <1 cm) PC1 hit-sharing (400< ρ_{DCA} <700 cm) && (0< DCA <1 cm) PC3 hit sharing
DCA *like-sign* (++,−−)	(200< ρ_{DCA} <320 cm) && (0< DCA <12 cm) PC1 hit-sharing (400< ρ_{DCA} <700 cm) && (0< DCA <1 cm) PC3 hit sharing
Track-splitting *like-sign* (++,−−)	($0 < DCA < 3$ cm) && ($0 < \theta < 0.020$ rad)

Table 5.4: Track pair cuts for 2007 Au+Au at $\sqrt{s_{NN}} = 200$ GeV

Parameter	**Cut**
DCA *unlike-sign* (−+,+−)	(125< ρ_{DCA} <140 cm) && (0< DCA <2 cm) HBD conversions (160< ρ_{DCA} <200 cm) && (0< DCA <1 cm) DC conversions (200< ρ_{DCA} <320 cm) && (0< DCA <12 cm) PC1 hit-sharing (320< ρ_{DCA} <400 cm) && (0< DCA <1 cm) PC1 hit-sharing (400< ρ_{DCA} <700 cm) && (0< DCA <1 cm) PC3 hit sharing
DCA *like-sign* (++,−−)	(200< ρ_{DCA} <320 cm) && (0< DCA <12 cm) PC1 hit-sharing (400< ρ_{DCA} <700 cm) && (0< DCA <1 cm) PC3 hit sharing
Track-splitting *like-sign* (++,−−)	($0 < DCA < 3$ cm) && ($0 < \theta < 0.025$ rad)

e^+e^- colliders. As a consequence, jet reconstruction algorithms had not been tested until recently in a high multiplicity environment and were found to be notoriously difficult to implement due to large underlying background present in each jet. Not until recently has there been significant progress made to use them successfully in heavy ion collisions. Because of this, more feasible methods were sought after such as the two-particle correlation method which will be described here.

The underlying idea behind the two-particle correlation method relies on the correlation of particles coming from the fragmentation process of a hard-scattering parton (jet). Because harder scattering partons (larger momentum transfer Q^2) have a larger probability to produce larger p_T particles, then the measurement of high-p_T tracks are a way to bias a measurement in the

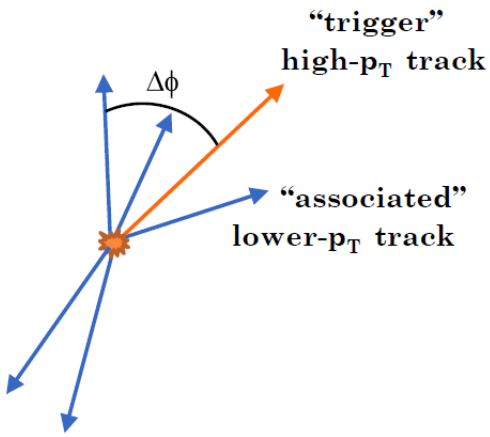

Figure 5.8: Azimuthal correlation of tracks in a two-particle correlations.

direction of jets. By correlating the remaining particles in the event relative to this high-p_T track (a.k.a *trigger*), a pair distribution can be constructed to measure the properties of jets. Figure 5.9 shows an illustration of a p+p collision system jet-induced distribution using this principle. In reality, it is not as easy to measure such a distribution measuring track pairs due to the *acceptance* (solid angle coverage of the PHENIX detector) and detector efficiency and a method has to be developed to correct for these effects. To this end, we describe the method of *event-mixing* in order extract the jet-induced correlations present in two-particle correlations.

5.4.1 Event Mixing: Acceptance and relative efficiency corrections to two-particle distributions

As much as one would like to have an idealized detector, the reality of the matter is that once azimuthal pair distributions ($d^2N^{ab}_{raw}/d\Delta\phi_{ab}$) are measured, hardly any physics can be extracted from these raw distributions until corrections have been made to it. Figure 5.10 shows an example of these

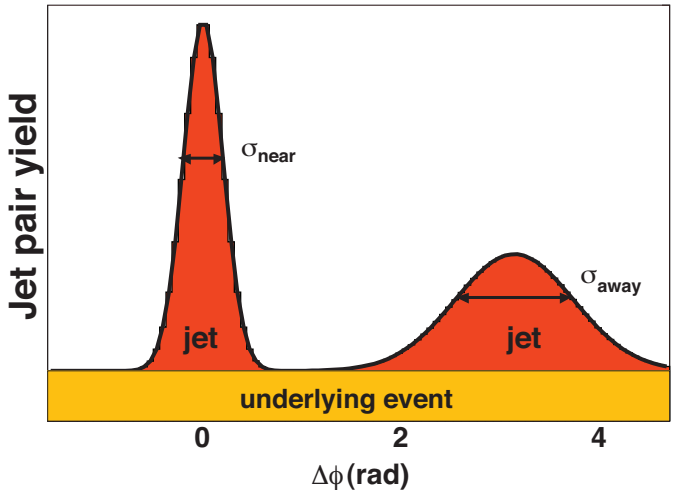

Figure 5.9: Illustration of jet-induced measurement using particle pair azimuthal ($\Delta\phi$) distributions.

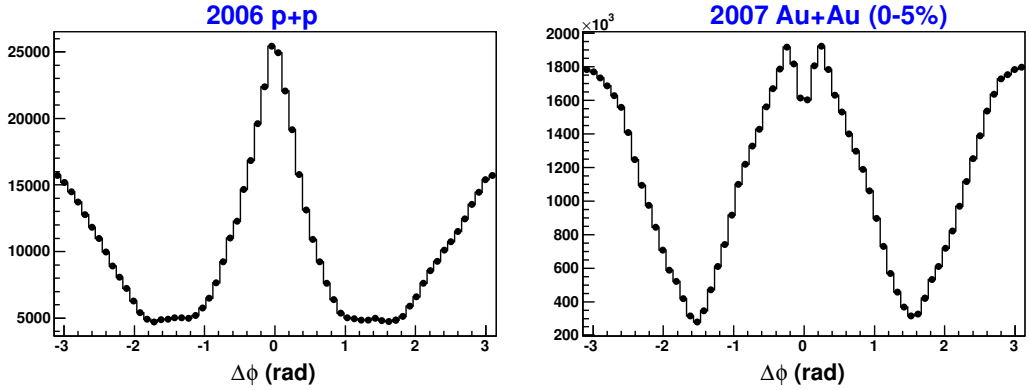

Figure 5.10: The uncorrected raw azimuthal hadron pair distribution ($dN^{ab}_{raw}/\Delta\phi_{ab}$) for p+p and Au+Au at $\sqrt{s_{NN}} = 200$ GeV.

raw distributions using the PHENIX detector. The observed $dN^{ab}_{raw}/d\Delta\phi_{ab}$ distribution can be understood as a convolution of the true pair distribution $d\mathbb{N}^{ab}/d\phi_a d\phi_b$ and the efficiency of the PHENIX detector to measure track

pairs $\varepsilon_2(\phi_a, \phi_b)$.

$$\frac{dN^{ab}_{raw}}{d\Delta\phi_{ab}} = \int d\phi_a d\phi_b \frac{d^2\mathbb{N}^{ab}}{d\phi_a d\phi_b} \varepsilon_2(\phi_a, \phi_b)\delta(\phi_a - \phi_b - \Delta\phi_{ab}) \tag{5.2}$$

Since we measure relative angles in two particle correlations, $d^2\mathbb{N}^{ab}/d\phi_a d\phi_b$ can be replaced by a function of the form $f(\phi_a - \phi_b)$.

$$\frac{dN^{ab}_{raw}}{d\Delta\phi_{ab}} = \int d\phi_a d\phi_b f(\phi_a - \phi_b)\varepsilon_2(\phi_a, \phi_b)\delta(\phi_a - \phi_b - \Delta\phi_{ab}) \tag{5.3}$$

Making a change of variables, $u = (\phi_a - \phi_b)/\sqrt{2}$ and $v = (\phi_a + \phi_b)/\sqrt{2}$, and integrating with respect to u, the distribution $f(\phi_a - \phi_b)$ can be factored out of the integral.

$$\begin{aligned}
\frac{dN^{ab}_{raw}}{d\Delta\phi_{ab}} &= \int d\phi_a d\phi_b f(\phi_a - \phi_b)\varepsilon_2(\phi_a, \phi_b)\delta(\phi_a - \phi_b - \Delta\phi_{ab}) \\
&= \int du dv \;\; f(u)\varepsilon_2(v + \Delta\phi_{ab}/\sqrt{2}, v - \Delta\phi_{ab}/\sqrt{2})\delta(\phi_a - \phi_b - \Delta\phi_{ab}) \\
&= f(\Delta\phi_{ab}) \int dv \;\; \varepsilon_2(v + \Delta\phi_{ab}/\sqrt{2}, v - \Delta\phi_{ab}/\sqrt{2})
\end{aligned} \tag{5.4}$$

There is a lot of information that is stored in the track pair efficiency $\varepsilon(\phi_a, \phi_b)$ such as the acceptance of the detector, ability of the detector to measure individual particles, track pair cuts, and time dependence of the detector to measure pairs, just to name a few [74]. One of the most obvious features that can be seen from Figure 5.10 is the effect of the PHENIX acceptance on the two-particle distribution which results in a triangular shaped distributions centered at $\Delta\phi_{ab} \sim 0$ and $\Delta\phi_{ab} \sim \pi$. The other obvious feature that can be seen is the implementation of track pair cuts in a high multiplicity environment. Although very similar pair cuts were used for both the p+p and Au+Au analysis, there are many more track pair artifacts that are present in high multiplicity environments as seen in the neighborhood of $\Delta\phi \sim 0$ bins.

To correct for the track pair efficiency $\varepsilon_2(\phi_a, \phi_b)$ a technique of *event-mixing* was employed to extract the true distribution. The principle behind *event-mixing* is to construct track pair distributions from uncorrelated events so that in this way one can remove the "*physics*" and retain the detector single particle *relative* efficiencies $\varepsilon_1(\phi_a)$ and $\varepsilon_1(\phi_b)$ in the two-particle distributions. Later we will see how to correct for the *absolute efficiencies*. Construction

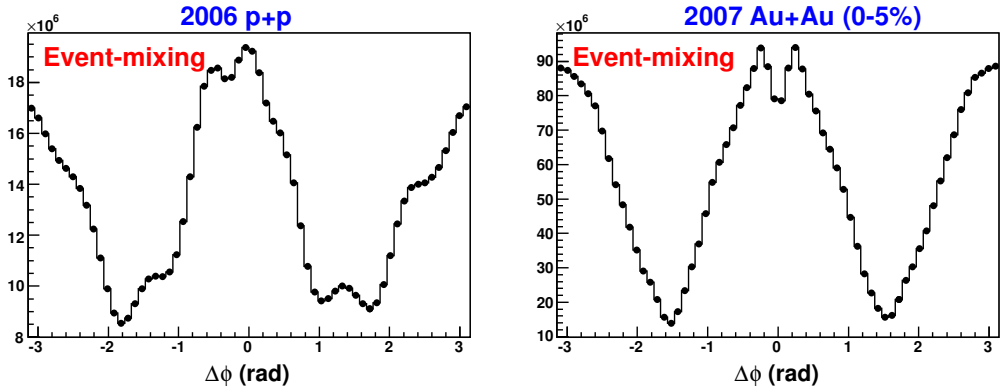

Figure 5.11: Hadron azimuthal pair distribution $dN^{ab}_{mix}/\Delta\phi_{ab}$ using *event-mixing* technique.

of *mixed-event* azimuthal pair distributions, as seen in Figure 5.11 can be described by the convolution of the true single particle distributions ($d\mathbb{N}^a/d\phi_a$ and $d\mathbb{N}^b/d\phi_b$) and their corresponding relative efficiencies in the detector ($\varepsilon_1(\phi_a)$ and $\varepsilon_1(\phi_b)$).

$$\frac{dN^{ab}_{mix}}{d\Delta\phi_{ab}} = \int d\phi_a d\phi_b \frac{d\mathbb{N}^a}{d\phi_a}\frac{d\mathbb{N}^b}{d\phi_b}\varepsilon_1(\phi_a)\varepsilon_1(\phi_b)\delta(\phi_a - \phi_b - \Delta\phi_{ab}) \tag{5.5}$$

Because the single particle distributions are rotationally invariant (assuming the detector subsystems such as the BBC's don't bias event selection toward a preferred azimuthal angle) and are therefore randomly distributed

in azimuth, they can be factored out of the integral.

$$\frac{dN^{ab}_{mix}}{d\Delta\phi_{ab}} = \frac{d\mathbb{N}^a}{d\phi_a}\frac{d\mathbb{N}^b}{d\phi_b}\int d\phi_a d\phi_b\ \varepsilon_1(\phi_a)\varepsilon_1(\phi_b)\delta(\phi_a - \phi_b - \Delta\phi_{ab}) \tag{5.6}$$

Using the same change of variables used for Equation 5.4, the *event-mixed* distribution can be cast in a similar form.

$$\frac{dN^{ab}_{mix}}{d\Delta\phi_{ab}} = \frac{d\mathbb{N}^a}{d\phi_a}\frac{d\mathbb{N}^b}{d\phi_b}\int dv\ \varepsilon_1(v + \Delta\phi_{ab}/\sqrt{2})\varepsilon_1(v - \Delta\phi_{ab}/\sqrt{2}) \tag{5.7}$$

Recall that the quantity that we wish to extract is $f(\Delta\phi_{ab})$ in Equation 5.4. In order to remove the track pair efficiency, the distribution can be divided *event-mixing* distribution to make a *correlation* distribution.

$$C(\Delta\phi_{ab}) \propto \frac{dN^{ab}_{raw}/d\Delta\phi_{ab}}{dN^{ab}_{mix}/d\Delta\phi_{ab}} \tag{5.8}$$

$$= \frac{f(\Delta\phi_{ab})\int dv\ \varepsilon_2(v + \Delta\phi_{ab}/\sqrt{2}, v - \Delta\phi_{ab}/\sqrt{2})}{\frac{d\mathbb{N}^a}{d\phi_a}\frac{d\mathbb{N}^b}{d\phi_b}\int dv\ \varepsilon_1(v + \Delta\phi_{ab}/\sqrt{2})\varepsilon_1(v - \Delta\phi_{ab}/\sqrt{2})} \tag{5.9}$$

$$\propto f(\Delta\phi_{ab}) \tag{5.10}$$

It should be emphasized that the preceding is only possible if the track pair efficiency, $\varepsilon_2(\phi_a, \phi_b)$, can be *factorized* into the single particle efficiencies, $\varepsilon_1(\phi_a)$ and $\varepsilon_1(\phi_b)$.

$$\varepsilon_2(v + \Delta\phi_{ab}/\sqrt{2}, v - \Delta\phi_{ab}/\sqrt{2}) \sim \varepsilon_1(v + \Delta\phi_{ab}/\sqrt{2})\varepsilon_1(v - \Delta\phi_{ab}/\sqrt{2}) \tag{5.11}$$

In order for this assumption to be a good approximation, similar acceptance, similar multiplicities, and the *exact* same pair cuts must be made to both the foreground and event-mixing distributions.

Event-mixing classes

To make the *efficiency factorization* a good approximation, both the foreground and event-mixing distributions are separated into *classes*. Some of the factors that have been determined to have a significant effect on the pair efficiency are the collision vertex of the event, multiplicity of the event, p_T of the tracks, relative charge between pairs, and even the measured position of the trigger particle (e.g. West vs. East arm). These factors will have different degree of significance depending on the signal-to-noise ratio (S/N) of the measurement. In particular, the *high* S/N ratio for jets in p+p means that the dependence is weaker when compared to a collision system, such as Au+Au, with an *extremely small* S/N ratio (S/N$\sim 10^{-4}$) where small changes in the pair efficiency can significantly affect the two-particle distribution.

To demonstrate some of these effects, Figure 5.12 illustrates the dependence of the event-mixing track pair acceptance as a function of collision vertex. The reason for this change in the shape of the distribution is due to the collision vertex deviating from the nominal vertex position of $z = 0$ which results in a reduction in acceptance to detect track pairs for topologically equivalent events. Although the effects due to displacements in collision vertex seem to be small, one must consider that the differences are still larger than 10^{-4}. Figure 5.13 shows the centrality dependence for event-mixing distributions while Figure 5.14 demonstrates the p_T dependence. With regards to the p_T dependence, the p_T differences observed tend to be more significant for lower p_T tracks, because of their larger radius of curvature, and become reduced for higher p_T. For this reason distributions using low-p_T tracks are usually segregated in bins of $\Delta p_T < 1$ GeV. A review of the event-mixing classes are tabulated in Table 5.5

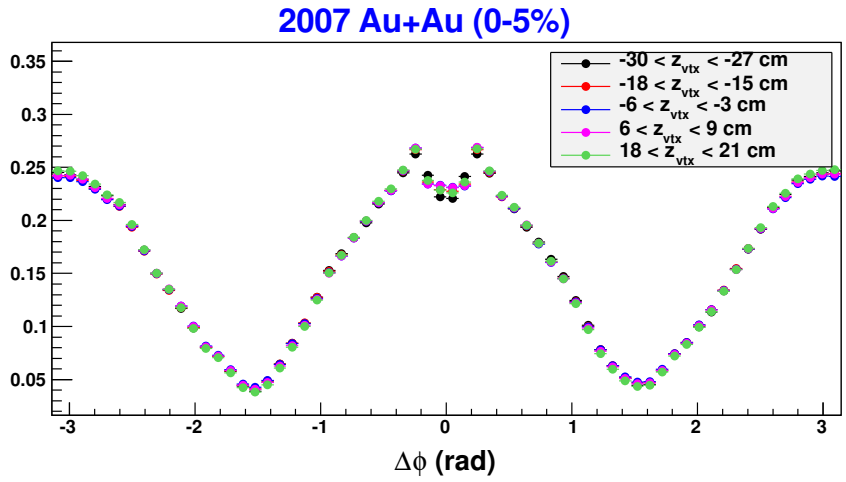

Figure 5.12: Illustration of a few normalized event-mixing track pair azimuthal distribution and their dependence on collision vertex z-coordinate for most central Au+Au events. Events were segregated into 3 cm z-vertex bins.

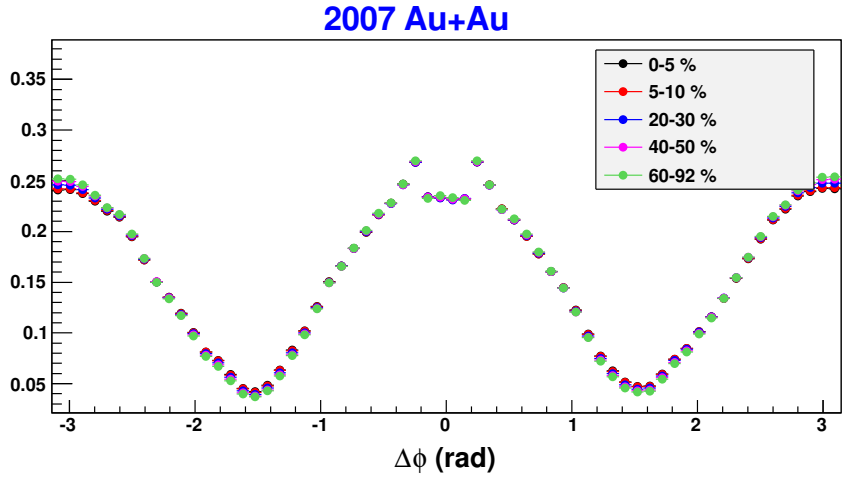

Figure 5.13: Centrality dependence of normalized mixed-event distributions.

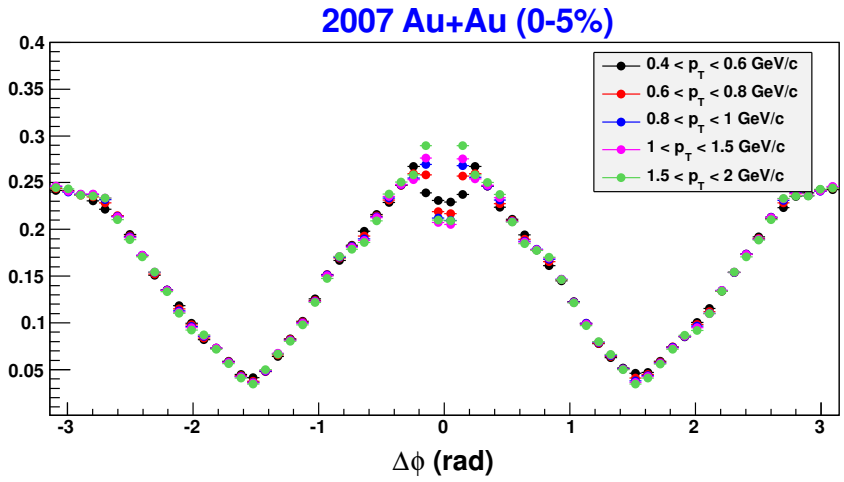

Figure 5.14: Normalized event-mixing $dN^{ab}/d\Delta\phi_{ab}$ dependence on track p_T. In this case the p_T^a is maintained constant as p_T^b is varied.

Table 5.5: Two-particle correlation event-mixing classes

Parameter	**Binning**
Centrality	0-5%, 0-10%, 10-20%, 20-30%, 30-40%, 40-50%, 50-60%, 60-92%
Event vertex	3 cm bins
p_T	0.2 GeV for lower p_T and relaxed up to 5 GeV for higher p_T
Arm	Binned in West and East arm

Construction of correlation $C(\Delta\phi_{ab})$

The raw and mixed-event distribution is measured for each bin in the 5D space (centrality, collision vertex, p_T^a, p_T^b, and arm) mentioned above and a correlation distribution constructed. To have a meaningful correlation $C(\Delta\phi_{ab})$ the mixed-event distribution is normalized to 2π in order to extract $dN^{ab}/d\Delta\phi_{ab}$ and then divided by the number of triggers, N^a measured

in that bin to measure the azimuthal distribution of pairs *per trigger*.

$$\frac{1}{N^a}C(\Delta\phi_{ab}) = \frac{1}{N^a}\frac{dN^{ab}_{raw}/d\Delta\phi_{ab}}{2\pi\frac{dN_{mix}/d\Delta\phi_{ab}}{\int d\Delta\phi_{ab} dN_{mix}/d\Delta\phi_{ab}}} \tag{5.12}$$

$$= \frac{1}{N^a}\frac{dN^{ab}}{d\Delta\phi_{ab}} \tag{5.13}$$

Furthermore, since some parameters are important only to correct for changes in efficiencies and acceptance (e.g. collision vertex), the bins from these parameters will be combined. To this end, the collision geometry and particle kinematics (i.e. centrality and p_T) dependence are parameters that the final results will be dependent on while the arm and collision vertex dependence are not and will be combined to produce an averaged correlation. Since each event classification bin is uncorrelated and can be thought as a different experiment, the correlations are combined by a weighted averaging procedure in *each* dimension.

$$\frac{1}{N^a}\frac{dN^{ab}_0}{d\Delta\phi_{ab}} = \frac{\sum_k^{N\text{ bins}} w_k \frac{1}{N^a_k}\frac{dN^{ab}_k}{d\Delta\phi_{ab}}}{\sum_k^{N\text{ bins}} w_k} \tag{5.14}$$

The weights, w_k, used are the fraction of triggers for that bin with respect to the total in that dimension ($w_k = N^a_k/N^a_{\text{total}}$). Finally, to obtain the *true* pair distribution, the single particle efficiency $\varepsilon_{sngl}(p^b_T)$, determined from a GEANT Monte Carlo simulation, must be applied to measure the number of associated tracks that should have been measured for every trigger.

$$\frac{1}{N^a}\frac{d\mathbb{N}^{ab}}{d\Delta\phi_{ab}} = \frac{1}{\varepsilon_{sngl}(p^b_T)N^a}\frac{dN^{ab}_0}{d\Delta\phi_{ab}} \tag{5.15}$$

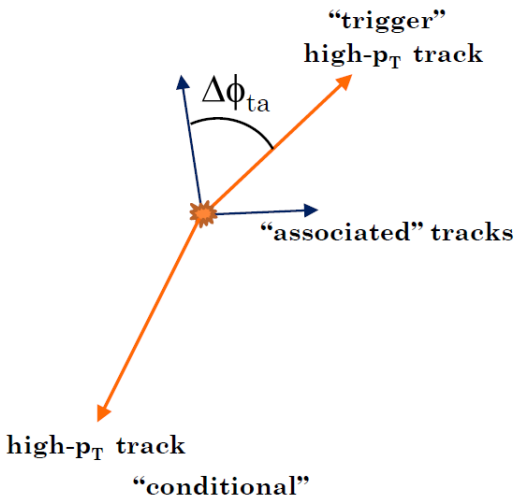

Figure 5.15: Illustration of 2+1 correlations demonstrating both *triggers*(orange) and the *associated* tracks(black).

5.5 2+1 correlations

As mentioned in Section 2.5.1, the two-particle correlation data suggests that production point of the jets being measured via this method is biased toward the surface of the collision overlap region. There are measurements that demonstrate some promise in the ability to reduce this effect (e.g. γ-$h^{\pm}$ correlations, jet reconstruction). The focus of this thesis is to determine if a bias reduction can be achieved by requiring there to be a second high-p_T track (a.k.a. conditional trigger) in the opposite hemisphere to the primary high-p_T track used in standard two-particle correlations (see Figure 5.15). It is left to the experiment to determine if the requirement of a *conditional* trigger, which reduces the azimuthal p_T asymmetry, will bias the event selection toward events that have a production point more towards the center of the medium. However, before this is unveiled the methodology for measuring 2+1 correlations will be presented.

5.5.1 Event-mixing for three-particle correlations

Since this is effectively a *three*-particle correlation, care must be taken to appropriately correct for acceptance and efficiencies as was done for two-particle correlations. Most of the mathematical framework for *event-mixing* is already in place from Section 5.4 so that all is needed is to extend to three particles by induction. In particular the raw distribution measured in 2+1 correlations is given by:

$$\begin{aligned}\frac{d^2N^{abc}_{raw}}{d\Delta\phi_{ab}d\Delta\phi_{ac}} &= \int d\phi_a d\phi_b d\phi_c \, \frac{d^3\mathbb{N}^{abc}}{d\phi_a d\phi_b d\phi_c}\varepsilon_3(\phi_a,\phi_b,\phi_c)\times \\ &\qquad \delta(\phi_a-\phi_b-\Delta\phi_{ab})\delta(\phi_a-\phi_c-\Delta\phi_{ac}) \qquad (5.16)\\ &= \int d\phi_a d\phi_b d\phi_c \, f(\phi_a-\phi_b,\phi_a-\phi_c)\varepsilon_3(\phi_a,\phi_b,\phi_c)\times \\ &\qquad \delta(\phi_a-\phi_b-\Delta\phi_{ab})\delta(\phi_a-\phi_c-\Delta\phi_{ac}) \qquad (5.17)\end{aligned}$$

Making a similar change of variables as in the two-particle case, $u=(\phi_a-\phi_b)/\sqrt{2}$, $v=(\phi_a+\phi_b)/\sqrt{2}$, $w=\phi_a-\phi_c$, the function, $f(\phi_a-\phi_b,\phi_a-\phi_c)$ which embodies the physics that is being pursued, can be factored out.

$$\begin{aligned}\frac{d^2N^{abc}_{raw}}{d\Delta\phi_{ab}d\Delta\phi_{ac}} &= \int dudvdw \, f(u,w)\varepsilon_3(v+u/\sqrt{2},v-u/\sqrt{2},v+u/\sqrt{2}-w)\times \\ &\qquad \delta(u-\Delta\phi_{ab})\delta(w-\Delta\phi_{ac}) \qquad (5.18)\\ &= f(\Delta\phi_{ab},\Delta\phi_{ac})\int dv\, \varepsilon_3(v+\Delta\phi_{ab}/\sqrt{2},v-\Delta\phi_{ab}/\sqrt{2},v+\Delta\phi_{ab}/\sqrt{2}-\Delta\phi_{ac}) \\ & \qquad (5.19)\end{aligned}$$

To construct the *event-mixing* three-particle distribution, the three tracks selected *must* come from three *uncorrelated* events (so as to remove the "*physics*"). Using two events would be undesireable since any two tracks coming from the same event would retain their *physics* correlations and only work to reduce the correlation that is being extracted (i.e $f(\Delta\phi_{ab},\Delta\phi_{ac})$).

The following represents the three-particle *mixed-event* distribution.

$$\begin{aligned}\frac{d^2N^{abc}_{mix}}{d\Delta\phi_{ab}d\Delta\phi_{ac}} &= \int d\phi_a d\phi_b d\phi_c \frac{d\mathbb{N}^a}{d\phi_a}\frac{d\mathbb{N}^b}{d\phi_b}\frac{d\mathbb{N}^c}{d\phi_c}\varepsilon_1(\phi_a)\varepsilon_1(\phi_b)\varepsilon_1(\phi_c)\times \\ &\qquad \delta(\phi_a-\phi_b-\Delta\phi_{ab})\delta(\phi_a-\phi_c-\Delta\phi_{ac}) \qquad (5.20)\\ &= \frac{d\mathbb{N}^a}{d\phi_a}\frac{d\mathbb{N}^b}{d\phi_b}\frac{d\mathbb{N}^c}{d\phi_c}\int dv\ \varepsilon_1(v+\Delta\phi_{ab}/\sqrt{2})\varepsilon_1(v-\Delta\phi_{ab}/\sqrt{2})\times \\ &\qquad \varepsilon_1(v+\Delta\phi_{ab}/\sqrt{2}-\Delta\phi_{ac}) \qquad (5.21)\end{aligned}$$

In the last step, the same arguments in two-particle event-mixing are made here to factor out the single particle distributions from the integral. Constructing the 2+1 correlation is achieved by dividing both the raw and mixed-event distributions.

$$\begin{aligned}C(\Delta\phi_{ab},\Delta\phi_{ac}) &\propto \frac{d^2N^{abc}_{raw}/d\Delta\phi_{ab}d\Delta\phi_{ac}}{d^2N^{abc}_{mix}/d\Delta\phi_{ab}d\Delta\phi_{ac}} \\ &= \frac{f(\Delta\phi_{ab},\Delta\phi_{ac})}{\frac{d\mathbb{N}^a}{d\phi_a}\frac{d\mathbb{N}^b}{d\phi_b}\frac{d\mathbb{N}^c}{d\phi_c}}\times \\ &\qquad \frac{\int dv\ \varepsilon_3(v+\Delta\phi_{ab}/\sqrt{2},v-\Delta\phi_{ab}/\sqrt{2},v+\Delta\phi_{ab}/\sqrt{2}-\Delta\phi_{ac})}{\int dv\ \varepsilon_1(v+\Delta\phi_{ab}/\sqrt{2})\varepsilon_1(v-\Delta\phi_{ab}/\sqrt{2})\varepsilon_1(v+\Delta\phi_{ab}/\sqrt{2}-\Delta\phi_{ac})} \\ &\propto f(\Delta\phi_{ab},\Delta\phi_{ac}) \qquad (5.22)\end{aligned}$$

As mentioned in the previous section, this approximation is legitimate only if the three-particle efficiency $\varepsilon_3(\phi_a,\phi_b,\phi_c)$ can be *factorized* into single-particle efficiencies.

Three-particle event-mixing classes

To achieve the above approximation, the same event-mixing classes were used as in two-particle correlations (i.e. centrality, track p_T, collision vertex, and arm) and, in addition, the relative azimuthal angle, $\Delta\phi_{tc}$, between the primary trigger and condtional trigger. The reason for adding this binning

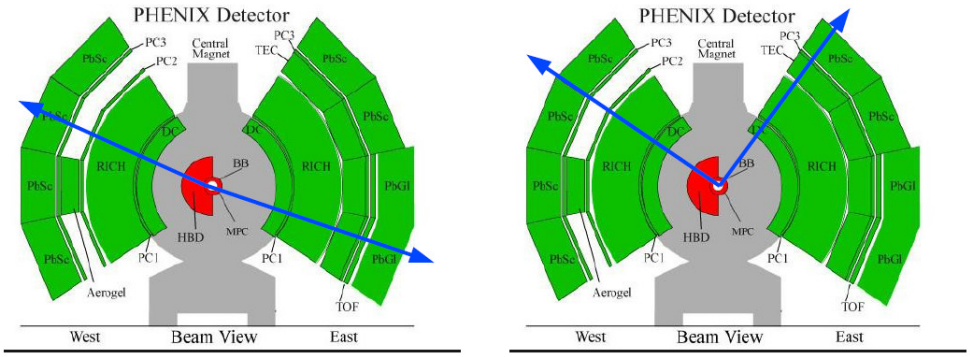

Figure 5.16: Two extreme scenarios for primary and conditional trigger (blue arrows) relative angle $\Delta\phi_{tc}$ which leads to differences in three-particle acceptance.

parameter is due to the change in acceptance in $\Delta\phi_{ta}$ depending on $\Delta\phi_{tc}$. Figure 5.16 illustrates two extreme scenarios where the relative angle of the primary and conditional trigger leads to different acceptances. Figure 5.17 shows the observed three-particle acceptance for most central 2007 Au+Au data. One deficiency that is immediately noticeable is the lack of acceptance for some $\Delta\phi_{ta}$ angles. Eventually this lack of acceptance will be compensated when correlation for both arms are combined.

Construction of 2+1 correlations

The 2+1 correlations were combined in the same way as the two-particle correlations to construct an azimuthal pair distribution per *two track* high-p_T trigger. The only difference was that for reasons of the acceptance depending on $\Delta\phi_{tc}$ and desiring to measure the most antipodal (back-to-back) triggers, an angle selection was made such that $|\pi - \Delta\phi_{tc}| < \delta$, where δ was typically

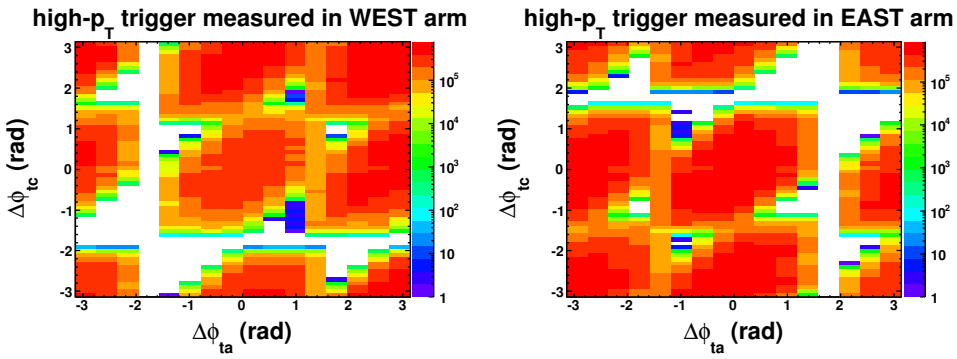

Figure 5.17: Three-particle mixed-event distributions (acceptance) for tracks above 1 GeV/c using 2007 Au+Au (0-5%) data. Depending on which arm (East or West) the primary trigger is measured in, a significant difference in the acceptance is observed.

chosen to be $\pi/8$.

$$\frac{dN^{ab}_{raw,mix}}{d\Delta\phi_{ab}} = \int_{\pi-\delta}^{\pi+\delta} d\Delta\phi_{ac}\, \frac{d^2N^{abc}_{raw,mix}}{d\Delta\phi_{ab}d\Delta\phi_{ac}} \tag{5.23}$$

The same procedure was followed to construct 2+1 correlations from the projected *raw* and *event-mixed* distributions for each event-mixed class. The mixed-event distribution was also normalized to 2π. However, the *per trigger* normalization of the correlation was performed by counting the number of high-p_T pairs, N^{ac}, measured.

$$\begin{aligned}\frac{1}{N^{ac}}C(\Delta\phi_{ab},\Delta\phi_{ac}) &= \frac{1}{N^{ac}}\frac{dN^{ab}_{raw}/d\Delta\phi_{ab}}{2\pi\frac{dN^{ab}_{mix}/d\Delta\phi_{ab}}{\int d\Delta\phi_{ab}\, dN^{ab}_{mix}/d\Delta\phi_{ab}}} \\ &= \frac{1}{N^{ac}}\frac{dN^{ab}}{d\Delta\phi_{ab}}\end{aligned} \tag{5.24}$$

The collision vertex and arm bins were combined as in two-particle correlations to make the distribution dependent only on the collision geometry and track kinematics. And finally it was corrected for the single particle *absolute* efficiency $\varepsilon_{sngl}(p_T^b)$.

$$\frac{1}{N^{ac}}\frac{d\mathbb{N}^{ab}}{d\Delta\phi_{ab}} = \frac{1}{\varepsilon_{sngl}(p_T^b)\ N^{ac}}\frac{dN_0^{ab}}{d\Delta\phi_{ab}} \tag{5.25}$$

5.6 Event Plane Ψ_n measurement

As a self-consistent measure of the correlated background in two-particle correlations, the correlated background coming from the bulk medium was measured using the same track cuts described in Section 5.2. To measure the correlated background the Fourier coefficients v_n, corresponding to *flow*, need to be measured which requires the measurement of the event plane on a per event basis. In this analysis, the event plane was determined using the Reaction Plane detector (RXNPL) which has a large pseudorapidity coverage ($1.0 < \eta < 2.8$).

Reaction Plane detector ADC calibration

The first step is to calibrate the RXNPL channel ADC measurements. The energy deposited in each channel by tracks in a given event is determined by the difference in the low-gain ADC measurements prior (*pre*-ADC) and after (*post*-ADC) an event. To each channel a raw cut was made to filter out unwanted ADC measurements.

- *pre*-ADC > 0
- *post*-ADC > 0

- 500 ns $< tdc <$ 1800 ns

Figure 5.18 shows the mean energy $\langle E_{raw} \rangle$ distribution per channel over the 2007 Au+Au dataset. To remove diffences in detector performance for

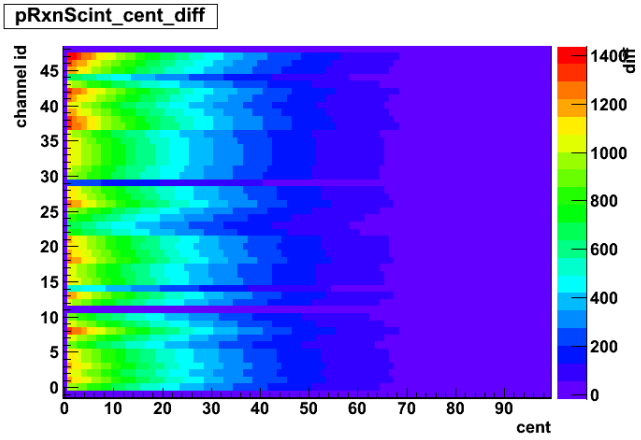

Figure 5.18: Raw energy deposition from the Reaction Plane detector. Energy deposition is calculated as the difference in *pre* and *post* ADC values for each channel and centrality

each channel, each energy measurement (E_{raw} =*post*-ADC - *pre*-ADC) was normalized the the mean energy:

$$E_{calib} = \frac{E_{raw}}{\langle E_{raw} \rangle} \tag{5.26}$$

Figure 5.19 shows the normalized distribution. The resultant distribution looks uniform aside from one channel (channel 11) which is due to a broken PMT in the South arm of the RXNPL. The broken PMT was masked out and handled by averaging the normalized energy measurements from neighboring channels.

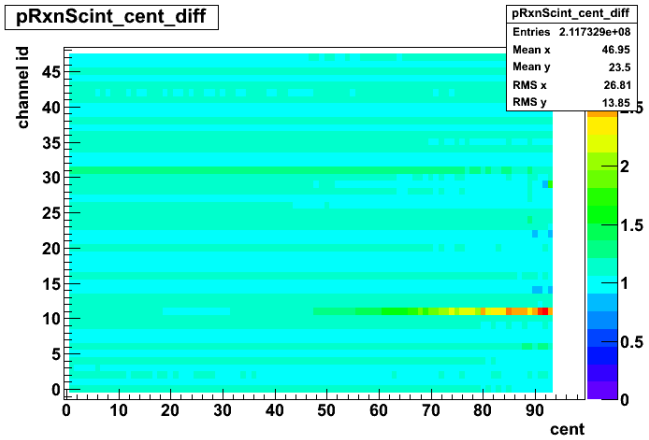

Figure 5.19: Normalized energy deposition $\langle E_{calib} \rangle$ from the Reaction Plane detector for each channel.

Re-centering of flow vectors $\mathbf{Q_n}$

Once the detector performance has been calibrated, we can proceed on to the next step in determining the event plane. The event plane is defined by:

$$\tan(n\Psi_n) = \frac{Q_{n,y}}{Q_{n,x}} \tag{5.27}$$

$$= \frac{\sum w_i \sin(n\phi_i)}{\sum w_i \cos(n\phi_i)} \tag{5.28}$$

where $w_i = E_{calib}$, and ϕ_i is the azimuthal measurement of the detector element. Figure 5.20 is the result of plotting the uncorrected event plane distribution. The oscillation in the event planes is due to drift in the flow vectors and results in an event plane oscillation of $\sim 20\%$. Determining the mean $Q_{n,x}$ and $Q_{n,y}$ we can evalute and correct for the drift in the flow vectors. The re-centered (corrected) flow vectors are calculated by subtracting the

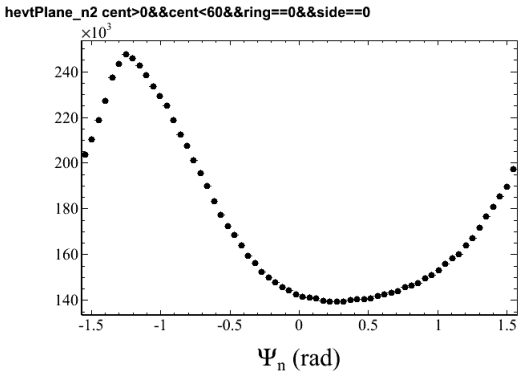

Figure 5.20: Raw event plane distribution ($dN/d\Psi_n$) for $n = 2$ harmonic

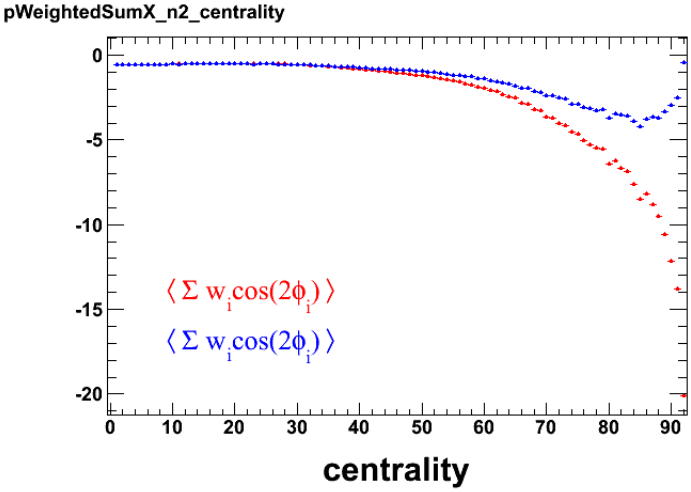

Figure 5.21: Mean values of $\langle Q_{n,x} \rangle$ and $\langle Q_{n,y} \rangle$ for $n = 2$ harmonic as a function of centrality.

mean value [75]:

$$Q_{n,x}^{corr} = \frac{Q_{n,x} - \langle Q_{n,x} \rangle}{\sigma_x} \tag{5.29}$$

$$Q_{n,y}^{corr} = \frac{Q_{n,y} - \langle Q_{n,y} \rangle}{\sigma_y} \tag{5.30}$$

From the corrected flow vectors, the Ψ_n distribution is determined to have a $\sim 3\%$ oscillation (Figure 5.22).

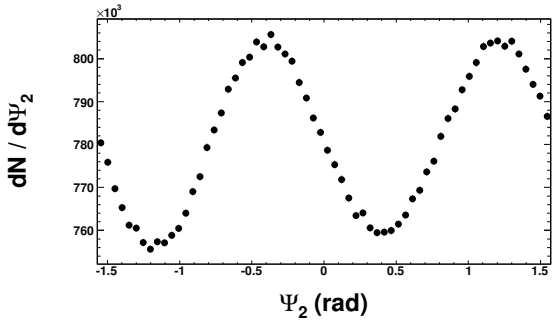

Figure 5.22: Result Ψ_n distribution for $n = 2$ harmonic after recentering of flow vectors.

Fourier flattening of Ψ_n distribution

The last step in producing a flat Ψ_n distribution is to find the Fourier representation of the distribution and extract the coefficients of the even and odd harmonics for each centrality bin [75]:

$$A_k = -\frac{2}{k}\langle \sin(nk\Psi_n) \rangle \tag{5.31}$$

$$B_k = \frac{2}{k}\langle \cos(nk\Psi_n) \rangle \tag{5.32}$$

Figure 5.23 and 5.24 show the extraction of A_n and B_n coefficients after recentering the Ψ_n distributions. Once this coefficients have been determined the correction to the event plane is given by (the sum was taken only up to $k = 8$):

$$\Delta\Psi_n = \sum_k A_k \cos(nk\Psi_n) + B_k \sin(nk\Psi_n) \tag{5.33}$$

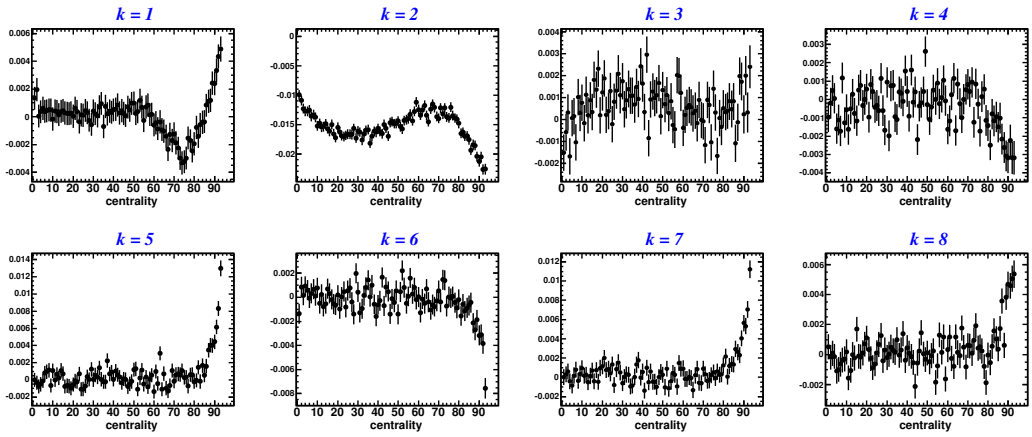

Figure 5.23: Example of A_k coefficients for $n = 2$ harmonic

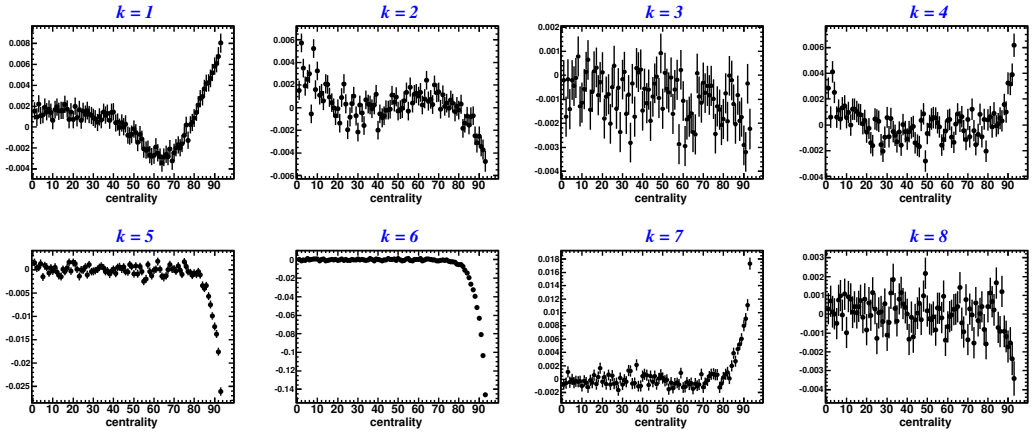

Figure 5.24: Example of B_k coefficients for $n = 2$ harmonic

Figure 5.25- 5.27 demonstrates the distribution of $\Delta\Psi_n$'s used to correct the event plane. To each event plane this correction factor is applied to obtain a corrected event plane angle (Ψ_n^{corr}):

$$\Psi_n^{corr} = \Psi_n + \Delta\Psi_n \tag{5.34}$$

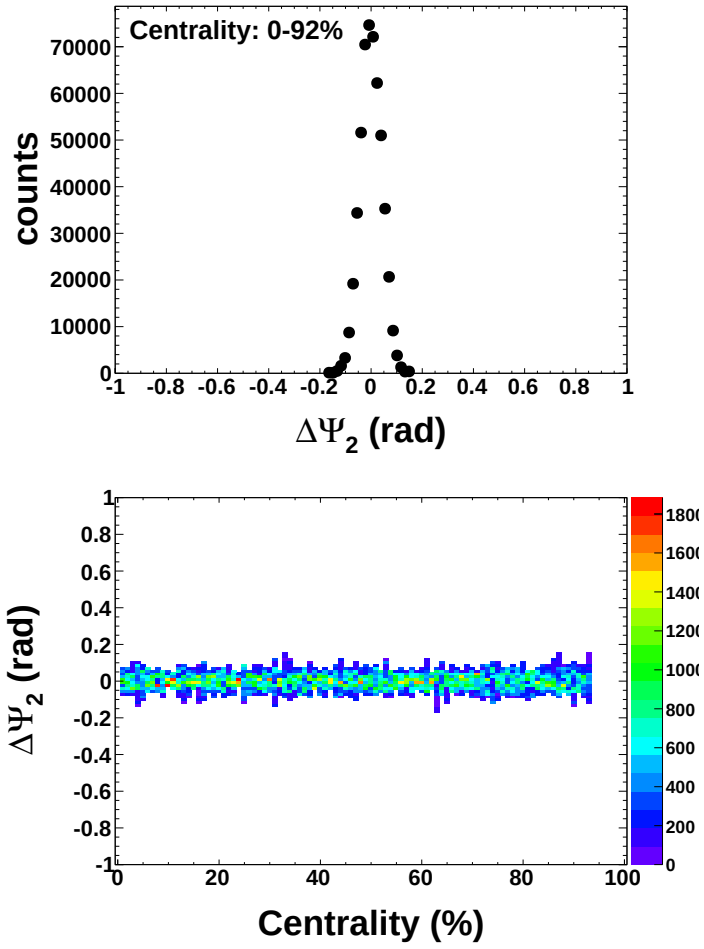

Figure 5.25: Distribution of $\Delta\Psi_2$ and its dependence on centrality.

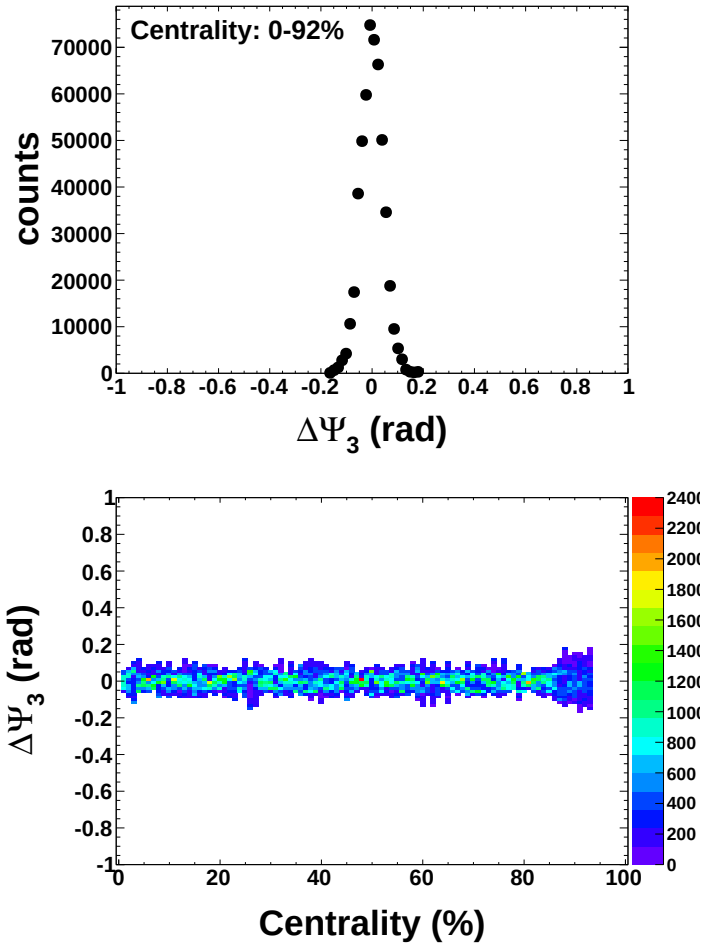

Figure 5.26: Distribution of $\Delta\Psi_3$ and its dependence on centrality.

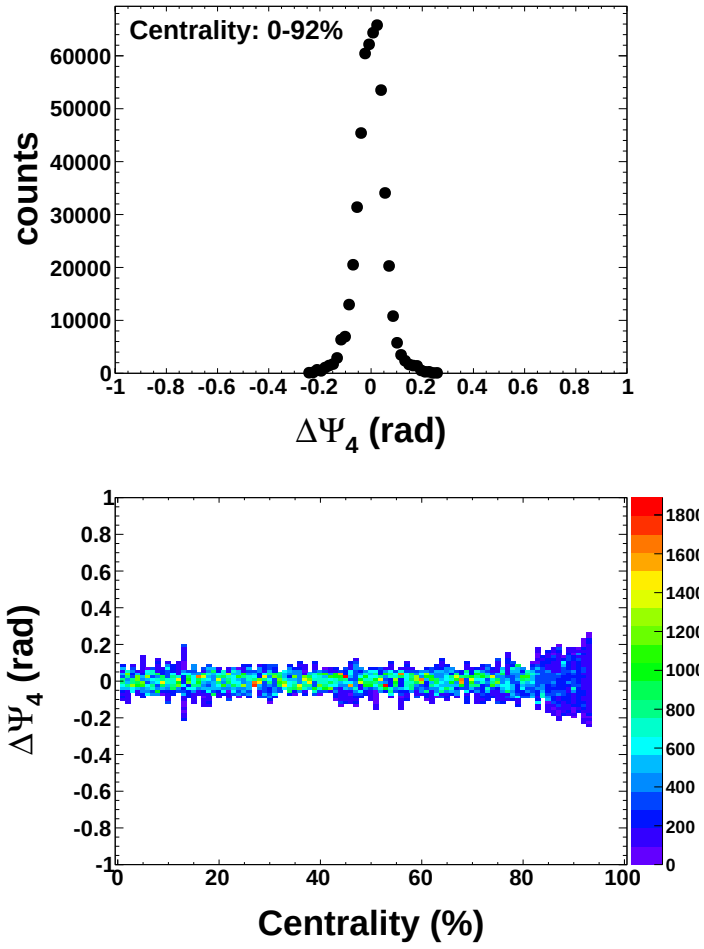

Figure 5.27: Distribution of $\Delta\Psi_4$ and its dependence on centrality.

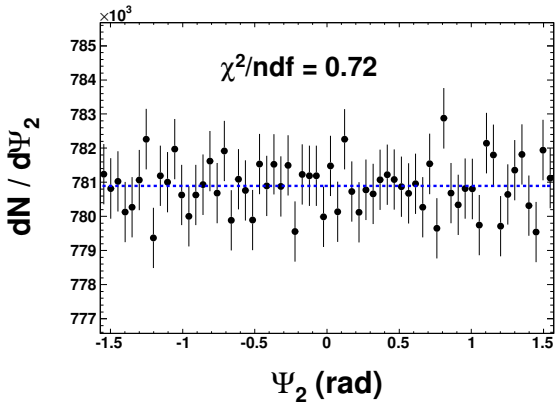

Figure 5.28: Distribution of Ψ_n's after Fourier flattening procedure. A flat line (blue) was fit to the distribution and is shown along with its χ^2/ndf.

Figure 5.28 shows the result of flattening the distribution along with a straight line fit to the data.

Event plane resolution via root finding

Although there are several methods of determine the dispersion correction $\langle\cos(2[\Psi_n - \Psi_{RP}])\rangle$ to the true event plane, the method of root finding from the sub-event dispersion is used in this analysis. Figure 5.29 shows the distribution for the sub-event dispersion between the RXNPL-north and RXNPL-south for the Ψ_2 event plane. For each centrality bin, the parameter χ is determined by solving for χ in the equation:

$$\sqrt{\langle\cos(mk[\Psi_N - \Psi_S])\rangle} = \frac{\sqrt{\pi}}{2}\chi\exp(-\chi^2/2)\left[I_{\frac{k-1}{2}}\left(\frac{\chi^2}{2}\right) + I_{\frac{k+1}{2}}\left(\frac{\chi^2}{2}\right)\right] \tag{5.35}$$

where $n = km$ and I_k are the modified Bessel functions of the first kind. Since what is extracted is the sub-event χ^{sub}, one can determine the full event χ by setting it to $\chi = \sqrt{2}\chi^{sub}$. Then one can plug χ into equation 5.36

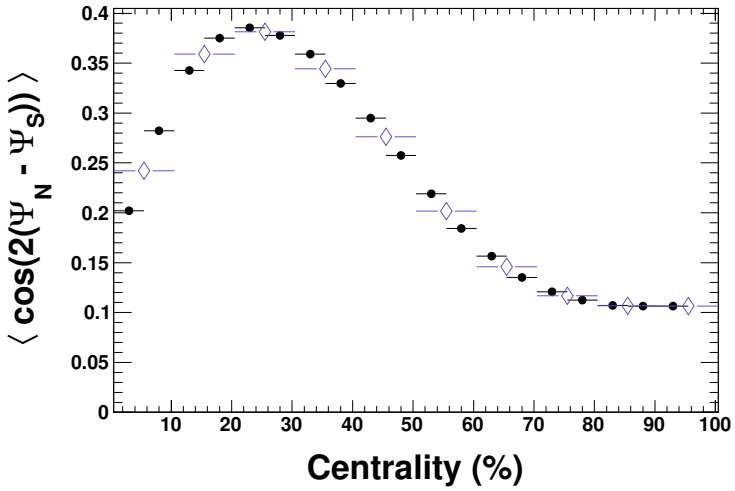

Figure 5.29: Sub-event dispersion for 5% (black) and 10% (blue) centrality bins for Ψ_2.

to determine the full event resolution.

$$\langle \cos(mk[\Psi_n - \Psi_{RP}]) \rangle = \frac{\sqrt{\pi}}{2} \chi \exp(-\chi^2/2) \left[I_{\frac{k-1}{2}} \left(\frac{\chi^2}{2} \right) + I_{\frac{k+1}{2}} \left(\frac{\chi^2}{2} \right) \right] \tag{5.36}$$

The full event resolution is shown in Figure 5.30. This event resolution will in turn be used in Section 5.7 to correct the flow Fourier coefficients (v_n) for the event plane dispersion.

5.7 Determination of flow Fourier harmonics v_n

The distribution of particles resulting from the geometry and collision fluctuations can be measured by analyzing the Fourier decomposition of the

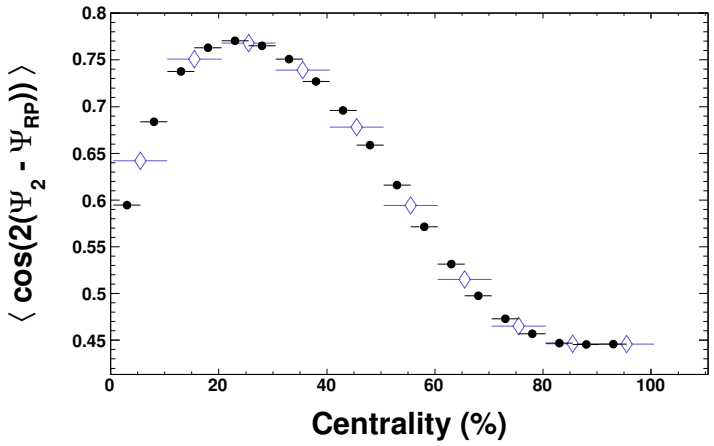

Figure 5.30: Full event Ψ_2 resolution for the Reaction Plane detector. The resolution is binned in 5% (black) and 10% (blue) centrality bins.

particle distribution:

$$\frac{d^2N}{d\phi dp_T} = \frac{N_0}{2\pi}\left\{1 + 2\sum_{n=1}^{\infty} v_n(p_T)\cos\left[n(\phi - \Psi_n)\right]\right\} \tag{5.37}$$

where v_n are the anisotropy coefficients, Ψ_n is the n-th order event plane, and ϕ is the azimuthal angle of the track. Once the event plane Ψ_n is measured one can measure the *uncorrected* anistropy coefficients, v_n^{raw}, by measuring the particle distribution relative to the event plane. Assuming that the event planes at all orders are *uncorrelated* for a given event ($\langle\Psi_n\Psi_m\rangle \sim 0$), a functional form is assumed (Equation 5.38) and fit to the data.

$$\frac{dN}{d(\phi - \Psi_n)} = N_0(1 + 2v_n^{raw}\cos(n[\phi - \Psi_n])) \qquad \text{if} \quad n \neq 2 \tag{5.38}$$

$$\frac{dN}{d(\phi - \Psi_2)} = N_0(1 + 2v_2^{raw}\cos(2[\phi - \Psi_2]) + 2v_4^{raw}\cos(4[\phi - \Psi_2])) \quad (5.39)$$

To measure the particle distribution relative to Ψ_2 and added fit parameter is added (v_4^{raw}) in order to better represent the data. This is needed since the elliptic flow geometry has a 4th order coefficient that is needed in order to correctly represent the elliptical shape of the overlap region in a heavy ion collision. Figure 5.31 to Figure 5.37 shows the raw $dN/d(\phi - \Psi_2)$ anisotropy distributions along with the fit to extract v_2^{raw}.

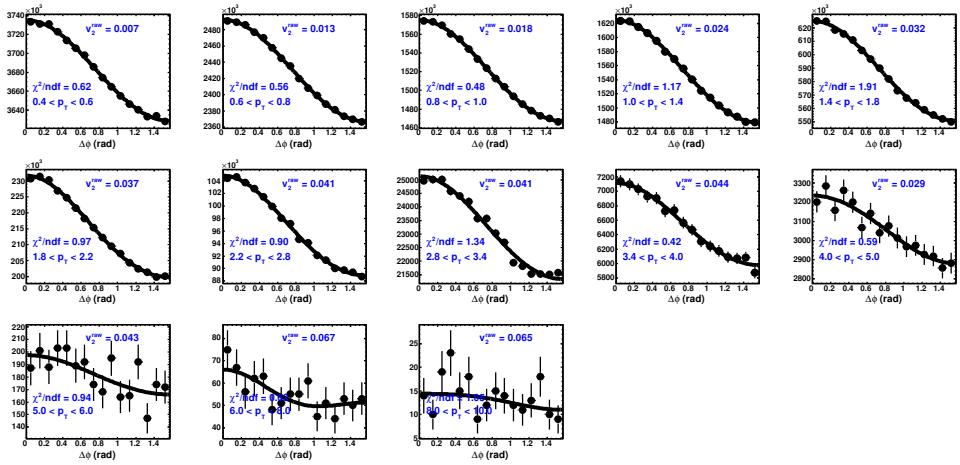

Figure 5.31: Track azimuthal distributions relative to event plane Ψ_2 for a given p_T bin and centrality 0%-10%. Equation 5.39 was fit to the data and v_2^{raw} coefficients extracted.

Since the measured v_n^{raw} coefficients are reduced due to the dispersion in the *measured* event plane, the coefficients need to be corrected:

$$v_n^{corr} = \frac{v_n^{raw}}{\text{Res}\{\Psi_n\}} = \frac{v_n^{raw}}{\langle\cos(n[\Psi_n - \Psi_{RP}])\rangle} \quad (5.40)$$

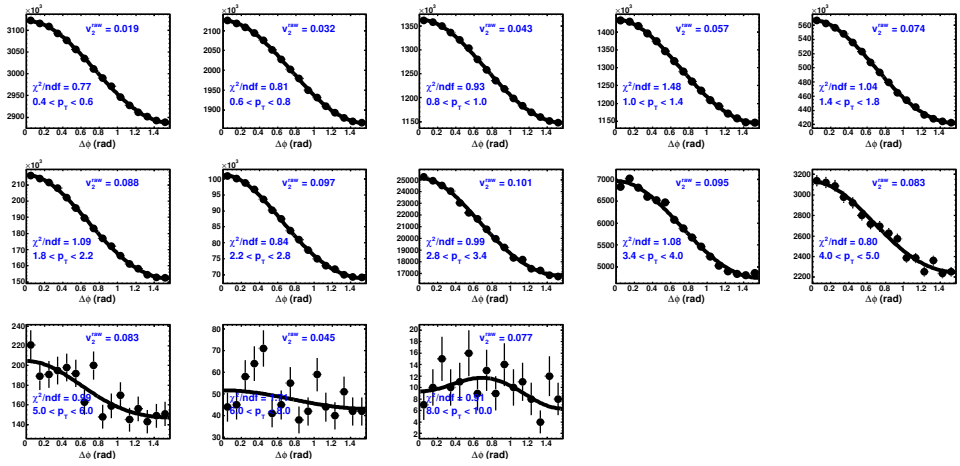

Figure 5.32: Track azimuthal distributions relative to event plane Ψ_2 for a given p_T bin and centrality 10%-20%. Equation 5.39 was fit to the data and v_2^{raw} coefficients extracted.

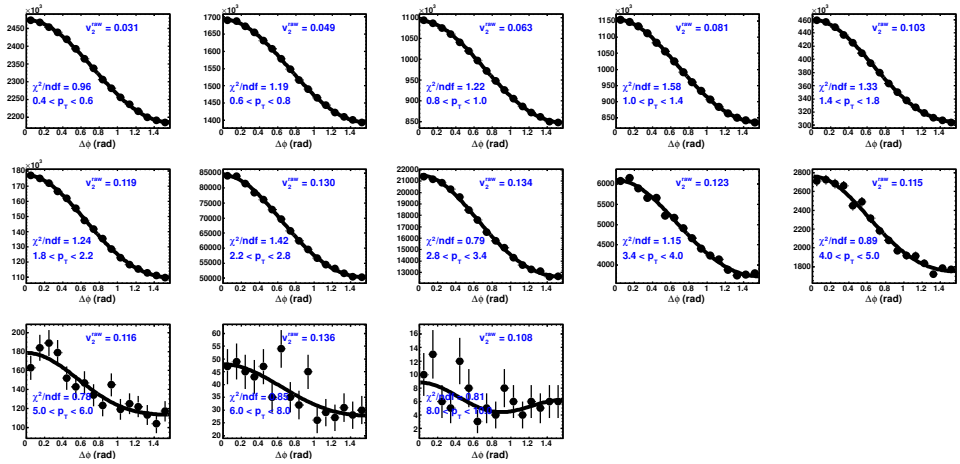

Figure 5.33: Track azimuthal distributions relative to event plane Ψ_2 for a given p_T bin and centrality 20%-30%. Equation 5.39 was fit to the data and v_2^{raw} coefficients extracted.

The resulting v_n coefficients are plotted in Figure 5.46.

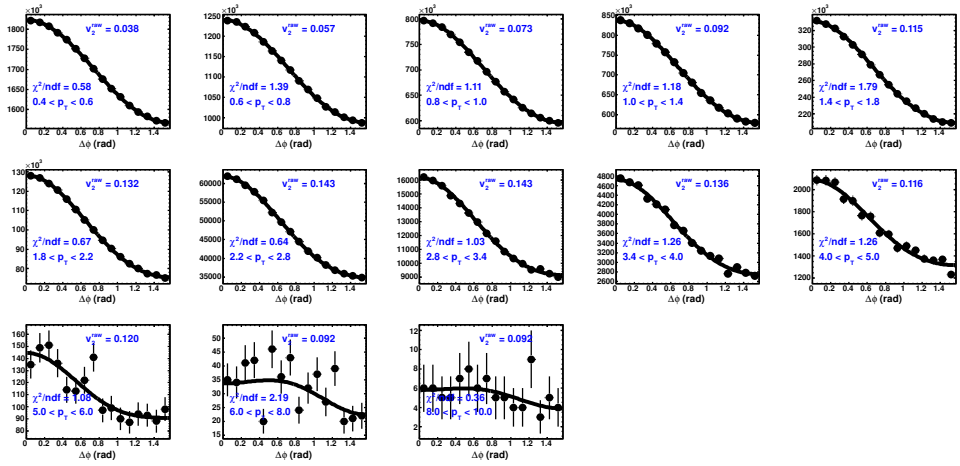

Figure 5.34: Track azimuthal distributions relative to event plane Ψ_2 for a given p_T bin and centrality 30%-40%. Equation 5.39 was fit to the data and v_2^{raw} coefficients extracted.

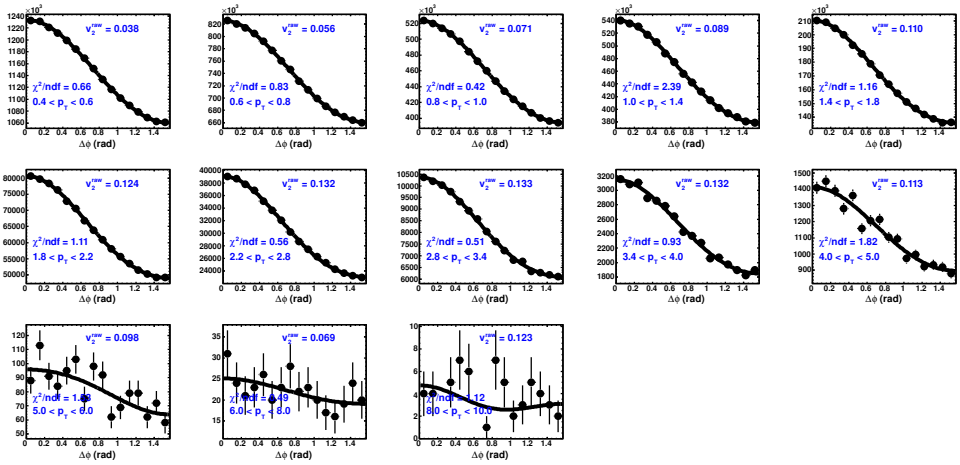

Figure 5.35: Track azimuthal distributions relative to event plane Ψ_2 for a given p_T bin and centrality 40%-50%. Equation 5.39 was fit to the data and v_2^{raw} coefficients extracted.

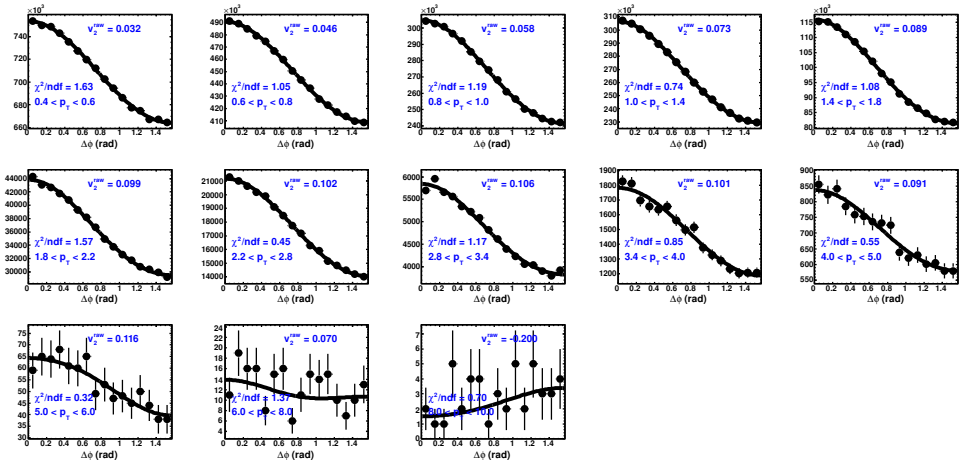

Figure 5.36: Track azimuthal distributions relative to event plane Ψ_2 for a given p_T bin and centrality 50%-60%. Equation 5.39 was fit to the data and v_2^{raw} coefficients extracted.

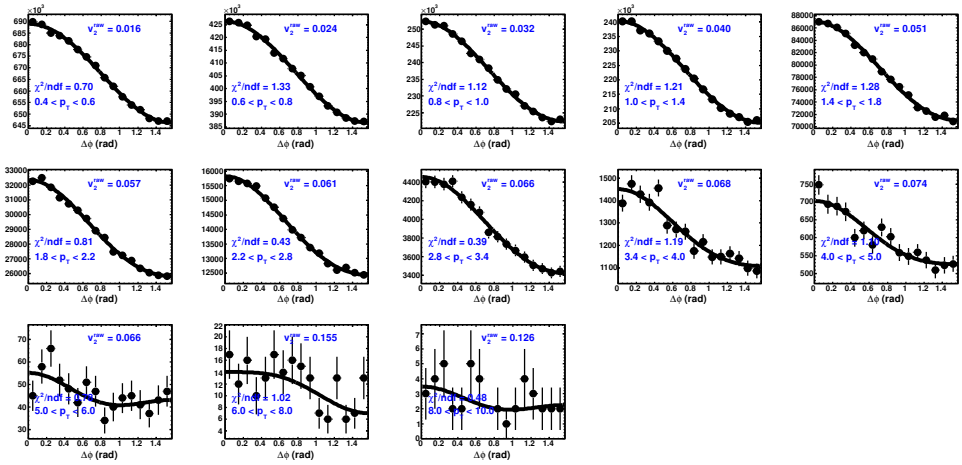

Figure 5.37: Track azimuthal distributions relative to event plane Ψ_2 for a given p_T bin and centrality 60%-92%. Equation 5.39 was fit to the data and v_2^{raw} coefficients extracted.

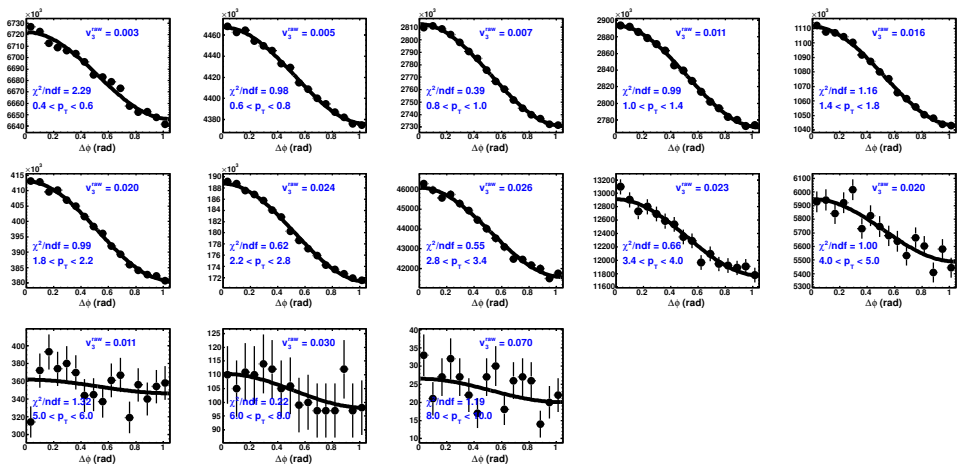

Figure 5.38: Track azimuthal distributions relative to event plane Ψ_3 for a given p_T bin and centrality 0%-20%. Equation 5.38 was fit to the data and v_3^{raw} coefficients extracted.

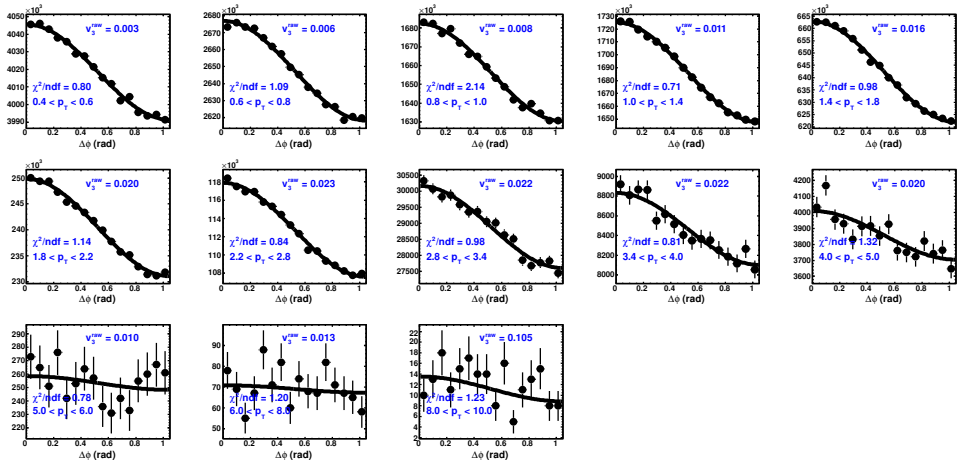

Figure 5.39: Track azimuthal distributions relative to event plane Ψ_3 for a given p_T bin and centrality 20%-40%. Equation 5.38 was fit to the data and v_3^{raw} coefficients extracted.

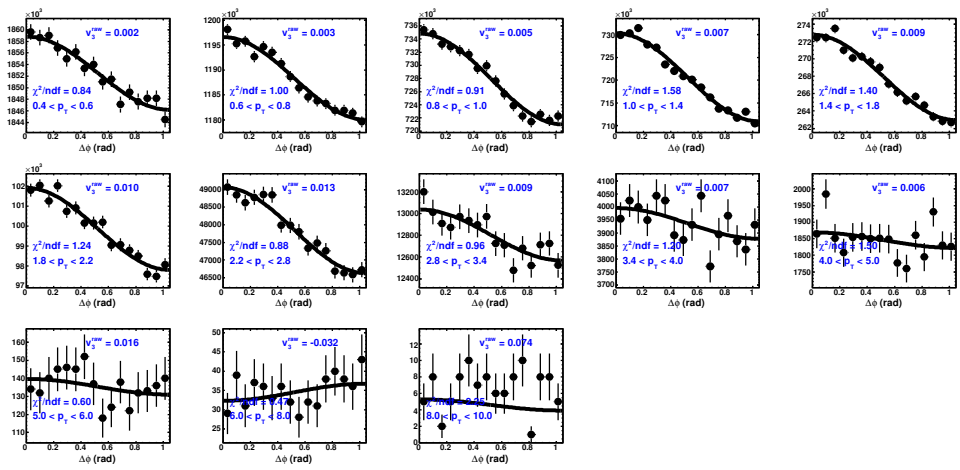

Figure 5.40: Track azimuthal distributions relative to event plane Ψ_3 for a given p_T bin and centrality 40%-60%. Equation 5.38 was fit to the data and v_3^{raw} coefficients extracted.

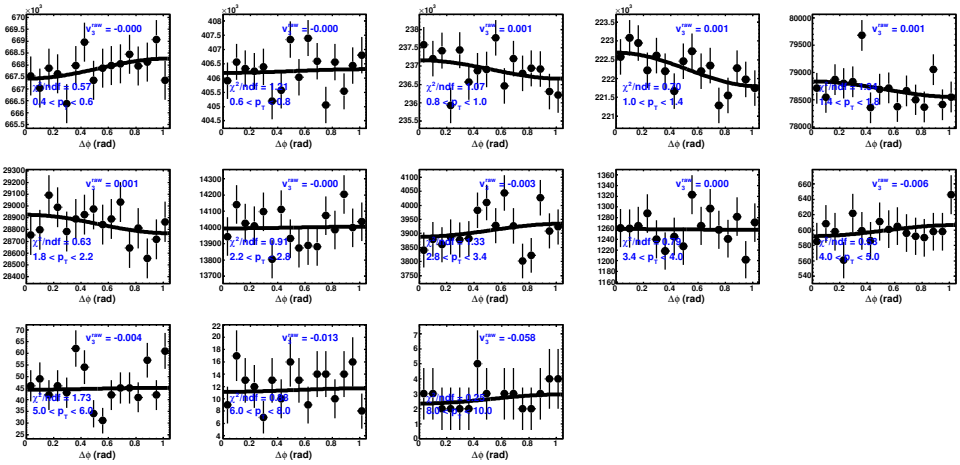

Figure 5.41: Track azimuthal distributions relative to event plane Ψ_3 for a given p_T bin and centrality 60%-92%. Equation 5.38 was fit to the data and v_3^{raw} coefficients extracted.

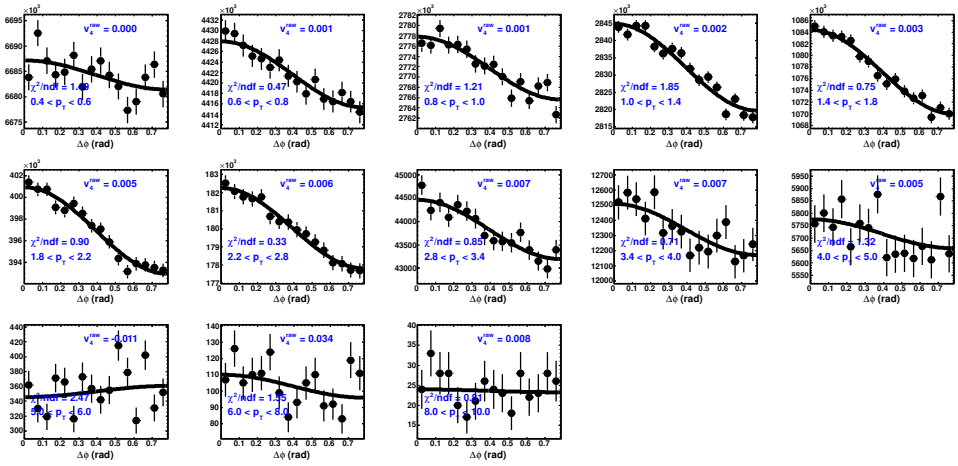

Figure 5.42: Track azimuthal distributions relative to event plane Ψ_4 for a given p_T bin and centrality 0%-20%. Equation 5.38 was fit to the data and v_4^{raw} coefficients extracted.

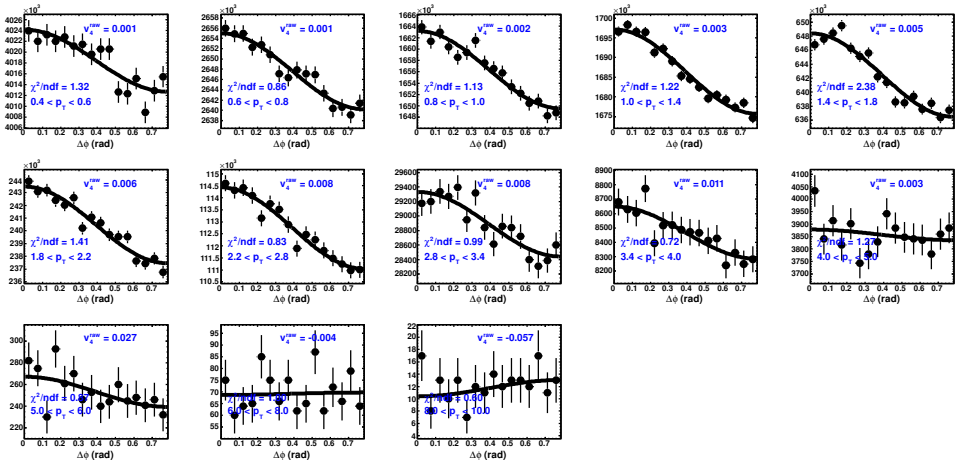

Figure 5.43: Track azimuthal distributions relative to event plane Ψ_4 for a given p_T bin and centrality 20%-40%. Equation 5.38 was fit to the data and v_4^{raw} coefficients extracted.

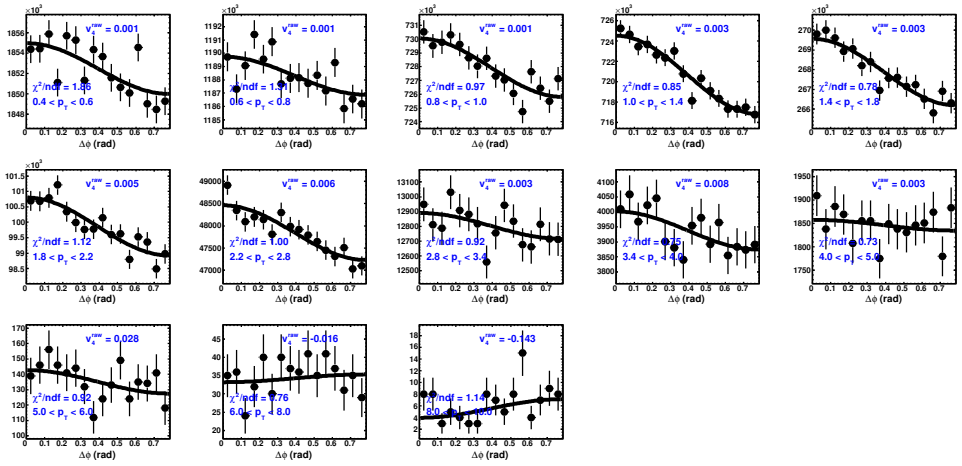

Figure 5.44: Track azimuthal distributions relative to event plane Ψ_4 for a given p_T bin and centrality 40%-60%. Equation 5.38 was fit to the data and v_4^{raw} coefficients extracted.

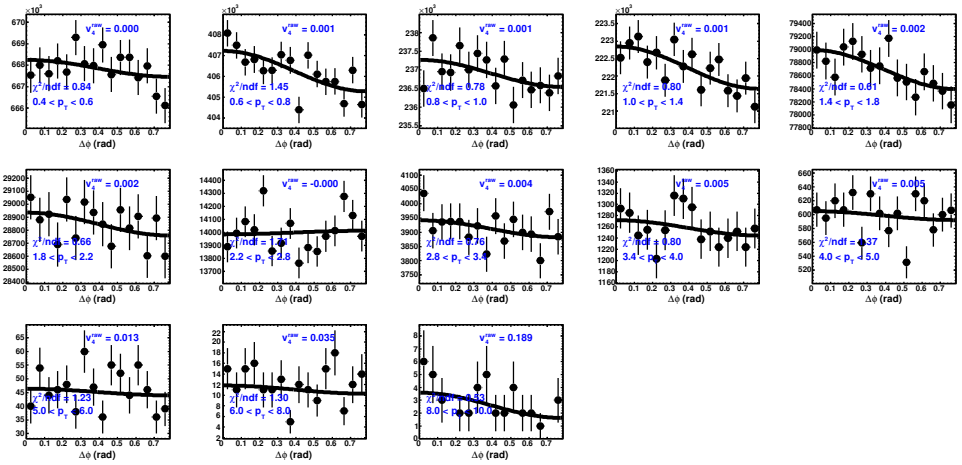

Figure 5.45: Track azimuthal distributions relative to event plane Ψ_4 for a given p_T bin and centrality 60%-92%. Equation 5.38 was fit to the data and v_4^{raw} coefficients extracted.

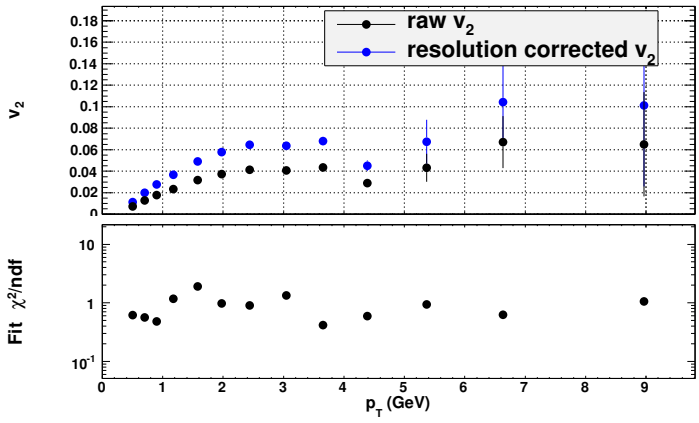

Figure 5.46: In the upper plot the anisotropy coefficients v_2 vs p_T for centrality 0%-10%. Shown in the lower plot is the goodness of fit (χ^2/ndf) for each p_T bin.

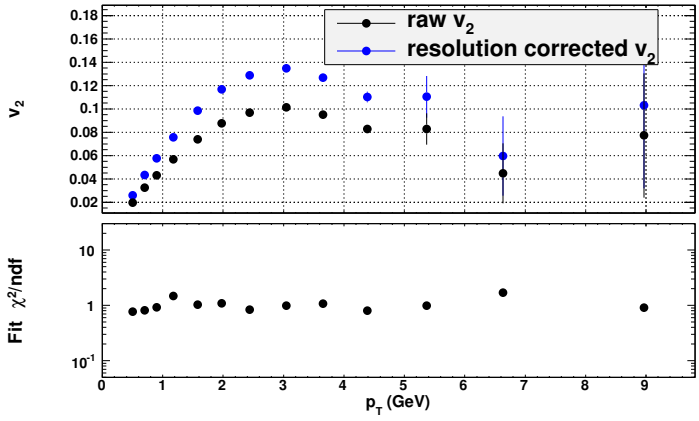

Figure 5.47: In the upper plot the anisotropy coefficients v_2 vs p_T for centrality 10%-20%. Shown in the lower plot is the goodness of fit (χ^2/ndf) for each p_T bin.

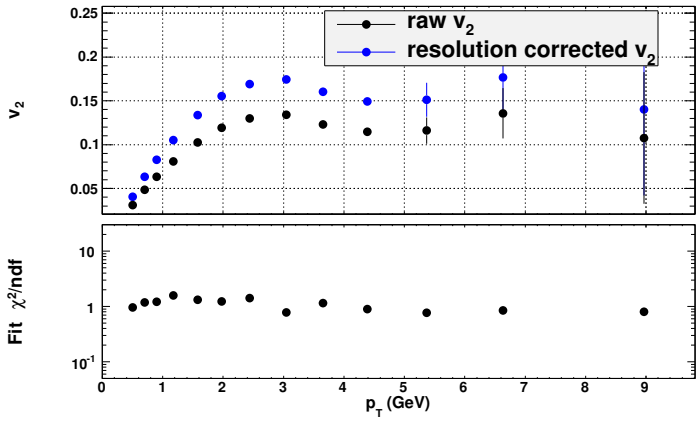

Figure 5.48: In the upper plot the anisotropy coefficients v_2 vs p_T for centrality 20%-30%. Shown in the lower plot is the goodness of fit (χ^2/ndf) for each p_T bin.

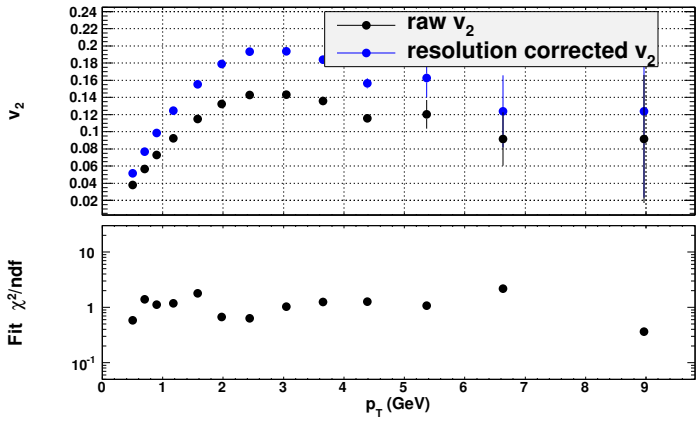

Figure 5.49: In the upper plot the anisotropy coefficients v_2 vs p_T for centrality 30%-40%. Shown in the lower plot is the goodness of fit (χ^2/ndf) for each p_T bin.

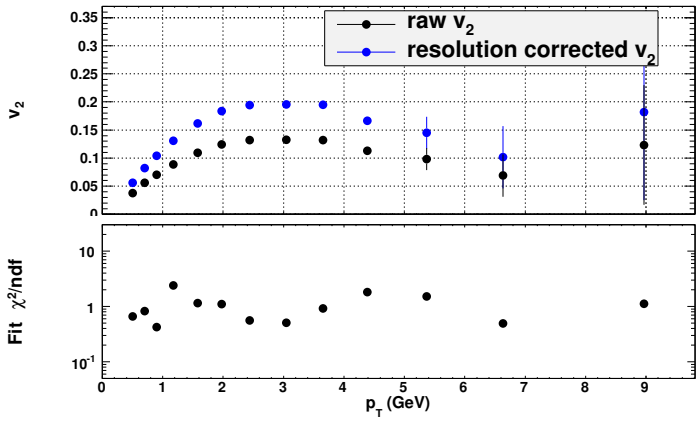

Figure 5.50: In the upper plot the anisotropy coefficients v_2 vs p_T for centrality 40%-50%. Shown in the lower plot is the goodness of fit (χ^2/ndf) for each p_T bin.

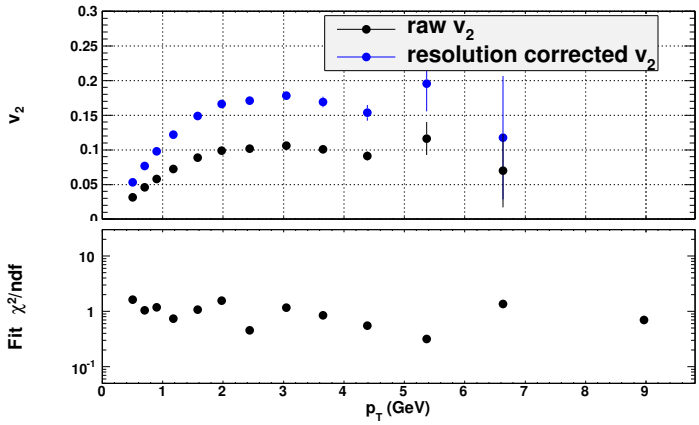

Figure 5.51: In the upper plot the anisotropy coefficients v_2 vs p_T for centrality 50%-60%. Shown in the lower plot is the goodness of fit (χ^2/ndf) for each p_T bin.

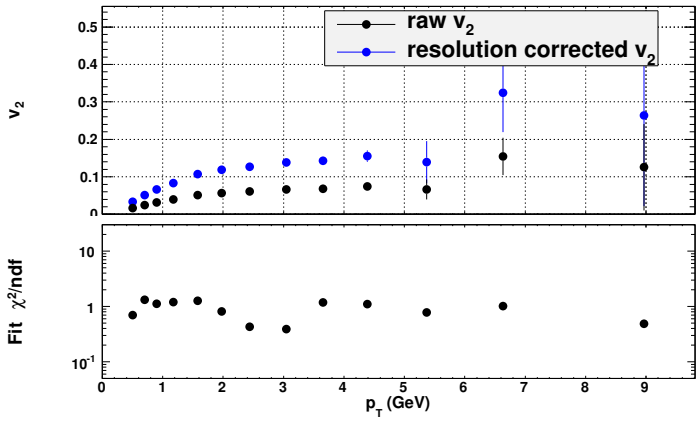

Figure 5.52: In the upper plot the anisotropy coefficients v_2 vs p_T for centrality 60%-92%. Shown in the lower plot is the goodness of fit (χ^2/ndf) for each p_T bin.

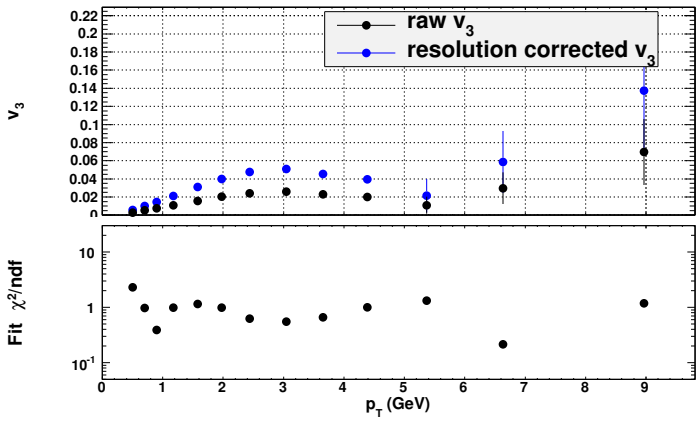

Figure 5.53: In the upper plot the anisotropy coefficients v_3 vs p_T for centrality 0%-20%. Shown in the lower plot is the goodness of fit (χ^2/ndf) for each p_T bin.

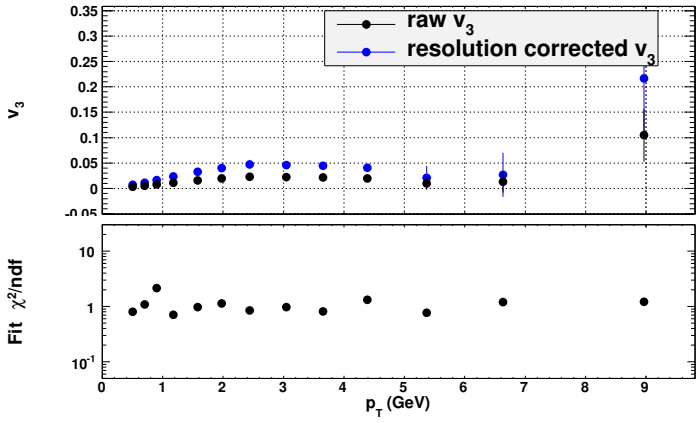

Figure 5.54: In the upper plot the anisotropy coefficients v_3 vs p_T for centrality 20%-40%. Shown in the lower plot is the goodness of fit (χ^2/ndf) for each p_T bin.

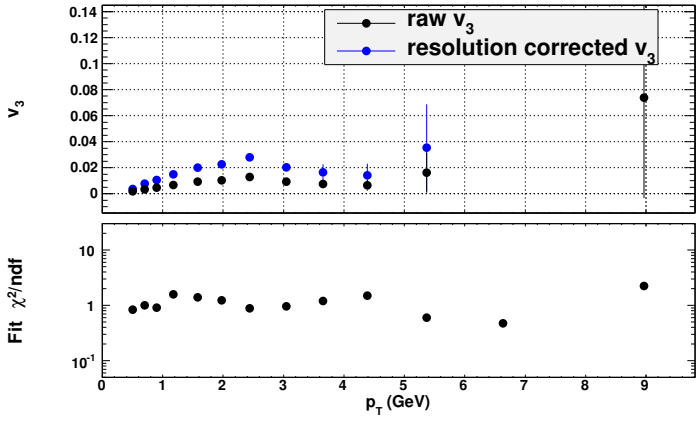

Figure 5.55: In the upper plot the anisotropy coefficients v_3 vs p_T for centrality 40%-60%. Shown in the lower plot is the goodness of fit (χ^2/ndf) for each p_T bin.

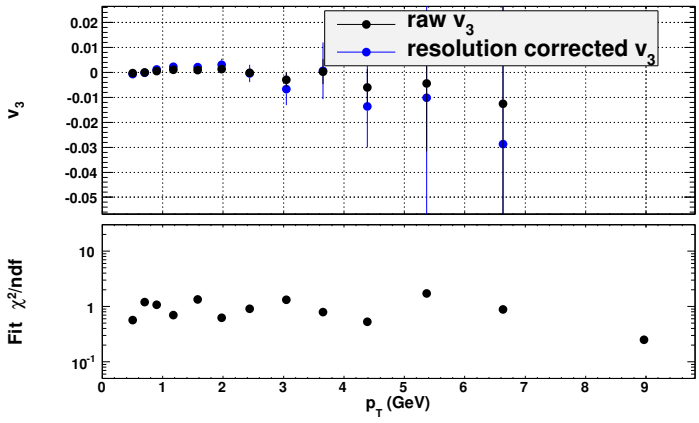

Figure 5.56: In the upper plot the anisotropy coefficients v_3 vs p_T for centrality 60%-92%. Shown in the lower plot is the goodness of fit (χ^2/ndf) for each p_T bin.

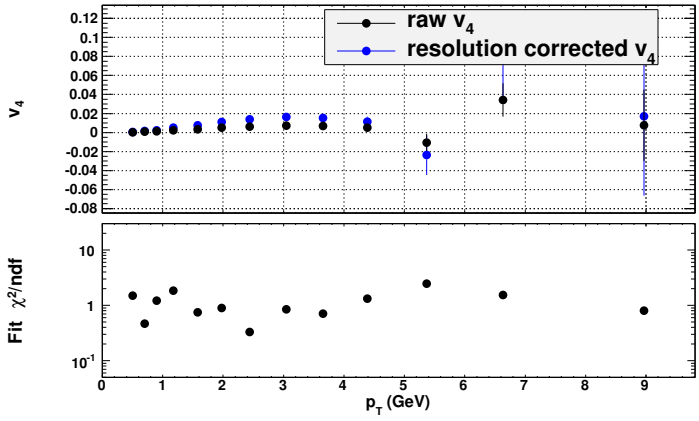

Figure 5.57: In the upper plot the anisotropy coefficients v_4 vs p_T for centrality 0%-20%. Shown in the lower plot is the goodness of fit (χ^2/ndf) for each p_T bin.

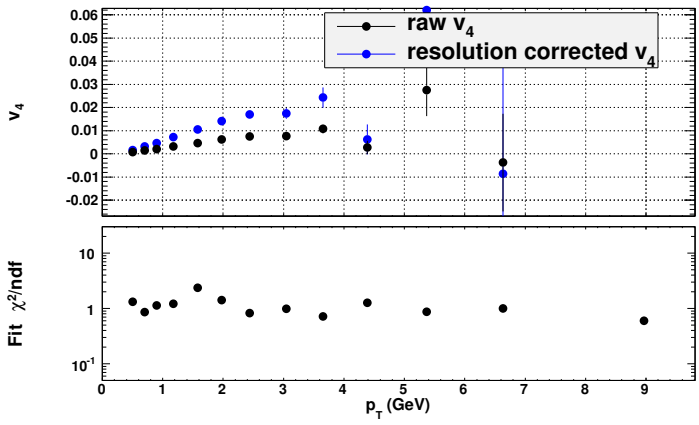

Figure 5.58: In the upper plot the anisotropy coefficients v_4 vs p_T for centrality 20%-40%. Shown in the lower plot is the goodness of fit (χ^2/ndf) for each p_T bin.

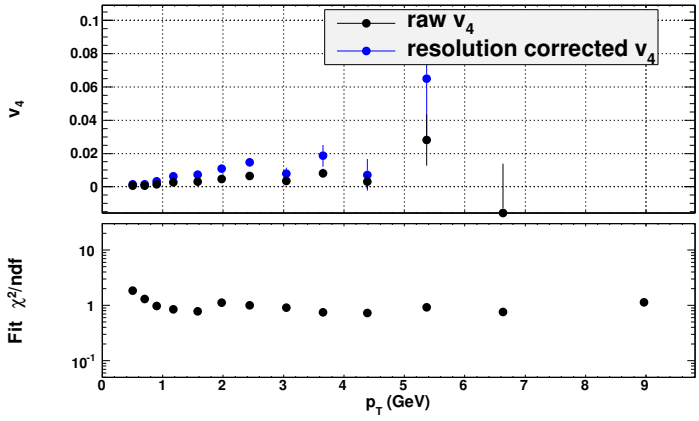

Figure 5.59: In the upper plot the anisotropy coefficients v_4 vs p_T for centrality 40%-60%. Shown in the lower plot is the goodness of fit (χ^2/ndf) for each p_T bin.

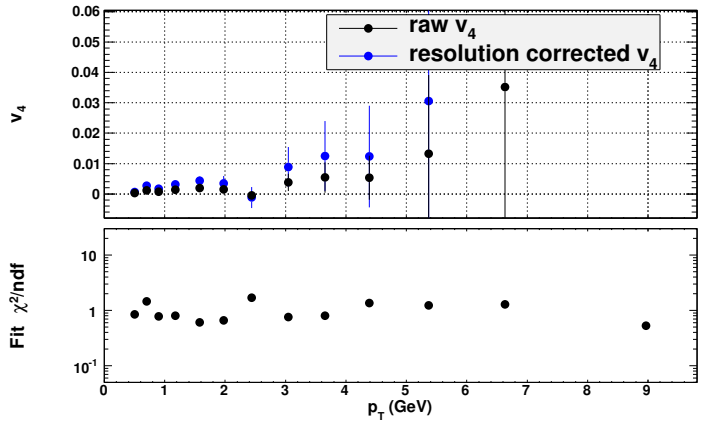

Figure 5.60: In the upper plot the anisotropy coefficients v_4 vs p_T for centrality 60%-92%. Shown in the lower plot is the goodness of fit (χ^2/ndf) for each p_T bin.

5.7.1 v_n in the presence of high-p_T particles

It has been questioned whether the measurement of anisotropy coefficients, v_n, from minimum bias events is appropriate for the subtraction of the *soft* background from two-particle correlations in order to extract jets (see Section 5.8). In particular the assumption that the v_2 coefficients, from the *trigger* and *associated* hadrons, are uncorrelated should be tested.

$$\langle v_2^t v_2^a \rangle \sim \langle v_2^t \rangle \langle v_2^a \rangle \tag{5.41}$$

To this end a study was performed using the 2004 Au+Au at $\sqrt{s_{NN}} = 200$ GeV data, where the hadron anisotropy coefficient v_2 was measured in the presence of high-p_T π^0 and then compared to those extracted from minimum bias data set [76].

The measurements were carried out in similar fashion as with minimum bias data except for a correction that needed to be made due to the distortion of the Ψ_2 event plane distribution. Although the Ψ_2 event plane in the 2004 Au+Au data was measured by the BBC's and subsequently flattened for minimum bias data, the distortion observed is attributed to the presence of a π^0 in the central arms which biases this subset of Ψ_2 event planes to be in the direction of the π^0 (see Figure 5.61). The following function was fit to the distribution to determine the magnitude of the correction needed for v_2, where α and B are parameters extracted from the fitting procedure.

$$g(\Psi_2) = \alpha(1 + B\cos(2\Psi_2)) \tag{5.42}$$

Since the selection of a high-p_T π^0 biases the event plane to be in the direction of the central arms, the measured distribution of hadrons with respect to the event plane result in an enhanced anisotropy coefficient. Therefore the correction made was to weigh each event such as to produce a flat Ψ_2

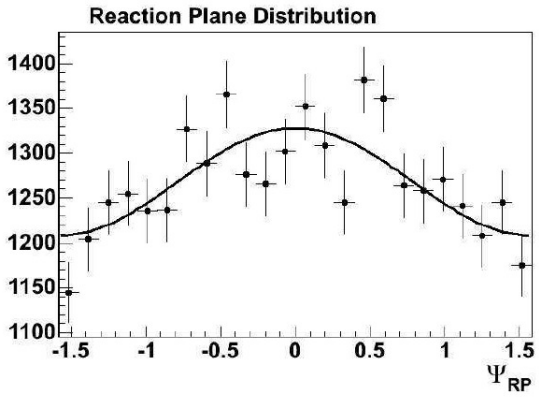

Figure 5.61: Example of the Ψ_2 event plane distribution as measured by the BBC's in the presence of a high-p_T π^0 ($5.0 < p_T < 10$ GeV) in 0-10% Au+Au collisions. An empirical function was fit to the distribution.

distribution and reduce the bias to the hadron $dN/d(\phi - \Psi_2)$ distribution. Figure 5.62 shows the comparison of the minimum bias and *triggered events*. Aside from most central collisions (0-10%), where no strong definitive statement can be made, there were no significant modifications observed to the hadron v_2 anisotropy coefficients. Therefore, for the background subtraction the hadron v_2 coefficients measured in the previous section will be used.

5.8 Jet extraction from two-particle correlations: The two source model

Once the Fourier flow coefficients, v_n, have been determined, the jet contribution to the two-particle correlation can be extracted using a model dependent approach. This approach, *the two-source model*, assumes that the contribu-

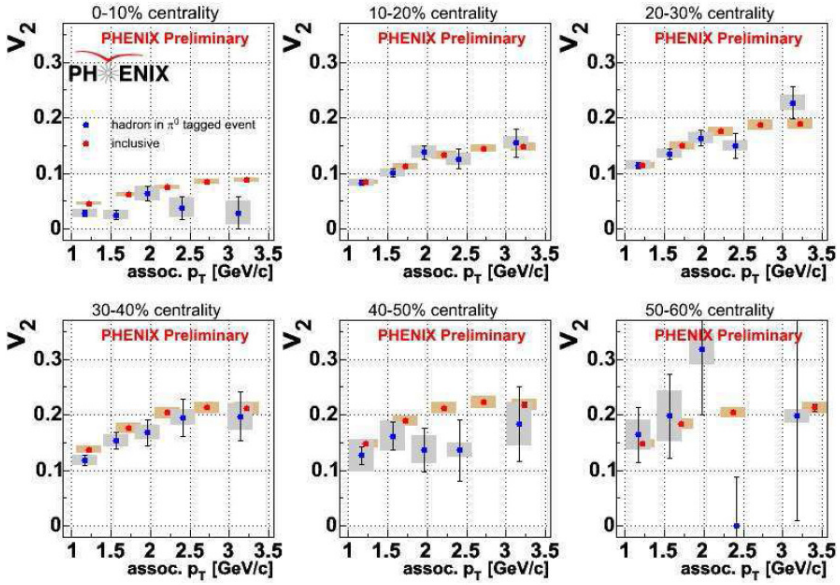

Figure 5.62: Comparison of hadron v_2 in minimum bias events (blue) to events in the presence of a high-p_T π^0 (red).

tions to two-particle correlations can be segregated into two sources:

$$\frac{1}{N^a}\frac{d\mathbb{N}^{ab}}{d\Delta\phi_{ab}} = J(\Delta\phi_{ab}) + B(\Delta\phi_{ab}) \tag{5.43}$$

The jet-induced contribution, $J(\Delta\phi_{ab})$ is due to hadron pairs originating from jets.

$$J(\Delta\phi_{ab}) \propto \frac{dN^{\text{jet}-\text{jet}}}{d\Delta\phi_{ab}} \tag{5.44}$$

Since the hadrons, at any given p_T, can come from the bulk flow, the correlations produced from these *soft* particles must be taken into account. The correlated background, $B(\Delta\phi_{ab})$ will come from a distribution where one, or

both, hadrons come from the soft background.

$$B(\Delta\phi_{ab}) \propto \left(\frac{dN^{\text{jet}-\text{soft}}}{d\Delta\phi_{ab}} + \frac{dN^{\text{soft}-\text{soft}}}{d\Delta\phi_{ab}} \right) \tag{5.45}$$

The "jet-soft" contribution cannot be accounted for properly due to the lack of hadron v_n coming from jets at all p_T. It was shown in Section 5.7.1 that for low-p_T hadrons, there was no significant difference in v_2 in events with high-p_T π^0's. Although there are measurements that have measured significant jet v_2 at the LHC [77], for RHIC it will be assumed to be insignificant keeping in mind that future measurements might reveal otherwise.

$$\left(\frac{dN^{\text{jet}-\text{soft}}}{d\Delta\phi_{ab}} + \frac{dN^{\text{soft}-\text{soft}}}{d\Delta\phi_{ab}} \right) \sim \frac{dN^{\text{soft}-\text{soft}}}{d\Delta\phi_{ab}} \tag{5.46}$$

The "soft-soft" contribution to the background can be estimated from the flow, v_n, coefficients and therefore the single particle distributions relative to the event plane Ψ_n.

$$\frac{dN}{d\phi} = \frac{N}{2\pi} \left\{ 1 + 2 \sum_{n=1}^{\infty} v_n(p_T) \cos[n(\phi - \Psi_n)] \right\} \tag{5.47}$$

Depending on how many particles, N, are used in the correlation, a convolution can be made with N corresponding distributions to obtain the "soft-soft" contribution at all orders.

$$\begin{aligned} \frac{dN^{\text{soft}-\text{soft}}}{d\Delta\phi_{ab} d\Delta\phi_{ac} ... d\Delta\phi_{aN}} \quad \propto \quad & \int d\phi_a d\phi_b d\phi_c ... d\phi_N \frac{dN}{d\phi_a} \frac{dN}{d\phi_b} \frac{dN}{d\phi_c} ... \frac{dN}{d\phi_N} \times \\ & \delta(\phi_a - \phi_b - \Delta\phi_{ab}) \delta(\phi_a - \phi_c - \Delta\phi_{ac}) .... \delta(\phi_a - \phi_N - \Delta\phi_{aN}) \end{aligned} \tag{5.48}$$

Appendix B has the procedure for determining these contributions. The "soft-soft" contribution to two particle correlations is given by:

$$\frac{dN^{\text{soft}-\text{soft}}}{d\Delta\phi_{ab}} \propto \left(1 + 2\sum_{n=1}^{\infty} v_n^a(p_T) v_n^b(p_T) \cos[n(\phi - \Psi_n)]\right) \tag{5.49}$$

In particular, for this analysis, only the $n = 2, 3, 4$ contributions are used to estimated the background. For three-particle correlations (i.e. 2+1 correlations) the "soft-soft" component calculated is a bit more involved and is represented using only v_2, v_3, v_4 coefficients:

$$\begin{aligned}
\frac{d^2N^{\text{soft}-\text{soft}}}{d\Delta\phi_{ab}d\Delta\phi_{ac}} \propto\ & \big(1 + 2v_2^a v_2^b \cos(2\Delta\phi_{ab}) + 2v_2^a v_2^c \cos(2\Delta\phi_{ac})\text{sinc}(\delta) + \\
& 2v_2^b v_2^c \cos(2[\Delta\phi_{ac} - \Delta\phi_{ab}])\text{sinc}(\delta) + 2v_3^a v_3^b \cos(3\Delta\phi_{ab}) + \\
& 2v_3^a v_3^c \cos(3\Delta\phi_{ac})\text{sinc}\left(\frac{3\delta}{2}\right) + 2v_3^b v_3^c \cos(3[\Delta\phi_{ac} - \Delta\phi_{ab}])\text{sinc}\left(\frac{3\delta}{2}\right) + \\
& 2v_4^a v_4^b \cos(4\Delta\phi_{ab}) + 2v_4^a v_4^c \cos(4\Delta\phi_{ac})\text{sinc}(2\delta) + \\
& 2v_4^b v_4^c \cos(4[\Delta\phi_{ac} - \Delta\phi_{ab}])\text{sinc}(2\delta) + \\
& 2v_2^a v_2^b v_4^c \cos(2\Delta\phi_{ab} - 4\Delta\phi_{ac})\text{sinc}(2\delta) + \\
& 2v_2^a v_4^b v_2^c \cos(4\Delta\phi_{ab} - 2\Delta\phi_{ac})\text{sinc}(\delta) + \\
& 2v_4^a v_2^b v_2^c \cos(2\Delta\phi_{ab} - 2\Delta\phi_{ac})\text{sinc}(\delta)
\end{aligned} \tag{5.50}$$

where δ is the $\Delta\phi_{ac}$ bin size discussed for Equation 5.23.

Now that the functional shapes of the background have been estimated, the only component left to determine is the scale of the background level. There are a couple of methods employed at PHENIX to determine the background level: ZYAM and ABS method. For this analysis, the ZYAM method was used and will be now discussed.

5.8.1 Background subtraction via ZYAM

The Zero Yield At Minimum (ZYAM) method is a subraction scheme where the jet-induced correlation is assumed to have zero yield at its minimum point [78]. Using Equation 5.49 the heavy ion background to two-particle correlations is assumed to be of the form,

$$B(\Delta\phi_{ab}) = \xi\left(1 + 2\sum_{n=1}^{\infty} v_n^a(p_T)v_n^b(p_T)\cos[n(\phi - \Psi_n)]\right) \quad (5.51)$$

where ξ will be a parameter determined by the ZYAM procedure. The same can be done for 2+1 correlations using Equation 5.50. For a p+p collision system, the background is assumed to be constant ($B(\Delta\phi_{ta}) = \xi$).

To estimate the background contribution in the ZYAM procedure, the ξ parameters is iteratively adjusted until $B(\Delta\phi_{ta})$ "just touches" the correlation.

$$\frac{1}{N^a}\frac{d\mathbb{N}^{ab}}{d\Delta\phi_{ab}} \geq B(\Delta\phi_{ab}) \qquad \text{for all } \Delta\phi_{ab} \quad (5.52)$$

Preliminary attempts to accomplish this technique using the data points resulted in large uncertainties in ξ due to the large statistical fluctuations that can occur in the data point belonging to a region of low acceptance ($\Delta\phi_{ab} \sim \pi/2$). This led to a preferred method of fitting an empirical function, $f(\Delta\phi_{ab})$ given by,

$$f(\Delta\phi_{ab}) = k_0 + \frac{A_1}{\sqrt{2\pi}s_1}\exp\left(\frac{-\Delta\phi_{ab}^2}{2s_1^2}\right) + \frac{A_2}{\sqrt{2\pi}s_2}\left\{\exp\left(\frac{-(\Delta\phi_{ab} - \pi)^2}{2s_2^2}\right) + \exp\left(\frac{-(\Delta\phi_{ab} + \pi)^2}{2s_2^2}\right)\right\} \quad (5.53)$$

that well represents the data and allowing the background, $B(\Delta\phi_{ab})$ or $B(\Delta\phi_{ab}, \Delta\phi_{ac})$, to approach $f(\Delta\phi_{ab})$ which results in a reduction of fluc-

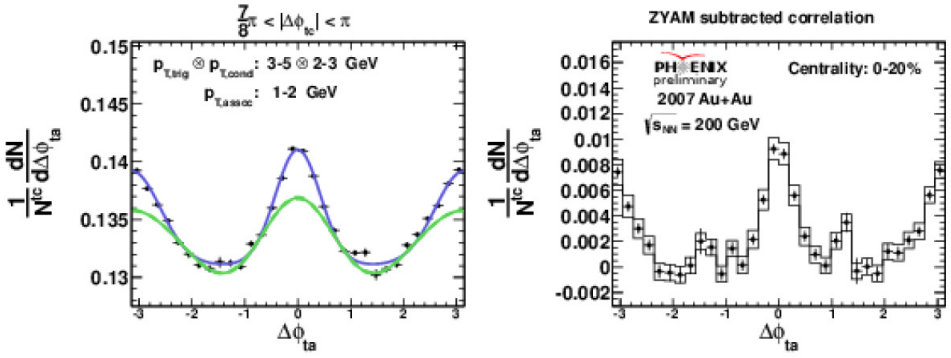

Figure 5.63: Example of ZYAM procedure for a 2+1 correlation in 2007 Au+Au. The left plot demonstrates background, $B(\Delta\phi_{ab})$ (green line), along with the emperical fit, $f(\Delta\phi_{ta})$ (blue line), to the data. Right plot is the result of the subtraction scheme.

tuations around low acceptance regions. Figure 5.63 illustrates the ZYAM procedure along with the subtraction of $B(\Delta\phi_{ab})$ in 2+1 correlations. The resultant correlation is the estimate of the jet-induced contribution $J(\Delta\phi_{ab})$. From $J(\Delta\phi_{ab})$, statements regarding jet modification in heavy ion collisions can start to be made.

5.8.2 Absolute efficiency corrections to $J(\Delta\phi_{ta})$

The *absolute* efficiency correction for this analysis were extracted from previous simulated efficiency measurements for both the 2006 p+p and 2007 Au+Au dataset [79]. The general idea behind generating the absolute efficiencies are the following:

1) Using an event-generator to create a distribution of particles representative of the distribution one wishes to analyze.

2) Use the distribution of particles generated as input to the PHENIX Integrated Simulation Application (PISA) to generate simulated detector

hit output for each particle. The PISA software contains a GEANT3 description of the materials and detector subsystems used in PHENIX.

3) Embed simulated detector hit output into real event data and execute the PHENIX reconstruction software.

4) Compare reconstructed output to embedded output to determine efficiency.

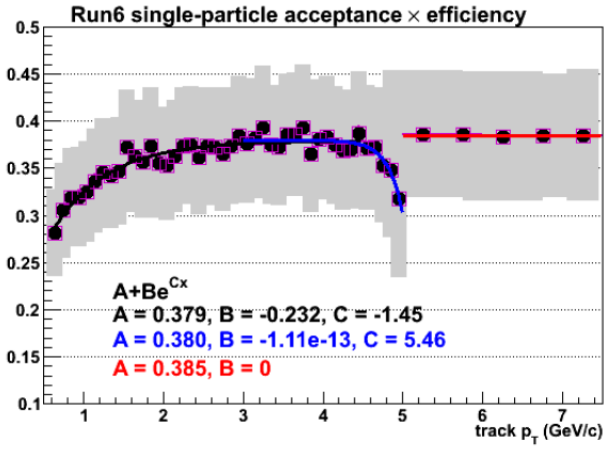

Figure 5.64: 2006 p+p (a.k.a. Run 6) acceptance × efficiency. The grey systematic error band represents the total statistical and systematic uncertainty, which is uniformly 16-17% of the efficiency values over the p_T range shown [79].

Figure 5.64 and Figure 5.65 show the efficiency of successfully reconstructing simulated hadrons in p+p and Au+Au events, respectively.

Important to all of this is the selection of *single particle* cuts assumed in the simulation. Table 5.6 shows the differences between this analysis and Reference [79] which only differ in the PC3 matching cut implemented. To determine and correct for any differences that might occur from differences

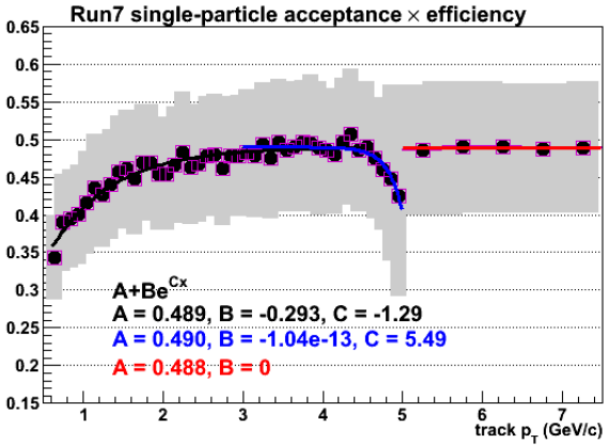

Figure 5.65: 2007 Au+Au (a.k.a. Run 7) acceptance × efficiency. The grey systematic error band represents the total statistical and systematic uncertainty, which is uniformly 16-17% of the efficiency values over the p_T range shown [79].

Table 5.6: Comparison of single-particle pass criterion for this analysis and Reference [79]

Analysis	`quality`	RICH n0	PC3 matching
Reference [79]	31 or 63	n0 < 0	$\sigma_{\mathrm{PC3}} < 2.0$
This analysis	31 or 63	n0 < 0	$\sigma_{\mathrm{PC3}} < 2.5$

in single particle cuts we use the following relation which must hold true:

$$\frac{dN^{\mathrm{true}}}{dp_T} = \frac{1}{\varepsilon^{\mathrm{A}}(p_T)}\frac{dN^{\mathrm{A}}}{dp_T} = \frac{1}{\varepsilon^{\mathrm{B}}(p_T)}\frac{dN^{\mathrm{B}}}{dp_T} \tag{5.54}$$

The labels A and B correspond to the different cuts applied in both analysis. Further more if we define the ratio of the distribution A to B,

$$R^{\mathrm{AB}} = \frac{dN^{\mathrm{A}}/dp_T}{dN^{\mathrm{B}}/dp_T} \tag{5.55}$$

then the efficiency for this analysis can be determined through:

$$\varepsilon^{\mathrm{A}}(p_T) = R^{\mathrm{AB}}\varepsilon^{\mathrm{B}}(p_T) \tag{5.56}$$

The $\varepsilon^{\mathrm{B}}(p_T)$ efficiencies can be determined from Figure 5.64 and 5.65 while the ratio R^{AB} was determined by measuring the ratio of the distributions (Figure 5.66 and 5.67). The measured efficiency for this analysis was

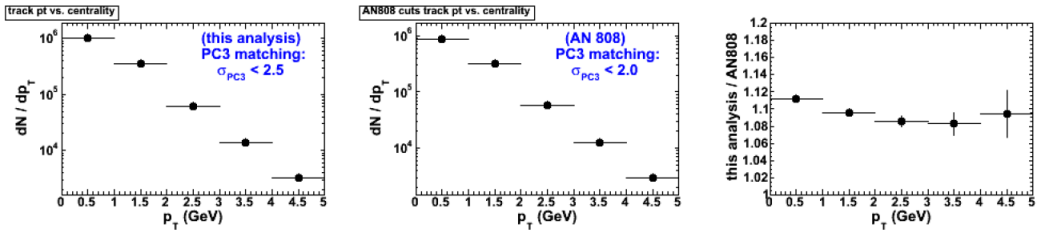

Figure 5.66: Transverse momentum distribution of hadrons in 2006 p+p data using single particle cuts in this analysis (left) Reference [79] (center) and the resulting ratio R^{AB} (right).

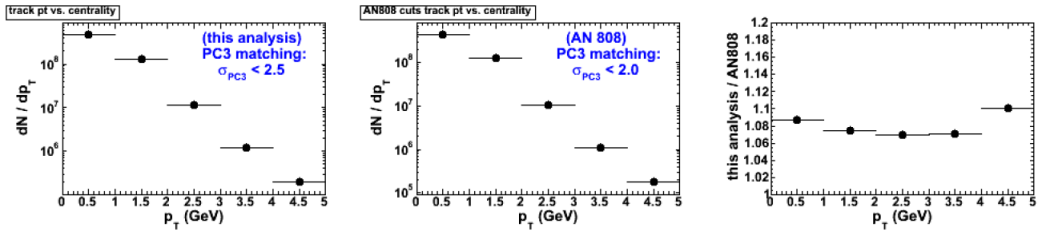

Figure 5.67: Transverse momentum distribution of hadrons in 2007 Au+Au data using single particle cuts in this analysis (left) Reference [79] (center) and the resulting ratio R^{AB} (right).

applied to the associated track in both two-particle and 2+1 correlations:

$$\frac{1}{N^a}\frac{d\mathbb{N}^a}{d\Delta\phi_{ab}} = \frac{1}{\varepsilon(p_T^b)N^a}\frac{dN^a}{d\Delta\phi_{ab}} \tag{5.57}$$

5.8.3 Systematic errors for $J(\Delta\phi_{ta})$

The systematic errors to the $J(\Delta\phi_{ta})$ distributions were determined from the following sources:

1) ZYAM fit and flow subtraction which is determined for each bin in every $J(\Delta\phi_{ta})$ distribution.

2) Single particle efficiency correction.

3) Track multiplicity time dependence.

Systematic error determination from ZYAM

To determine the uncertainty in the ZYAM procedure, the first step is to determine the uncertainty in the fitting procedure. Recall that the emperical fit to the the raw correlation is given by,

$$\begin{aligned} f(\Delta\phi) &= k_0 + \frac{A_1}{\sqrt{2\pi}s_1}\exp\left(\frac{-\Delta\phi^2}{2s_1^2}\right) + \\ &\quad \frac{A_2}{\sqrt{2\pi}s_2}\left\{\exp\left(\frac{-(\Delta\phi-\pi)^2}{2s_2^2}\right) + \exp\left(\frac{-(\Delta\phi+\pi)^2}{2s_2^2}\right)\right\} \end{aligned} \quad (5.58)$$

where A_i are the integral normalization, s_i are the Gaussian widths of the distribution, and k_0 is a relative constant . From the fitting procedure[1] one can access the uncertainties in the floating parameters used to the data. The uncertainty in $f(\Delta\phi)$ is then determined from propagation of errors:

$$\sigma_f^2 = \left(\frac{\partial f}{\partial y_i}\right)^2 \sigma_{y_i}^2 \qquad \text{where} \qquad y_i \in \{k_0, A_1, A_2, s_2, s_2\} \quad (5.59)$$

[1]The fitting is done via `TMinuit` minmization packages available through the CERN ROOT software.

An upper and lower uncertainty of the fitting function, $f(\Delta\phi)$, can be constructed from this uncertainty:

$$f^{\pm}(\Delta\phi) = f(\Delta\phi) + \sigma_f \tag{5.60}$$

Since the ZYAM procedure uses the background function, $B(\Delta\phi)$, to iteratively approach the fitted function, $f(\Delta\phi)$, to find the zero yield at minimum, it is important to determine the uncertainties in the shape in $B(\Delta\phi)$. The shape of $B(\Delta\phi)$ for Au+Au is determined from the v_n coefficient values used. If the lower and upper uncertainty in v_n is defined by,

$$v_n^{\pm} = v_n \pm \sigma_v \tag{5.61}$$

then the lower and upper uncertainty in $B(\Delta\phi)$, which will be denoted by $B^{\pm}(\Delta\phi)$, can be determined by including $v_n^{\pm}$ into Equation 5.49 and 5.50. Therefore the maximum uncertainty in $J(\Delta\phi)$ is given by,

$$J^{\pm}(\Delta\phi) = f^{\pm}(\Delta\phi) - B^{\mp}(\Delta\phi) \tag{5.62}$$

The relative systematic error is given by,

$$\frac{\sigma^{\text{sys}}_{\text{ZYAM}}}{J(\Delta\phi)} = \frac{J^{\pm}(\Delta\phi) - J(\Delta\phi)}{J(\Delta\phi)} \tag{5.63}$$

Systematic error from single particle efficiency

The single particle efficiency sytematic is quoted in Section 5.8.2 and taken to be 17% for both Au+Au and p+p .

$$\frac{\sigma^{\text{sys}}_{\varepsilon}}{\varepsilon} = 17\% \tag{5.64}$$

Systematic error from track multiplicity time dependence

The final systematic determined for $J(\Delta\phi_{ta})$ comes from the multiplicity time dependence. Figure 5.68 illustrates the time dependence of average

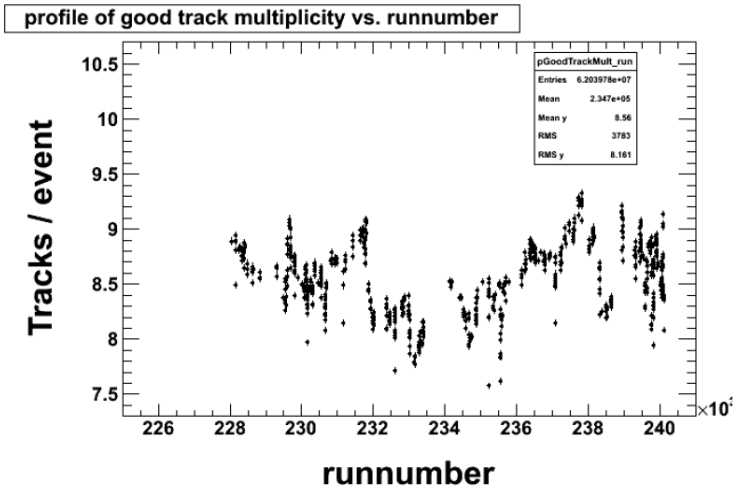

Figure 5.68: Average number of tracks measured per event over time. "Runnumber" refers to the data collection period over an unspecified unit of time.

track measurements per event. There was concern that some of the outliers in the distribution represented run-numbers's that somehow had distorted track distributions. To determine the integrity of these outliers, a few run-number's were chosen and the count of events per multiplicity distribution plotted (see Figure 5.69). From the distribution there were no obvious distortions to the distribution to indicate the removal of this run-number. Further study of run 235231 consisted of binning the event multiplicity distribution into centrality bins. Figure 5.70 shows the distributions along with a Poisson distribution determined from mean and normalized to the integral of the distribution plotted on top of the data. The very good agreement between the Poisson distribution and the data demonstrates that there are no obvious pathologies

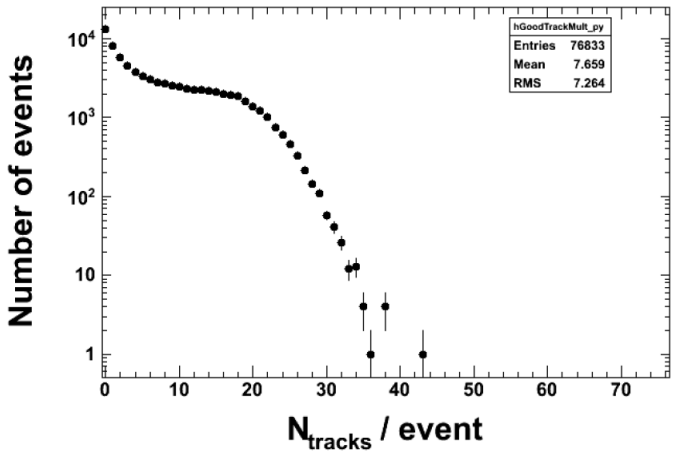

Figure 5.69: Event multiplicity for selected run-number 235231.

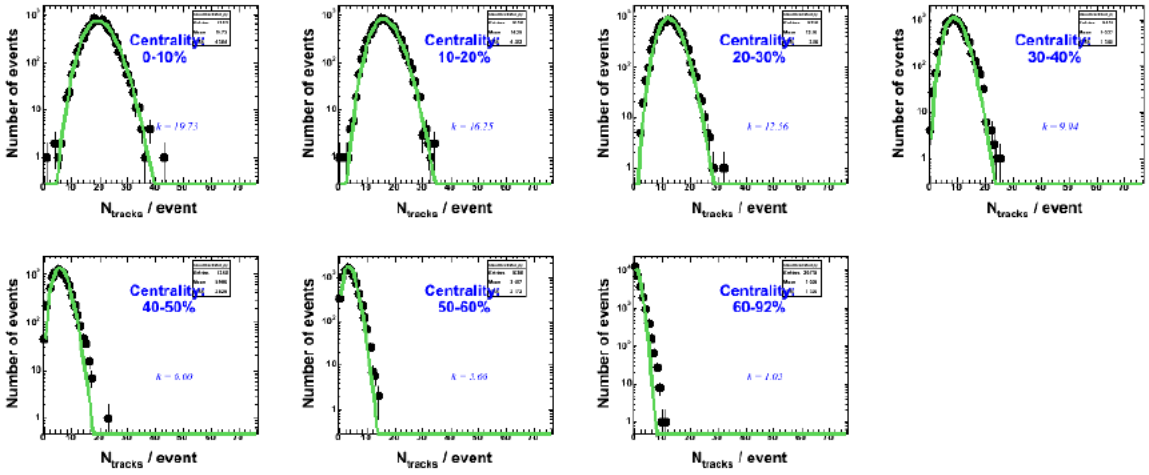

Figure 5.70: Centrality binned event multiplicity for run-number 235231. Poisson distribution determined from mean and normalized to the integral of the distribution is shown in green. The event multiplicity follows a negative binomial distribution which converges to Poisson for large multiplicities (hence, the slight disagreement at most peripheral collisions).

with these run-number's.

Therefore the large fluctuations observed in the event multiplicity (Figure 5.68) might be due to inefficiencies in the detector that change over time. To incorporate this time-dependent effect, the systematic applied was determined as the maximum relative deviation of the mean multiplicity, $\langle \mathrm{M} \rangle$ in the Figure 5.68 distribution:

$$\frac{\sigma_{\mathrm{M}}}{\langle \mathrm{M} \rangle} = 11\% \tag{5.65}$$

Combining systematic errors

The systematic errors described above were combined in quadrature to determine the overall systematic error in $J(\Delta\phi_{ta})$:

$$\sigma^{\mathrm{sys}}_{\mathrm{total}} = \frac{\sigma^{\mathrm{sys}}_{\mathrm{ZYAM}}}{J(\Delta\phi_{ta})} \oplus \frac{\sigma^{\mathrm{sys}}_{\varepsilon}}{\varepsilon} \oplus \frac{\sigma^{\mathrm{sys}}_{\mathrm{M}}}{\langle M \rangle} \tag{5.66}$$

Chapter 6

Results

In this chapter an in-depth analysis of the jet-induced correlations, $J(\Delta\phi_{ta})$ and $J(\Delta\phi_{ta}, \Delta\phi_{tc})$, is carried out. An initial look at the shape of $J(\Delta\phi_{ta})$ is studied followed by integration of the *near-side* and *away-side* region of $J(\Delta\phi_{ta})$. A ratio of the near-side to away-side integrated yield is made and dependence on p_T evaluated. To all of these studies, p+p is used as a unmodified baseline reference $J(\Delta\phi_{ta})$ distributions and compared to heavy ion collision system Au+Au.

6.1 The two-particle $J(\Delta\phi_{ta})$ correlations

Although there are other two-particle correlation studies underway at PHENIX using the 2007 Au+Au dataset [80], the two-particle correlations measured using the methods described in Chapter 5 will be presented for self-consistency. In addition, comparing to previously published two-particle correlation results using the 2004 Au+Au dataset [36], there have been some advances in the estimation of the background having to do with the identification of v_3 anisotropy coefficient. Figure 6.1 to Figure 6.4 illustrates the two-particle correlations for the 2007 Au+Au dataset while using the 2006 p+p dataset as

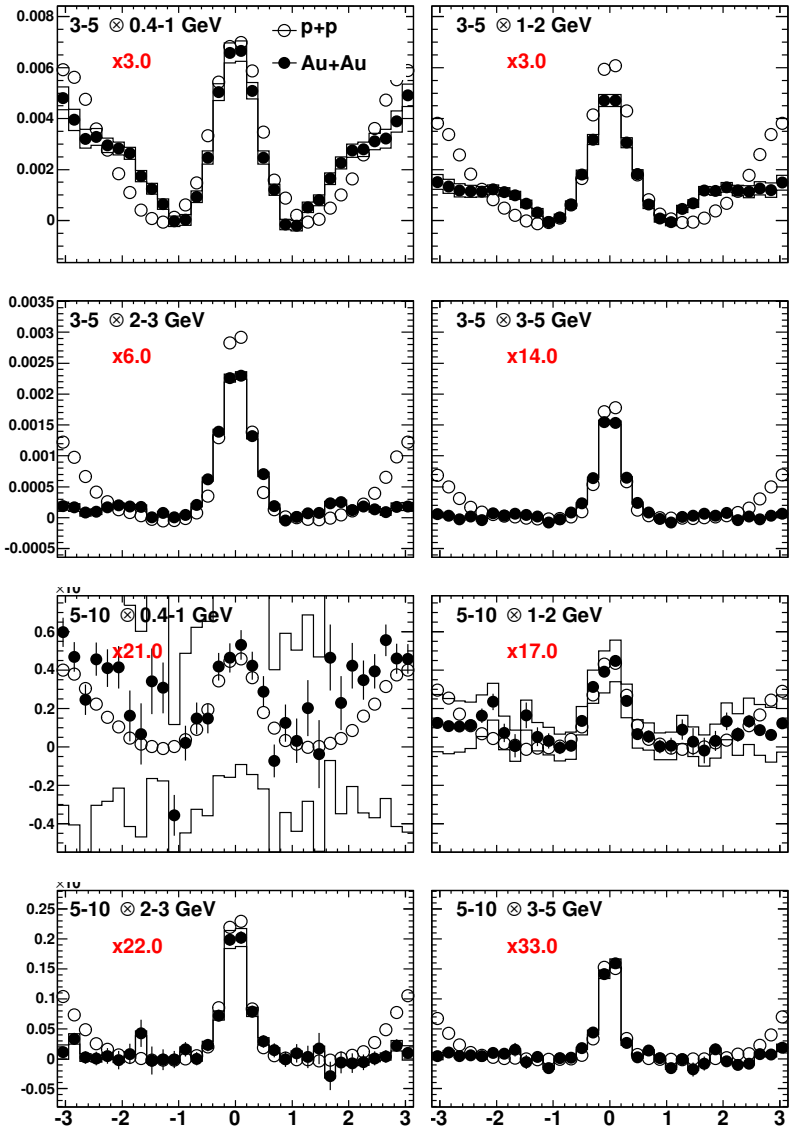

Figure 6.1: Comparison of 2007 Au+Au for 0-20% centrality with 2006 p+p . Plotted is $J(\Delta\phi_{ta})$ while scaling of Au+Au is shown in red.

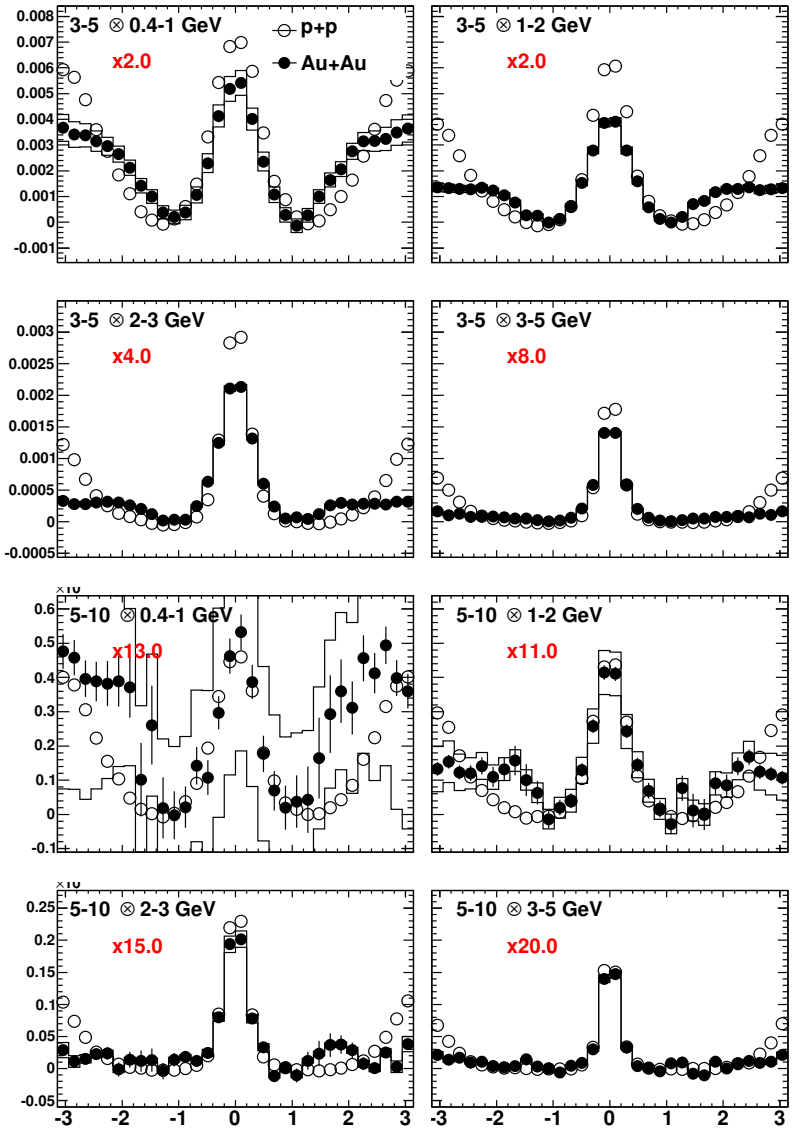

Figure 6.2: Comparison of 2007 Au+Au for 20-40% centrality with 2006 p+p . Plotted is $J(\Delta\phi_{ta})$ while scaling of Au+Au is shown in red.

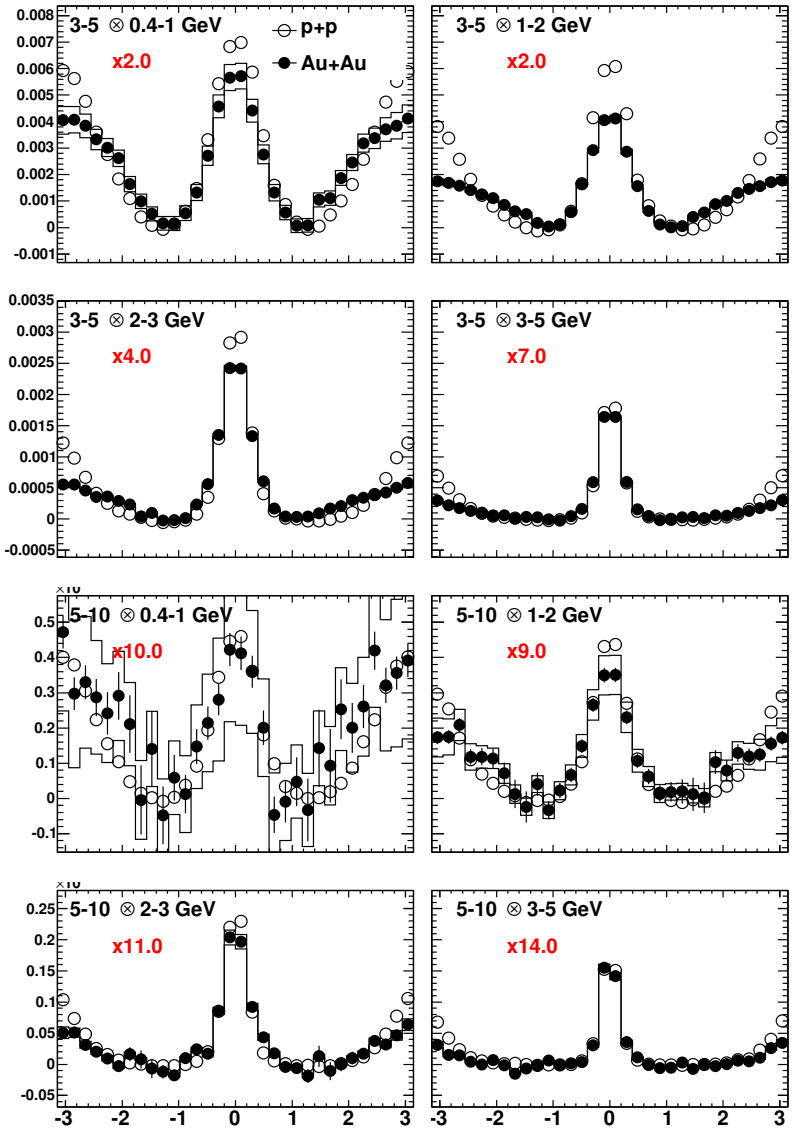

Figure 6.3: Comparison of 2007 Au+Au for 40-60% centrality with 2006 p+p . Plotted is $J(\Delta\phi_{ta})$ while scaling of Au+Au is shown in red.

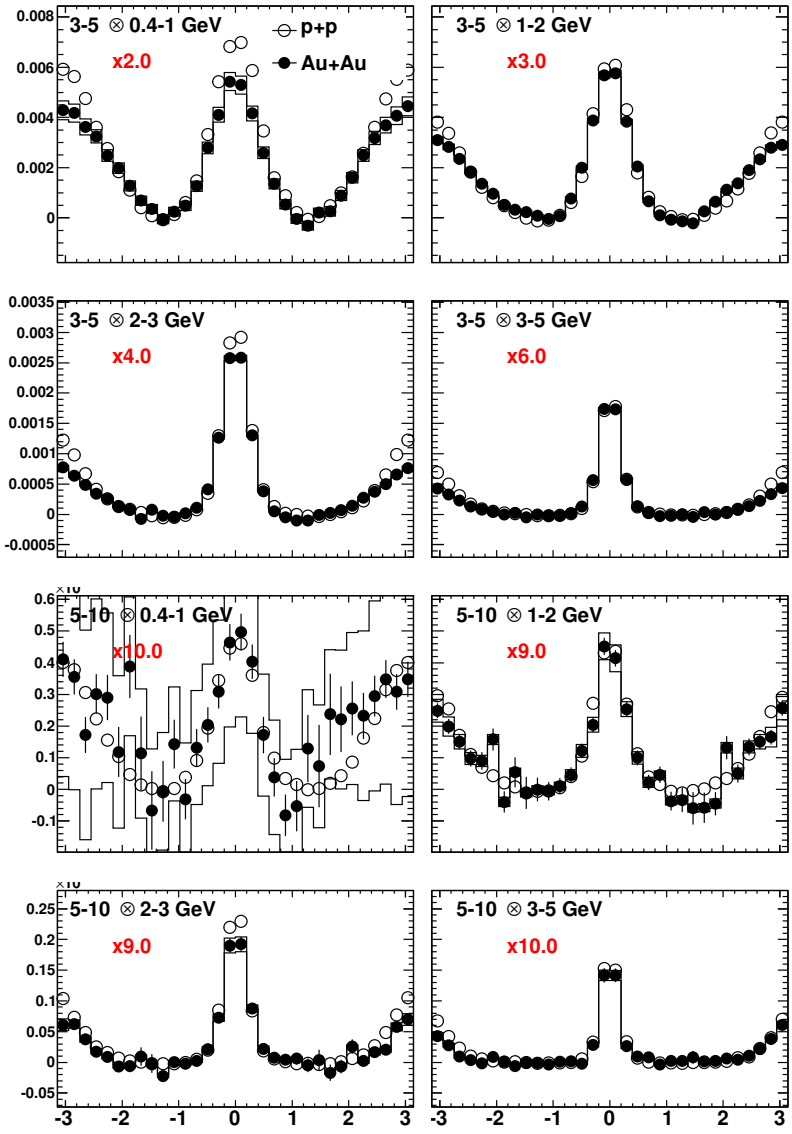

Figure 6.4: Comparison of 2007 Au+Au for 60-92% centrality with 2006 p+p . Plotted is $J(\Delta\phi_{ta})$ while scaling of Au+Au is shown in red.

a baseline reference. Comparing to Figure 2.12, an immediate consequence of the inclusion of v_3 in the estimation of the background, $B(\Delta\phi_{ta})$, results in a significant reduction in the "double hump" away-side jet-induced correlation ($|\pi - \Delta\phi_{ta}| \sim 1.1$). Remnants can still be observed in the lowest associated $p_{T\mathrm{a}}$ bins but seem to be smaller in magnitude relative to the magnitude of the away-side signal around $\Delta\phi_{ta} \sim \pi$.

The higher p_T correlations confirms previous observations of the disappearance of the away-side correlation, i.e. jet quenching, while the near-side jet stays relatively unmodified. This measurement, in conjunction with previously published PHENIX results [36], seems to confirm the postulated dominant mechanism for two-particle correlations where the majority of di-jet production is expected to be produced at the surface of the dense QCD medium resulting in a nearly unquenched jet combined with a quenched jet partner that is oriented into the medium. Conservation of energy-momentum should imply that the energy must go somewhere. A hint to this conundrum might lie in the observation of low-p_T associated particles. It might seem suggestive that if the trigger $p_{T\mathrm{t}}$ bin is held constant, the away-side correlation seems to *grow* in magnitude as the associate $p_{T\mathrm{a}}$ is reduced in most central events. The statistical and systematic errors in v_n seem too small to account for the large away-side magnitude observed in low-p_T associated hadrons. This might be suggestive that the low-p_T away-side being observed are remnants of the quenched jet.

In the following study, a look at the addition of a high-p_T particle to the away-side jet will be analyzed and will be compared to p+p collisions using the exact same kinematic constraints.

6.2 The 2+1 particle $J(\Delta\phi_{ta})$ correlations

In an effort to bias the kinematics towards di-jets, it was decided to constrain the relative azimuthal angle, $\Delta\phi_{tc}$, between the trigger and conditional to be approximately antipodal (i.e. back-to-back). To achieve this, the relative azimuthal angle was restricted as follows.

$$|\pi - \Delta\phi_{tc}| < \frac{\pi}{8} \tag{6.1}$$

The correlations and background subtraction were done according to Section 5.5.

The $J(\Delta\phi_{ta}, \Delta\phi_{tc})$ distributions for p+p collisions (baseline)

The jet-induced 2+1 correlation distributions, $J(\Delta\phi_{ta}, \Delta\phi_{tc})$, are presented here for 2006 p+p collected data. The kinematic selection ($p_{T\mathrm{t}}$, $p_{T\mathrm{c}}$, $p_{T\mathrm{a}}$, $\Delta\phi_{tc}$, etc...) for all three particle in p+p are identical to the kinematic selections done for the Au+Au distributions, as will be shown. Since a dense nuclear medium is *not* expected to be formed in p+p collisions, these distributions will serve as a reference for comparison for Au+Au to determine the degree of modification for the jet-induced correlations measured in this method. Figure 6.5 and Figure 6.6 show the 2+1 correlations where a particular range in the trigger transverse momentum, $p_{T\mathrm{t}}$, has been selected for each figure while allowing the p_T of the other particles to vary.

A few properties can be inferred from the 2+1 correlations that differ from two-particle correlations. In comparison to two-particle correlations, where the $J(\Delta\phi_{ta})$ distributions display an asymmetric amplitude (jets) with respect to $\Delta\phi_{ta}$, the $J(\Delta\phi_{ta}, \Delta\phi_{tc})$ distributions seem to demonstrate a more symmetric distribution. The asymmetry in two-particle correlations, if one assumes that the only contribution is jets, can be attributed to the initial

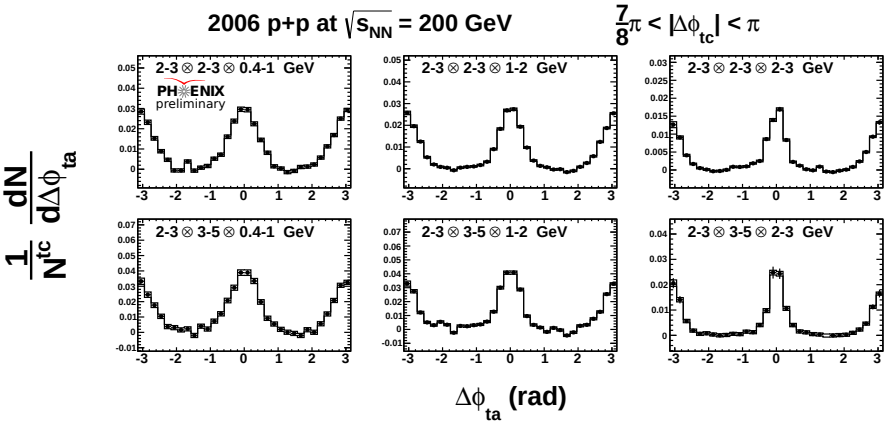

Figure 6.5: Background subtracted 2+1 correlations in 2006 p+p at $\sqrt{s_{NN}} = 200$ GeV. For p_T ranges, $p_{T\mathrm{t}} \otimes p_{T\mathrm{c}} \otimes p_{T\mathrm{a}}$. A trigger *trigger* p_T of $2 < p_{T\mathrm{t}} < 3$ GeV is selected for all plots. Each row and column represents a different *conditional* trigger and *associated* p_T selection, respectively.

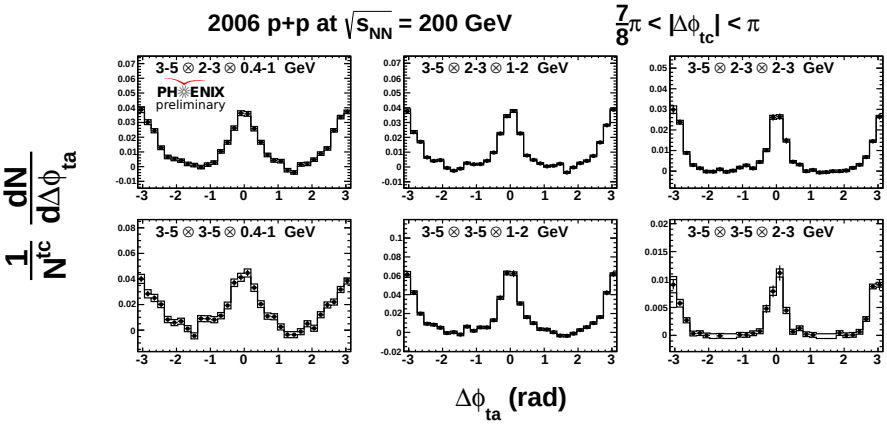

Figure 6.6: Background subtracted 2+1 correlations in 2006 p+p at $\sqrt{s_{NN}} = 200$ GeV. For p_T ranges, $p_{T\mathrm{t}} \otimes p_{T\mathrm{c}} \otimes p_{T\mathrm{a}}$. a trigger *trigger* p_T of $3 < p_{T\mathrm{t}} < 5$ GeV is selected for all plots. Each row and column represents a different *conditional* trigger and *associated* p_T selection, respectively.

momentum fraction x_1 and x_2 of the initial leading-order hard scattering process ($a + b \to c + d$) at the partonic level,

$$\frac{d^3\sigma}{dx_1 dx_2 d\cos\theta^*} = \frac{1}{s}\sum_{ab} f_a(x_1) f_b(x_2) \frac{\pi\alpha_s(Q^2)}{2x_1 x_2}\Sigma^{ab}(\cos\theta^*) \tag{6.2}$$

where $f_a(x_1)$, $f_b(x_2)$ are the parton distribution functions and $\Sigma^{ab}(\cos\theta^*)$ is the angular distribution in the center-of-mass frame. The observed final state distribution is governed by the fragmentation functions $D_{c,d}^{h^\pm}(z, \mu^2)$ for each outgoing parton. The asymmetry in jet amplitude seen in two-particle correlations can arise from two scattering partons that have significantly different x_1 and x_2 initial momentum fractions which causes an asymmetry with respect to pseudorapity, η, in the laboratory frame. Furthermore, the small pseudorapidity acceptance in the central region limits the measure of di-jets where the partonic hard processes are *boosted* in the laboratory frame. However, the situation is different in 2+1 correlations due to the requirement of the additional high-p_T track in the opposite direction of the primary trigger. In particular, for selected trigger and conditional p_T that are in the same range, the two partons generating the observed jet-induced distribution are expected to come from a process where both incoming partons a, b have approximately equal initial momentum fraction x_1 and x_2. Significant deviations can be attributed to j_T distribution, initial k_T, or even the bin width of the selected $\Delta\phi_{tc}$ bin.

The $J(\Delta\phi_{ta}, \Delta\phi_{tc})$ distributions for Au+Au collisions

The jet-induced correlations for Au+Au collisions are presented here for the 2007 data. The correlations were generated using four centrality bins: 0-20%, 20-40%, 40-60%, and 60-92%. Various p_T ranges were selected to attempt to control the hard scattering kinematics of the initial state partons. The $J(\Delta\phi_{ta}, \Delta\phi_{tc})$ correlations are suggestive of a large di-jet production when compared to two-particle correlations in Au+Au and don't seem to show the same broadening away-side effects.

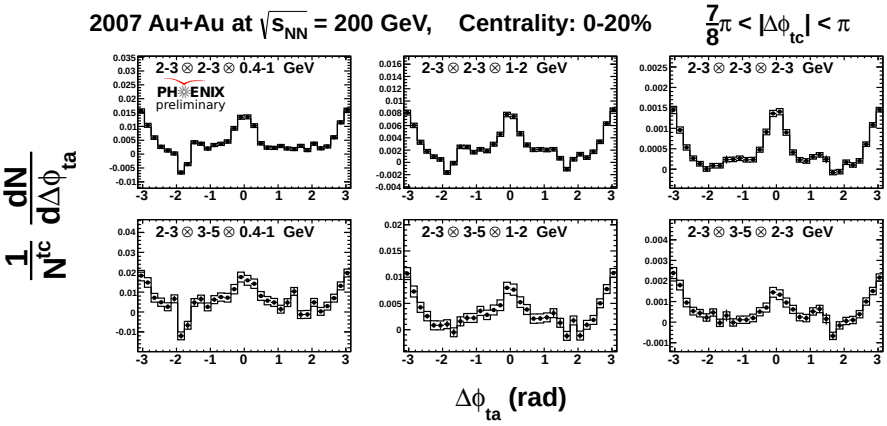

Figure 6.7: Background subtracted 2+1 correlations in Au+Au in 0-20% central collisions. For p_T ranges, $p_{T\mathrm{t}} \otimes p_{T\mathrm{c}} \otimes p_{T\mathrm{a}}$, a trigger *trigger* p_T of $2 < p_{T\mathrm{t}} < 3$ GeV is selected for all plots. Each row and column represents a different *conditional* trigger and *associated* p_T selection, respectively.

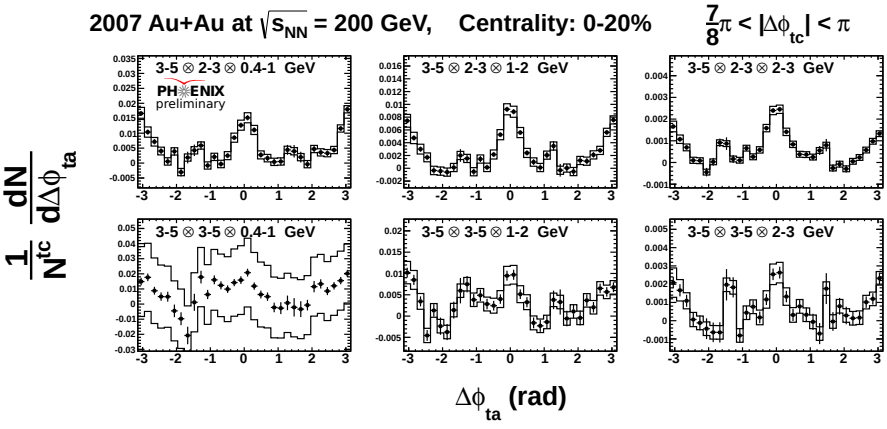

Figure 6.8: Background subtracted 2+1 correlations in Au+Au in 0-20% central collisions. For p_T ranges, $p_{T\mathrm{t}} \otimes p_{T\mathrm{c}} \otimes p_{T\mathrm{a}}$, a trigger *trigger* p_T of $3 < p_{T\mathrm{t}} < 5$ GeV is selected for all plots. Each row and column represents a different *conditional* trigger and *associated* p_T selection, respectively.

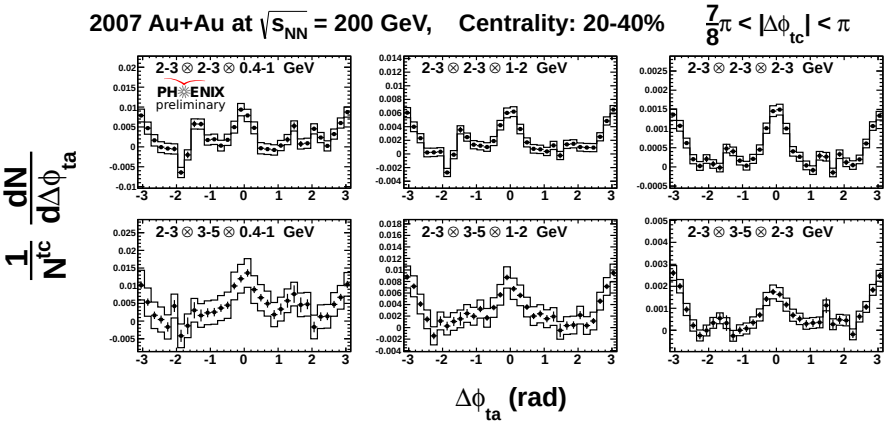

Figure 6.9: Background subtracted 2+1 correlations in Au+Au in 20-40% central collisions. For p_T ranges, $p_{T\mathrm{t}} \otimes p_{T\mathrm{c}} \otimes p_{T\mathrm{a}}$, a trigger *trigger* p_T of $2 < p_{T\mathrm{t}} < 3$ GeV is selected for all plots. Each row and column represents a different *conditional* trigger and *associated* p_T selection, respectively.

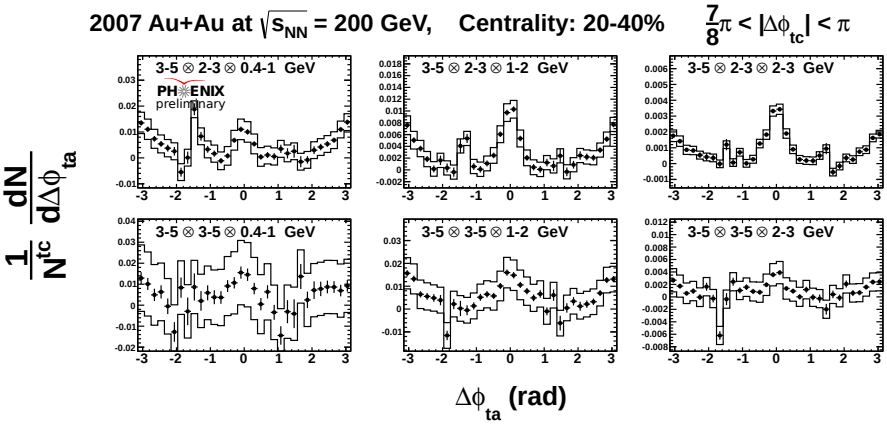

Figure 6.10: Background subtracted 2+1 correlations in Au+Au in 20-40% central collisions. For p_T ranges, $p_{T\mathrm{t}} \otimes p_{T\mathrm{c}} \otimes p_{T\mathrm{a}}$, a trigger *trigger* p_T of $3 < p_{T\mathrm{t}} < 5$ GeV is selected for all plots. Each row and column represents a different *conditional* trigger and *associated* p_T selection, respectively.

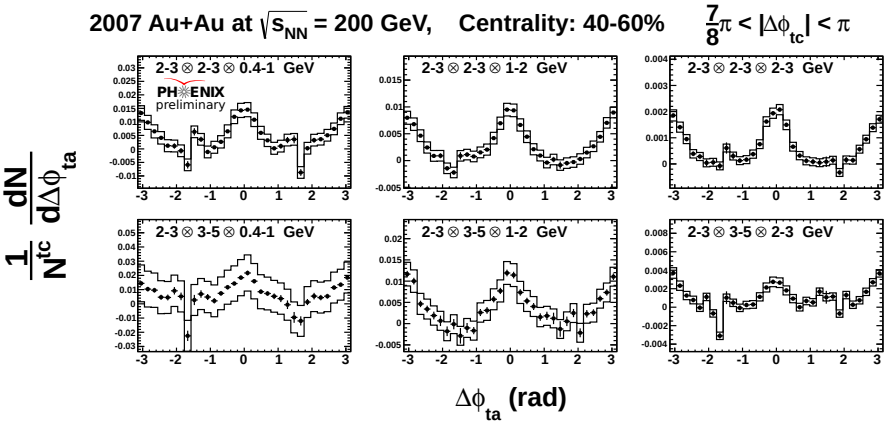

Figure 6.11: Background subtracted 2+1 correlations in Au+Au in 40-60% central collisions. For p_T ranges, $p_{T\mathrm{t}} \otimes p_{T\mathrm{c}} \otimes p_{T\mathrm{a}}$, a trigger *trigger* p_T of $2 < p_{T\mathrm{t}} < 3$ GeV is selected for all plots. Each row and column represents a different *conditional* trigger and *associated* p_T selection, respectively.

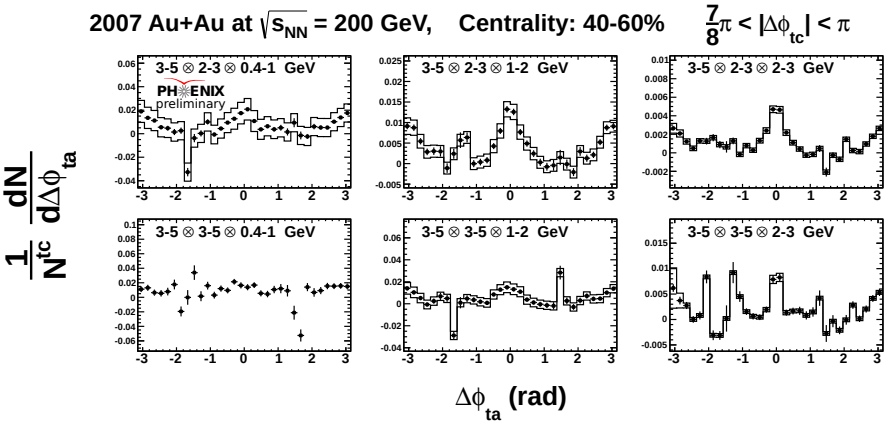

Figure 6.12: Background subtracted 2+1 correlations in Au+Au in 40-60% central collisions. For p_T ranges, $p_{T\mathrm{t}} \otimes p_{T\mathrm{c}} \otimes p_{T\mathrm{a}}$, a trigger *trigger* p_T of $3 < p_{T\mathrm{t}} < 5$ GeV is selected for all plots. Each row and column represents a different *conditional* trigger and *associated* p_T selection, respectively.

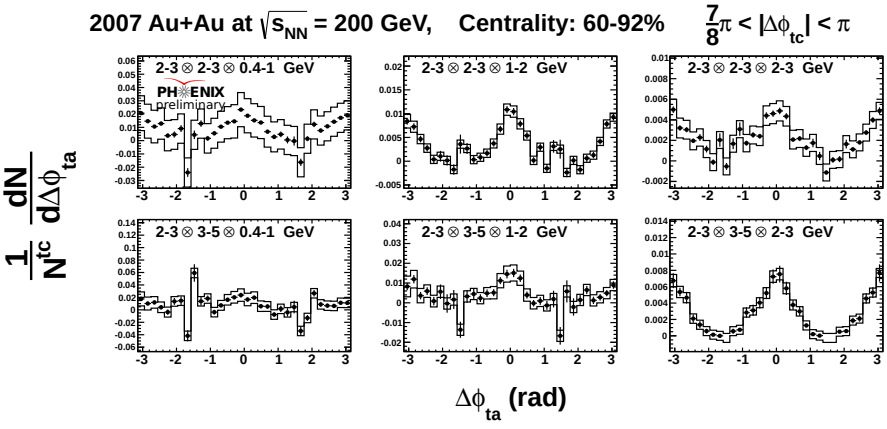

Figure 6.13: Background subtracted 2+1 correlations in Au+Au in 60-92% central collisions. For p_T ranges, $p_{T\mathrm{t}} \otimes p_{T\mathrm{c}} \otimes p_{T\mathrm{a}}$, a trigger *trigger* p_T of $2 < p_{T\mathrm{t}} < 3$ GeV is selected for all plots. Each row and column represents a different *conditional* trigger and *associated* p_T selection, respectively.

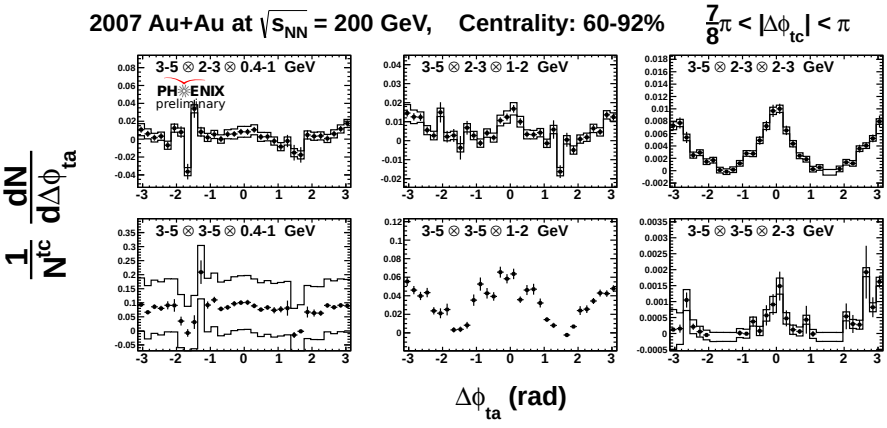

Figure 6.14: Background subtracted 2+1 correlations in Au+Au in 60-92% central collisions. For p_T ranges, $p_{T\mathrm{t}} \otimes p_{T\mathrm{c}} \otimes p_{T\mathrm{a}}$, a trigger *trigger* p_T of $3 < p_{T\mathrm{t}} < 5$ GeV is selected for all plots. Each row and column represents a different *conditional* trigger and *associated* p_T selection, respectively.

Comparison of two-particle to 2+1 correlations in Au+Au

To compare the difference in methods for Au+Au, a comparison of two-particle and 2+1 method is performed. By comparing both methods, a qualitative comparison can be made for the 2+1 method to determine if many of the features that are seen in the two-particle away-side correlation can be identified with the addition of the away-side high-p_T particle.

Figure 6.15 compares various $p_{T\mathrm{t}} \otimes p_{T\mathrm{a}}$ bins for both methods in the most central collisions (0-20%) while selecting a particular $p_{T\mathrm{c}}$ range. It is noteworthy to mention that a significant di-jet induced correlation is observed in the 2+1 method when compared to the two-particle method. There are large fluctuations in the 2+1 method, but many of those fluctuations are observed around $\Delta\phi_{ta} \sim \pi/2$ which can be attributed to the relatively poor acceptance in the 2+1 method. Figures 6.16 to 6.18 demonstrates the effect of moving towards more peripheral events where same di-jet induced correlations are observed.

From the limited information that has been presented thus far, a few scenarios can be put forward in an attempt to explain the difference in shapes for both methods.

a) Assuming similar event partonic kinematic selection, the 2+1 correlation method is *not* sensitive to the medium and as a result what is being observed is the unmodified di-jet induced correlations.

b) Assuming similar event partonic kinematic selection, the 2+1 correlation method is sensitive but the jets in these events travel a different path length, L, than jets measured in the two-particle method and as a result are quenched less in the medium

c) Different partonic kinematic selections are made for both methods, considering the requirement of the antipodal high-p_T particle in 2+1 cor-

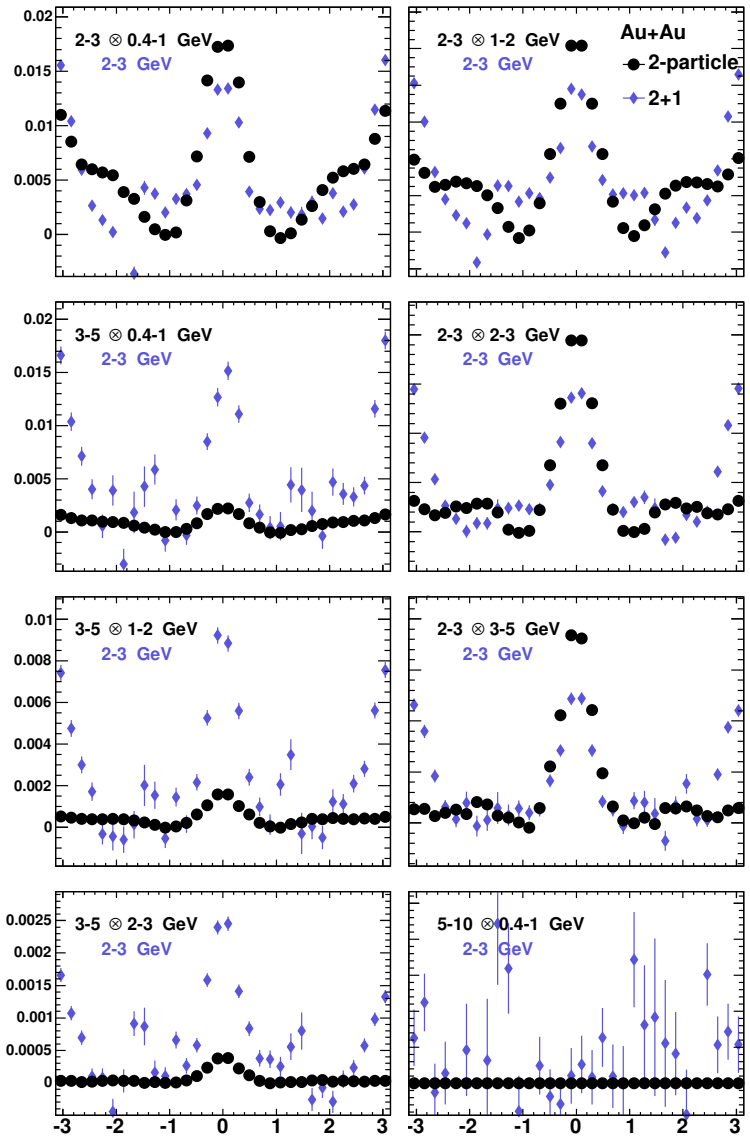

Figure 6.15: Comparison of two-particle and 2+1 method in Au+Au. Centrality 0-20% events are selected for various $p_{T\mathrm{t}} \otimes p_{T\mathrm{a}}$ (black) and a fixed $p_{T\mathrm{c}}$ range (purple) for 2+1 method.

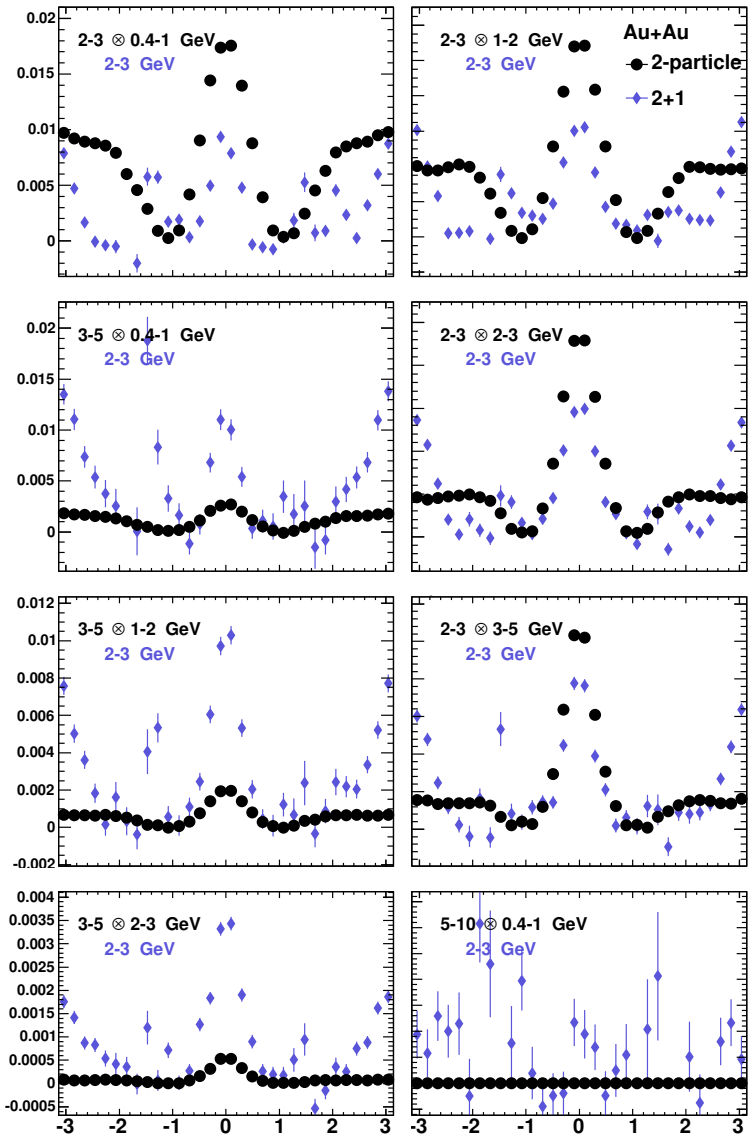

Figure 6.16: Comparison of two-particle and 2+1 method in Au+Au. Centrality 20-40% events are selected for various $p_{T\mathrm{t}} \otimes p_{T\mathrm{a}}$ (black) and a fixed $p_{T\mathrm{c}}$ range (purple) for 2+1 method.

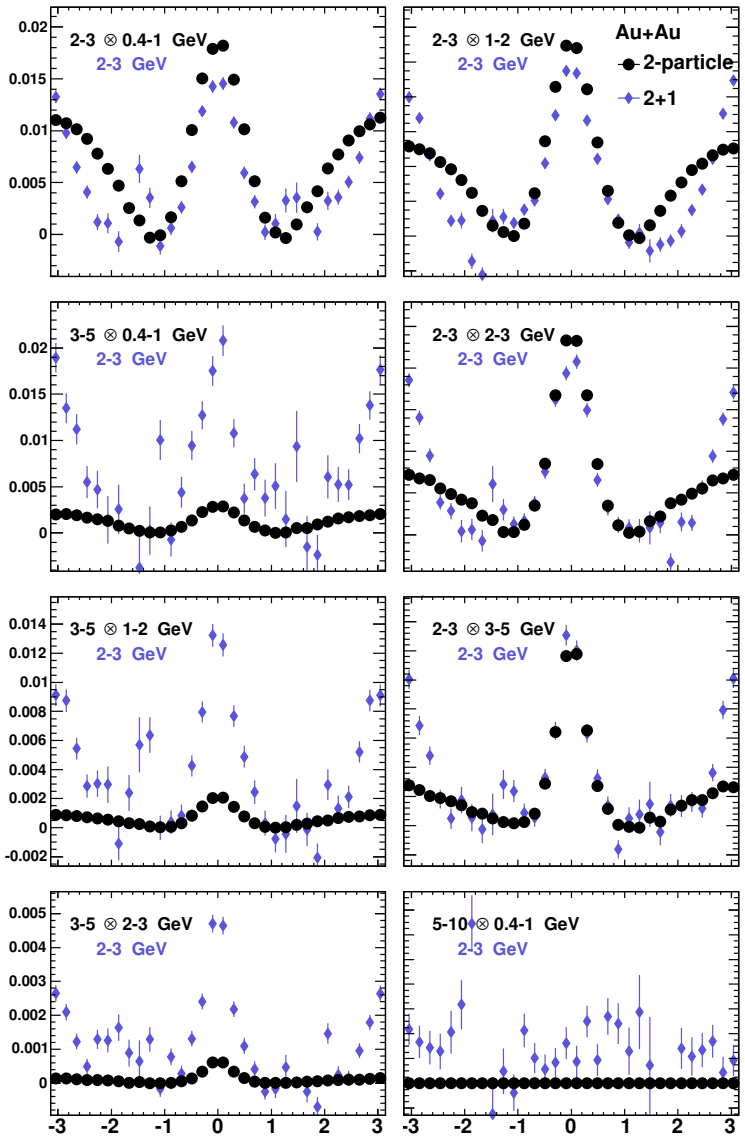

Figure 6.17: Comparison of two-particle and 2+1 method in Au+Au. Centrality 40-60% events are selected for various $p_{T\mathrm{t}} \otimes p_{T\mathrm{a}}$ (black) and a fixed $p_{T\mathrm{c}}$ range (purple) for 2+1 method.

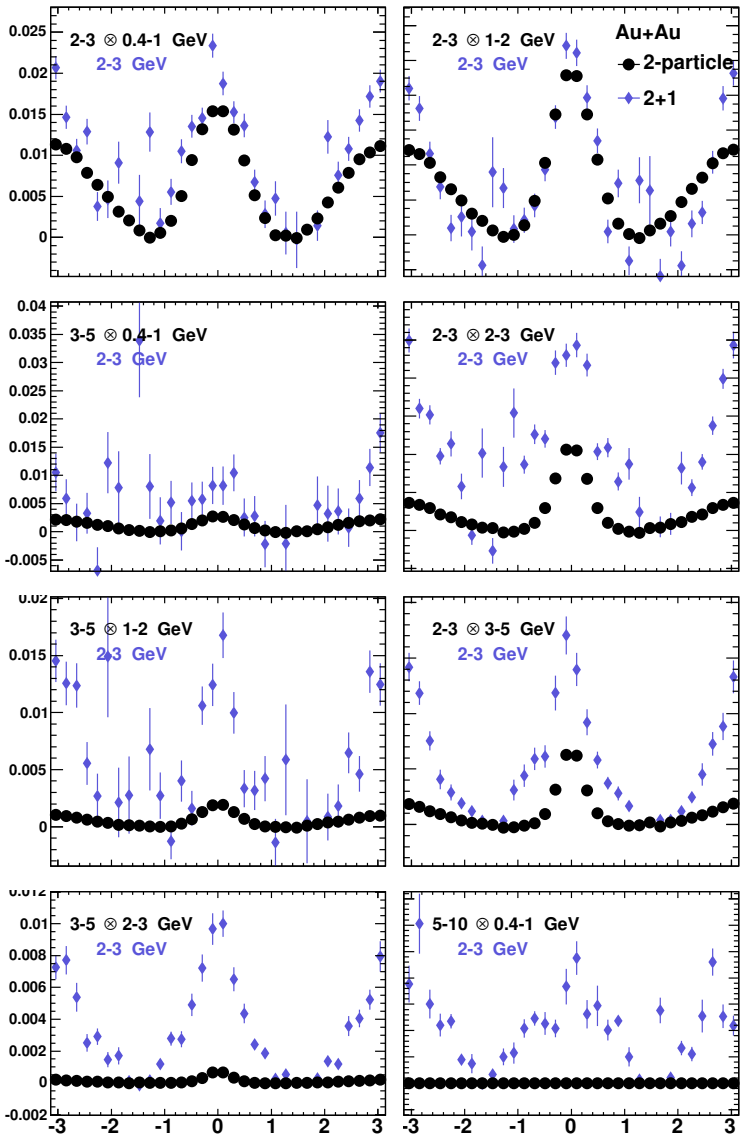

Figure 6.18: Comparison of two-particle and 2+1 method in Au+Au. Centrality 60-92% events are selected for various $p_{T\mathrm{t}} \otimes p_{T\mathrm{a}}$ (black) and a fixed $p_{T\mathrm{c}}$ range (purple) for 2+1 method.

relations, and are not directly comparable. For example see discussion regarding the kinematics in 2+1 p+p section.

Given that a second high-p_T particle is required, it would be hard to believe that scenario c) would not be a significant factor in the observed correlations. The easiest scenario to eliminate would be a) by comparing Au+Au and p+p in the 2+1 method. In the next section a comparison of the near-side to the away-side correlation will be made and compared with p+p to determine if the 2+1 correlation is sensitive to the medium.

6.3 Near-side to away-side jet comparison

To measure modifications in yields in Au+Au relative to p+p collisions, the particle pair yields on the *near-side* (closest to trigger, $\Delta\phi_{ta} \lesssim \pi/2$) and *away-side* (farthest from trigger) are extracted and compared. More formally the yields are defined as follows:

$$Y_{\text{near}} = \int_{0}^{\pi/3} d|\Delta\phi_{ta}|\ J(\Delta\phi_{ta}) \tag{6.3}$$

$$Y_{\text{away}} = \int_{2\pi/3}^{\pi} d|\Delta\phi_{ta}|\ J(\Delta\phi_{ta}) \tag{6.4}$$

The limits were purposefully chosen to stay away from regions of low acceptance where the distributions are susceptible to large fluctuations, i.e. $\Delta\phi_{ta} \sim \pi/2$.

6.3.1 Near-side yield comparison of Au+Au and p+p

In Figure 6.19 to Figure 6.22 the near-side yield dependence on *associated*-p_T is plotted for all centrality bins in Au+Au compared with p+p collisions. For each plot, a particular range in trigger and conditional p_T is selected. The most notable feature of most central Au+Au collisions is the suppresion in hadron pair yield is observed in *all* combinations of p_T selection. As the transition to more peripheral events is made, the suppression is less apparent to the point where in the most peripheral events (60-92%), the suppression is minimal and most of the data points are in agreement with p+p within the systematic error bars.

This behavior is consistent with the significant suppression in yield observed in two-particle Au+Au collisions, i.e. a significant deviation from the p+p spectra. This is an indication that the 2+1 correlation method *is sen-*

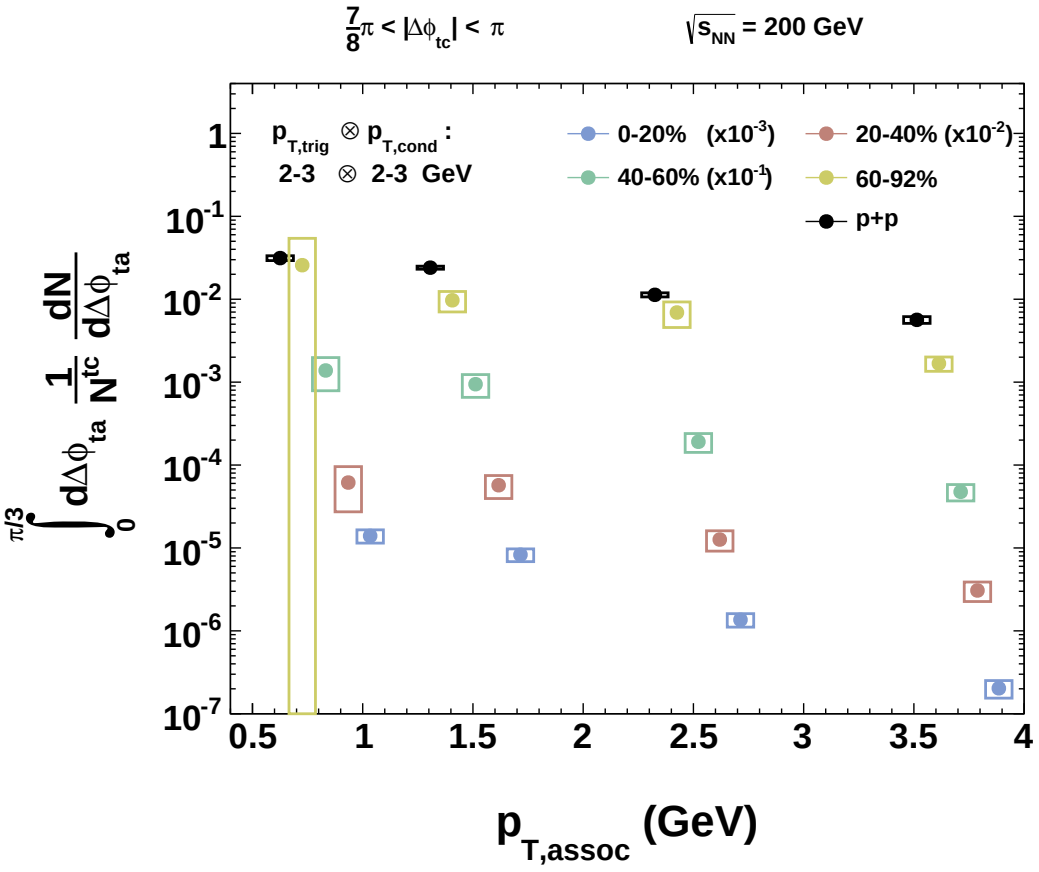

Figure 6.19: Shown is Au+Au and p+p near-side yield dependence on associated particle $p_{T,\text{assoc}}$ for all centrality bins. Trigger and conditional p_T selection is $2-3$ GeV for both particles.

sitive to the effects of jet-quenching observed in the literature. There was much speculation, and in addition some measurements that will be discussed in Chapter 7, that the 2+1 measurement would not be sensitive to such effects and instead would be dominated by "tangential" jets, which are jets produced at the surface of the medium where both jets experience a minimal path length, L, in the medium. Such measurements, as seen in this analysis,

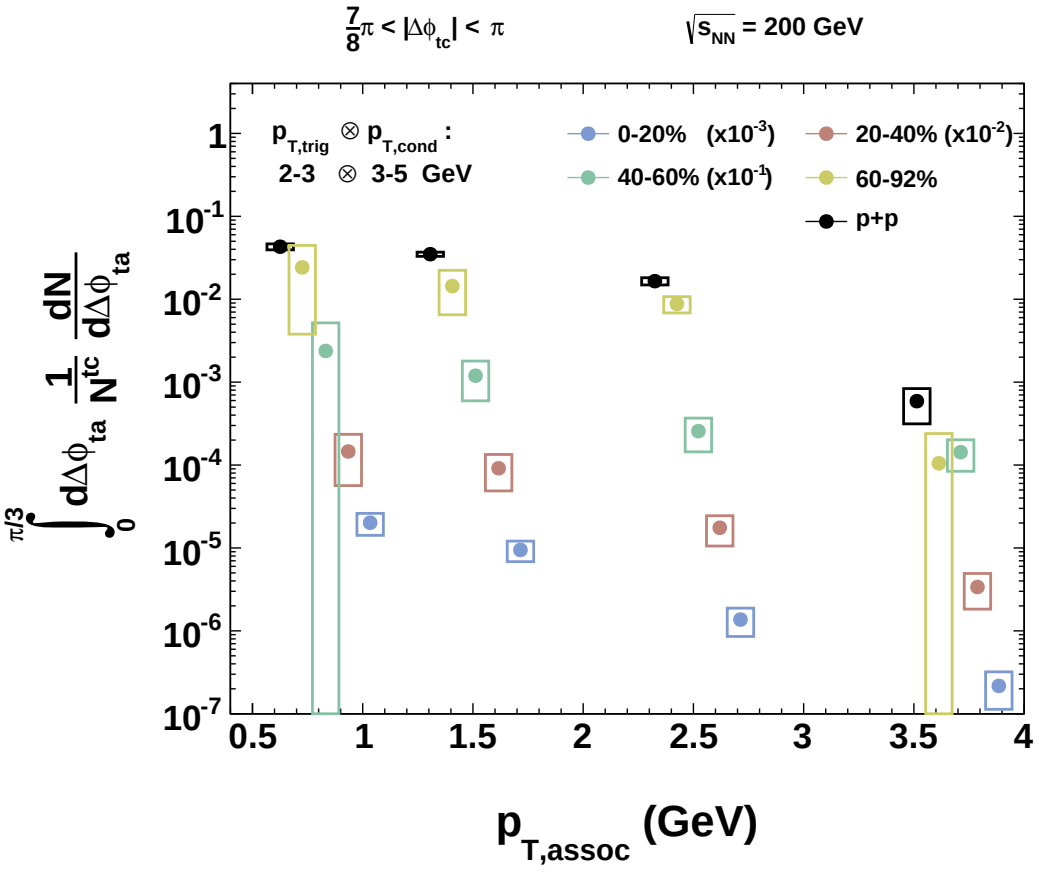

Figure 6.20: Shown is Au+Au and p+p near-side yield dependence on associated particle $p_{T,\mathrm{assoc}}$ for all centrality bins. Trigger and conditional p_T selection is $2 < p_{T,\mathrm{trig}} < 3$ GeV and $3 < p_{T,\mathrm{cond}} < 5$ GeV, respectively.

are encouraging since it suggests that there might be a possibility to study the path length dependence of jet production in the medium.

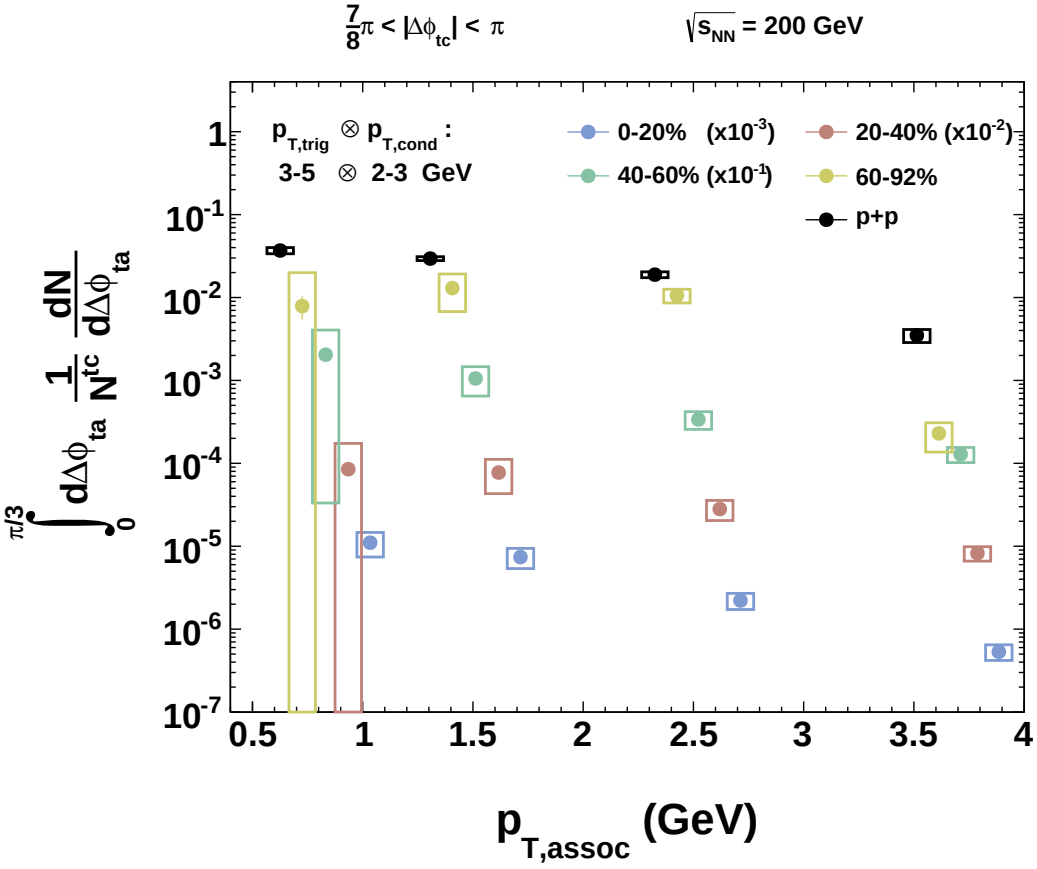

Figure 6.21: Shown is Au+Au and p+p near-side yield dependence on associated particle $p_{T,\mathrm{assoc}}$ for all centrality bins. Trigger and conditional p_T selection is $3 < p_{T,\mathrm{trig}} < 5$ GeV and $2 < p_{T,\mathrm{cond}} < 3$ GeV, respectively.

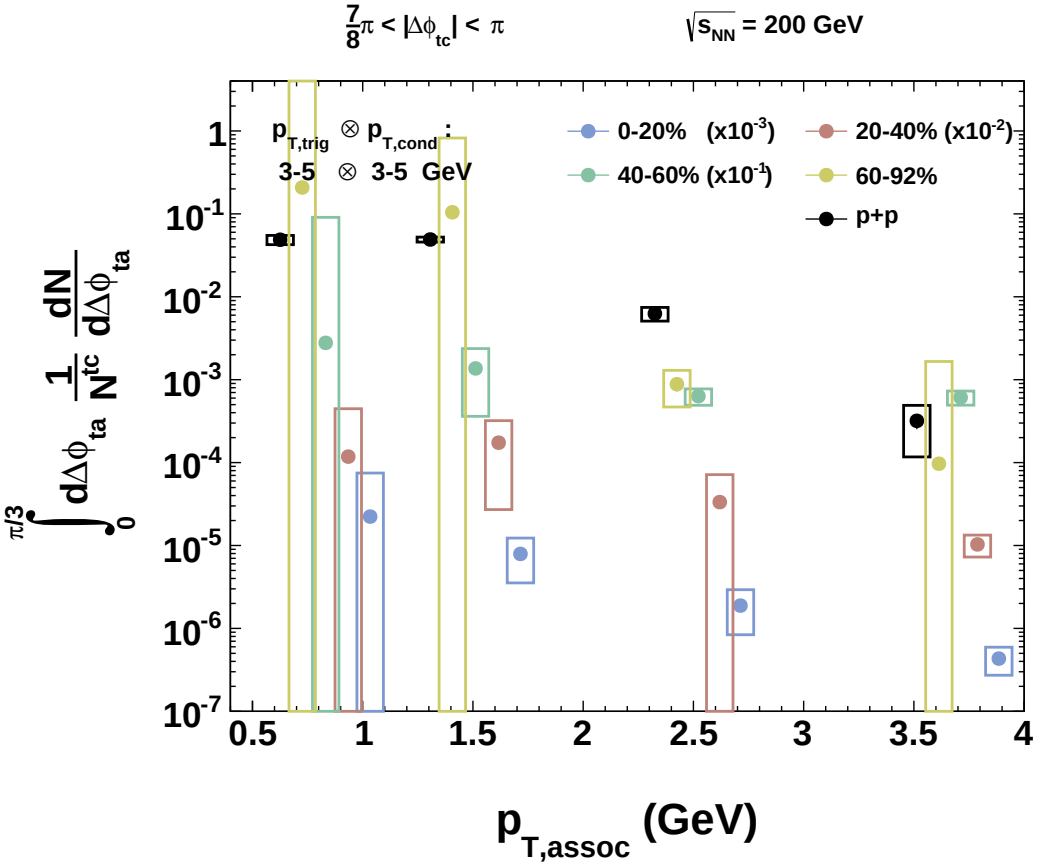

Figure 6.22: Shown is Au+Au and p+p near-side yield dependence on associated particle $p_{T,\mathrm{assoc}}$ for all centrality bins. Trigger and conditional p_T selection is $3-5$ GeV for both particles.

6.3.2 Away-side yield comparison of Au+Au and p+p

To further investigate this suppression, the away-side pair yields are plotted in Figure 6.23 to Figure 6.26. It should be noted that the labeling of the near-side and away-side for events that require two high-p_T tracks is somewhat superficial at this point. But we will continue to label them as such so that a comparison to two-particle correlations can be made.

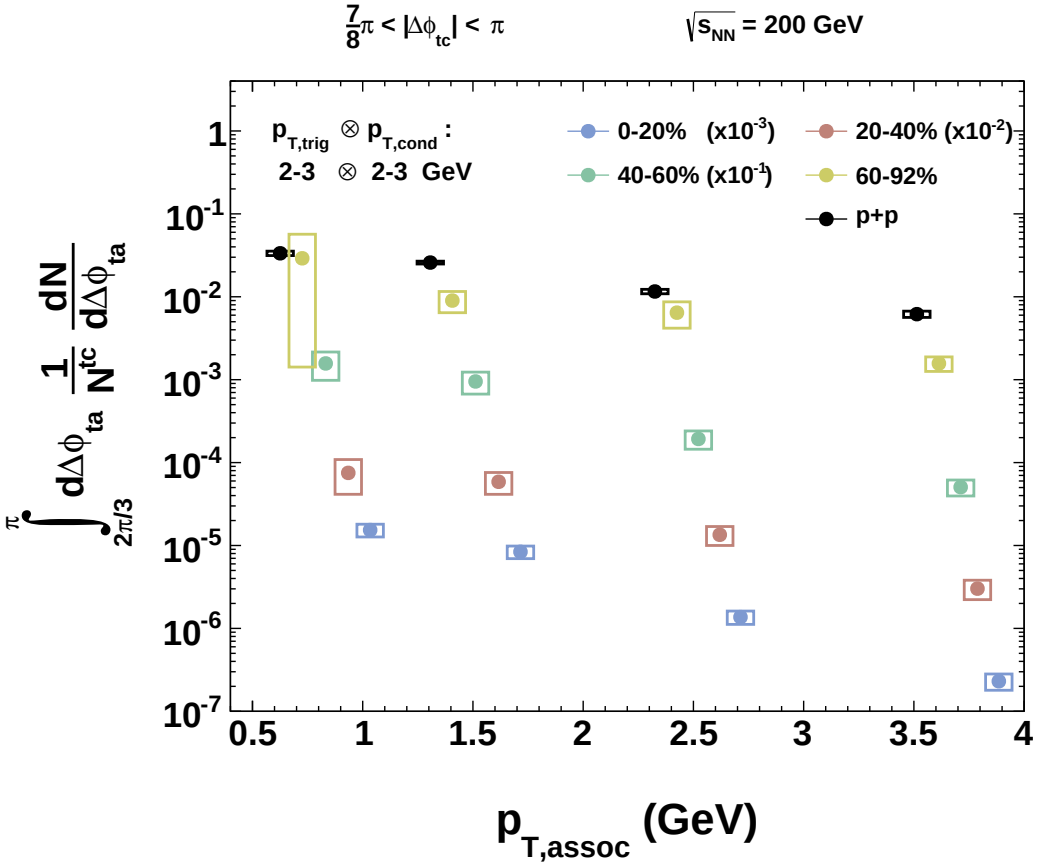

Figure 6.23: Shown is Au+Au and p+p away-side yield dependence on associated particle $p_{T,\mathrm{assoc}}$ for all centrality bins. Trigger and conditional p_T selection is $2-3$ GeV for both particles.

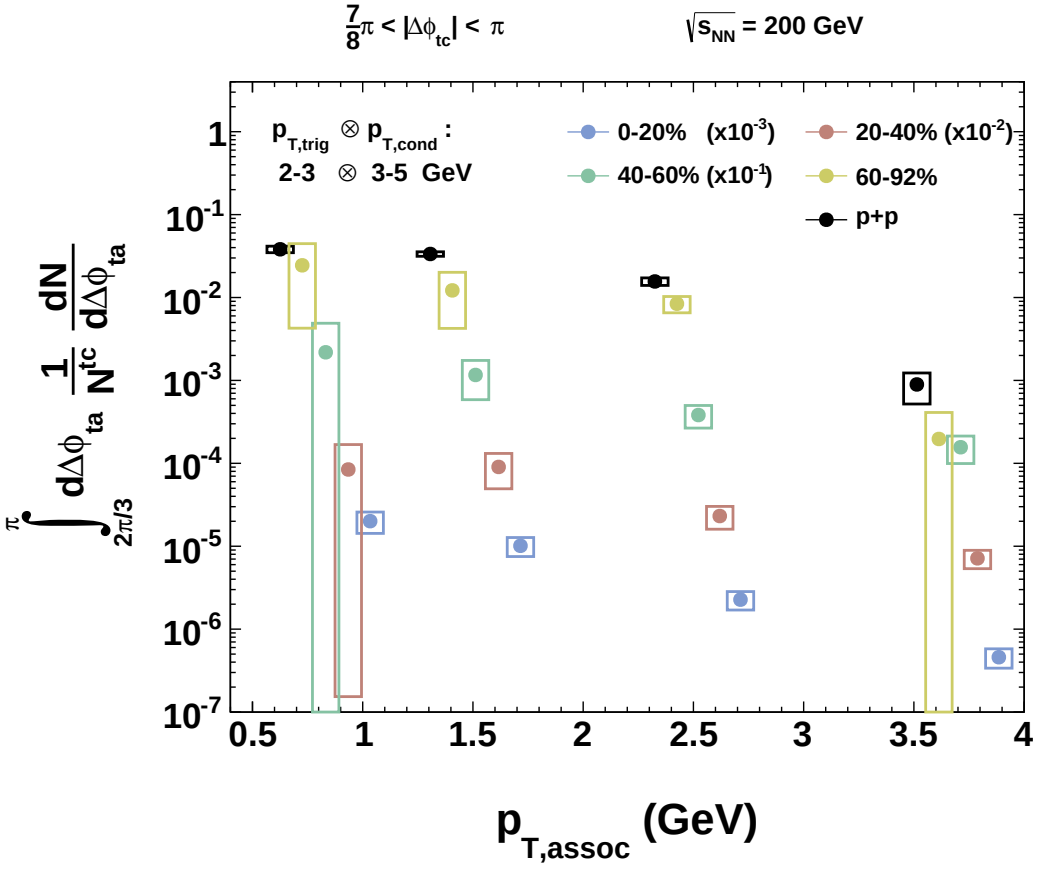

Figure 6.24: Shown is Au+Au and p+p away-side yield dependence on associated particle $p_{T,\mathrm{assoc}}$ for all centrality bins. Trigger and conditional p_T selection is $2 < p_{T,\mathrm{trig}} < 3$ GeV and $3 < p_{T,\mathrm{cond}} < 5$ GeV, respectively.

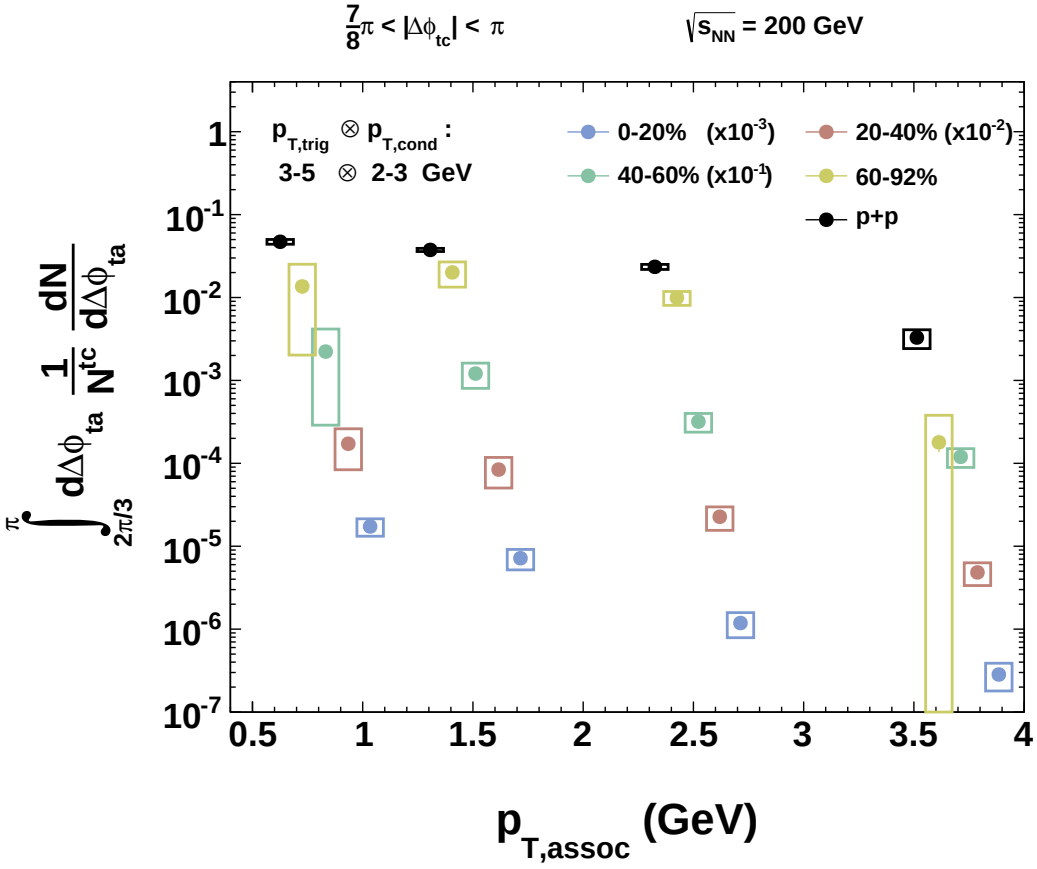

Figure 6.25: Shown is Au+Au and p+p away-side yield dependence on associated particle $p_{T,\mathrm{assoc}}$ for all centrality bins. Trigger and conditional p_T selection is $3 < p_{T,\mathrm{trig}} < 5$ GeV and $2 < p_{T,\mathrm{cond}} < 3$ GeV, respectively.

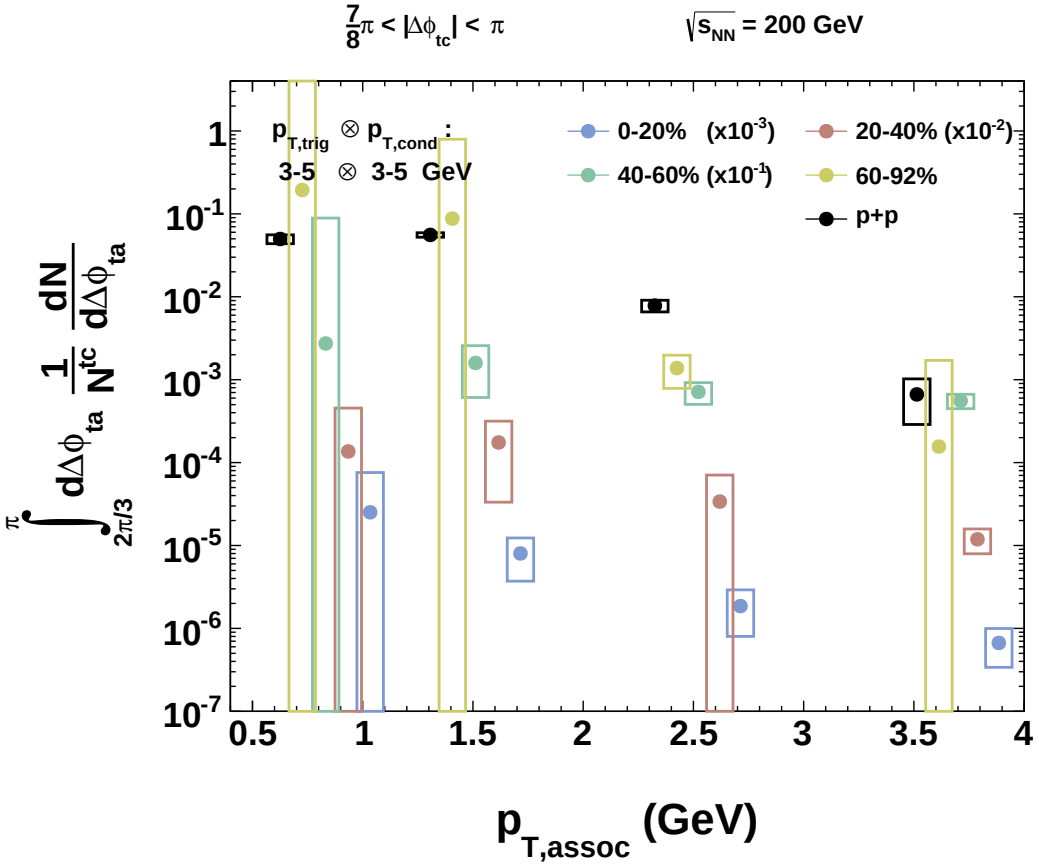

Figure 6.26: Shown is Au+Au and p+p away-side yield dependence on associated particle $p_{T,\mathrm{assoc}}$ for all centrality bins. Trigger and conditional p_T selection is $3-5$ GeV for both particles.

6.4 Near-side to Away-side yield ratio

One of the more striking features of the two-particle measurement was the significant effect that the high-p_T trigger had on the away-side jet-induced correlation when compared to the relatively unmodified near-side correlation. This was the basis for the hypothesis that the presence of a high-p_T trigger was biasing for the selection of events with jets production near the surface of the medium. In the 2+1 correlation method, with the benefit of an additional trigger on the away-side correlation, a comparative study can be made on the effect on *associated* particle production with the presence of a trigger on both sides. To achieve this, a ratio of the near-side to away-side yields, which were measured above, was determined.

$$R = \frac{Y_{\text{near}}}{Y_{\text{away}}} \tag{6.5}$$

Figure 6.27 to Figure 6.30 demonstrates the ratio, R, dependence on *associated* p_T given a particular selection of trigger and conditional p_T range for both Au+Au and p+p . The trigger and conditional pair p_T ($p_{T\text{t}} \otimes p_{T\text{c}}$) is increased for each panel.

Some of the observed trends seen in the data are to be expected. For example, in any panel where the same range in trigger and conditional p_T is selected ($p_{T\text{t}} \simeq p_{T\text{c}}$), the ratio should be close to unity ($R \simeq 1$) which is what is observed in Figure 6.27 and Figure 6.30. The limitation in statistics in the highest trigger, conditional pair p_T bin ($3-5 \otimes 3-5$ GeV) which affects the background subtraction, is responsible for the slight deviation in the last two data points in Figure 6.30.

The more striking feature observed when asymmetric trigger and conditional particle p_T range is selected as in Figure 6.28 and Figure 6.29. An increase in partner particle (associated particle) production in the direction of the higher p_T particle is measured. The effect is minimal in p+p but can still

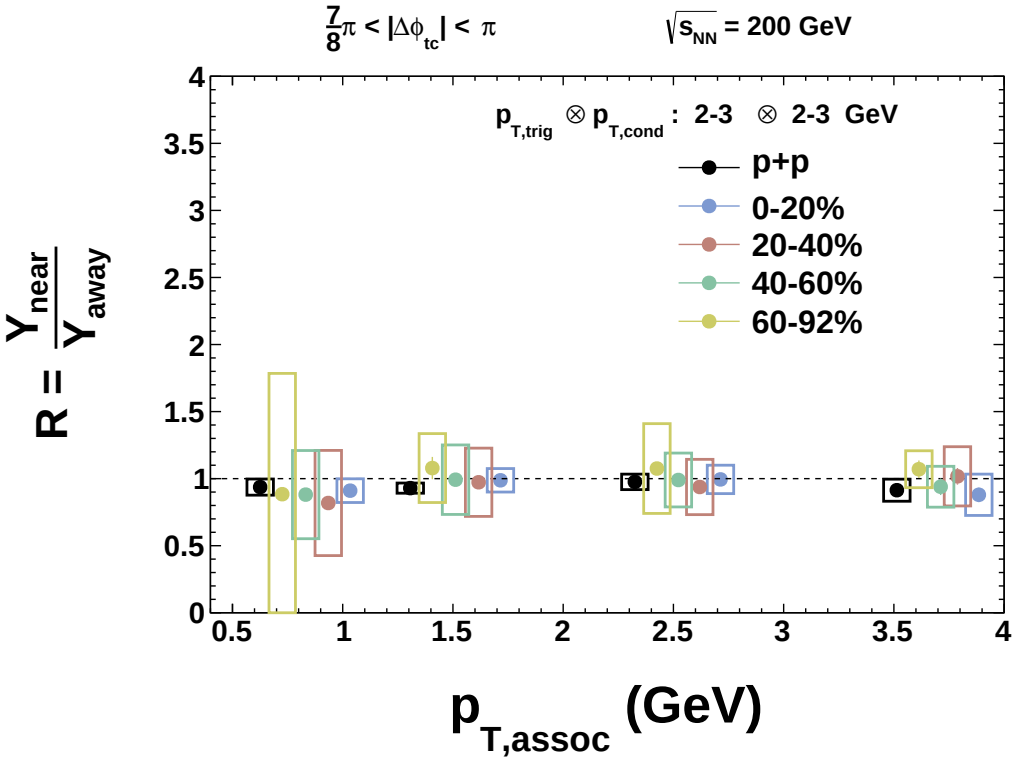

Figure 6.27: Shown is Au+Au and p+p away-side yield dependence on associated particle $p_{T,\mathrm{assoc}}$ for all centrality bins. Trigger and conditional p_T selection is $2-3$ GeV for both particles.

be seen in while significantly more pronounced in Au+Au collisions. From these measurements, the source of this effect can be speculated to be coming from jets, but cannot conclusively rule out other effects such as particles coming from the thermalized medium.

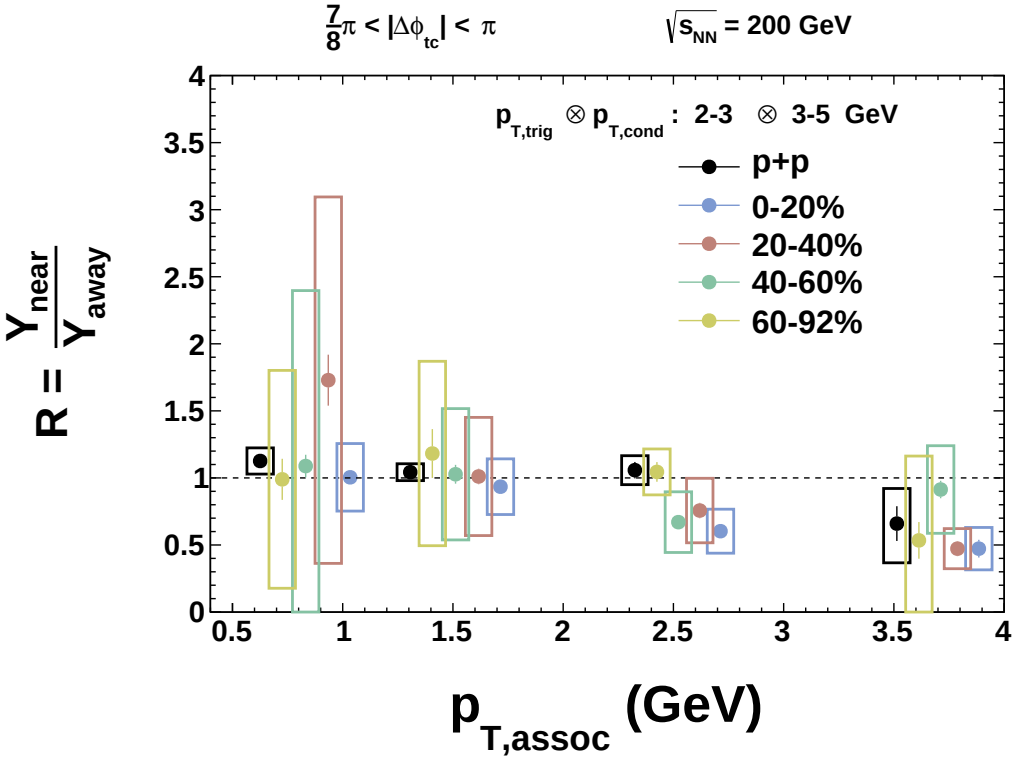

Figure 6.28: Shown is Au+Au and p+p away-side yield dependence on associated particle $p_{T,\mathrm{assoc}}$ for all centrality bins. Trigger and conditional p_T selection is $2 < p_{T,\mathrm{trig}} < 3$ GeV and $3 < p_{T,\mathrm{cond}} < 5$ GeV, respectively.

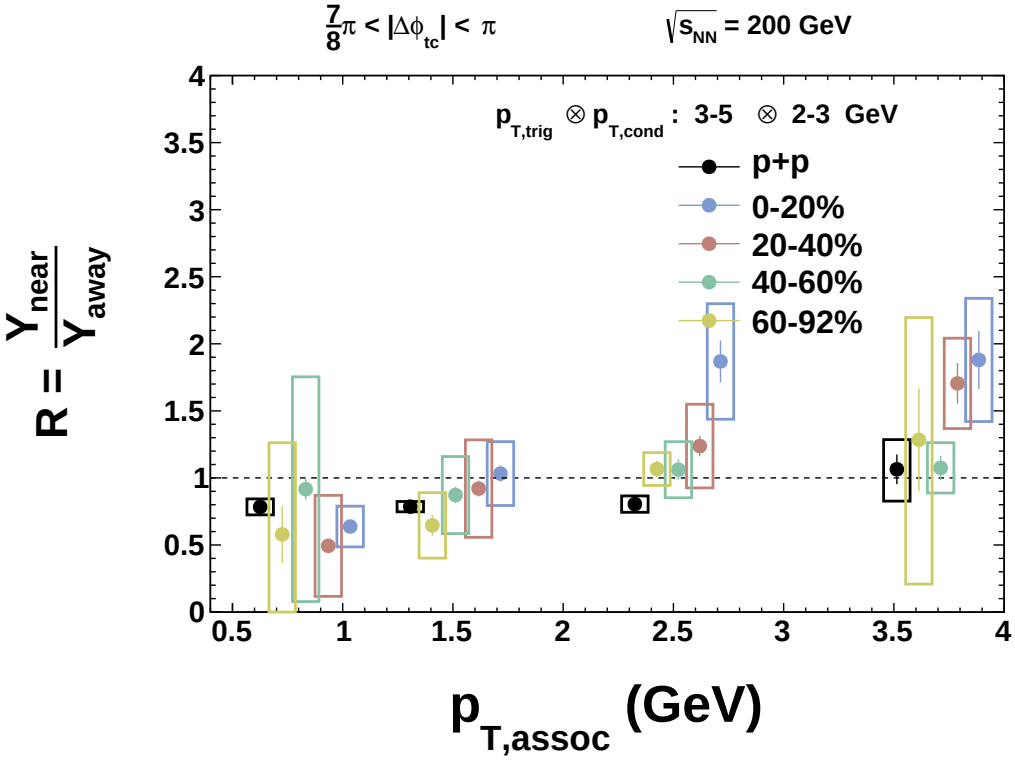

Figure 6.29: Shown is Au+Au and p+p away-side yield dependence on associated particle $p_{T,\mathrm{assoc}}$ for all centrality bins. Trigger and conditional p_T selection is $3 < p_{T,\mathrm{trig}} < 5$ GeV and $2 < p_{T,\mathrm{cond}} < 3$ GeV, respectively.

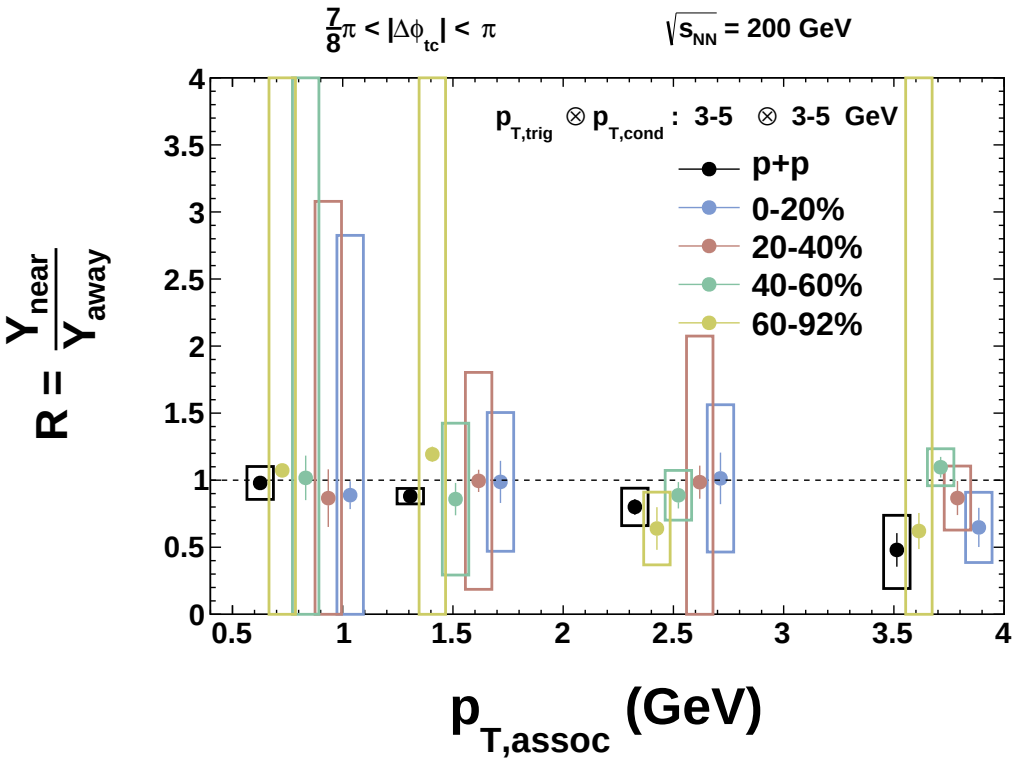

Figure 6.30: Shown is Au+Au and p+p away-side yield dependence on associated particle $p_{T,\text{assoc}}$ for all centrality bins. Trigger and conditional p_T selection is $3-5$ GeV for both particles.

6.4.1 Centrality (N_{part}) dependence of near-side to away-side ratio

In order to determine the collision geometry dependence on the yield ratio (R), the centrality dependence was analyzed for various particle p_T selections. The N_{part} corresponding to the centrality bins chosen in this analysis are found in References [81] [73] and are tabulated in Table 6.1.

Table 6.1: N_{part} for Au+Au at $\sqrt{s_{NN}} = 200$ GeV.

Centrality	N_{part}
0-20%	280.5
20-40%	141.5
40-60%	61.6
60-92%	14.5

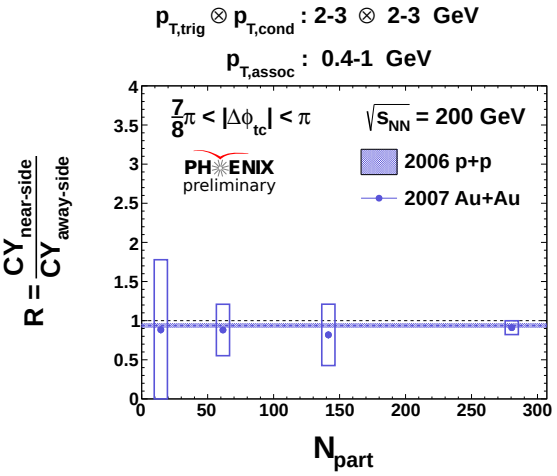

Figure 6.31: Near-to-away side ratio dependence on N_{part}.

Figure 6.31 to 6.42 show the N_{part} dependence on the ratio. Although most of the bins don't exhibit a significant deviation due to the size of the systematic errors, it is interesting to observe that in the most central bin,

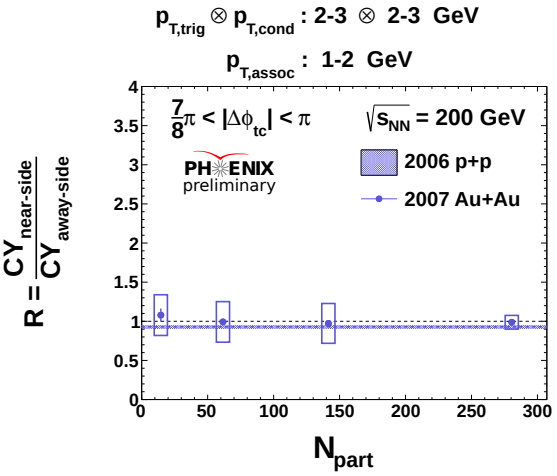

Figure 6.32: Near-to-away side ratio dependence on $N_{\rm part}$.

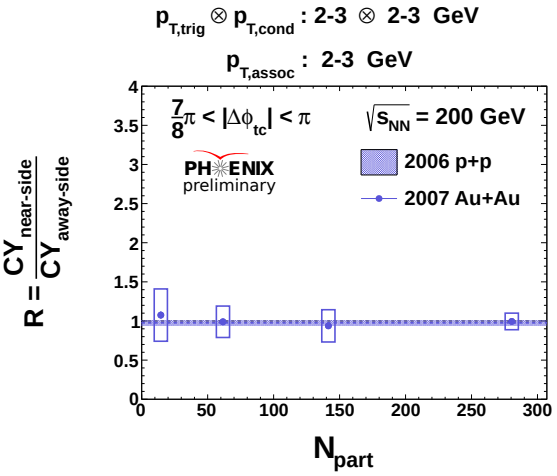

Figure 6.33: Near-to-away side ratio dependence on $N_{\rm part}$.

there seems to be a significant deviation in cases where the trigger and conditional high-p_T particle are asymmetric and in the bin $2-5 \otimes 3-5$ GeV. It could be argued that there is a systematic increase in the suppresion in these bins as one moves to higher N_{part}. However, more statistics will be needed

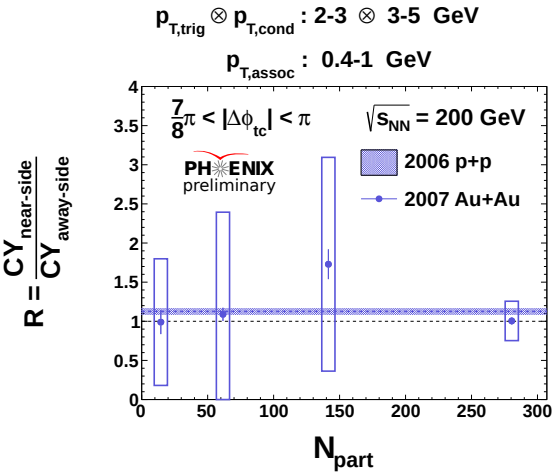

Figure 6.34: Near-to-away side ratio dependence on $N_{\rm part}$.

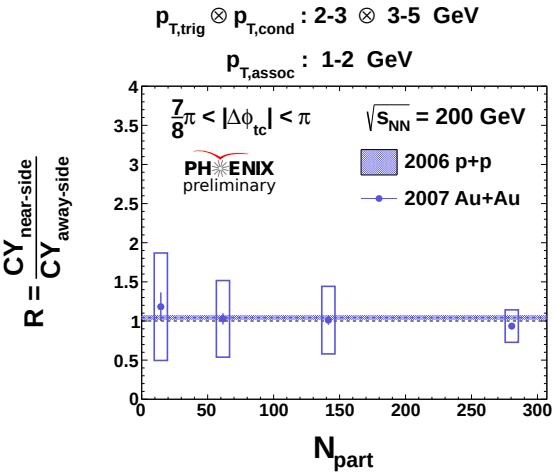

Figure 6.35: Near-to-away side ratio dependence on $N_{\rm part}$.

to confirm this behavior.

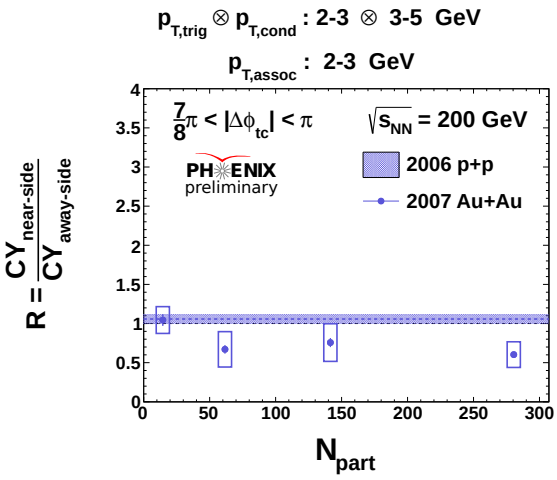

Figure 6.36: Near-to-away side ratio dependence on $N_{\rm part}$.

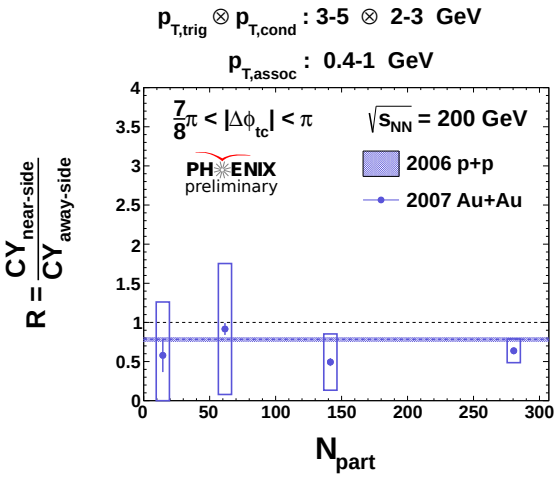

Figure 6.37: Near-to-away side ratio dependence on $N_{\rm part}$.

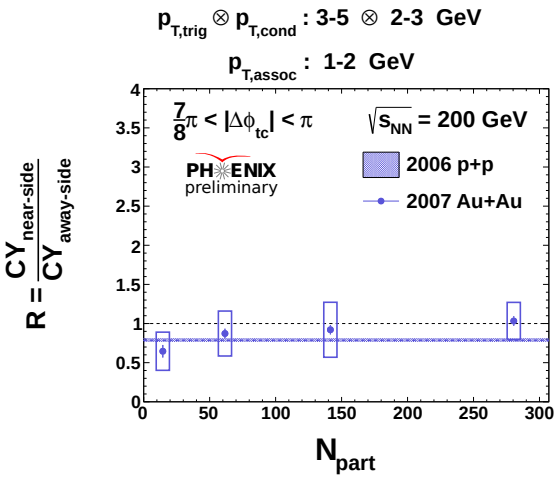

Figure 6.38: Near-to-away side ratio dependence on $N_{\rm part}$.

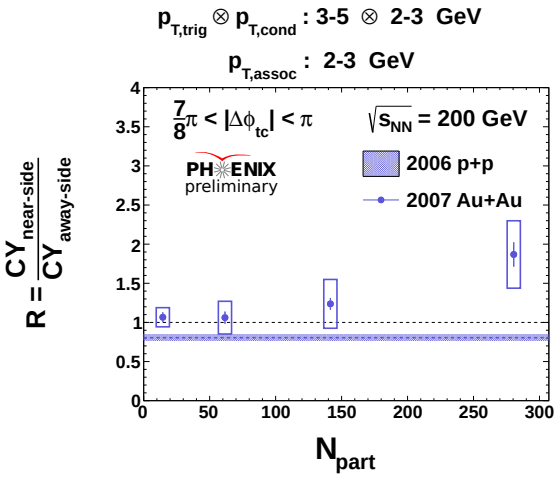

Figure 6.39: Near-to-away side ratio dependence on $N_{\rm part}$.

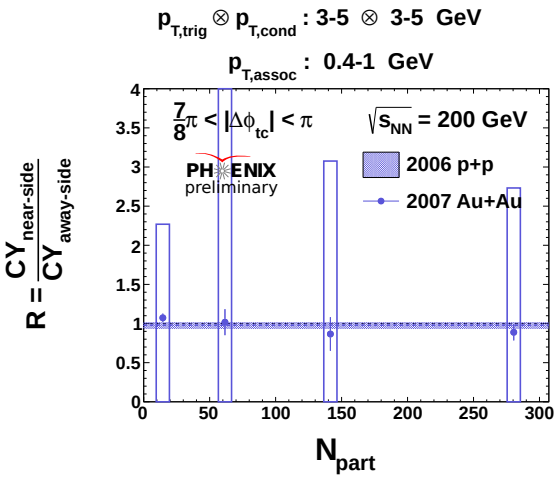

Figure 6.40: Near-to-away side ratio dependence on $N_{\rm part}$.

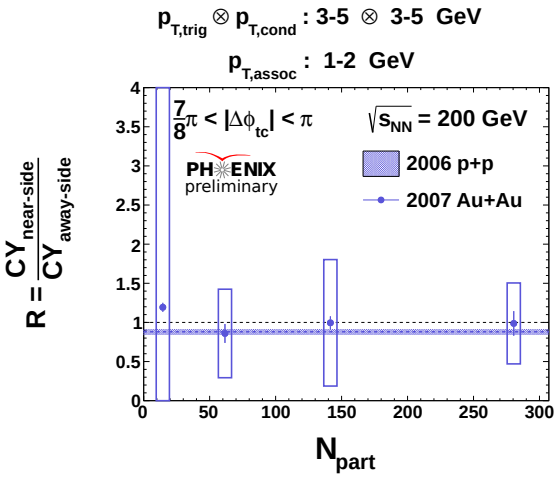

Figure 6.41: Near-to-away side ratio dependence on $N_{\rm part}$.

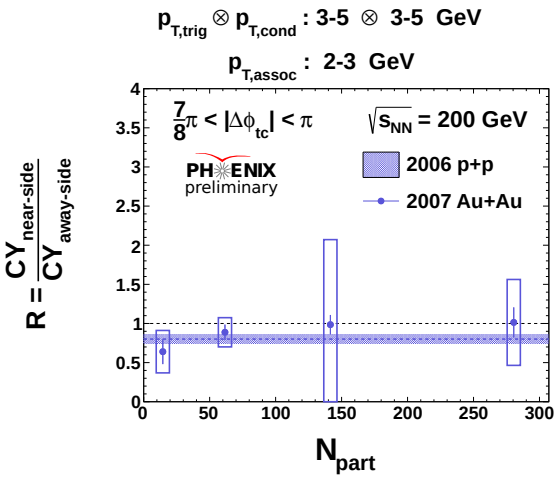

Figure 6.42: Near-to-away side ratio dependence on $N_{\rm part}$.

Chapter 7

Discussion and Outlook

A comparative study of two-particle correlations in the presence of an additional high-p_T particle, i.e. 2+1 correlations, has been presented. From the integrated yields Y_{near}, Y_{away} and ratio, a conclusion is made that significant modification is observed in Au+Au relative to p+p using the 2+1 correlation method. Such effects are interpreted as due to the hard-scattering parton interacting with the strongly interacting medium.

This observation is in conflict with previous measurements made at RHIC where no significant modification was found using the same method [41] [42]. This can be due to many factors, including a difference in the subtraction of the correlated background. Also, it is not clear that the correct event-mixing technique is used in reference [41] and [42] compared to this analysis. It would be interesting to see if similar techniques are employed as presented in this thesis, whether a suppression in particle production on the near-side relative to the away-side can be observed.

In addition, a study of two-particle correlations has been continued with further refinements to the background subtraction (i.e. inclusion of v_3) which reveal that the away-side correlation disappears for high-p_T triggers and high-p_T associated hadrons only to reappear as the p_T of the associated hadron

is lowered. This observation suggests that the remnants of the jet being produced opposite to the high-p_T trigger, and subsequently quenched, are being observed in low-p_T away-side correlations.

Although it may seem currently that two-particle correlation measurements are being displaced by jet reconstruction algorithms, it is not obvious that jet reconstruction measurements will provide a complete description of jet quenching especially in a scenario where the away-side jet is quenched substantially and is not clearly distinguishable from the correlated background. Two-particle measurements and reconstructed jet-particle correlations should still, in principle, provide a constraint on whether the away-side jet is being fully described by reconstructed jets.

Bibliography

[1] J.D. Jackson. *Classical Electrodynamics*. John Wiley & Sons, New York, NY, 1999.

[2] Herbert Goldstein, Charles P. Poole, and John L. Safko. *Classical Mechanics*. Addison-Wesley, 2001.

[3] P. W. Anderson. More is different. *Science*, 177(4047):393–396, 1972.

[4] J. Chadwick. POSSIBLE EXISTENCE OF A NEUTRON. *Nature*, 129:312, 1932.

[5] W. Heisenberg. ber den bau der atomkerne. i. *Zeitschrift fr Physik*, 77:1–11, 1932.

[6] C. N. Yang and R. L. Mills. Conservation of isotopic spin and isotopic gauge invariance. *Phys. Rev.*, 96:191–195, Oct 1954.

[7] E. D. Bloom, D. H. Coward, H. DeStaebler, J. Drees, G. Miller, L. W. Mo, R. E. Taylor, M. Breidenbach, J. I. Friedman, G. C. Hartmann, and H. W. Kendall. High-energy inelastic *e-p* scattering at 6° and 10°. *Phys. Rev. Lett.*, 23:930–934, Oct 1969.

[8] Gerard 't Hooft. Renormalizable Lagrangians for Massive Yang-Mills Fields. *Nucl.Phys.*, B35:167–188, 1971.

[9] Erick J. Weinberg. Radiative corrections as the origin of spontaneous symmetry breaking. 1973. arXiv:hep-th/0507214.

[10] H. David Politzer. Reliable Perturbative Results for Strong Interactions? *Phys.Rev.Lett.*, 30:1346–1349, 1973.

[11] D.J. Gross and Frank Wilczek. Ultraviolet Behavior of Nonabelian Gauge Theories. *Phys.Rev.Lett.*, 30:1343–1346, 1973.

[12] David J. Gross. Asymptotic Freedom and QCD-a Historical Perspective. *Nuclear Physics B - Proceedings Supplements*, 135(0):193 – 211, 2004. Loops and Legs in Quantum Field Theory. Proceedings of the 7th DESY Workshop on Elementary Particle Theory.

[13] Kenneth G. Wilson. Confinement of quarks. *Phys. Rev. D*, 10:2445–2459, Oct 1974.

[14] Enrico Fermi. High energy nuclear events. *Progress of Theoretical Physics*, 5(4):570–583, 1950.

[15] S.Z. Belenkij and L.D. Landau. Hydrodynamic theory of multiple production of particles. *Nuovo Cim.Suppl.*, 3S10:15, 1956.

[16] T. D. Lee and G. C. Wick. Vacuum stability and vacuum excitation in a spin-0 field theory. *Phys. Rev. D*, 9:2291–2316, Apr 1974.

[17] Michael L. Miller, Klaus Reygers, Stephen J. Sanders, and Peter Steinberg. Glauber modeling in high energy nuclear collisions. *Ann.Rev.Nucl.Part.Sci.*, 57:205–243, 2007.

[18] B. Alver *et. al.* System size, energy, pseudorapidity, and centrality dependence of elliptic flow. *Phys. Rev. Lett.*, 98:242302, Jun 2007.

[19] B. Alver and G. Roland. Collision-geometry fluctuations and triangular flow in heavy-ion collisions. *Phys. Rev. C*, 81:054905, May 2010.

[20] K. Adcox *et. al.* Suppression of hadrons with large transverse momentum in central $au + au$ collisions at $\sqrt{s_{\rm NN}} = 130$GeV. *Phys. Rev. Lett.*, 88:022301, Dec 2001.

[21] C. Adler *et. al.* Centrality dependence of high-p_T hadron suppression in Au + Au collisions at $\sqrt{s_{NN}} = 130$GeV. *Phys. Rev. Lett.*, 89:202301, Oct 2002.

[22] J. D. Bjorken. Highly relativistic nucleus-nucleus collisions: The central rapidity region. *Phys. Rev. D*, 27:140–151, Jan 1983.

[23] Christopher Kelly. Continuum results for light hadrons from 2+1 flavour domain wall qcd, 2010. Ph.D. thesis.

[24] A. Bazavov, T. Bhattacharya, M. Cheng, N.H. Christ, C. DeTar, et al. Equation of state and QCD transition at finite temperature. *Phys.Rev.*, D80:014504, 2009.

[25] Peter F. Kolb and Ulrich W. Heinz. Hydrodynamic description of ultra-relativistic heavy ion collisions. 2003. arXiv:nucl-th/0305084.

[26] Jean-Yves Ollitrault. Relativistic hydrodynamics for heavy-ion collisions. *European Journal of Physics*, 29(2):275, 2008.

[27] John C. Collins, Davison E. Soper, and George F. Sterman. Factorization of Hard Processes in QCD. *Adv.Ser.Direct.High Energy Phys.*, 5:1–91, 1988.

[28] R. Baier, Yu.L. Dokshitzer, A.H. Mueller, S. Peign, and D. Schiff. Radiative energy loss of high energy quarks and gluons in a finite-volume quark-gluon plasma. *Nuclear Physics B*, 483(12):291 – 320, 1997.

[29] I.M. Vitev. Multiple parton interactions in dense QCD matter via the reaction operator approach, 2002. Ph.D. thesis.

[30] M. Gyulassy, P. Levai, and I. Vitev. Reaction operator approach to non-abelian energy loss. *Nuclear Physics B*, 594(12):371 – 419, 2001.

[31] Peter Arnold, Guy D. Moore, and Laurence G. Yaffe. Photon and gluon emission in relativistic plasmas. *Journal of High Energy Physics*, 2002(06):030, 2002.

[32] R. D. Field and R. P. Feynman. Quark elastic scattering as a source of high-transverse-momentum mesons. *Phys. Rev. D*, 15:2590–2616, May 1977.

[33] R.P. Feynman, R.D. Field, and G.C. Fox. Correlations among particles and jets produced with large transverse momenta. *Nuclear Physics B*, 128(1):1 – 65, 1977.

[34] S.S. Adler *et. al.* Jet properties from dihadron correlations in $p + p$ collisions at $\sqrt{s} = 200$ GeV. *Phys. Rev. D*, 74:072002, Oct 2006.

[35] C. Adler *et. al.* Disappearance of back-to-back high-p_T hadron correlations in central Au + Au collisions at $\sqrt{s_{NN}} = 200$ GeV. *Phys. Rev. Lett.*, 90:082302, Feb 2003.

[36] A. Adare *et. al.* Dihadron azimuthal correlations in au+au collisions at $\sqrt{s_{NN}} = 200$ gev. *Phys. Rev. C*, 78:014901, Jul 2008.

[37] B.I. Abelev et al. Long range rapidity correlations and jet production in high energy nuclear collisions. *Phys.Rev.*, C80:064912, 2009.

[38] A. Adare *et. al.* Medium modification of jet fragmentation in Au+Au collisions at $\sqrt{s_{NN}} = 200$ GeV measured in direct photon-hadron correlations. 2012. arXiv:1212.3323 [nucl-ex].

[39] S. Chatrchyan *et. al.* Studies of jet quenching using isolated-photon+jet correlations in PbPb and pp collisions at $\sqrt{s_{NN}} = 2.76$ TeV. *Physics Letters B*, 718(3):773 – 794, 2013.

[40] Thorsten Renk and Kari J. Eskola. Prospects of medium tomography using back-to-back hadron correlations. *Phys. Rev. C*, 75:054910, May 2007.

[41] H. Agakishiev *et. al.* Experimental studies of di-jet survival and surface emission bias in **Au+Au** collisions via angular correlations with respect to back-to-back leading hadrons. *Phys. Rev. C*, 83:061901, Jun 2011.

[42] Hua Pei. Studies of di-jets in Au+Au collisions using angular correlations with respect to back-to-back leading hadrons. 2012. arXiv/nucl-ex:1212.1653.

[43] Yue-Shi Lai and Brian A. Cole. Jet reconstruction in hadronic collisions by Gaussian filtering. 2008. arXiv:0806.1499 [nucl-ex].

[44] Yue-Shi Lai. Probing medium-induced energy loss with direct jet reconstruction in p+p and Cu+Cu collisions at PHENIX. *Nucl.Phys.*, A830:251C–254C, 2009.

[45] G. Aad *et. al.* Observation of a Centrality-Dependent Dijet Asymmetry in Lead-Lead Collisions at $\sqrt{s_{\rm NN}} = 2.76$ TeV with the ATLAS Detector at the LHC. *Phys. Rev. Lett.*, 105:252303, Dec 2010.

[46] S.S. Adler *et. al.* Jet structure from dihadron correlations in $d + \mathrm{Au}$ collisions at $\sqrt{s_{NN}} = 200$ gev. *Phys. Rev. C*, 73:054903, May 2006.

[47] M. Harrison, T. Ludlam, and S. Ozaki. RHIC project overview. *Nuclear Instruments and Methods in Physics Research Section A: Accelerators,*

Spectrometers, Detectors and Associated Equipment, 499(23):235 – 244, 2003.

[48] R. Middleton. A versatile high intensity negative ion source. *Nuclear Instruments and Methods in Physics Research*, 214(23):139 – 150, 1983.

[49] A.G. Ruggiero. Tandems as injectors for synchrotrons. *Nuclear Instruments and Methods in Physics Research Section A: Accelerators, Spectrometers, Detectors and Associated Equipment*, 328(12):3 – 9, 1993.

[50] P. Thieberger. Possible use of synchrotrons as post-acceleration boosters for tandems. *Nuclear Instruments and Methods in Physics Research*, 220(1):209 – 210, 1984.

[51] E.J.N. Wilson. *An Introduction to Particle Accelerators*. Oxford University Press, 2001.

[52] Mario Conte and William W. Mackay. *An Introduction to the Physics of Particle Accelerators*. World Scientific Publishing, 1991.

[53] Y.Y. Lee, D.S. Barton, J. Claus, J.G. Cottingham, E.D. Courant, et al. The AGS Booster Lattice. *Conf.Proc.*, C870316:865, 1987.

[54] W.T. Weng. Status of the AGS Booster Project. *First European Particle Accelerator Conference*, page 436, 1988.

[55] H. Hahn, E. Forsyth, H. Foelsche, M. Harrison, J. Kewisch, G. Parzen, S. Peggs, E. Raka, A. Ruggiero, A. Stevens, S. Tepikian, P. Thieberger, D. Trbojevic, J. Wei, E. Willen, S. Ozaki, and S.Y. Lee. The RHIC design overview. *Nuclear Instruments and Methods in Physics Research Section A: Accelerators, Spectrometers, Detectors and Associated Equipment*, 499(23):245 – 263, 2003.

[56] H. Akikawa *et. al.* PHENIX Muon Arms. *Nuclear Instruments and Methods in Physics Research Section A: Accelerators, Spectrometers, Detectors and Associated Equipment*, 499(23):537 – 548, 2003.

[57] M. Allen *et. al.* PHENIX inner detectors. *Nuclear Instruments and Methods in Physics Research Section A: Accelerators, Spectrometers, Detectors and Associated Equipment*, 499(23):549 – 559, 2003.

[58] Sasha Milov. Centrality determination using BBC in Au+Au and Cu+Cu collisions at $\sqrt{s_{NN}} = 200$ GeV. *PHENIX internal Analysis Note 461*, 2005.

[59] C Adler, A Denisov, E Garcia, M Murray, H Stroebele, and S White. The RHIC zero degree calorimeters. *Nuclear Instruments and Methods in Physics Research Section A: Accelerators, Spectrometers, Detectors and Associated Equipment*, 470(3):488 – 499, 2001.

[60] C. Adler, A. Denisov, E. Garcia, M. Murray, H. Strobele, and S. White. The RHIC zero-degree calorimeters. *Nuclear Instruments and Methods in Physics Research Section A: Accelerators, Spectrometers, Detectors and Associated Equipment*, 499(23):433 – 436, 2003.

[61] E. Richardson *et. al.* A reaction plane detector for PHENIX at RHIC. *Nuclear Instruments and Methods in Physics Research Section A: Accelerators, Spectrometers, Detectors and Associated Equipment*, 636(1):99 – 107, 2011.

[62] W. Blum, W. Riegler, and L. Rolandi. *Particle Detection with Drift Chambers*. Springer, 2008.

[63] Konrad Kleinknecht. *Detectors for particle radiation*. Cambridge University Press, 1998.

[64] K. Adcox *et. al.* {PHENIX} central arm tracking detectors. *Nuclear Instruments and Methods in Physics Research Section A: Accelerators, Spectrometers, Detectors and Associated Equipment*, 499(23):489 – 507, 2003. ¡ce:title¿The Relativistic Heavy Ion Collider Project: {RHIC} and its Detectors¡/ce:title¿.

[65] K. Adcox *et. al.* Construction and performance of the PHENIX pad chambers. *Nuclear Instruments and Methods in Physics Research Section A: Accelerators, Spectrometers, Detectors and Associated Equipment*, 497(23):263 – 293, 2003.

[66] M. Aizawa *et. al.* PHENIX central arm particle ID detectors. *Nuclear Instruments and Methods in Physics Research Section A: Accelerators, Spectrometers, Detectors and Associated Equipment*, 499(23):508 – 520, 2003.

[67] Claus Grupen. *Particle Detectors*. Cambridge University Press, 1996.

[68] J.T Mitchell and *et. al.* Event reconstruction in the PHENIX central arm spectrometers. *Nuclear Instruments and Methods in Physics Research Section A: Accelerators, Spectrometers, Detectors and Associated Equipment*, 482(12):491 – 512, 2002.

[69] L Aphecetche *et. al.* PHENIX calorimeter. *Nuclear Instruments and Methods in Physics Research Section A: Accelerators, Spectrometers, Detectors and Associated Equipment*, 499(23):521 – 536, 2003.

[70] D. Ben-Tzvi and M.B. Sandler. A combinatorial Hough transform. *Pattern Recognition Letters*, 11(3):167 – 174, 1990.

[71] Mattias Ohlsson, Carsten Peterson, and Alan L. Yuille. Track finding with deformable templates the elastic arms approach. *Computer Physics Communications*, 71(12):77 – 98, 1992.

[72] RHIC Run Overview. http://www.rhichome.bnl.gov/RHIC/Runs/. Accessed: 2013/03/02.

[73] K. Reygers. Glauber Monte-Carlo calculations for Au+Au collisions at $\sqrt{s_{NN}} = 200$ GeV. *PHENIX internal Analysis Note 169*, 2003.

[74] Paul Stankus. Notes on mixed event pairs. PHENIX Internal Physics Working Group presentation, 2012.

[75] S. Afanasiev and *et. al.* Systematic studies of elliptic flow measurements in Au + Au collisions at $\sqrt{s_{NN}} = 200$ GeV. *Phys. Rev. C*, 80:024909, Aug 2009.

[76] Eric Vazquez. Jet modification and a comparative study of hadron v_2 measurements in $\sqrt{s_{NN}} = 200$-GeV Au + Au collisions at RHIC-PHENIX. *Int.J.Mod.Phys.*, E16:1901–1905, 2007.

[77] Measurement of the azimuthal dependence of inclusive jet yields in Pb+Pb collisions at sqrt(s) = 2.76 TeV with the ATLAS detector. Technical Report ATLAS-CONF-2012-116, CERN, Geneva, Aug 2012.

[78] N. N. Ajitanand, J. M. Alexander, P. Chung, W. G. Holzmann, M. Issah, Roy A. Lacey, A. Shevel, A. Taranenko, and P. Danielewicz. Decomposition of harmonic and jet contributions to particle-pair correlations at ultrarelativistic energies. *Phys. Rev. C*, 72:011902, Jul 2005.

[79] A. Adare *et. al.* Single particle and embedding $h^{\pm}$ acceptance and efficiency corrections for central arm analyses in Run 6 and 7. *PHENIX internal Analysis Note 808*, 2009.

[80] Takahito Todoroki. Two particle correlation measurements at PHENIX. 2012.

[81] R. Wei *et. al.* Glauber calculations of centrality dependent varibales in Au+Au collisions at $\sqrt{s_{NN}}$ = 200 GeV (Run 7). *PHENIX internal Analysis Note 768*, 2009.

Appendix A

Distance-of-closest-approach

Here we demonstrate how to construct the DCA from reconstructed variables. For each track we construct a 3-vector from variables determined at the drift chamber reference radius ($\rho_{DC} = 220cm$) as shown in Figure A.1. We start by defining a vector $\mathbf{p}$ from the origin of the coordinate system to the position of the track at the drift chamber reference radius:

$$\begin{aligned} \mathbf{p} &= (p_x, p_y, p_z) && \text{(A.1)} \\ p_x &= \rho_{DC} \cos(\phi_{DC}) && \text{(A.2)} \\ p_y &= \rho_{DC} \sin(\phi_{DC}) && \text{(A.3)} \\ p_z &= z_{DC} && \text{(A.4)} \end{aligned}$$

We follow by creating another vector $\mathbf{n}$ which represents the direction of the track from the vector $\mathbf{p}$:

$$\begin{aligned} \mathbf{n} &= (n_x, n_y, n_z) && \text{(A.5)} \\ n_x &= \rho_{DC} \cos(\phi_{DC} - \alpha) && \text{(A.6)} \\ n_y &= \rho_{DC} \sin(\phi_{DC} - \alpha) && \text{(A.7)} \\ n_z &= \rho_{DC} / \tan(\beta) && \text{(A.8)} \end{aligned}$$

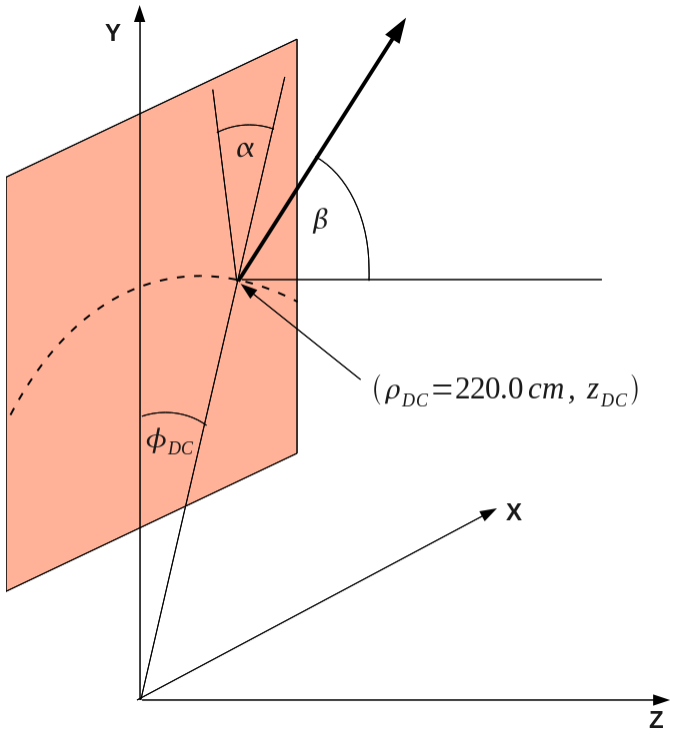

Figure A.1: Defining the variables used to construct 3-vector for each track

So, for a given track, we can use these two vectors to define a parametrized straight line representing the track:

$$\mathbf{f}(t) = \mathbf{p} + t\mathbf{n} \tag{A.9}$$

Now, we're in position to calculate the DCA for a given track pair:

$$\mathbf{f_1}(t) = \mathbf{p_1} + t\mathbf{n_1} \tag{A.10}$$

$$\mathbf{f_2}(s) = \mathbf{p_2} + s\mathbf{n_2} \tag{A.11}$$

We start by performing a translation of the coordinate system such that one of the tracks is a linear subspace of the coordinate system:

$$\mathbf{f_1'}(t) = \mathbf{f_1}(t) - \mathbf{p_1} = t\mathbf{n_1} \tag{A.12}$$

$$\mathbf{f_2'}(s) = \mathbf{f_2}(s) - \mathbf{p_1} = \mathbf{\Delta p} + s\mathbf{n_2} \tag{A.13}$$

$$\tag{A.14}$$

We determine the projection of $\mathbf{f_2}$ in the direction of $\mathbf{f_1}$:

$$\mathbf{r} = (\mathbf{f_2'}(s) \cdot \hat{\mathbf{n}}_\mathbf{1})\hat{\mathbf{n}}_\mathbf{1} \tag{A.15}$$

From here it becomes a minimization problem to determine the parameters

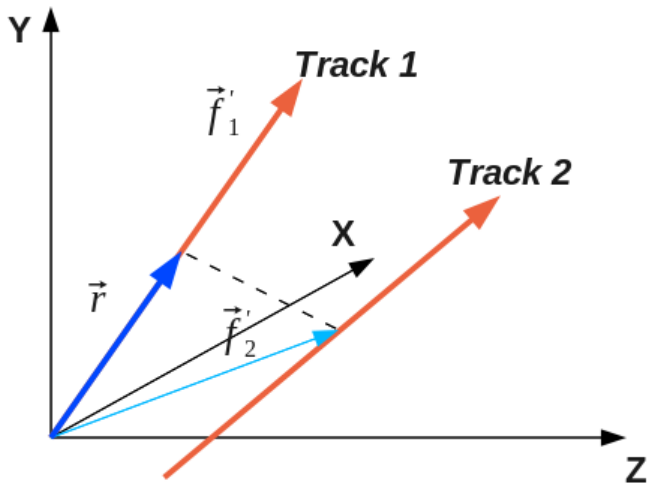

Figure A.2: Definition of variables after translation into local coordinate system.

t and s at the DCA:

$$\frac{d}{ds}\|\mathbf{r} - \mathbf{f_2'}\|^2 = 0 \tag{A.16}$$

The solutions are:

$$t_{_{DCA}} = \frac{\hat{\mathbf{n}}_{\mathbf{1}} \cdot \Delta\mathbf{p} - (\hat{\mathbf{n}}_{\mathbf{2}} \cdot \Delta\mathbf{p})(\hat{\mathbf{n}}_{\mathbf{1}} \cdot \hat{\mathbf{n}}_{\mathbf{2}})}{1 - (\hat{\mathbf{n}}_{\mathbf{1}} \cdot \hat{\mathbf{n}}_{\mathbf{2}})^2} \tag{A.17}$$

$$s_{_{DCA}} = \frac{\hat{\mathbf{n}}_{\mathbf{2}} \cdot \Delta\mathbf{p} - (\hat{\mathbf{n}}_{\mathbf{1}} \cdot \Delta\mathbf{p})(\hat{\mathbf{n}}_{\mathbf{2}} \cdot \hat{\mathbf{n}}_{\mathbf{1}})}{1 - (\hat{\mathbf{n}}_{\mathbf{1}} \cdot \hat{\mathbf{n}}_{\mathbf{2}})^2} \tag{A.18}$$

Now we define the DCA in the following manner:

$$\mathbf{r}_{\mathbf{DCA}} = \mathbf{f}_{\mathbf{2}}(s_{_{DCA}}) - \mathbf{f}_{\mathbf{1}}(t_{_{DCA}}) \tag{A.19}$$

$$DCA = \|\mathbf{f}_{\mathbf{2}}(s_{_{DCA}}) - \mathbf{f}_{\mathbf{1}}(t_{_{DCA}})\| \tag{A.20}$$

To determine the radial cylindrical distance from the origin ($\rho_{_{DCA}}$) to the DCA we average the perpendicular projections of the $\mathbf{f}_{\mathbf{1}}$ and $\mathbf{f}_{\mathbf{2}}$ vectors.

$$\rho_{_{DCA,1}} = (\mathbf{f}_{\mathbf{1}}(s_{_{DCA}}))_{\perp} \tag{A.21}$$

$$\rho_{_{DCA,2}} = (\mathbf{f}_{\mathbf{2}}(t_{_{DCA}}))_{\perp} \tag{A.22}$$

$$\rho_{_{DCA}} = \frac{\rho_{_{DCA,1}} + \rho_{_{DCA,2}}}{2} \tag{A.23}$$

Appendix B

Correlation background $B(\Delta\phi_{ta}, \Delta\phi_{tc})$ determination

To correct for heavy ion correlated background contribution in 2+1 correlations one has to perform a 3-particle convolution of single particle distributions with respect to the event plane (Ψ_n). The single particle distribution is given by:

$$\frac{dN}{d\phi} = \frac{N}{2\pi}\left\{1 + 2\sum_{n=1}^{\infty} v_n \cos\left[n(\phi - \Psi_{RP})\right]\right\} \tag{B.1}$$

In general for the measurement of N particles, the flow contribution is given by:

$$\begin{aligned}\frac{d^N N^{abc...N}}{d\Delta\phi_{ab}\Delta\phi_{ac}....\Delta\phi_{aN}} &= \int d\phi_a d\phi_b d\phi_c ... d\phi_N \frac{dN}{d\phi_a}\frac{dN}{d\phi_b}\frac{dN}{d\phi_c}...\frac{dN}{d\phi_N} \times \\ &\delta(\phi_a - \phi_b - \Delta\phi_{ab})\delta(\phi_a - \phi_c - \Delta\phi_{ac})....\delta(\phi_a - \phi_N - \Delta\phi_{aN})\end{aligned} \tag{B.2}$$

For this analysis, we're looking at the measurement of 3 particles which collapses the previous equation into the convolution of three single particle

distributions:

$$\frac{d^3N^{abc}}{d\Delta\phi_{ab}d\Delta\phi_{ac}} = \int d\phi_a d\phi_b d\phi_c \frac{dN}{d\phi_a}\frac{dN}{d\phi_b}\frac{dN}{d\phi_c} \times \delta(\phi_a - \phi_b - \Delta\phi_{ab})\delta(\phi_a - \phi_c - \Delta\phi_{ac}) \quad \text{(B.3)}$$

For the sake of simplicity, we can determine the elliptic flow contribution by truncating the distribution at v_2:

$$\frac{dN}{d\phi} \simeq \frac{N}{2\pi}\left\{1 + 2v_2\cos[2(\phi - \Psi_{RP})]\right\} \quad \text{(B.4)}$$

Therefore the three particle elliptic flow contribution is given by:

$$\begin{aligned}\frac{d^3N^{abc}}{d\Delta\phi_{ab}d\Delta\phi_{ac}} = {} & \frac{N^aN^bN^c}{8\pi^3}\int d\phi_a d\phi_b d\phi_c \left\{1 + 2v_2^a\cos\left[2(\phi_a - \Psi_{RP})\right]\right\} \times \\ & \left\{1 + 2v_2^b\cos[2(\phi_b - \Psi_{RP})]\right\}\left\{1 + 2v_2^c\cos[2(\phi_c - \Psi_{RP})]\right\} \times \\ & \delta(\phi_a - \phi_b - \Delta\phi_{ab})\delta(\phi_a - \phi_c - \Delta\phi_{ac}) \end{aligned} \quad \text{(B.5)}$$

Integrating with respect to ϕ_b and ϕ_c (i.e. removing the δ-functions), we get:

$$\begin{aligned}\frac{d^3N^{abc}}{d\Delta\phi_{ab}d\Delta\phi_{ac}} = {} & \frac{N^aN^bN^c}{8\pi^3}\int d\phi_a \left\{1 + 2v_2^a\cos\left[2(\phi_a - \Psi_{RP})\right]\right\} \times \\ & \left\{1 + 2v_2^b\cos[2(\phi_a - \Delta\phi_{ab} - \Psi_{RP})]\right\} \times \\ & \left\{1 + 2v_2^c\cos[2(\phi_a - \Delta\phi_{ac} - \Psi_{RP})]\right\} \end{aligned} \quad \text{(B.6)}$$

Expanding out all terms:

$$\begin{aligned}\frac{d^3N^{abc}}{d\Delta\phi_{ab}d\Delta\phi_{ac}} = {} & \frac{N^aN^bN^c}{8\pi^3}\int d\phi_a \{1 + 2v_2^a\cos\left[2(\phi_a - \Psi_{RP})\right] + \\ & 2v_2^b\cos[2(\phi_a - \Delta\phi_{ab} - \Psi_{RP})] + 2v_2^c\cos[2(\phi_a - \Delta\phi_{ac} - \Psi_{RP})] + \\ & 4v_2^av_2^b\cos\left[2(\phi_a - \Psi_{RP})\right]\cos[2(\phi_a - \Delta\phi_{ab} - \Psi_{RP})] + \end{aligned}$$

$$4v_2^a v_2^c \cos\left[2(\phi_a - \Psi_{RP})\right] \cos[2(\phi_a - \Delta\phi_{ac} - \Psi_{RP})] + 4v_2^b v_2^c \cos\left[2(\phi_a - \Delta\phi_{ab} - \Psi_{RP})\right] \cos[2(\phi_a - \Delta\phi_{ac} - \Psi_{RP})] + 8v_2^a v_2^b v_2^c \cos\left[2(\phi_a - \Psi_{RP})\right] \cos\left[2(\phi_a - \Delta\phi_{ab} - \Psi_{RP})\right] \times \cos[2(\phi_a - \Delta\phi_{ac} - \Psi_{RP})]\} \tag{B.7}$$

To simplify the above integral we will note the following:

$$\int_0^{2\pi} dx \cos(nx + C) = 0 \tag{B.8}$$

where n is an integer and C = constant. We will also employ the following trigonometric identity:

$$\cos(A)\cos(B) = \frac{1}{2}\left[\cos(A - B) + \cos(A + B)\right] \tag{B.9}$$

Using (B.8) the linear terms of (B.7) vanish:

$$\frac{d^3N^{abc}}{d\Delta\phi_{ab}d\Delta\phi_{ac}} = \frac{N^a N^b N^c}{8\pi^3}\int d\phi_a\{1 + 4v_2^a v_2^b \cos\left[2(\phi_a - \Psi_{RP})\right] \cos[2(\phi_a - \Delta\phi_{ab} - \Psi_{RP})] + 4v_2^a v_2^c \cos\left[2(\phi_a - \Psi_{RP})\right] \cos[2(\phi_a - \Delta\phi_{ac} - \Psi_{RP})] + 4v_2^b v_2^c \cos\left[2(\phi_a - \Delta\phi_{ab} - \Psi_{RP})\right] \cos[2(\phi_a - \Delta\phi_{ac} - \Psi_{RP})] + 8v_2^a v_2^b v_2^c \cos\left[2(\phi_a - \Psi_{RP})\right] \cos\left[2(\phi_a - \Delta\phi_{ab} - \Psi_{RP})\right] \times \cos[2(\phi_a - \Delta\phi_{ac} - \Psi_{RP})]\} \tag{B.10}$$

Using the trigonometric identity (B.9), we expand the second order terms:

$$\cos\left[2(\phi_a - \Psi_{RP})\right] \cos[2(\phi_a - \Delta\phi_{ab} - \Psi_{RP})] = \frac{1}{2}\left\{\cos\left(2\Delta\phi_{ab}\right) + \cos\left(4\phi_a - 2\Delta\phi_{ab} - 4\Psi_{RP}\right)\right\} \tag{B.11}$$

$$\cos\left[2(\phi_a - \Psi_{RP})\right] \cos[2(\phi_a - \Delta\phi_{ac} - \Psi_{RP})] =$$

$$\frac{1}{2}\{\cos(2\Delta\phi_{ac}) + \cos(4\phi_a - 2\Delta\phi_{ac} - 4\Psi_{RP})\} \tag{B.12}$$

$$\cos[2(\phi_a - \Delta\phi_{ab} - \Psi_{RP})]\cos[2(\phi_a - \Delta\phi_{ac} - \Psi_{RP})] = \frac{1}{2}\{\cos(2\Delta\phi_{ab} - 2\Delta\phi_{ac}) + \cos(4\phi_a - 2\Delta\phi_{ab} - 2\Delta\phi_{ac} - 4\Psi_{RP})\} \tag{B.13}$$

For each expansion above, the second term vanishes because of (B.8). Therefore, we've simplified the expansion to the following form:

$$\begin{aligned}\frac{d^3N^{abc}}{d\Delta\phi_{ab}d\Delta\phi_{ac}} = \frac{N^aN^bN^c}{8\pi^3}\int d\phi_a\{1 + 2v_2^av_2^b\cos(2\Delta\phi_{ab}) + \\ 2v_2^av_2^c\cos(2\Delta\phi_{ac}) + 2v_2^bv_2^c\cos(2\Delta\phi_{ab} - 2\Delta\phi_{ac}) + \\ 8v_2^av_2^bv_2^c\cos[2(\phi_a - \Psi_{RP})]\cos[2(\phi_a - \Delta\phi_{ab} - \Psi_{RP})] \times \\ \cos[2(\phi_a - \Delta\phi_{ac} - \Psi_{RP})]\}\end{aligned} \tag{B.14}$$

The last step is to expand the cubic term:

$$\begin{aligned}\cos[2(\phi_a - \Psi_{RP})]\cos[2(\phi_a - \Delta\phi_{ab} - \Psi_{RP})]\cos[2(\phi_a - \Delta\phi_{ac} - \Psi_{RP})] = \\ \frac{1}{4}\{\cos(-2\phi_a + 2\Delta\phi_{ab} + 2\Delta\phi_{ac} + 2\Psi_{RP}) + \\ \cos(2\phi_a + 2\Delta\phi_{ab} - 2\Delta\phi_{ac} + 2\Psi_{RP}) + \\ \cos(2\phi_a - 2\Delta\phi_{ab} + 2\Delta\phi_{ac} - 2\Psi_{RP}) + \\ \cos(6\phi_a - 2\Delta\phi_{ab} - 2\Delta\phi_{ac} - 6\Psi_{RP})\}\end{aligned} \tag{B.15}$$

But because of (B.8), all of these terms vanish, hence there are no cubic terms contributing to the 3-particle elliptic flow:

$$\begin{aligned}\frac{d^3N^{abc}}{d\Delta\phi_{ab}d\Delta\phi_{ac}} = \frac{N^aN^bN^c}{8\pi^3}\int d\phi_a\{1 + 2v_2^av_2^b\cos(2\Delta\phi_{ab}) + \\ 2v_2^av_2^c\cos(2\Delta\phi_{ac}) + 2v_2^bv_2^c\cos(2\Delta\phi_{ab} - 2\Delta\phi_{ac})\}\end{aligned}$$

$$= \frac{N^a N^b N^c}{4\pi^2}\{1 + 2v_2^a v_2^b \cos(2\Delta\phi_{ab}) + 2v_2^a v_2^c \cos(2\Delta\phi_{ac}) + 2v_2^b v_2^c \cos(2\Delta\phi_{ab} - 2\Delta\phi_{ac})\} \quad \text{(B.16)}$$

$$= B(\Delta\phi_{ta}, \Delta\phi_{tc}) \quad \text{(B.17)}$$

If the ZYAM method is used to subtract $B(\Delta\phi_{ta}, \Delta\phi_{tc})$ from $C(\Delta\phi_{ta}, \Delta\phi_{tc})$, then $\frac{N^a N^b N^c}{4\pi^2} \longrightarrow \xi$ and ξ is used as a free parameter to be determined by the ZYAM method (see Section 5.8).

B.1 generalization of $B(\Delta\phi_{ta}, \Delta\phi_{tc})$ for higher harmonics

The same procedure can be followed to include higher order harmonics (or a much more sane suggestion would be to plug it into Mathematica). The general formula to include all harmonics:

$$\frac{d^3N^{abc}}{d\Delta\phi_{ab}d\Delta\phi_{ac}} = \frac{N^a N^b N^c}{4\pi^2}\left\{1 + 2\sum_n v_n^a v_n^b \cos(n\Delta\phi_{ab}) + v_n^a v_n^c \cos(n\Delta\phi_{ac}) + v_n^c v_n^b \cos(n[\Delta\phi_{ab} - \Delta\phi_{ac}])\right\} \quad \text{(B.18)}$$

In this analysis, we project out the *pair* $\Delta\phi_{ta}$ axis and select for a selected range in $\Delta\phi_{tc}$. If a $\Delta\phi_{ac}$ bin range is selected of size c and bin center of $\Delta\phi'_{ac}$ the formula becomes:

$$\frac{dN^{ab}}{d\Delta\phi_{ab}}\Big|_{\Delta\phi'_{ac}} = \frac{1}{c}\int_{\Delta\phi'_{ac}-\frac{c}{2}}^{\Delta\phi'_{ac}+\frac{c}{2}} d\Delta\phi_{ac} \quad \frac{d^3N^{abc}}{d\Delta\phi_{ab}d\Delta\phi_{ac}}$$

$$= \frac{N^a N^b N^c}{4\pi^2}\left\{1 + 2\sum_n v_n^a v_n^b \cos(n\Delta\phi_{ab}) + v_n^a v_n^c \cos(n\Delta\phi'_{ac})\text{sinc}\left(\frac{nc}{2}\right) + v_n^b v_n^c \cos(n[\Delta\phi'_{ac} - \Delta\phi_{ab}])\text{sinc}\left(\frac{nc}{2}\right)\right\} \quad \text{(B.19)}$$

Appendix C

$J(\Delta\phi_{ta})$ Correlations Data Tables

Table C.1: **Two-particle p+p jet-induced correlation for $p_{T,\mathrm{trig}}$: 2-3 GeV/c.**

$p_{T,\mathrm{assoc}}$	$\Delta\phi$	$J(\Delta\phi_{ta})$	**Stat. Error**	**Syst. Error**
0.4-1 GeV/c	-3.04	0.01477	6.9×10^{-5}	-0.0002 +0.0002
	-2.85	0.01419	7.1×10^{-5}	-0.00018 +0.00018
	-2.65	0.01243	7.2×10^{-5}	-0.00016 +0.00016
	-2.45	0.01005	7.1×10^{-5}	-0.00014 +0.00014
	-2.26	0.007753	7.2×10^{-5}	-0.00012 +0.00012
	-2.06	0.005739	7.8×10^{-5}	-0.00011 +0.00011
	-1.87	0.003641	8.3×10^{-5}	-9.9×10^{-5} $+9.9 \times 10^{-5}$
	-1.67	0.001386	7.9×10^{-5}	-9.4×10^{-5} $+9.4 \times 10^{-5}$
	-1.47	-9.233×10^{-7}	7.2×10^{-5}	-8.9×10^{-5} $+8.9 \times 10^{-5}$
	-1.28	-0.0001187	7.1×10^{-5}	-8.5×10^{-5} $+8.5 \times 10^{-5}$
	-1.08	0.0006226	7.2×10^{-5}	-8.6×10^{-5} $+8.6 \times 10^{-5}$
	-0.88	0.002294	6.7×10^{-5}	-9.2×10^{-5} $+9.2 \times 10^{-5}$

Table C.1 – (p+p, $p_{T,\text{trig}}$: 2-3 GeV/c)continued from previous page

$p_{T,\text{assoc}}$	$\Delta\phi$	$J(\Delta\phi_{ta})$	**Stat. Error**	**Syst. Error**
	-0.69	0.005191	6.1×10^{-5}	-9.9×10^{-5} $+9.9 \times 10^{-5}$
	-0.49	0.01088	6.3×10^{-5}	-0.00012 +0.00012
	-0.29	0.01614	6.8×10^{-5}	-0.00015 +0.00015
	-0.10	0.01978	6.9×10^{-5}	-0.00018 +0.00018
	0.10	0.02039	7×10^{-5}	-0.00018 +0.00018
	0.29	0.01735	7.1×10^{-5}	-0.00015 +0.00015
	0.49	0.01176	6.9×10^{-5}	-0.00012 +0.00012
	0.69	0.006174	6.9×10^{-5}	-9.9×10^{-5} $+9.9 \times 10^{-5}$
	0.88	0.003246	7.6×10^{-5}	-9.2×10^{-5} $+9.2 \times 10^{-5}$
	1.08	0.0009616	7.6×10^{-5}	-8.6×10^{-5} $+8.6 \times 10^{-5}$
	1.28	-2.019×10^{-5}	7.2×10^{-5}	-8.5×10^{-5} $+8.5 \times 10^{-5}$
	1.47	0.0004138	7.3×10^{-5}	-8.9×10^{-5} $+8.9 \times 10^{-5}$
	1.67	0.001275	7.8×10^{-5}	-9.4×10^{-5} $+9.4 \times 10^{-5}$
	1.87	0.003203	8×10^{-5}	-9.9×10^{-5} $+9.9 \times 10^{-5}$
	2.06	0.004911	7.3×10^{-5}	-0.00011 +0.00011
	2.26	0.007208	7×10^{-5}	-0.00012 +0.00012
	2.45	0.01003	7.2×10^{-5}	-0.00014 +0.00014
	2.65	0.01249	7.3×10^{-5}	-0.00016 +0.00016
	2.85	0.0141	7.2×10^{-5}	-0.00018 +0.00018
	3.04	0.01478	6.9×10^{-5}	-0.0002 +0.0002
1-2 GeV/c	-3.04	0.008646	3.8×10^{-5}	-5.2×10^{-5} $+5.2 \times 10^{-5}$
	-2.85	0.007976	3.7×10^{-5}	-4.5×10^{-5} $+4.5 \times 10^{-5}$
	-2.65	0.006612	3.7×10^{-5}	-3.6×10^{-5} $+3.6 \times 10^{-5}$
	-2.45	0.005056	3.7×10^{-5}	-2.8×10^{-5} $+2.8 \times 10^{-5}$
	-2.26	0.003747	3.7×10^{-5}	-2.5×10^{-5} $+2.5 \times 10^{-5}$
	-2.06	0.002655	3.8×10^{-5}	-2.4×10^{-5} $+2.4 \times 10^{-5}$
	-1.87	0.001863	4×10^{-5}	-2.2×10^{-5} $+2.2 \times 10^{-5}$

Table C.1 – (p+p, $p_{T,\text{trig}}$: 2-3 GeV/c)continued from previous page

$p_{T,\text{assoc}}$	$\Delta\phi$	$J(\Delta\phi_{ta})$	**Stat. Error**	**Syst. Error**
	-1.67	0.0009439	4.1×10^{-5}	-2×10^{-5} $+2 \times 10^{-5}$
	-1.47	3.731×10^{-5}	4.1×10^{-5}	-1.8×10^{-5} $+1.8 \times 10^{-5}$
	-1.28	-0.0003278	3.6×10^{-5}	-1.7×10^{-5} $+1.7 \times 10^{-5}$
	-1.08	-0.0002672	3.1×10^{-5}	-1.7×10^{-5} $+1.7 \times 10^{-5}$
	-0.88	0.0003374	2.9×10^{-5}	-1.9×10^{-5} $+1.9 \times 10^{-5}$
	-0.69	0.002118	3×10^{-5}	-2.4×10^{-5} $+2.4 \times 10^{-5}$
	-0.49	0.00501	3.3×10^{-5}	-2.7×10^{-5} $+2.7 \times 10^{-5}$
	-0.29	0.01061	3.7×10^{-5}	-3.5×10^{-5} $+3.5 \times 10^{-5}$
	-0.10	0.01489	4×10^{-5}	-5.6×10^{-5} $+5.6 \times 10^{-5}$
	0.10	0.0152	4.1×10^{-5}	-5.6×10^{-5} $+5.6 \times 10^{-5}$
	0.29	0.01151	4×10^{-5}	-3.5×10^{-5} $+3.5 \times 10^{-5}$
	0.49	0.005963	3.6×10^{-5}	-2.7×10^{-5} $+2.7 \times 10^{-5}$
	0.69	0.003035	3.5×10^{-5}	-2.4×10^{-5} $+2.4 \times 10^{-5}$
	0.88	0.001282	3.5×10^{-5}	-1.9×10^{-5} $+1.9 \times 10^{-5}$
	1.08	0.0004353	3.6×10^{-5}	-1.7×10^{-5} $+1.7 \times 10^{-5}$
	1.28	-8.479×10^{-5}	3.8×10^{-5}	-1.7×10^{-5} $+1.7 \times 10^{-5}$
	1.47	-0.0002144	3.8×10^{-5}	-1.8×10^{-5} $+1.8 \times 10^{-5}$
	1.67	0.0003712	3.6×10^{-5}	-2×10^{-5} $+2 \times 10^{-5}$
	1.87	0.001057	3.5×10^{-5}	-2.2×10^{-5} $+2.2 \times 10^{-5}$
	2.06	0.002095	3.5×10^{-5}	-2.4×10^{-5} $+2.4 \times 10^{-5}$
	2.26	0.003324	3.5×10^{-5}	-2.5×10^{-5} $+2.5 \times 10^{-5}$
	2.45	0.004765	3.6×10^{-5}	-2.8×10^{-5} $+2.8 \times 10^{-5}$
	2.65	0.00647	3.6×10^{-5}	-3.6×10^{-5} $+3.6 \times 10^{-5}$
	2.85	0.007958	3.7×10^{-5}	-4.5×10^{-5} $+4.5 \times 10^{-5}$
	3.04	0.008676	3.8×10^{-5}	-5.2×10^{-5} $+5.2 \times 10^{-5}$
2-3 GeV/c	-3.04	0.002428	1.7×10^{-5}	-1.7×10^{-5} $+1.7 \times 10^{-5}$
	-2.85	0.002131	1.6×10^{-5}	-1.3×10^{-5} $+1.3 \times 10^{-5}$

Table C.1 – (p+p, $p_{T,\text{trig}}$: 2-3 GeV/c)continued from previous page

$p_{T,\text{assoc}}$	$\Delta\phi$	$J(\Delta\phi_{ta})$	**Stat. Error**	**Syst. Error**
	-2.65	0.00161	1.5×10^{-5}	-9.4×10^{-6} $+9.4 \times 10^{-6}$
	-2.45	0.001115	1.5×10^{-5}	-7.6×10^{-6} $+7.6 \times 10^{-6}$
	-2.26	0.000776	1.5×10^{-5}	-7.3×10^{-6} $+7.3 \times 10^{-6}$
	-2.06	0.0005358	1.5×10^{-5}	-6.6×10^{-6} $+6.6 \times 10^{-6}$
	-1.87	0.0003324	1.4×10^{-5}	-5.5×10^{-6} $+5.5 \times 10^{-6}$
	-1.67	0.0002127	1.6×10^{-5}	-4.7×10^{-6} $+4.7 \times 10^{-6}$
	-1.47	5.82×10^{-5}	1.6×10^{-5}	-4.3×10^{-6} $+4.3 \times 10^{-6}$
	-1.28	-0.0001379	1.3×10^{-5}	-4.2×10^{-6} $+4.2 \times 10^{-6}$
	-1.08	-0.0001467	1×10^{-5}	-4.2×10^{-6} $+4.2 \times 10^{-6}$
	-0.88	-7.43×10^{-5}	9.9×10^{-6}	-4.3×10^{-6} $+4.3 \times 10^{-6}$
	-0.69	0.0002475	1.1×10^{-5}	-5.5×10^{-6} $+5.5 \times 10^{-6}$
	-0.49	0.001019	1.3×10^{-5}	-8.8×10^{-6} $+8.8 \times 10^{-6}$
	-0.29	0.003153	1.6×10^{-5}	-9.9×10^{-6} $+9.9 \times 10^{-6}$
	-0.10	0.005616	2×10^{-5}	-2×10^{-5} $+2 \times 10^{-5}$
	0.10	0.005906	2.1×10^{-5}	-2×10^{-5} $+2 \times 10^{-5}$
	0.29	0.003487	1.8×10^{-5}	-9.9×10^{-6} $+9.9 \times 10^{-6}$
	0.49	0.0013	1.4×10^{-5}	-8.8×10^{-6} $+8.8 \times 10^{-6}$
	0.69	0.0005241	1.3×10^{-5}	-5.5×10^{-6} $+5.5 \times 10^{-6}$
	0.88	0.0001968	1.3×10^{-5}	-4.3×10^{-6} $+4.3 \times 10^{-6}$
	1.08	0.0001128	1.3×10^{-5}	-4.2×10^{-6} $+4.2 \times 10^{-6}$
	1.28	8.088×10^{-6}	1.5×10^{-5}	-4.2×10^{-6} $+4.2 \times 10^{-6}$
	1.47	-8.562×10^{-5}	1.4×10^{-5}	-4.3×10^{-6} $+4.3 \times 10^{-6}$
	1.67	-3.22×10^{-5}	1.3×10^{-5}	-4.7×10^{-6} $+4.7 \times 10^{-6}$
	1.87	0.0001134	1.2×10^{-5}	-5.5×10^{-6} $+5.5 \times 10^{-6}$
	2.06	0.0003386	1.3×10^{-5}	-6.6×10^{-6} $+6.6 \times 10^{-6}$
	2.26	0.0006488	1.4×10^{-5}	-7.3×10^{-6} $+7.3 \times 10^{-6}$
	2.45	0.001023	1.4×10^{-5}	-7.6×10^{-6} $+7.6 \times 10^{-6}$

Table C.1 – (p+p, $p_{T,\text{trig}}$: 2-3 GeV/c)continued from previous page

$p_{T,\text{assoc}}$	$\Delta\phi$	$J(\Delta\phi_{ta})$	**Stat. Error**	**Syst. Error**
	2.65	0.001548	1.5×10^{-5}	-9.4×10^{-6} $+9.4 \times 10^{-6}$
	2.85	0.002139	1.6×10^{-5}	-1.3×10^{-5} $+1.3 \times 10^{-5}$
	3.04	0.002467	1.7×10^{-5}	-1.7×10^{-5} $+1.7 \times 10^{-5}$
3-5 GeV/c	-3.04	0.001188	1.1×10^{-5}	-9.2×10^{-6} $+9.2 \times 10^{-6}$
	-2.85	0.0009667	1×10^{-5}	-6.6×10^{-6} $+6.6 \times 10^{-6}$
	-2.65	0.0006626	9×10^{-6}	-4.2×10^{-6} $+4.2 \times 10^{-6}$
	-2.45	0.0004167	8.2×10^{-6}	-3.9×10^{-6} $+3.9 \times 10^{-6}$
	-2.26	0.0002548	7.9×10^{-6}	-3.6×10^{-6} $+3.6 \times 10^{-6}$
	-2.06	0.000162	7.5×10^{-6}	-2.8×10^{-6} $+2.8 \times 10^{-6}$
	-1.87	0.0001051	7.3×10^{-6}	-2.1×10^{-6} $+2.1 \times 10^{-6}$
	-1.67	6.665×10^{-5}	8.1×10^{-6}	-1.9×10^{-6} $+1.9 \times 10^{-6}$
	-1.47	1.631×10^{-5}	8.1×10^{-6}	-1.8×10^{-6} $+1.8 \times 10^{-6}$
	-1.28	-5.518×10^{-5}	6×10^{-6}	-1.8×10^{-6} $+1.8 \times 10^{-6}$
	-1.08	-5.862×10^{-5}	4.9×10^{-6}	-1.8×10^{-6} $+1.8 \times 10^{-6}$
	-0.88	-4.499×10^{-5}	4.6×10^{-6}	-1.8×10^{-6} $+1.8 \times 10^{-6}$
	-0.69	5.593×10^{-5}	5.4×10^{-6}	-2.1×10^{-6} $+2.1 \times 10^{-6}$
	-0.49	0.0003127	6.6×10^{-6}	-4.3×10^{-6} $+4.3 \times 10^{-6}$
	-0.29	0.001239	9.5×10^{-6}	-5.4×10^{-6} $+5.4 \times 10^{-6}$
	-0.10	0.002691	1.3×10^{-5}	-1.2×10^{-5} $+1.2 \times 10^{-5}$
	0.10	0.002887	1.4×10^{-5}	-1.2×10^{-5} $+1.2 \times 10^{-5}$
	0.29	0.001369	1×10^{-5}	-5.4×10^{-6} $+5.4 \times 10^{-6}$
	0.49	0.0004349	7.8×10^{-6}	-4.3×10^{-6} $+4.3 \times 10^{-6}$
	0.69	0.0001597	6.8×10^{-6}	-2.1×10^{-6} $+2.1 \times 10^{-6}$
	0.88	6.086×10^{-5}	6.3×10^{-6}	-1.8×10^{-6} $+1.8 \times 10^{-6}$
	1.08	2.686×10^{-5}	6.6×10^{-6}	-1.8×10^{-6} $+1.8 \times 10^{-6}$
	1.28	-3.55×10^{-6}	7.2×10^{-6}	-1.8×10^{-6} $+1.8 \times 10^{-6}$
	1.47	-4.76×10^{-5}	6.6×10^{-6}	-1.8×10^{-6} $+1.8 \times 10^{-6}$

Table C.1 – (p+p, $p_{T,\text{trig}}$: 2-3 GeV/c)continued from previous page

$p_{T,\text{assoc}}$	$\Delta\phi$	$J(\Delta\phi_{ta})$	**Stat. Error**	**Syst. Error**
	1.67	-2.757×10^{-5}	6×10^{-6}	-1.9 $\times10^{-6}$ +1.9 $\times10^{-6}$
	1.87	2.791×10^{-5}	5.9×10^{-6}	-2.1 $\times10^{-6}$ +2.1 $\times10^{-6}$
	2.06	8.189×10^{-5}	6.2×10^{-6}	-2.8 $\times10^{-6}$ +2.8 $\times10^{-6}$
	2.26	0.00022	7.3×10^{-6}	-3.6 $\times10^{-6}$ +3.6 $\times10^{-6}$
	2.45	0.0003794	7.8×10^{-6}	-3.9 $\times10^{-6}$ +3.9 $\times10^{-6}$
	2.65	0.0006384	8.6×10^{-6}	-4.2 $\times10^{-6}$ +4.2 $\times10^{-6}$
	2.85	0.0009614	1×10^{-5}	-6.6 $\times10^{-6}$ +6.6 $\times10^{-6}$
	3.04	0.001217	1.1×10^{-5}	-9.2 $\times10^{-6}$ +9.2 $\times10^{-6}$

Table C.2: **Two-particle 0-20% Au+Au jet-induced correlation for $p_{T,\mathrm{trig}}$: 2-3 GeV/c.**

$p_{T,\mathrm{assoc}}$	$\Delta\phi$	$J(\Delta\phi_{ta})$	**Stat. Error**	**Syst. Error**
0.4-1 GeV/c	-3.04	0.01099	9.7×10^{-5}	-0.00038 +0.00038
	-2.85	0.008508	9.8×10^{-5}	-0.00035 +0.00035
	-2.65	0.006431	0.0001	-0.00031 +0.00031
	-2.45	0.005982	0.00011	-0.00026 +0.00026
	-2.26	0.005695	0.00013	-0.00023 +0.00023
	-2.06	0.005442	0.00014	-0.00021 +0.00021
	-1.87	0.003906	0.00017	-0.00019 +0.00019
	-1.67	0.003251	0.00021	-0.00018 +0.00018
	-1.47	0.00161	0.00023	-0.00017 +0.00017
	-1.28	0.0004741	0.00018	-0.00017 +0.00017
	-1.08	-5.87×10^{-5}	0.00014	-0.00017 +0.00017
	-0.88	0.0001672	0.00012	-0.00018 +0.00018
	-0.69	0.003124	0.00011	-0.00019 +0.00019
	-0.49	0.007157	0.0001	-0.00023 +0.00023
	-0.29	0.01414	9.4×10^{-5}	-0.00029 +0.00029
	-0.10	0.01724	9.9×10^{-5}	-0.00035 +0.00035
	0.10	0.01734	0.0001	-0.00035 +0.00035
	0.29	0.01397	9.4×10^{-5}	-0.00029 +0.00029
	0.49	0.00713	0.0001	-0.00023 +0.00023
	0.69	0.002962	0.00011	-0.00019 +0.00019
	0.88	0.0003007	0.00012	-0.00018 +0.00018
	1.08	-0.0003245	0.00014	-0.00017 +0.00017
	1.28	9.941×10^{-5}	0.00018	-0.00017 +0.00017
	1.47	0.001357	0.00021	-0.00017 +0.00017
	1.67	0.002589	0.00021	-0.00018 +0.00018

Table C.2 – (0-20% Au+Au, $p_{T,\mathrm{trig}}$: 2-3 GeV/c) continued from previous page

$p_{T,\mathrm{assoc}}$	$\Delta\phi$	$J(\Delta\phi_{ta})$	**Stat. Error**	**Syst. Error**
	1.87	0.004074	0.00017	-0.00019 +0.00019
	2.06	0.005201	0.00014	-0.00021 +0.00021
	2.26	0.005817	0.00013	-0.00023 +0.00023
	2.45	0.00601	0.00011	-0.00026 +0.00026
	2.65	0.006443	0.0001	-0.00031 +0.00031
	2.85	0.008778	9.7×10^{-5}	-0.00035 +0.00035
	3.04	0.01135	9.6×10^{-5}	-0.00038 +0.00038
1-2 GeV/c	-3.04	0.003947	4.4×10^{-5}	-0.00032 +0.00032
	-2.85	0.003241	4.5×10^{-5}	-0.00031 +0.00031
	-2.65	0.002468	4.6×10^{-5}	-0.00028 +0.00028
	-2.45	0.002587	5.1×10^{-5}	-0.00025 +0.00025
	-2.26	0.002755	5.7×10^{-5}	-0.00023 +0.00023
	-2.06	0.002669	6.8×10^{-5}	-0.0002 +0.0002
	-1.87	0.002523	7.7×10^{-5}	-0.00019 +0.00019
	-1.67	0.002005	9.8×10^{-5}	-0.00017 +0.00017
	-1.47	0.001305	0.00011	-0.00017 +0.00017
	-1.28	0.0002853	8×10^{-5}	-0.00016 +0.00016
	-1.08	-0.0003127	6.5×10^{-5}	-0.00016 +0.00016
	-0.88	8.485×10^{-5}	5.4×10^{-5}	-0.00016 +0.00016
	-0.69	0.001567	5.1×10^{-5}	-0.00017 +0.00017
	-0.49	0.004248	4.6×10^{-5}	-0.00019 +0.00019
	-0.29	0.006994	4.4×10^{-5}	-0.00023 +0.00023
	-0.10	0.01016	4.5×10^{-5}	-0.00026 +0.00026
	0.10	0.01016	4.6×10^{-5}	-0.00026 +0.00026
	0.29	0.007	4.4×10^{-5}	-0.00023 +0.00023
	0.49	0.004265	4.7×10^{-5}	-0.00019 +0.00019
	0.69	0.001674	5.1×10^{-5}	-0.00017 +0.00017

Table C.2 – (0-20% Au+Au, $p_{T,\text{trig}}$: 2-3 GeV/c) continued from previous page

$p_{T,\text{assoc}}$	$\Delta\phi$	$J(\Delta\phi_{ta})$	**Stat. Error**	**Syst. Error**
	0.88	0.0002238	5.4×10^{-5}	-0.00016 +0.00016
	1.08	-0.0002071	6.5×10^{-5}	-0.00016 +0.00016
	1.28	0.0003728	8.1×10^{-5}	-0.00016 +0.00016
	1.47	0.00125	0.00011	-0.00017 +0.00017
	1.67	0.002096	9.8×10^{-5}	-0.00017 +0.00017
	1.87	0.002526	7.7×10^{-5}	-0.00019 +0.00019
	2.06	0.002731	6.8×10^{-5}	-0.0002 +0.0002
	2.26	0.002717	5.7×10^{-5}	-0.00023 +0.00023
	2.45	0.002625	5.1×10^{-5}	-0.00025 +0.00025
	2.65	0.002499	4.6×10^{-5}	-0.00028 +0.00028
	2.85	0.003143	4.5×10^{-5}	-0.00031 +0.00031
	3.04	0.004032	4.4×10^{-5}	-0.00032 +0.00032
2-3 GeV/c	-3.04	0.0003141	1.2×10^{-5}	-6.5×10^{-5} $+6.5 \times 10^{-5}$
	-2.85	0.0002307	1.2×10^{-5}	-6.2×10^{-5} $+6.2 \times 10^{-5}$
	-2.65	0.0001695	1.3×10^{-5}	-5.7×10^{-5} $+5.7 \times 10^{-5}$
	-2.45	0.0001913	1.4×10^{-5}	-5.1×10^{-5} $+5.1 \times 10^{-5}$
	-2.26	0.0002552	1.6×10^{-5}	-4.5×10^{-5} $+4.5 \times 10^{-5}$
	-2.06	0.00024	1.9×10^{-5}	-4×10^{-5} $+4 \times 10^{-5}$
	-1.87	0.0002849	2.1×10^{-5}	-3.7×10^{-5} $+3.7 \times 10^{-5}$
	-1.67	0.0002843	2.7×10^{-5}	-3.5×10^{-5} $+3.5 \times 10^{-5}$
	-1.47	0.0001969	2.9×10^{-5}	-3.3×10^{-5} $+3.3 \times 10^{-5}$
	-1.28	1.983×10^{-5}	2.2×10^{-5}	-3.2×10^{-5} $+3.2 \times 10^{-5}$
	-1.08	-9.766×10^{-6}	1.8×10^{-5}	-3.1×10^{-5} $+3.1 \times 10^{-5}$
	-0.88	7.314×10^{-6}	1.5×10^{-5}	-3.1×10^{-5} $+3.1 \times 10^{-5}$
	-0.69	0.0002189	1.4×10^{-5}	-3.2×10^{-5} $+3.2 \times 10^{-5}$
	-0.49	0.0006767	1.3×10^{-5}	-3.5×10^{-5} $+3.5 \times 10^{-5}$
	-0.29	0.001303	1.2×10^{-5}	-4.3×10^{-5} $+4.3 \times 10^{-5}$

Table C.2 – (0-20% Au+Au, $p_{T,\text{trig}}$: 2-3 GeV/c) continued from previous page

$p_{T,\text{assoc}}$	$\Delta\phi$	$J(\Delta\phi_{ta})$	**Stat. Error**	**Syst. Error**
	-0.10	0.001942	1.2×10^{-5}	-5.3×10^{-5} $+5.3 \times 10^{-5}$
	0.10	0.001942	1.2×10^{-5}	-5.3×10^{-5} $+5.3 \times 10^{-5}$
	0.29	0.001304	1.2×10^{-5}	-4.3×10^{-5} $+4.3 \times 10^{-5}$
	0.49	0.0006746	1.3×10^{-5}	-3.5×10^{-5} $+3.5 \times 10^{-5}$
	0.69	0.0002228	1.4×10^{-5}	-3.2×10^{-5} $+3.2 \times 10^{-5}$
	0.88	7.999×10^{-6}	1.5×10^{-5}	-3.1×10^{-5} $+3.1 \times 10^{-5}$
	1.08	-8.718×10^{-7}	1.8×10^{-5}	-3.1×10^{-5} $+3.1 \times 10^{-5}$
	1.28	3.097×10^{-5}	2.2×10^{-5}	-3.2×10^{-5} $+3.2 \times 10^{-5}$
	1.47	0.0001978	2.9×10^{-5}	-3.3×10^{-5} $+3.3 \times 10^{-5}$
	1.67	0.0002792	2.7×10^{-5}	-3.5×10^{-5} $+3.5 \times 10^{-5}$
	1.87	0.0002925	2.1×10^{-5}	-3.7×10^{-5} $+3.7 \times 10^{-5}$
	2.06	0.0002374	1.9×10^{-5}	-4×10^{-5} $+4 \times 10^{-5}$
	2.26	0.0002531	1.6×10^{-5}	-4.5×10^{-5} $+4.5 \times 10^{-5}$
	2.45	0.0001899	1.4×10^{-5}	-5.1×10^{-5} $+5.1 \times 10^{-5}$
	2.65	0.000175	1.3×10^{-5}	-5.7×10^{-5} $+5.7 \times 10^{-5}$
	2.85	0.0002292	1.2×10^{-5}	-6.2×10^{-5} $+6.2 \times 10^{-5}$
	3.04	0.0003131	1.2×10^{-5}	-6.5×10^{-5} $+6.5 \times 10^{-5}$
3-5 GeV/c	-3.04	2.639×10^{-5}	4×10^{-6}	-1.1×10^{-5} $+1.1 \times 10^{-5}$
	-2.85	2.733×10^{-5}	4.1×10^{-6}	-1×10^{-5} $+1 \times 10^{-5}$
	-2.65	1.378×10^{-5}	4.2×10^{-6}	-8.7×10^{-6} $+8.7 \times 10^{-6}$
	-2.45	1.963×10^{-5}	4.6×10^{-6}	-7.4×10^{-6} $+7.4 \times 10^{-6}$
	-2.26	2.595×10^{-5}	5.2×10^{-6}	-6.4×10^{-6} $+6.4 \times 10^{-6}$
	-2.06	1.741×10^{-5}	6.2×10^{-6}	-5.7×10^{-6} $+5.7 \times 10^{-6}$
	-1.87	4.115×10^{-5}	7×10^{-6}	-5.4×10^{-6} $+5.4 \times 10^{-6}$
	-1.67	3.635×10^{-5}	9×10^{-6}	-5.1×10^{-6} $+5.1 \times 10^{-6}$
	-1.47	1.439×10^{-5}	9.6×10^{-6}	-4.8×10^{-6} $+4.8 \times 10^{-6}$
	-1.28	1.047×10^{-5}	7.2×10^{-6}	-4.6×10^{-6} $+4.6 \times 10^{-6}$

Table C.2 – (0-20% Au+Au, $p_{T,\text{trig}}$: 2-3 GeV/c) continued from previous page

$p_{T,\text{assoc}}$	$\Delta\phi$	$J(\Delta\phi_{ta})$	**Stat. Error**	**Syst. Error**
	-1.08	1.018×10^{-6}	5.9×10^{-6}	-4.4×10^{-6} $+4.4 \times 10^{-6}$
	-0.88	-9.087×10^{-6}	4.9×10^{-6}	-4.4×10^{-6} $+4.4 \times 10^{-6}$
	-0.69	2.937×10^{-5}	4.6×10^{-6}	-4.9×10^{-6} $+4.9 \times 10^{-6}$
	-0.49	0.0001108	4.2×10^{-6}	-5.5×10^{-6} $+5.5 \times 10^{-6}$
	-0.29	0.0002113	3.9×10^{-6}	-7.2×10^{-6} $+7.2 \times 10^{-6}$
	-0.10	0.0003678	4×10^{-6}	-1×10^{-5} $+1 \times 10^{-5}$
	0.10	0.0003614	4×10^{-6}	-1×10^{-5} $+1 \times 10^{-5}$
	0.29	0.0002211	3.9×10^{-6}	-7.2×10^{-6} $+7.2 \times 10^{-6}$
	0.49	9.734×10^{-5}	4.2×10^{-6}	-5.5×10^{-6} $+5.5 \times 10^{-6}$
	0.69	3.209×10^{-5}	4.6×10^{-6}	-4.9×10^{-6} $+4.9 \times 10^{-6}$
	0.88	4.793×10^{-6}	4.9×10^{-6}	-4.4×10^{-6} $+4.4 \times 10^{-6}$
	1.08	-6.522×10^{-7}	5.9×10^{-6}	-4.4×10^{-6} $+4.4 \times 10^{-6}$
	1.28	1.058×10^{-5}	7.2×10^{-6}	-4.6×10^{-6} $+4.6 \times 10^{-6}$
	1.47	-2.361×10^{-6}	9.6×10^{-6}	-4.8×10^{-6} $+4.8 \times 10^{-6}$
	1.67	2.951×10^{-5}	9×10^{-6}	-5.1×10^{-6} $+5.1 \times 10^{-6}$
	1.87	2.86×10^{-5}	7×10^{-6}	-5.4×10^{-6} $+5.4 \times 10^{-6}$
	2.06	3.239×10^{-5}	6.2×10^{-6}	-5.7×10^{-6} $+5.7 \times 10^{-6}$
	2.26	2.468×10^{-5}	5.2×10^{-6}	-6.4×10^{-6} $+6.4 \times 10^{-6}$
	2.45	1.369×10^{-5}	4.6×10^{-6}	-7.4×10^{-6} $+7.4 \times 10^{-6}$
	2.65	1.085×10^{-5}	4.2×10^{-6}	-8.7×10^{-6} $+8.7 \times 10^{-6}$
	2.85	2.45×10^{-5}	4×10^{-6}	-1×10^{-5} $+1 \times 10^{-5}$
	3.04	2.925×10^{-5}	4×10^{-6}	-1.1×10^{-5} $+1.1 \times 10^{-5}$

Table C.3: **Two-particle 20-40% Au+Au jet-induced correlation for $p_{T,\mathrm{trig}}$: 2-3 GeV/c.**

$p_{T,\mathrm{assoc}}$	$\Delta\phi$	$J(\Delta\phi_{ta})$	**Stat. Error**	**Syst. Error**
0.4-1 GeV/c	-3.04	0.009702	9.8×10^{-5}	-0.00099 +0.00099
	-2.85	0.00921	9.9×10^{-5}	-0.00094 +0.00094
	-2.65	0.008905	0.0001	-0.00086 +0.00086
	-2.45	0.008784	0.00011	-0.00076 +0.00076
	-2.26	0.008577	0.00013	-0.00067 +0.00067
	-2.06	0.007908	0.00014	-0.00061 +0.00061
	-1.87	0.006017	0.00017	-0.00056 +0.00056
	-1.67	0.004584	0.00021	-0.00053 +0.00053
	-1.47	0.00286	0.00023	-0.00052 +0.00052
	-1.28	0.0009141	0.00018	-0.00051 +0.00051
	-1.08	0.0002599	0.00014	-0.00052 +0.00052
	-0.88	0.0009464	0.00012	-0.00055 +0.00055
	-0.69	0.004154	0.00011	-0.00061 +0.00061
	-0.49	0.009031	0.0001	-0.0007 +0.0007
	-0.29	0.01443	9.6×10^{-5}	-0.00082 +0.00082
	-0.10	0.01738	0.0001	-0.0009 +0.0009
	0.10	0.01755	0.0001	-0.0009 +0.0009
	0.29	0.01395	9.6×10^{-5}	-0.00082 +0.00082
	0.49	0.008772	0.0001	-0.0007 +0.0007
	0.69	0.003903	0.00011	-0.00061 +0.00061
	0.88	0.0009248	0.00012	-0.00055 +0.00055
	1.08	0.0003508	0.00014	-0.00052 +0.00052
	1.28	0.0006801	0.00018	-0.00051 +0.00051
	1.47	0.002427	0.00022	-0.00052 +0.00052
	1.67	0.00454	0.00021	-0.00053 +0.00053

Table C.3 – (20-40% Au+Au, $p_{T,\mathrm{trig}}$: 2-3 GeV/c) continued from previous page

$p_{T,\mathrm{assoc}}$	$\Delta\phi$	$J(\Delta\phi_{ta})$	**Stat. Error**	**Syst. Error**
	1.87	0.006292	0.00017	-0.00056 +0.00056
	2.06	0.007943	0.00014	-0.00061 +0.00061
	2.26	0.008485	0.00013	-0.00067 +0.00067
	2.45	0.008775	0.00011	-0.00076 +0.00076
	2.65	0.008919	0.0001	-0.00086 +0.00086
	2.85	0.009491	9.9×10^{-5}	-0.00094 +0.00094
	3.04	0.009768	9.7×10^{-5}	-0.00099 +0.00099
1-2 GeV/c	-3.04	0.00401	4.5×10^{-5}	-0.0004 +0.0004
	-2.85	0.003768	4.6×10^{-5}	-0.00038 +0.00038
	-2.65	0.003757	4.7×10^{-5}	-0.00035 +0.00035
	-2.45	0.003949	5.2×10^{-5}	-0.00031 +0.00031
	-2.26	0.004099	5.8×10^{-5}	-0.00027 +0.00027
	-2.06	0.003968	6.8×10^{-5}	-0.00025 +0.00025
	-1.87	0.003364	7.8×10^{-5}	-0.00023 +0.00023
	-1.67	0.002463	9.9×10^{-5}	-0.00022 +0.00022
	-1.47	0.001368	0.00011	-0.00021 +0.00021
	-1.28	0.0003529	8.1×10^{-5}	-0.0002 +0.0002
	-1.08	-5.897×10^{-5}	6.5×10^{-5}	-0.00021 +0.00021
	-0.88	0.0004432	5.4×10^{-5}	-0.00022 +0.00022
	-0.69	0.002194	5.1×10^{-5}	-0.00024 +0.00024
	-0.49	0.005134	4.7×10^{-5}	-0.00028 +0.00028
	-0.29	0.008225	4.6×10^{-5}	-0.00032 +0.00032
	-0.10	0.01081	4.7×10^{-5}	-0.00036 +0.00036
	0.10	0.01084	4.7×10^{-5}	-0.00036 +0.00036
	0.29	0.008358	4.6×10^{-5}	-0.00032 +0.00032
	0.49	0.005136	4.8×10^{-5}	-0.00028 +0.00028
	0.69	0.002088	5.1×10^{-5}	-0.00024 +0.00024

Table C.3 – (20-40% Au+Au, $p_{T,\mathrm{trig}}$: 2-3 GeV/c) continued from previous page

$p_{T,\mathrm{assoc}}$	$\Delta\phi$	$J(\Delta\phi_{ta})$	**Stat. Error**	**Syst. Error**
	0.88	0.0002843	5.5×10^{-5}	-0.00022 +0.00022
	1.08	-5.884×10^{-5}	6.5×10^{-5}	-0.00021 +0.00021
	1.28	0.0003332	8.2×10^{-5}	-0.0002 +0.0002
	1.47	0.001326	0.00011	-0.00021 +0.00021
	1.67	0.002549	9.9×10^{-5}	-0.00022 +0.00022
	1.87	0.003342	7.8×10^{-5}	-0.00023 +0.00023
	2.06	0.003979	6.8×10^{-5}	-0.00025 +0.00025
	2.26	0.003943	5.8×10^{-5}	-0.00027 +0.00027
	2.45	0.003859	5.2×10^{-5}	-0.00031 +0.00031
	2.65	0.003808	4.7×10^{-5}	-0.00035 +0.00035
	2.85	0.003838	4.6×10^{-5}	-0.00038 +0.00038
	3.04	0.003876	4.5×10^{-5}	-0.0004 +0.0004
2-3 GeV/c	-3.04	0.0004609	1.3×10^{-5}	-4.7×10^{-5} $+4.7 \times 10^{-5}$
	-2.85	0.0004351	1.3×10^{-5}	-4.4×10^{-5} $+4.4 \times 10^{-5}$
	-2.65	0.0004501	1.3×10^{-5}	-3.8×10^{-5} $+3.8 \times 10^{-5}$
	-2.45	0.0004716	1.5×10^{-5}	-3.3×10^{-5} $+3.3 \times 10^{-5}$
	-2.26	0.0004776	1.6×10^{-5}	-2.8×10^{-5} $+2.8 \times 10^{-5}$
	-2.06	0.0004918	1.9×10^{-5}	-2.6×10^{-5} $+2.6 \times 10^{-5}$
	-1.87	0.0004605	2.2×10^{-5}	-2.4×10^{-5} $+2.4 \times 10^{-5}$
	-1.67	0.0004173	2.8×10^{-5}	-2.3×10^{-5} $+2.3 \times 10^{-5}$
	-1.47	0.0002732	3×10^{-5}	-2.2×10^{-5} $+2.2 \times 10^{-5}$
	-1.28	9.187×10^{-5}	2.3×10^{-5}	-2.1×10^{-5} $+2.1 \times 10^{-5}$
	-1.08	5.015×10^{-5}	1.8×10^{-5}	-2.1×10^{-5} $+2.1 \times 10^{-5}$
	-0.88	6.525×10^{-5}	1.5×10^{-5}	-2.3×10^{-5} $+2.3 \times 10^{-5}$
	-0.69	0.0003297	1.5×10^{-5}	-2.5×10^{-5} $+2.5 \times 10^{-5}$
	-0.49	0.0008518	1.3×10^{-5}	-2.9×10^{-5} $+2.9 \times 10^{-5}$
	-0.29	0.001637	1.3×10^{-5}	-3.8×10^{-5} $+3.8 \times 10^{-5}$

Table C.3 – (20-40% Au+Au, $p_{T,\text{trig}}$: 2-3 GeV/c) continued from previous page

$p_{T,\text{assoc}}$	$\Delta\phi$	$J(\Delta\phi_{ta})$	**Stat. Error**	**Syst. Error**
	-0.10	0.002286	1.3×10^{-5}	-4.6×10^{-5} $+4.6 \times 10^{-5}$
	0.10	0.002291	1.3×10^{-5}	-4.6×10^{-5} $+4.6 \times 10^{-5}$
	0.29	0.001635	1.3×10^{-5}	-3.8×10^{-5} $+3.8 \times 10^{-5}$
	0.49	0.0008544	1.3×10^{-5}	-2.9×10^{-5} $+2.9 \times 10^{-5}$
	0.69	0.000335	1.5×10^{-5}	-2.5×10^{-5} $+2.5 \times 10^{-5}$
	0.88	6.368×10^{-5}	1.5×10^{-5}	-2.3×10^{-5} $+2.3 \times 10^{-5}$
	1.08	4.648×10^{-5}	1.8×10^{-5}	-2.1×10^{-5} $+2.1 \times 10^{-5}$
	1.28	9.35×10^{-5}	2.3×10^{-5}	-2.1×10^{-5} $+2.1 \times 10^{-5}$
	1.47	0.0002815	3×10^{-5}	-2.2×10^{-5} $+2.2 \times 10^{-5}$
	1.67	0.0004098	2.8×10^{-5}	-2.3×10^{-5} $+2.3 \times 10^{-5}$
	1.87	0.000463	2.2×10^{-5}	-2.4×10^{-5} $+2.4 \times 10^{-5}$
	2.06	0.000493	1.9×10^{-5}	-2.6×10^{-5} $+2.6 \times 10^{-5}$
	2.26	0.0004765	1.6×10^{-5}	-2.8×10^{-5} $+2.8 \times 10^{-5}$
	2.45	0.0004749	1.5×10^{-5}	-3.3×10^{-5} $+3.3 \times 10^{-5}$
	2.65	0.000453	1.3×10^{-5}	-3.8×10^{-5} $+3.8 \times 10^{-5}$
	2.85	0.0004371	1.3×10^{-5}	-4.4×10^{-5} $+4.4 \times 10^{-5}$
	3.04	0.0004592	1.3×10^{-5}	-4.7×10^{-5} $+4.7 \times 10^{-5}$
3-5 GeV/c	-3.04	7.775×10^{-5}	4.3×10^{-6}	-9.7×10^{-6} $+9.7 \times 10^{-6}$
	-2.85	7.68×10^{-5}	4.4×10^{-6}	-8.8×10^{-6} $+8.8 \times 10^{-6}$
	-2.65	6.747×10^{-5}	4.6×10^{-6}	-7.3×10^{-6} $+7.3 \times 10^{-6}$
	-2.45	6.911×10^{-5}	5×10^{-6}	-6×10^{-6} $+6 \times 10^{-6}$
	-2.26	6.947×10^{-5}	5.6×10^{-6}	-5.3×10^{-6} $+5.3 \times 10^{-6}$
	-2.06	6.896×10^{-5}	6.6×10^{-6}	-4.9×10^{-6} $+4.9 \times 10^{-6}$
	-1.87	7.174×10^{-5}	7.5×10^{-6}	-4.6×10^{-6} $+4.6 \times 10^{-6}$
	-1.67	6.295×10^{-5}	9.6×10^{-6}	-4.3×10^{-6} $+4.3 \times 10^{-6}$
	-1.47	3.313×10^{-5}	1×10^{-5}	-4×10^{-6} $+4 \times 10^{-6}$
	-1.28	1.024×10^{-5}	7.7×10^{-6}	-3.8×10^{-6} $+3.8 \times 10^{-6}$

Table C.3 – (20-40% Au+Au, $p_{T,\mathrm{trig}}$: 2-3 GeV/c) continued from previous page

$p_{T,\mathrm{assoc}}$	$\Delta\phi$	$J(\Delta\phi_{ta})$	**Stat. Error**	**Syst. Error**
	-1.08	2.054×10^{-5}	6.3×10^{-6}	-3.8×10^{-6} $+3.8 \times 10^{-6}$
	-0.88	1.38×10^{-5}	5.2×10^{-6}	-4.2×10^{-6} $+4.2 \times 10^{-6}$
	-0.69	5.996×10^{-5}	5×10^{-6}	-4.9×10^{-6} $+4.9 \times 10^{-6}$
	-0.49	0.0001469	4.6×10^{-6}	-5.5×10^{-6} $+5.5 \times 10^{-6}$
	-0.29	0.0003188	4.4×10^{-6}	-7.4×10^{-6} $+7.4 \times 10^{-6}$
	-0.10	0.0005162	4.5×10^{-6}	-1×10^{-5} $+1 \times 10^{-5}$
	0.10	0.00051	4.5×10^{-6}	-1×10^{-5} $+1 \times 10^{-5}$
	0.29	0.000304	4.4×10^{-6}	-7.4×10^{-6} $+7.4 \times 10^{-6}$
	0.49	0.0001535	4.6×10^{-6}	-5.5×10^{-6} $+5.5 \times 10^{-6}$
	0.69	6.144×10^{-5}	5×10^{-6}	-4.9×10^{-6} $+4.9 \times 10^{-6}$
	0.88	1.022×10^{-5}	5.2×10^{-6}	-4.2×10^{-6} $+4.2 \times 10^{-6}$
	1.08	1.161×10^{-5}	6.2×10^{-6}	-3.8×10^{-6} $+3.8 \times 10^{-6}$
	1.28	4.474×10^{-6}	7.7×10^{-6}	-3.8×10^{-6} $+3.8 \times 10^{-6}$
	1.47	3.345×10^{-5}	1×10^{-5}	-4×10^{-6} $+4 \times 10^{-6}$
	1.67	4.767×10^{-5}	9.6×10^{-6}	-4.3×10^{-6} $+4.3 \times 10^{-6}$
	1.87	6.353×10^{-5}	7.4×10^{-6}	-4.6×10^{-6} $+4.6 \times 10^{-6}$
	2.06	7.481×10^{-5}	6.6×10^{-6}	-4.9×10^{-6} $+4.9 \times 10^{-6}$
	2.26	7.737×10^{-5}	5.6×10^{-6}	-5.3×10^{-6} $+5.3 \times 10^{-6}$
	2.45	7.578×10^{-5}	5×10^{-6}	-6×10^{-6} $+6 \times 10^{-6}$
	2.65	6.961×10^{-5}	4.6×10^{-6}	-7.3×10^{-6} $+7.3 \times 10^{-6}$
	2.85	6.841×10^{-5}	4.4×10^{-6}	-8.8×10^{-6} $+8.8 \times 10^{-6}$
	3.04	8.103×10^{-5}	4.3×10^{-6}	-9.7×10^{-6} $+9.7 \times 10^{-6}$

Table C.4: **Two-particle 40-60% Au+Au jet-induced correlation for $p_{T,\mathrm{trig}}$: 2-3 GeV/c.**

$p_{T,\mathrm{assoc}}$	$\Delta\phi$	$J(\Delta\phi_{ta})$	**Stat. Error**	**Syst. Error**
0.4-1 GeV/c	-3.04	0.01104	0.00011	-0.001 +0.001
	-2.85	0.01073	0.00011	-0.00098 +0.00098
	-2.65	0.01012	0.00011	-0.00089 +0.00089
	-2.45	0.009216	0.00012	-0.00079 +0.00079
	-2.26	0.007769	0.00014	-0.0007 +0.0007
	-2.06	0.006329	0.00016	-0.00063 +0.00063
	-1.87	0.004708	0.00019	-0.00058 +0.00058
	-1.67	0.00253	0.00023	-0.00055 +0.00055
	-1.47	0.001342	0.00025	-0.00054 +0.00054
	-1.28	-0.0003045	0.0002	-0.00053 +0.00053
	-1.08	-5.958×10^{-5}	0.00015	-0.00054 +0.00054
	-0.88	0.001665	0.00013	-0.00057 +0.00057
	-0.69	0.005138	0.00012	-0.00064 +0.00064
	-0.49	0.01005	0.00011	-0.00074 +0.00074
	-0.29	0.01505	0.0001	-0.00086 +0.00086
	-0.10	0.0179	0.00011	-0.00094 +0.00094
	0.10	0.01819	0.00011	-0.00094 +0.00094
	0.29	0.01493	0.0001	-0.00086 +0.00086
	0.49	0.01016	0.00011	-0.00074 +0.00074
	0.69	0.005121	0.00012	-0.00064 +0.00064
	0.88	0.001623	0.00013	-0.00057 +0.00057
	1.08	0.000188	0.00016	-0.00054 +0.00054
	1.28	-0.0003355	0.0002	-0.00053 +0.00053
	1.47	0.0009723	0.00024	-0.00054 +0.00054
	1.67	0.002638	0.00023	-0.00055 +0.00055

Table C.4 – (40-60% Au+Au, $p_{T,\mathrm{trig}}$: 2-3 GeV/c) continued from previous page

$p_{T,\mathrm{assoc}}$	$\Delta\phi$	$J(\Delta\phi_{ta})$	**Stat. Error**	**Syst. Error**
	1.87	0.004162	0.00019	-0.00058 +0.00058
	2.06	0.006344	0.00016	-0.00063 +0.00063
	2.26	0.007727	0.00014	-0.0007 +0.0007
	2.45	0.00907	0.00012	-0.00079 +0.00079
	2.65	0.009939	0.00011	-0.00089 +0.00089
	2.85	0.01062	0.00011	-0.00098 +0.00098
	3.04	0.01126	0.00011	-0.001 +0.001
1-2 GeV/c	-3.04	0.005146	4.8×10^{-5}	-0.00028 +0.00028
	-2.85	0.004993	4.9×10^{-5}	-0.00026 +0.00026
	-2.65	0.004765	5×10^{-5}	-0.00024 +0.00024
	-2.45	0.004267	5.5×10^{-5}	-0.00021 +0.00021
	-2.26	0.003851	6.1×10^{-5}	-0.00018 +0.00018
	-2.06	0.003231	7.2×10^{-5}	-0.00016 +0.00016
	-1.87	0.002482	8.3×10^{-5}	-0.00015 +0.00015
	-1.67	0.001456	0.00011	-0.00014 +0.00014
	-1.47	0.0006038	0.00012	-0.00014 +0.00014
	-1.28	0.0002409	8.6×10^{-5}	-0.00014 +0.00014
	-1.08	1.113×10^{-5}	6.9×10^{-5}	-0.00014 +0.00014
	-0.88	0.00072	5.7×10^{-5}	-0.00015 +0.00015
	-0.69	0.002464	5.4×10^{-5}	-0.00016 +0.00016
	-0.49	0.005453	5.1×10^{-5}	-0.00019 +0.00019
	-0.29	0.008585	4.9×10^{-5}	-0.00023 +0.00023
	-0.10	0.01094	5.1×10^{-5}	-0.00026 +0.00026
	0.10	0.01081	5.1×10^{-5}	-0.00026 +0.00026
	0.29	0.008445	4.9×10^{-5}	-0.00023 +0.00023
	0.49	0.005381	5.1×10^{-5}	-0.00019 +0.00019
	0.69	0.00261	5.5×10^{-5}	-0.00016 +0.00016

Table C.4 – (40-60% Au+Au, $p_{T,\mathrm{trig}}$: 2-3 GeV/c) continued from previous page

$p_{T,\mathrm{assoc}}$	$\Delta\phi$	$J(\Delta\phi_{ta})$	**Stat. Error**	**Syst. Error**
	0.88	0.0007651	5.8×10^{-5}	-0.00015 +0.00015
	1.08	6.383×10^{-5}	6.9×10^{-5}	-0.00014 +0.00014
	1.28	-0.0001013	8.6×10^{-5}	-0.00014 +0.00014
	1.47	0.0006354	0.00011	-0.00014 +0.00014
	1.67	0.001458	0.00011	-0.00014 +0.00014
	1.87	0.002319	8.2×10^{-5}	-0.00015 +0.00015
	2.06	0.003087	7.2×10^{-5}	-0.00016 +0.00016
	2.26	0.003791	6.1×10^{-5}	-0.00018 +0.00018
	2.45	0.00417	5.5×10^{-5}	-0.00021 +0.00021
	2.65	0.004658	5×10^{-5}	-0.00024 +0.00024
	2.85	0.004961	4.9×10^{-5}	-0.00026 +0.00026
	3.04	0.005051	4.8×10^{-5}	-0.00028 +0.00028
2-3 GeV/c	-3.04	0.0007204	1.4×10^{-5}	-3.5×10^{-5} $+3.5 \times 10^{-5}$
	-2.85	0.0006731	1.4×10^{-5}	-3.1×10^{-5} $+3.1 \times 10^{-5}$
	-2.65	0.0006559	1.4×10^{-5}	-2.7×10^{-5} $+2.7 \times 10^{-5}$
	-2.45	0.0005544	1.6×10^{-5}	-2.2×10^{-5} $+2.2 \times 10^{-5}$
	-2.26	0.0004901	1.7×10^{-5}	-1.9×10^{-5} $+1.9 \times 10^{-5}$
	-2.06	0.0004211	2.1×10^{-5}	-1.8×10^{-5} $+1.8 \times 10^{-5}$
	-1.87	0.0003763	2.3×10^{-5}	-1.7×10^{-5} $+1.7 \times 10^{-5}$
	-1.67	0.0002266	3×10^{-5}	-1.6×10^{-5} $+1.6 \times 10^{-5}$
	-1.47	0.0001742	3.3×10^{-5}	-1.5×10^{-5} $+1.5 \times 10^{-5}$
	-1.28	3.279×10^{-5}	2.4×10^{-5}	-1.4×10^{-5} $+1.4 \times 10^{-5}$
	-1.08	2.955×10^{-5}	1.9×10^{-5}	-1.4×10^{-5} $+1.4 \times 10^{-5}$
	-0.88	0.0001162	1.6×10^{-5}	-1.6×10^{-5} $+1.6 \times 10^{-5}$
	-0.69	0.0003492	1.5×10^{-5}	-1.8×10^{-5} $+1.8 \times 10^{-5}$
	-0.49	0.0008515	1.5×10^{-5}	-2×10^{-5} $+2 \times 10^{-5}$
	-0.29	0.001675	1.4×10^{-5}	-2.7×10^{-5} $+2.7 \times 10^{-5}$

Table C.4 – (40-60% Au+Au, $p_{T,\text{trig}}$: 2-3 GeV/c) continued from previous page

$p_{T,\text{assoc}}$	$\Delta\phi$	$J(\Delta\phi_{ta})$	**Stat. Error**	**Syst. Error**
	-0.10	0.002331	1.4×10^{-5}	-3.6×10^{-5} $+3.6 \times 10^{-5}$
	0.10	0.002328	1.4×10^{-5}	-3.6×10^{-5} $+3.6 \times 10^{-5}$
	0.29	0.001676	1.4×10^{-5}	-2.7×10^{-5} $+2.7 \times 10^{-5}$
	0.49	0.000849	1.5×10^{-5}	-2×10^{-5} $+2 \times 10^{-5}$
	0.69	0.00035	1.5×10^{-5}	-1.8×10^{-5} $+1.8 \times 10^{-5}$
	0.88	0.0001149	1.6×10^{-5}	-1.6×10^{-5} $+1.6 \times 10^{-5}$
	1.08	2.345×10^{-5}	1.9×10^{-5}	-1.4×10^{-5} $+1.4 \times 10^{-5}$
	1.28	3.776×10^{-5}	2.4×10^{-5}	-1.4×10^{-5} $+1.4 \times 10^{-5}$
	1.47	0.0001636	3.2×10^{-5}	-1.5×10^{-5} $+1.5 \times 10^{-5}$
	1.67	0.000221	3×10^{-5}	-1.6×10^{-5} $+1.6 \times 10^{-5}$
	1.87	0.000379	2.3×10^{-5}	-1.7×10^{-5} $+1.7 \times 10^{-5}$
	2.06	0.0004204	2.1×10^{-5}	-1.8×10^{-5} $+1.8 \times 10^{-5}$
	2.26	0.0004924	1.7×10^{-5}	-1.9×10^{-5} $+1.9 \times 10^{-5}$
	2.45	0.0005528	1.6×10^{-5}	-2.2×10^{-5} $+2.2 \times 10^{-5}$
	2.65	0.0006534	1.4×10^{-5}	-2.7×10^{-5} $+2.7 \times 10^{-5}$
	2.85	0.0006744	1.4×10^{-5}	-3.1×10^{-5} $+3.1 \times 10^{-5}$
	3.04	0.0007198	1.4×10^{-5}	-3.5×10^{-5} $+3.5 \times 10^{-5}$
3-5 GeV/c	-3.04	0.0001387	5×10^{-6}	-8.2×10^{-6} $+8.2 \times 10^{-6}$
	-2.85	0.0001216	5.1×10^{-6}	-7.1×10^{-6} $+7.1 \times 10^{-6}$
	-2.65	0.0001017	5.2×10^{-6}	-5.6×10^{-6} $+5.6 \times 10^{-6}$
	-2.45	9.384×10^{-5}	5.6×10^{-6}	-4.6×10^{-6} $+4.6 \times 10^{-6}$
	-2.26	8.287×10^{-5}	6.2×10^{-6}	-4.1×10^{-6} $+4.1 \times 10^{-6}$
	-2.06	6.961×10^{-5}	7.4×10^{-6}	-3.9×10^{-6} $+3.9 \times 10^{-6}$
	-1.87	4.588×10^{-5}	8.3×10^{-6}	-3.5×10^{-6} $+3.5 \times 10^{-6}$
	-1.67	4.065×10^{-5}	1.1×10^{-5}	-3.2×10^{-6} $+3.2 \times 10^{-6}$
	-1.47	2.412×10^{-5}	1.2×10^{-5}	-3×10^{-6} $+3 \times 10^{-6}$
	-1.28	1.228×10^{-5}	8.6×10^{-6}	-2.9×10^{-6} $+2.9 \times 10^{-6}$

Table C.4 – (40-60% Au+Au, $p_{T,\text{trig}}$: 2-3 GeV/c) continued from previous page

$p_{T,\text{assoc}}$	$\Delta\phi$	$J(\Delta\phi_{ta})$	**Stat. Error**	**Syst. Error**
	-1.08	8.004×10^{-6}	6.9×10^{-6}	-2.9×10^{-6} $+2.9 \times 10^{-6}$
	-0.88	1.188×10^{-5}	5.8×10^{-6}	-3.1×10^{-6} $+3.1 \times 10^{-6}$
	-0.69	4.06×10^{-5}	5.5×10^{-6}	-3.8×10^{-6} $+3.8 \times 10^{-6}$
	-0.49	0.0001442	5.2×10^{-6}	-4.6×10^{-6} $+4.6 \times 10^{-6}$
	-0.29	0.0003216	5.1×10^{-6}	-5.7×10^{-6} $+5.7 \times 10^{-6}$
	-0.10	0.0005825	5.5×10^{-6}	-9.5×10^{-6} $+9.5 \times 10^{-6}$
	0.10	0.0005882	5.5×10^{-6}	-9.5×10^{-6} $+9.5 \times 10^{-6}$
	0.29	0.0003266	5.1×10^{-6}	-5.7×10^{-6} $+5.7 \times 10^{-6}$
	0.49	0.0001353	5.2×10^{-6}	-4.6×10^{-6} $+4.6 \times 10^{-6}$
	0.69	5.707×10^{-5}	5.5×10^{-6}	-3.8×10^{-6} $+3.8 \times 10^{-6}$
	0.88	2.836×10^{-6}	5.7×10^{-6}	-3.1×10^{-6} $+3.1 \times 10^{-6}$
	1.08	-3.746×10^{-6}	6.9×10^{-6}	-2.9×10^{-6} $+2.9 \times 10^{-6}$
	1.28	-6.729×10^{-6}	8.5×10^{-6}	-2.9×10^{-6} $+2.9 \times 10^{-6}$
	1.47	2.725×10^{-5}	1.2×10^{-5}	-3×10^{-6} $+3 \times 10^{-6}$
	1.67	1.311×10^{-5}	1.1×10^{-5}	-3.2×10^{-6} $+3.2 \times 10^{-6}$
	1.87	5.493×10^{-5}	8.3×10^{-6}	-3.5×10^{-6} $+3.5 \times 10^{-6}$
	2.06	6.792×10^{-5}	7.4×10^{-6}	-3.9×10^{-6} $+3.9 \times 10^{-6}$
	2.26	8.811×10^{-5}	6.2×10^{-6}	-4.1×10^{-6} $+4.1 \times 10^{-6}$
	2.45	8.704×10^{-5}	5.6×10^{-6}	-4.6×10^{-6} $+4.6 \times 10^{-6}$
	2.65	0.0001115	5.2×10^{-6}	-5.6×10^{-6} $+5.6 \times 10^{-6}$
	2.85	0.0001345	5.1×10^{-6}	-7.1×10^{-6} $+7.1 \times 10^{-6}$
	3.04	0.0001318	4.9×10^{-6}	-8.2×10^{-6} $+8.2 \times 10^{-6}$

Table C.5: **Two-particle 60-92% Au+Au jet-induced correlation for $p_{T,\mathrm{trig}}$: 2-3 GeV/c.**

$p_{T,\mathrm{assoc}}$	$\Delta\phi$	$J(\Delta\phi_{ta})$	**Stat. Error**	**Syst. Error**
0.4-1 GeV/c	-3.04	0.0113	0.00011	-0.00076 +0.00076
	-2.85	0.0108	0.00012	-0.00072 +0.00072
	-2.65	0.009773	0.00012	-0.00065 +0.00065
	-2.45	0.007848	0.00013	-0.00057 +0.00057
	-2.26	0.006403	0.00015	-0.0005 +0.0005
	-2.06	0.004952	0.00017	-0.00045 +0.00045
	-1.87	0.003136	0.00021	-0.00042 +0.00042
	-1.67	0.002091	0.00026	-0.0004 +0.0004
	-1.47	0.0008609	0.00028	-0.00038 +0.00038
	-1.28	-2.405×10^{-5}	0.00021	-0.00037 +0.00037
	-1.08	0.0005522	0.00017	-0.00038 +0.00038
	-0.88	0.002036	0.00014	-0.00039 +0.00039
	-0.69	0.005052	0.00013	-0.00043 +0.00043
	-0.49	0.009417	0.00012	-0.0005 +0.0005
	-0.29	0.01318	0.00011	-0.00061 +0.00061
	-0.10	0.01535	0.00012	-0.00069 +0.00069
	0.10	0.01535	0.00012	-0.00069 +0.00069
	0.29	0.01315	0.00011	-0.00061 +0.00061
	0.49	0.00938	0.00012	-0.0005 +0.0005
	0.69	0.005158	0.00013	-0.00043 +0.00043
	0.88	0.002374	0.00014	-0.00039 +0.00039
	1.08	0.0002743	0.00017	-0.00038 +0.00038
	1.28	0.0002268	0.00022	-0.00037 +0.00037
	1.47	-5.956×10^{-5}	0.00026	-0.00038 +0.00038
	1.67	0.0009692	0.00025	-0.0004 +0.0004

Table C.5 – (60-92% Au+Au, $p_{T,\mathrm{trig}}$: 2-3 GeV/c) continued from previous page

$p_{T,\mathrm{assoc}}$	$\Delta\phi$	$J(\Delta\phi_{ta})$	**Stat. Error**	**Syst. Error**
	1.87	0.002324	0.0002	-0.00042 +0.00042
	2.06	0.004269	0.00017	-0.00045 +0.00045
	2.26	0.006058	0.00015	-0.0005 +0.0005
	2.45	0.007844	0.00013	-0.00057 +0.00057
	2.65	0.009528	0.00012	-0.00065 +0.00065
	2.85	0.01036	0.00012	-0.00072 +0.00072
	3.04	0.01111	0.00011	-0.00076 +0.00076
1-2 GeV/c	-3.04	0.004852	5×10^{-5}	-0.00015 +0.00015
	-2.85	0.004624	5.1×10^{-5}	-0.00014 +0.00014
	-2.65	0.004129	5.3×10^{-5}	-0.00012 +0.00012
	-2.45	0.003292	5.8×10^{-5}	-9.8×10^{-5} $+9.8 \times 10^{-5}$
	-2.26	0.002614	6.4×10^{-5}	-8.5×10^{-5} $+8.5 \times 10^{-5}$
	-2.06	0.001973	7.6×10^{-5}	-7.8×10^{-5} $+7.8 \times 10^{-5}$
	-1.87	0.001206	8.7×10^{-5}	-7.3×10^{-5} $+7.3 \times 10^{-5}$
	-1.67	0.0008061	0.00011	-6.9×10^{-5} $+6.9 \times 10^{-5}$
	-1.47	0.0002519	0.00012	-6.5×10^{-5} $+6.5 \times 10^{-5}$
	-1.28	-0.0001114	8.9×10^{-5}	-6.2×10^{-5} $+6.2 \times 10^{-5}$
	-1.08	-1.328×10^{-5}	7.1×10^{-5}	-6.3×10^{-5} $+6.3 \times 10^{-5}$
	-0.88	0.0005362	5.9×10^{-5}	-6.8×10^{-5} $+6.8 \times 10^{-5}$
	-0.69	0.001952	5.6×10^{-5}	-7.5×10^{-5} $+7.5 \times 10^{-5}$
	-0.49	0.004115	5.3×10^{-5}	-8.5×10^{-5} $+8.5 \times 10^{-5}$
	-0.29	0.006912	5.2×10^{-5}	-0.00011 +0.00011
	-0.10	0.00914	5.5×10^{-5}	-0.00015 +0.00015
	0.10	0.009109	5.5×10^{-5}	-0.00015 +0.00015
	0.29	0.006903	5.2×10^{-5}	-0.00011 +0.00011
	0.49	0.00431	5.4×10^{-5}	-8.5×10^{-5} $+8.5 \times 10^{-5}$
	0.69	0.002074	5.7×10^{-5}	-7.5×10^{-5} $+7.5 \times 10^{-5}$

Table C.5 – (60-92% Au+Au, $p_{T,\text{trig}}$: 2-3 GeV/c) continued from previous page

$p_{T,\text{assoc}}$	$\Delta\phi$	$J(\Delta\phi_{ta})$	**Stat. Error**	**Syst. Error**
	0.88	0.000645	6×10^{-5}	-6.8 $\times 10^{-5}$ +6.8 $\times 10^{-5}$
	1.08	4.611×10^{-5}	7.1×10^{-5}	-6.3 $\times 10^{-5}$ +6.3 $\times 10^{-5}$
	1.28	-0.0001837	9×10^{-5}	-6.2 $\times 10^{-5}$ +6.2 $\times 10^{-5}$
	1.47	0.0002499	0.00012	-6.5 $\times 10^{-5}$ +6.5 $\times 10^{-5}$
	1.67	0.0006401	0.00011	-6.9 $\times 10^{-5}$ +6.9 $\times 10^{-5}$
	1.87	0.00108	8.6×10^{-5}	-7.3 $\times 10^{-5}$ +7.3 $\times 10^{-5}$
	2.06	0.001864	7.6×10^{-5}	-7.8 $\times 10^{-5}$ +7.8 $\times 10^{-5}$
	2.26	0.00263	6.4×10^{-5}	-8.5 $\times 10^{-5}$ +8.5 $\times 10^{-5}$
	2.45	0.003284	5.8×10^{-5}	-9.8 $\times 10^{-5}$ +9.8 $\times 10^{-5}$
	2.65	0.004093	5.3×10^{-5}	-0.00012 +0.00012
	2.85	0.004684	5.1×10^{-5}	-0.00014 +0.00014
	3.04	0.004886	5×10^{-5}	-0.00015 +0.00015
2-3 GeV/c	-3.04	0.0007263	1.5×10^{-5}	-2.6 $\times 10^{-5}$ +2.6 $\times 10^{-5}$
	-2.85	0.0006776	1.5×10^{-5}	-2.2 $\times 10^{-5}$ +2.2 $\times 10^{-5}$
	-2.65	0.0005889	1.6×10^{-5}	-1.8 $\times 10^{-5}$ +1.8 $\times 10^{-5}$
	-2.45	0.000424	1.7×10^{-5}	-1.4 $\times 10^{-5}$ +1.4 $\times 10^{-5}$
	-2.26	0.0003497	1.8×10^{-5}	-1.3 $\times 10^{-5}$ +1.3 $\times 10^{-5}$
	-2.06	0.0002199	2.2×10^{-5}	-1.2 $\times 10^{-5}$ +1.2 $\times 10^{-5}$
	-1.87	0.0001572	2.5×10^{-5}	-1.1 $\times 10^{-5}$ +1.1 $\times 10^{-5}$
	-1.67	7.054×10^{-5}	3.2×10^{-5}	-1 $\times 10^{-5}$ +1 $\times 10^{-5}$
	-1.47	6.46×10^{-5}	3.5×10^{-5}	-9.5 $\times 10^{-6}$ +9.5 $\times 10^{-6}$
	-1.28	-5.727×10^{-5}	2.5×10^{-5}	-9 $\times 10^{-6}$ +9 $\times 10^{-6}$
	-1.08	-3.466×10^{-5}	2×10^{-5}	-8.9 $\times 10^{-6}$ +8.9 $\times 10^{-6}$
	-0.88	4.389×10^{-5}	1.7×10^{-5}	-9.2 $\times 10^{-6}$ +9.2 $\times 10^{-6}$
	-0.69	0.0001963	1.6×10^{-5}	-1.1 $\times 10^{-5}$ +1.1 $\times 10^{-5}$
	-0.49	0.0005866	1.6×10^{-5}	-1.4 $\times 10^{-5}$ +1.4 $\times 10^{-5}$
	-0.29	0.001363	1.6×10^{-5}	-1.7 $\times 10^{-5}$ +1.7 $\times 10^{-5}$

Table C.5 – (60-92% Au+Au, $p_{T,\text{trig}}$: 2-3 GeV/c) continued from previous page

$p_{T,\text{assoc}}$	$\Delta\phi$	$J(\Delta\phi_{ta})$	**Stat. Error**	**Syst. Error**
	-0.10	0.00212	1.7×10^{-5}	-2.8×10^{-5} $+2.8 \times 10^{-5}$
	0.10	0.002106	1.7×10^{-5}	-2.8×10^{-5} $+2.8 \times 10^{-5}$
	0.29	0.001357	1.6×10^{-5}	-1.7×10^{-5} $+1.7 \times 10^{-5}$
	0.49	0.0005853	1.6×10^{-5}	-1.4×10^{-5} $+1.4 \times 10^{-5}$
	0.69	0.0001993	1.6×10^{-5}	-1.1×10^{-5} $+1.1 \times 10^{-5}$
	0.88	4.137×10^{-5}	1.7×10^{-5}	-9.2×10^{-6} $+9.2 \times 10^{-6}$
	1.08	-3.587×10^{-5}	2×10^{-5}	-8.9×10^{-6} $+8.9 \times 10^{-6}$
	1.28	-5.989×10^{-5}	2.5×10^{-5}	-9×10^{-6} $+9 \times 10^{-6}$
	1.47	6.578×10^{-5}	3.5×10^{-5}	-9.5×10^{-6} $+9.5 \times 10^{-6}$
	1.67	6.925×10^{-5}	3.2×10^{-5}	-1×10^{-5} $+1 \times 10^{-5}$
	1.87	0.0001646	2.5×10^{-5}	-1.1×10^{-5} $+1.1 \times 10^{-5}$
	2.06	0.0002157	2.2×10^{-5}	-1.2×10^{-5} $+1.2 \times 10^{-5}$
	2.26	0.0003545	1.9×10^{-5}	-1.3×10^{-5} $+1.3 \times 10^{-5}$
	2.45	0.0004248	1.7×10^{-5}	-1.4×10^{-5} $+1.4 \times 10^{-5}$
	2.65	0.00059	1.6×10^{-5}	-1.8×10^{-5} $+1.8 \times 10^{-5}$
	2.85	0.0006727	1.5×10^{-5}	-2.2×10^{-5} $+2.2 \times 10^{-5}$
	3.04	0.0007257	1.5×10^{-5}	-2.6×10^{-5} $+2.6 \times 10^{-5}$
3-5 GeV/c	-3.04	0.0001831	6×10^{-6}	-8.3×10^{-6} $+8.3 \times 10^{-6}$
	-2.85	0.0001576	6.1×10^{-6}	-6.8×10^{-6} $+6.8 \times 10^{-6}$
	-2.65	0.0001204	6.1×10^{-6}	-5×10^{-6} $+5 \times 10^{-6}$
	-2.45	9.43×10^{-5}	6.6×10^{-6}	-4.1×10^{-6} $+4.1 \times 10^{-6}$
	-2.26	6.715×10^{-5}	7.1×10^{-6}	-3.8×10^{-6} $+3.8 \times 10^{-6}$
	-2.06	3.667×10^{-5}	8.2×10^{-6}	-3.5×10^{-6} $+3.5 \times 10^{-6}$
	-1.87	1.593×10^{-5}	9.2×10^{-6}	-3.1×10^{-6} $+3.1 \times 10^{-6}$
	-1.67	6.316×10^{-6}	1.2×10^{-5}	-2.7×10^{-6} $+2.7 \times 10^{-6}$
	-1.47	-3.269×10^{-6}	1.3×10^{-5}	-2.6×10^{-6} $+2.6 \times 10^{-6}$
	-1.28	-2.703×10^{-5}	9.2×10^{-6}	-2.5×10^{-6} $+2.5 \times 10^{-6}$

Table C.5 – (60-92% Au+Au, $p_{T,\text{trig}}$: 2-3 GeV/c) continued from previous page

$p_{T,\text{assoc}}$	$\Delta\phi$	$J(\Delta\phi_{ta})$	**Stat. Error**	**Syst. Error**
	-1.08	-2.512×10^{-5}	7.4×10^{-6}	-2.5×10^{-6} $+2.5\times10^{-6}$
	-0.88	-1.132×10^{-5}	6.2×10^{-6}	-2.5×10^{-6} $+2.5\times10^{-6}$
	-0.69	1.166×10^{-5}	5.9×10^{-6}	-2.8×10^{-6} $+2.8\times10^{-6}$
	-0.49	9.364×10^{-5}	5.9×10^{-6}	-4.2×10^{-6} $+4.2\times10^{-6}$
	-0.29	0.000313	6.5×10^{-6}	-4.8×10^{-6} $+4.8\times10^{-6}$
	-0.10	0.0006271	7.8×10^{-6}	-9.6×10^{-6} $+9.6\times10^{-6}$
	0.10	0.000622	7.7×10^{-6}	-9.6×10^{-6} $+9.6\times10^{-6}$
	0.29	0.0003061	6.4×10^{-6}	-4.8×10^{-6} $+4.8\times10^{-6}$
	0.49	0.0001016	5.9×10^{-6}	-4.2×10^{-6} $+4.2\times10^{-6}$
	0.69	2.82×10^{-5}	6×10^{-6}	-2.8×10^{-6} $+2.8\times10^{-6}$
	0.88	5.478×10^{-6}	6.3×10^{-6}	-2.5×10^{-6} $+2.5\times10^{-6}$
	1.08	-1.047×10^{-5}	7.5×10^{-6}	-2.5×10^{-6} $+2.5\times10^{-6}$
	1.28	-5.708×10^{-6}	9.4×10^{-6}	-2.5×10^{-6} $+2.5\times10^{-6}$
	1.47	1.901×10^{-5}	1.3×10^{-5}	-2.6×10^{-6} $+2.6\times10^{-6}$
	1.67	-1.629×10^{-5}	1.2×10^{-5}	-2.7×10^{-6} $+2.7\times10^{-6}$
	1.87	1.87×10^{-5}	9.2×10^{-6}	-3.1×10^{-6} $+3.1\times10^{-6}$
	2.06	3.318×10^{-5}	8.2×10^{-6}	-3.5×10^{-6} $+3.5\times10^{-6}$
	2.26	6.159×10^{-5}	7×10^{-6}	-3.8×10^{-6} $+3.8\times10^{-6}$
	2.45	8.398×10^{-5}	6.5×10^{-6}	-4.1×10^{-6} $+4.1\times10^{-6}$
	2.65	0.0001155	6×10^{-6}	-5×10^{-6} $+5\times10^{-6}$
	2.85	0.0001548	6×10^{-6}	-6.8×10^{-6} $+6.8\times10^{-6}$
	3.04	0.0001873	6×10^{-6}	-8.3×10^{-6} $+8.3\times10^{-6}$

Table C.6: **Two-particle p+p jet-induced correlation for $p_{T,\mathrm{trig}}$: 3-5 GeV/c.**

$p_{T,\mathrm{assoc}}$	$\Delta\phi$	$J(\Delta\phi_{ta})$	**Stat. Error**	**Syst. Error**
0.4-1 GeV/c	-3.04	0.005923	3.8×10^{-5}	-6.7×10^{-5} $+6.7 \times 10^{-5}$
	-2.85	0.005628	3.9×10^{-5}	-6×10^{-5} $+6 \times 10^{-5}$
	-2.65	0.004761	3.9×10^{-5}	-4.9×10^{-5} $+4.9 \times 10^{-5}$
	-2.45	0.0036	3.8×10^{-5}	-4×10^{-5} $+4 \times 10^{-5}$
	-2.26	0.002757	3.8×10^{-5}	-3.5×10^{-5} $+3.5 \times 10^{-5}$
	-2.06	0.001835	4.1×10^{-5}	-3.2×10^{-5} $+3.2 \times 10^{-5}$
	-1.87	0.0011	4.4×10^{-5}	-3×10^{-5} $+3 \times 10^{-5}$
	-1.67	0.0004083	4×10^{-5}	-2.8×10^{-5} $+2.8 \times 10^{-5}$
	-1.47	8.115×10^{-5}	3.7×10^{-5}	-2.6×10^{-5} $+2.6 \times 10^{-5}$
	-1.28	-6.948×10^{-5}	3.7×10^{-5}	-2.5×10^{-5} $+2.5 \times 10^{-5}$
	-1.08	0.0001312	3.7×10^{-5}	-2.5×10^{-5} $+2.5 \times 10^{-5}$
	-0.88	0.0006162	3.4×10^{-5}	-2.8×10^{-5} $+2.8 \times 10^{-5}$
	-0.69	0.001476	3.2×10^{-5}	-3.2×10^{-5} $+3.2 \times 10^{-5}$
	-0.49	0.003323	3.3×10^{-5}	-3.6×10^{-5} $+3.6 \times 10^{-5}$
	-0.29	0.005429	3.7×10^{-5}	-4.9×10^{-5} $+4.9 \times 10^{-5}$
	-0.10	0.006831	3.8×10^{-5}	-6.6×10^{-5} $+6.6 \times 10^{-5}$
	0.10	0.006981	3.8×10^{-5}	-6.6×10^{-5} $+6.6 \times 10^{-5}$
	0.29	0.005865	3.9×10^{-5}	-4.9×10^{-5} $+4.9 \times 10^{-5}$
	0.49	0.00347	3.6×10^{-5}	-3.6×10^{-5} $+3.6 \times 10^{-5}$
	0.69	0.001593	3.5×10^{-5}	-3.2×10^{-5} $+3.2 \times 10^{-5}$
	0.88	0.000876	4×10^{-5}	-2.8×10^{-5} $+2.8 \times 10^{-5}$
	1.08	0.0002077	4×10^{-5}	-2.5×10^{-5} $+2.5 \times 10^{-5}$
	1.28	-6.506×10^{-5}	3.7×10^{-5}	-2.5×10^{-5} $+2.5 \times 10^{-5}$
	1.47	5.044×10^{-5}	3.8×10^{-5}	-2.6×10^{-5} $+2.6 \times 10^{-5}$
	1.67	0.0004842	4.1×10^{-5}	-2.8×10^{-5} $+2.8 \times 10^{-5}$

Table C.6 – (p+p , $p_{T,\text{trig}}$: 3-5 GeV/c) continued from previous page

$p_{T,\text{assoc}}$	$\Delta\phi$	$J(\Delta\phi_{ta})$	**Stat. Error**	**Syst. Error**
	1.87	0.0009981	4.2×10^{-5}	-3×10^{-5} $+3 \times 10^{-5}$
	2.06	0.00163	3.9×10^{-5}	-3.2×10^{-5} $+3.2 \times 10^{-5}$
	2.26	0.002578	3.7×10^{-5}	-3.5×10^{-5} $+3.5 \times 10^{-5}$
	2.45	0.003608	3.9×10^{-5}	-4×10^{-5} $+4 \times 10^{-5}$
	2.65	0.004731	4×10^{-5}	-4.9×10^{-5} $+4.9 \times 10^{-5}$
	2.85	0.00552	4×10^{-5}	-6×10^{-5} $+6 \times 10^{-5}$
	3.04	0.005889	3.8×10^{-5}	-6.7×10^{-5} $+6.7 \times 10^{-5}$
1-2 GeV/c	-3.04	0.003808	2.3×10^{-5}	-2.4×10^{-5} $+2.4 \times 10^{-5}$
	-2.85	0.003372	2.2×10^{-5}	-2×10^{-5} $+2 \times 10^{-5}$
	-2.65	0.00258	2.1×10^{-5}	-1.5×10^{-5} $+1.5 \times 10^{-5}$
	-2.45	0.001828	2×10^{-5}	-1.2×10^{-5} $+1.2 \times 10^{-5}$
	-2.26	0.001218	2×10^{-5}	-1.1×10^{-5} $+1.1 \times 10^{-5}$
	-2.06	0.0008091	2×10^{-5}	-1×10^{-5} $+1 \times 10^{-5}$
	-1.87	0.0004794	2×10^{-5}	-8.8×10^{-6} $+8.8 \times 10^{-6}$
	-1.67	0.0002074	2.1×10^{-5}	-7.6×10^{-6} $+7.6 \times 10^{-6}$
	-1.47	-1.065×10^{-5}	2.1×10^{-5}	-6.9×10^{-6} $+6.9 \times 10^{-6}$
	-1.28	-0.0001307	1.8×10^{-5}	-6.7×10^{-6} $+6.7 \times 10^{-6}$
	-1.08	-8.52×10^{-5}	1.6×10^{-5}	-6.7×10^{-6} $+6.7 \times 10^{-6}$
	-0.88	9.916×10^{-5}	1.5×10^{-5}	-7.2×10^{-6} $+7.2 \times 10^{-6}$
	-0.69	0.0006104	1.5×10^{-5}	-9.7×10^{-6} $+9.7 \times 10^{-6}$
	-0.49	0.001651	1.8×10^{-5}	-1.2×10^{-5} $+1.2 \times 10^{-5}$
	-0.29	0.004152	2.1×10^{-5}	-1.5×10^{-5} $+1.5 \times 10^{-5}$
	-0.10	0.00593	2.4×10^{-5}	-2.7×10^{-5} $+2.7 \times 10^{-5}$
	0.10	0.006073	2.4×10^{-5}	-2.7×10^{-5} $+2.7 \times 10^{-5}$
	0.29	0.004301	2.2×10^{-5}	-1.5×10^{-5} $+1.5 \times 10^{-5}$
	0.49	0.001788	1.9×10^{-5}	-1.2×10^{-5} $+1.2 \times 10^{-5}$
	0.69	0.0008177	1.8×10^{-5}	-9.7×10^{-6} $+9.7 \times 10^{-6}$

Table C.6 – (p+p , $p_{T,\text{trig}}$: 3-5 GeV/c) continued from previous page

$p_{T,\text{assoc}}$	$\Delta\phi$	$J(\Delta\phi_{ta})$	**Stat. Error**	**Syst. Error**
	0.88	0.0002487	1.8×10^{-5}	-7.2 $\times 10^{-6}$ +7.2 $\times 10^{-6}$
	1.08	5.569×10^{-5}	1.8×10^{-5}	-6.7 $\times 10^{-6}$ +6.7 $\times 10^{-6}$
	1.28	-8.024×10^{-5}	2×10^{-5}	-6.7 $\times 10^{-6}$ +6.7 $\times 10^{-6}$
	1.47	-5.76×10^{-5}	2×10^{-5}	-6.9 $\times 10^{-6}$ +6.9 $\times 10^{-6}$
	1.67	9.207×10^{-5}	1.9×10^{-5}	-7.6 $\times 10^{-6}$ +7.6 $\times 10^{-6}$
	1.87	0.0003842	1.8×10^{-5}	-8.8 $\times 10^{-6}$ +8.8 $\times 10^{-6}$
	2.06	0.0006704	1.8×10^{-5}	-1 $\times 10^{-5}$ +1 $\times 10^{-5}$
	2.26	0.001149	1.9×10^{-5}	-1.1 $\times 10^{-5}$ +1.1 $\times 10^{-5}$
	2.45	0.001773	2×10^{-5}	-1.2 $\times 10^{-5}$ +1.2 $\times 10^{-5}$
	2.65	0.00259	2.1×10^{-5}	-1.5 $\times 10^{-5}$ +1.5 $\times 10^{-5}$
	2.85	0.003381	2.2×10^{-5}	-2 $\times 10^{-5}$ +2 $\times 10^{-5}$
	3.04	0.003807	2.3×10^{-5}	-2.4 $\times 10^{-5}$ +2.4 $\times 10^{-5}$
2-3 GeV/c	-3.04	0.001224	1.1×10^{-5}	-9.4 $\times 10^{-6}$ +9.4 $\times 10^{-6}$
	-2.85	0.0009798	1×10^{-5}	-6.8 $\times 10^{-6}$ +6.8 $\times 10^{-6}$
	-2.65	0.0006691	9×10^{-6}	-4.4 $\times 10^{-6}$ +4.4 $\times 10^{-6}$
	-2.45	0.0004114	8.3×10^{-6}	-4 $\times 10^{-6}$ +4 $\times 10^{-6}$
	-2.26	0.0002552	8×10^{-6}	-3.7 $\times 10^{-6}$ +3.7 $\times 10^{-6}$
	-2.06	0.0001317	7.3×10^{-6}	-2.9 $\times 10^{-6}$ +2.9 $\times 10^{-6}$
	-1.87	8.065×10^{-5}	7.2×10^{-6}	-2.2 $\times 10^{-6}$ +2.2 $\times 10^{-6}$
	-1.67	3.008×10^{-5}	7.7×10^{-6}	-1.9 $\times 10^{-6}$ +1.9 $\times 10^{-6}$
	-1.47	-2.524×10^{-5}	7.6×10^{-6}	-1.9 $\times 10^{-6}$ +1.9 $\times 10^{-6}$
	-1.28	-5.341×10^{-5}	6.1×10^{-6}	-1.8 $\times 10^{-6}$ +1.8 $\times 10^{-6}$
	-1.08	-4.632×10^{-5}	5.2×10^{-6}	-1.8 $\times 10^{-6}$ +1.8 $\times 10^{-6}$
	-0.88	-1.547×10^{-5}	5×10^{-6}	-1.9 $\times 10^{-6}$ +1.9 $\times 10^{-6}$
	-0.69	7.811×10^{-5}	5.7×10^{-6}	-2.1 $\times 10^{-6}$ +2.1 $\times 10^{-6}$
	-0.49	0.0003501	7×10^{-6}	-4.4 $\times 10^{-6}$ +4.4 $\times 10^{-6}$
	-0.29	0.001295	9.9×10^{-6}	-5.6 $\times 10^{-6}$ +5.6 $\times 10^{-6}$

Table C.6 – (p+p , $p_{T,\text{trig}}$: 3-5 GeV/c) continued from previous page

$p_{T,\text{assoc}}$	$\Delta\phi$	$J(\Delta\phi_{ta})$	**Stat. Error**	**Syst. Error**
	-0.10	0.002828	1.4×10^{-5}	-1.2×10^{-5} $+1.2 \times 10^{-5}$
	0.10	0.002917	1.4×10^{-5}	-1.2×10^{-5} $+1.2 \times 10^{-5}$
	0.29	0.001384	1×10^{-5}	-5.6×10^{-6} $+5.6 \times 10^{-6}$
	0.49	0.0004041	7.8×10^{-6}	-4.4×10^{-6} $+4.4 \times 10^{-6}$
	0.69	0.0001287	6.8×10^{-6}	-2.1×10^{-6} $+2.1 \times 10^{-6}$
	0.88	1.521×10^{-5}	6.1×10^{-6}	-1.9×10^{-6} $+1.9 \times 10^{-6}$
	1.08	-1.608×10^{-6}	6.5×10^{-6}	-1.8×10^{-6} $+1.8 \times 10^{-6}$
	1.28	-2.786×10^{-5}	7.1×10^{-6}	-1.8×10^{-6} $+1.8 \times 10^{-6}$
	1.47	-3.204×10^{-5}	7×10^{-6}	-1.9×10^{-6} $+1.9 \times 10^{-6}$
	1.67	-4.649×10^{-6}	6.6×10^{-6}	-1.9×10^{-6} $+1.9 \times 10^{-6}$
	1.87	4.515×10^{-5}	6.3×10^{-6}	-2.2×10^{-6} $+2.2 \times 10^{-6}$
	2.06	0.0001066	6.7×10^{-6}	-2.9×10^{-6} $+2.9 \times 10^{-6}$
	2.26	0.0002213	7.5×10^{-6}	-3.7×10^{-6} $+3.7 \times 10^{-6}$
	2.45	0.0003933	8.1×10^{-6}	-4×10^{-6} $+4 \times 10^{-6}$
	2.65	0.0006521	8.9×10^{-6}	-4.4×10^{-6} $+4.4 \times 10^{-6}$
	2.85	0.0009849	1×10^{-5}	-6.8×10^{-6} $+6.8 \times 10^{-6}$
	3.04	0.001225	1.1×10^{-5}	-9.4×10^{-6} $+9.4 \times 10^{-6}$
3-5 GeV/c	-3.04	0.0006885	8×10^{-6}	-5.8×10^{-6} $+5.8 \times 10^{-6}$
	-2.85	0.0004993	6.8×10^{-6}	-3.7×10^{-6} $+3.7 \times 10^{-6}$
	-2.65	0.0003106	5.7×10^{-6}	-2.4×10^{-6} $+2.4 \times 10^{-6}$
	-2.45	0.000166	4.8×10^{-6}	-2.4×10^{-6} $+2.4 \times 10^{-6}$
	-2.26	9.115×10^{-5}	4.4×10^{-6}	-1.9×10^{-6} $+1.9 \times 10^{-6}$
	-2.06	4.895×10^{-5}	4×10^{-6}	-1.2×10^{-6} $+1.2 \times 10^{-6}$
	-1.87	2.661×10^{-5}	3.7×10^{-6}	-8.7×10^{-7} $+8.7 \times 10^{-7}$
	-1.67	1.383×10^{-5}	4.1×10^{-6}	-8.2×10^{-7} $+8.2 \times 10^{-7}$
	-1.47	-5.485×10^{-6}	3.9×10^{-6}	-8.1×10^{-7} $+8.1 \times 10^{-7}$
	-1.28	-1.958×10^{-5}	2.9×10^{-6}	-8.1×10^{-7} $+8.1 \times 10^{-7}$

Table C.6 – (p+p , $p_{T,\text{trig}}$: 3-5 GeV/c) continued from previous page

$p_{T,\text{assoc}}$	$\Delta\phi$	$J(\Delta\phi_{ta})$	**Stat. Error**	**Syst. Error**
	-1.08	-2.302×10^{-5}	2.3×10^{-6}	-8.1×10^{-7} +8.1×10^{-7}
	-0.88	-1.432×10^{-5}	2.3×10^{-6}	-8.1×10^{-7} +8.1×10^{-7}
	-0.69	1.147×10^{-5}	2.7×10^{-6}	-8.2×10^{-7} +8.2×10^{-7}
	-0.49	9.496×10^{-5}	3.5×10^{-6}	-1.8×10^{-6} +1.8×10^{-6}
	-0.29	0.0005366	6.1×10^{-6}	-4×10^{-6} +4×10^{-6}
	-0.10	0.001714	1×10^{-5}	-8.3×10^{-6} +8.3×10^{-6}
	0.10	0.00178	1.1×10^{-5}	-8.3×10^{-6} +8.3×10^{-6}
	0.29	0.0005811	6.5×10^{-6}	-4×10^{-6} +4×10^{-6}
	0.49	0.0001214	4.1×10^{-6}	-1.8×10^{-6} +1.8×10^{-6}
	0.69	3.207×10^{-5}	3.4×10^{-6}	-8.2×10^{-7} +8.2×10^{-7}
	0.88	1.761×10^{-6}	2.9×10^{-6}	-8.1×10^{-7} +8.1×10^{-7}
	1.08	-7.847×10^{-6}	3.1×10^{-6}	-8.1×10^{-7} +8.1×10^{-7}
	1.28	-9.267×10^{-6}	3.5×10^{-6}	-8.1×10^{-7} +8.1×10^{-7}
	1.47	-1.489×10^{-5}	3.3×10^{-6}	-8.1×10^{-7} +8.1×10^{-7}
	1.67	-3.815×10^{-6}	3.2×10^{-6}	-8.2×10^{-7} +8.2×10^{-7}
	1.87	1.135×10^{-5}	3.1×10^{-6}	-8.7×10^{-7} +8.7×10^{-7}
	2.06	3.262×10^{-5}	3.4×10^{-6}	-1.2×10^{-6} +1.2×10^{-6}
	2.26	8.008×10^{-5}	4.1×10^{-6}	-1.9×10^{-6} +1.9×10^{-6}
	2.45	0.0001575	4.6×10^{-6}	-2.4×10^{-6} +2.4×10^{-6}
	2.65	0.0003015	5.6×10^{-6}	-2.4×10^{-6} +2.4×10^{-6}
	2.85	0.0005008	6.8×10^{-6}	-3.7×10^{-6} +3.7×10^{-6}
	3.04	0.0006924	8×10^{-6}	-5.8×10^{-6} +5.8×10^{-6}

Table C.7: **Two-particle 0-20% Au+Au jet-induced correlation for $p_{T,\mathrm{trig}}$: 3-5 GeV/c.**

$p_{T,\mathrm{assoc}}$	$\Delta\phi$	$J(\Delta\phi_{ta})$	**Stat. Error**	**Syst. Error**
0.4-1 GeV/c	-3.04	0.001599	3.3×10^{-5}	-0.00015 +0.00015
	-2.85	0.001318	3.3×10^{-5}	-0.00014 +0.00014
	-2.65	0.00107	3.5×10^{-5}	-0.00012 +0.00012
	-2.45	0.001094	3.8×10^{-5}	-0.00011 +0.00011
	-2.26	0.0009847	4.3×10^{-5}	-9.4×10^{-5} $+9.4 \times 10^{-5}$
	-2.06	0.00094	4.9×10^{-5}	-8.4×10^{-5} $+8.4 \times 10^{-5}$
	-1.87	0.000877	5.9×10^{-5}	-7.8×10^{-5} $+7.8 \times 10^{-5}$
	-1.67	0.0005808	7.2×10^{-5}	-7.4×10^{-5} $+7.4 \times 10^{-5}$
	-1.47	0.0004145	7.7×10^{-5}	-7.1×10^{-5} $+7.1 \times 10^{-5}$
	-1.28	0.0002156	6×10^{-5}	-6.8×10^{-5} $+6.8 \times 10^{-5}$
	-1.08	-1.191×10^{-5}	4.7×10^{-5}	-6.7×10^{-5} $+6.7 \times 10^{-5}$
	-0.88	8.129×10^{-6}	4×10^{-5}	-7×10^{-5} $+7 \times 10^{-5}$
	-0.69	0.0003112	3.7×10^{-5}	-7.5×10^{-5} $+7.5 \times 10^{-5}$
	-0.49	0.0008234	3.4×10^{-5}	-8.6×10^{-5} $+8.6 \times 10^{-5}$
	-0.29	0.00168	3.2×10^{-5}	-0.00011 +0.00011
	-0.10	0.002192	3.4×10^{-5}	-0.00013 +0.00013
	0.10	0.002216	3.4×10^{-5}	-0.00013 +0.00013
	0.29	0.001698	3.2×10^{-5}	-0.00011 +0.00011
	0.49	0.0008242	3.5×10^{-5}	-8.6×10^{-5} $+8.6 \times 10^{-5}$
	0.69	0.000402	3.7×10^{-5}	-7.5×10^{-5} $+7.5 \times 10^{-5}$
	0.88	-5.128×10^{-5}	4.1×10^{-5}	-7×10^{-5} $+7 \times 10^{-5}$
	1.08	-6.8×10^{-5}	4.9×10^{-5}	-6.7×10^{-5} $+6.7 \times 10^{-5}$
	1.28	0.0001735	6.2×10^{-5}	-6.8×10^{-5} $+6.8 \times 10^{-5}$
	1.47	0.0002659	7.3×10^{-5}	-7.1×10^{-5} $+7.1 \times 10^{-5}$
	1.67	0.0005471	7×10^{-5}	-7.4×10^{-5} $+7.4 \times 10^{-5}$

Table C.7 – (0-20% Au+Au, $p_{T,\text{trig}}$: 3-5 GeV/c) continued from previous page

$p_{T,\text{assoc}}$	$\Delta\phi$	$J(\Delta\phi_{ta})$	**Stat. Error**	**Syst. Error**
	1.87	0.0007522	5.8×10^{-5}	-7.8 $\times 10^{-5}$ +7.8 $\times 10^{-5}$
	2.06	0.0009136	4.9×10^{-5}	-8.4 $\times 10^{-5}$ +8.4 $\times 10^{-5}$
	2.26	0.0009313	4.3×10^{-5}	-9.4 $\times 10^{-5}$ +9.4 $\times 10^{-5}$
	2.45	0.001035	3.8×10^{-5}	-0.00011 +0.00011
	2.65	0.00107	3.5×10^{-5}	-0.00012 +0.00012
	2.85	0.001296	3.3×10^{-5}	-0.00014 +0.00014
	3.04	0.001639	3.3×10^{-5}	-0.00015 +0.00015
1-2 GeV/c	-3.04	0.000504	1.5×10^{-5}	-9.7 $\times 10^{-5}$ +9.7 $\times 10^{-5}$
	-2.85	0.0004465	1.5×10^{-5}	-9.3 $\times 10^{-5}$ +9.3 $\times 10^{-5}$
	-2.65	0.0003938	1.6×10^{-5}	-8.6 $\times 10^{-5}$ +8.6 $\times 10^{-5}$
	-2.45	0.0003816	1.7×10^{-5}	-7.7 $\times 10^{-5}$ +7.7 $\times 10^{-5}$
	-2.26	0.0003774	1.9×10^{-5}	-6.8 $\times 10^{-5}$ +6.8 $\times 10^{-5}$
	-2.06	0.0004068	2.3×10^{-5}	-6.1 $\times 10^{-5}$ +6.1 $\times 10^{-5}$
	-1.87	0.0003729	2.6×10^{-5}	-5.6 $\times 10^{-5}$ +5.6 $\times 10^{-5}$
	-1.67	0.0003293	3.4×10^{-5}	-5.3 $\times 10^{-5}$ +5.3 $\times 10^{-5}$
	-1.47	0.0002175	3.6×10^{-5}	-5 $\times 10^{-5}$ +5 $\times 10^{-5}$
	-1.28	0.000107	2.7×10^{-5}	-4.8 $\times 10^{-5}$ +4.8 $\times 10^{-5}$
	-1.08	-2.035×10^{-5}	2.2×10^{-5}	-4.7 $\times 10^{-5}$ +4.7 $\times 10^{-5}$
	-0.88	3.783×10^{-5}	1.8×10^{-5}	-4.7 $\times 10^{-5}$ +4.7 $\times 10^{-5}$
	-0.69	0.0002058	1.7×10^{-5}	-4.9 $\times 10^{-5}$ +4.9 $\times 10^{-5}$
	-0.49	0.0006039	1.6×10^{-5}	-5.4 $\times 10^{-5}$ +5.4 $\times 10^{-5}$
	-0.29	0.001059	1.5×10^{-5}	-6.5 $\times 10^{-5}$ +6.5 $\times 10^{-5}$
	-0.10	0.001571	1.5×10^{-5}	-7.7 $\times 10^{-5}$ +7.7 $\times 10^{-5}$
	0.10	0.00157	1.6×10^{-5}	-7.7 $\times 10^{-5}$ +7.7 $\times 10^{-5}$
	0.29	0.001019	1.5×10^{-5}	-6.5 $\times 10^{-5}$ +6.5 $\times 10^{-5}$
	0.49	0.0006094	1.6×10^{-5}	-5.4 $\times 10^{-5}$ +5.4 $\times 10^{-5}$
	0.69	0.0002076	1.7×10^{-5}	-4.9 $\times 10^{-5}$ +4.9 $\times 10^{-5}$

Table C.7 – (0-20% Au+Au, $p_{T,\text{trig}}$: 3-5 GeV/c) continued from previous page

$p_{T,\text{assoc}}$	$\Delta\phi$	$J(\Delta\phi_{ta})$	**Stat. Error**	**Syst. Error**
	0.88	2.846×10^{-5}	1.9×10^{-5}	-4.7×10^{-5} $+4.7 \times 10^{-5}$
	1.08	-2.049×10^{-5}	2.2×10^{-5}	-4.7×10^{-5} $+4.7 \times 10^{-5}$
	1.28	0.0001521	2.8×10^{-5}	-4.8×10^{-5} $+4.8 \times 10^{-5}$
	1.47	0.0002238	3.6×10^{-5}	-5×10^{-5} $+5 \times 10^{-5}$
	1.67	0.0003915	3.4×10^{-5}	-5.3×10^{-5} $+5.3 \times 10^{-5}$
	1.87	0.0003848	2.6×10^{-5}	-5.6×10^{-5} $+5.6 \times 10^{-5}$
	2.06	0.0004336	2.3×10^{-5}	-6.1×10^{-5} $+6.1 \times 10^{-5}$
	2.26	0.000391	1.9×10^{-5}	-6.8×10^{-5} $+6.8 \times 10^{-5}$
	2.45	0.0003778	1.7×10^{-5}	-7.7×10^{-5} $+7.7 \times 10^{-5}$
	2.65	0.0004208	1.6×10^{-5}	-8.6×10^{-5} $+8.6 \times 10^{-5}$
	2.85	0.0003991	1.5×10^{-5}	-9.3×10^{-5} $+9.3 \times 10^{-5}$
	3.04	0.0004954	1.5×10^{-5}	-9.7×10^{-5} $+9.7 \times 10^{-5}$
2-3 GeV/c	-3.04	3.083×10^{-5}	4.1×10^{-6}	-1.1×10^{-5} $+1.1 \times 10^{-5}$
	-2.85	2.759×10^{-5}	4.2×10^{-6}	-1×10^{-5} $+1 \times 10^{-5}$
	-2.65	1.338×10^{-5}	4.3×10^{-6}	-9×10^{-6} $+9 \times 10^{-6}$
	-2.45	1.59×10^{-5}	4.8×10^{-6}	-7.6×10^{-6} $+7.6 \times 10^{-6}$
	-2.26	2.805×10^{-5}	5.4×10^{-6}	-6.5×10^{-6} $+6.5 \times 10^{-6}$
	-2.06	3.353×10^{-5}	6.4×10^{-6}	-5.9×10^{-6} $+5.9 \times 10^{-6}$
	-1.87	3.039×10^{-5}	7.2×10^{-6}	-5.5×10^{-6} $+5.5 \times 10^{-6}$
	-1.67	2.902×10^{-5}	9.3×10^{-6}	-5.2×10^{-6} $+5.2 \times 10^{-6}$
	-1.47	1.211×10^{-6}	9.9×10^{-6}	-5×10^{-6} $+5 \times 10^{-6}$
	-1.28	1.283×10^{-5}	7.5×10^{-6}	-4.7×10^{-6} $+4.7 \times 10^{-6}$
	-1.08	7.112×10^{-7}	6.1×10^{-6}	-4.5×10^{-6} $+4.5 \times 10^{-6}$
	-0.88	7.484×10^{-6}	5×10^{-6}	-4.5×10^{-6} $+4.5 \times 10^{-6}$
	-0.69	3.388×10^{-5}	4.7×10^{-6}	-5.1×10^{-6} $+5.1 \times 10^{-6}$
	-0.49	0.0001033	4.3×10^{-6}	-5.7×10^{-6} $+5.7 \times 10^{-6}$
	-0.29	0.0002313	4×10^{-6}	-7.4×10^{-6} $+7.4 \times 10^{-6}$

Table C.7 – (0-20% Au+Au, $p_{T,\mathrm{trig}}$: 3-5 GeV/c) continued from previous page

$p_{T,\mathrm{assoc}}$	$\Delta\phi$	$J(\Delta\phi_{ta})$	**Stat. Error**	**Syst. Error**
	-0.10	0.0003761	4.1×10^{-6}	-1.1×10^{-5} $+1.1 \times 10^{-5}$
	0.10	0.0003833	4.1×10^{-6}	-1.1×10^{-5} $+1.1 \times 10^{-5}$
	0.29	0.0002199	4×10^{-6}	-7.4×10^{-6} $+7.4 \times 10^{-6}$
	0.49	0.0001169	4.4×10^{-6}	-5.7×10^{-6} $+5.7 \times 10^{-6}$
	0.69	3.099×10^{-5}	4.8×10^{-6}	-5.1×10^{-6} $+5.1 \times 10^{-6}$
	0.88	-7.713×10^{-6}	5.1×10^{-6}	-4.5×10^{-6} $+4.5 \times 10^{-6}$
	1.08	2.48×10^{-6}	6.1×10^{-6}	-4.5×10^{-6} $+4.5 \times 10^{-6}$
	1.28	1.187×10^{-5}	7.5×10^{-6}	-4.7×10^{-6} $+4.7 \times 10^{-6}$
	1.47	1.253×10^{-5}	1×10^{-5}	-5×10^{-6} $+5 \times 10^{-6}$
	1.67	3.832×10^{-5}	9.3×10^{-6}	-5.2×10^{-6} $+5.2 \times 10^{-6}$
	1.87	4.165×10^{-5}	7.2×10^{-6}	-5.5×10^{-6} $+5.5 \times 10^{-6}$
	2.06	2.013×10^{-5}	6.4×10^{-6}	-5.9×10^{-6} $+5.9 \times 10^{-6}$
	2.26	3.011×10^{-5}	5.3×10^{-6}	-6.5×10^{-6} $+6.5 \times 10^{-6}$
	2.45	2.205×10^{-5}	4.8×10^{-6}	-7.6×10^{-6} $+7.6 \times 10^{-6}$
	2.65	1.486×10^{-5}	4.3×10^{-6}	-9×10^{-6} $+9 \times 10^{-6}$
	2.85	2.934×10^{-5}	4.2×10^{-6}	-1×10^{-5} $+1 \times 10^{-5}$
	3.04	3.025×10^{-5}	4.1×10^{-6}	-1.1×10^{-5} $+1.1 \times 10^{-5}$
3-5 GeV/c	-3.04	4.291×10^{-6}	1.3×10^{-6}	-2.3×10^{-6} $+2.3 \times 10^{-6}$
	-2.85	2.41×10^{-6}	1.4×10^{-6}	-1.6×10^{-6} $+1.6 \times 10^{-6}$
	-2.65	-1.958×10^{-6}	1.4×10^{-6}	-1.1×10^{-6} $+1.1 \times 10^{-6}$
	-2.45	1.261×10^{-6}	1.6×10^{-6}	-1.1×10^{-6} $+1.1 \times 10^{-6}$
	-2.26	-2.769×10^{-6}	1.7×10^{-6}	-9.2×10^{-7} $+9.2 \times 10^{-7}$
	-2.06	5.028×10^{-6}	2.1×10^{-6}	-7.4×10^{-7} $+7.4 \times 10^{-7}$
	-1.87	2.401×10^{-6}	2.4×10^{-6}	-6.5×10^{-7} $+6.5 \times 10^{-7}$
	-1.67	4.404×10^{-6}	3.1×10^{-6}	-6.3×10^{-7} $+6.3 \times 10^{-7}$
	-1.47	3.396×10^{-6}	3.3×10^{-6}	-6.3×10^{-7} $+6.3 \times 10^{-7}$
	-1.28	1.486×10^{-6}	2.5×10^{-6}	-6.3×10^{-7} $+6.3 \times 10^{-7}$

Table C.7 – (0-20% Au+Au, $p_{T,\mathrm{trig}}$: 3-5 GeV/c) continued from previous page

$p_{T,\mathrm{assoc}}$	$\Delta\phi$	$J(\Delta\phi_{ta})$	**Stat. Error**	**Syst. Error**
	-1.08	-5.466×10^{-6}	2×10^{-6}	-6.3×10^{-7} $+6.3\times10^{-7}$
	-0.88	-1.837×10^{-6}	1.7×10^{-6}	-6.3×10^{-7} $+6.3\times10^{-7}$
	-0.69	5.938×10^{-6}	1.6×10^{-6}	-6.7×10^{-7} $+6.7\times10^{-7}$
	-0.49	1.661×10^{-5}	1.4×10^{-6}	-9.8×10^{-7} $+9.8\times10^{-7}$
	-0.29	4.56×10^{-5}	1.4×10^{-6}	-1.2×10^{-6} $+1.2\times10^{-6}$
	-0.10	0.0001105	1.5×10^{-6}	-2.3×10^{-6} $+2.3\times10^{-6}$
	0.10	0.0001098	1.5×10^{-6}	-2.3×10^{-6} $+2.3\times10^{-6}$
	0.29	4.628×10^{-5}	1.4×10^{-6}	-1.2×10^{-6} $+1.2\times10^{-6}$
	0.49	1.688×10^{-5}	1.4×10^{-6}	-9.8×10^{-7} $+9.8\times10^{-7}$
	0.69	6.081×10^{-6}	1.6×10^{-6}	-6.7×10^{-7} $+6.7\times10^{-7}$
	0.88	-1.645×10^{-6}	1.7×10^{-6}	-6.3×10^{-7} $+6.3\times10^{-7}$
	1.08	-5.402×10^{-6}	2×10^{-6}	-6.3×10^{-7} $+6.3\times10^{-7}$
	1.28	9.333×10^{-7}	2.5×10^{-6}	-6.3×10^{-7} $+6.3\times10^{-7}$
	1.47	2.38×10^{-6}	3.3×10^{-6}	-6.3×10^{-7} $+6.3\times10^{-7}$
	1.67	4.768×10^{-6}	3.1×10^{-6}	-6.3×10^{-7} $+6.3\times10^{-7}$
	1.87	2.448×10^{-6}	2.4×10^{-6}	-6.5×10^{-7} $+6.5\times10^{-7}$
	2.06	5.34×10^{-6}	2.1×10^{-6}	-7.4×10^{-7} $+7.4\times10^{-7}$
	2.26	-2.63×10^{-6}	1.7×10^{-6}	-9.2×10^{-7} $+9.2\times10^{-7}$
	2.45	1.482×10^{-6}	1.6×10^{-6}	-1.1×10^{-6} $+1.1\times10^{-6}$
	2.65	-1.755×10^{-6}	1.4×10^{-6}	-1.1×10^{-6} $+1.1\times10^{-6}$
	2.85	2.049×10^{-6}	1.4×10^{-6}	-1.6×10^{-6} $+1.6\times10^{-6}$
	3.04	4.44×10^{-6}	1.3×10^{-6}	-2.3×10^{-6} $+2.3\times10^{-6}$

Table C.8: **Two-particle 20-40% Au+Au jet-induced correlation for $p_{T,\mathrm{trig}}$: 3-5 GeV/c.**

$p_{T,\mathrm{assoc}}$	$\Delta\phi$	$J(\Delta\phi_{ta})$	**Stat. Error**	**Syst. Error**
0.4-1 GeV/c	-3.04	0.001834	3.4×10^{-5}	-0.00026 +0.00026
	-2.85	0.001706	3.5×10^{-5}	-0.00025 +0.00025
	-2.65	0.001692	3.6×10^{-5}	-0.00023 +0.00023
	-2.45	0.001574	4×10^{-5}	-0.0002 +0.0002
	-2.26	0.001477	4.5×10^{-5}	-0.00017 +0.00017
	-2.06	0.001327	5.1×10^{-5}	-0.00016 +0.00016
	-1.87	0.001059	6.2×10^{-5}	-0.00015 +0.00015
	-1.67	0.0007088	7.6×10^{-5}	-0.00014 +0.00014
	-1.47	0.0005004	8.1×10^{-5}	-0.00013 +0.00013
	-1.28	0.0001921	6.3×10^{-5}	-0.00013 +0.00013
	-1.08	0.0001028	5×10^{-5}	-0.00013 +0.00013
	-0.88	0.000191	4.2×10^{-5}	-0.00014 +0.00014
	-0.69	0.0005282	3.8×10^{-5}	-0.00015 +0.00015
	-0.49	0.001148	3.6×10^{-5}	-0.00018 +0.00018
	-0.29	0.002065	3.4×10^{-5}	-0.00022 +0.00022
	-0.10	0.002589	3.6×10^{-5}	-0.00024 +0.00024
	0.10	0.002708	3.6×10^{-5}	-0.00024 +0.00024
	0.29	0.002006	3.4×10^{-5}	-0.00022 +0.00022
	0.49	0.001178	3.7×10^{-5}	-0.00018 +0.00018
	0.69	0.0005352	3.9×10^{-5}	-0.00015 +0.00015
	0.88	0.0001452	4.3×10^{-5}	-0.00014 +0.00014
	1.08	-6.799×10^{-5}	5.1×10^{-5}	-0.00013 +0.00013
	1.28	0.0001314	6.5×10^{-5}	-0.00013 +0.00013
	1.47	0.0005018	7.7×10^{-5}	-0.00013 +0.00013
	1.67	0.0008209	7.4×10^{-5}	-0.00014 +0.00014

Table C.8 – (20-40% Au+Au, $p_{T,\text{trig}}$: 3-5 GeV/c) continued from previous page

$p_{T,\text{assoc}}$	$\Delta\phi$	$J(\Delta\phi_{ta})$	**Stat. Error**	**Syst. Error**
	1.87	0.001031	6×10^{-5}	-0.00015 +0.00015
	2.06	0.00138	5.1×10^{-5}	-0.00016 +0.00016
	2.26	0.001571	4.5×10^{-5}	-0.00017 +0.00017
	2.45	0.001577	4×10^{-5}	-0.0002 +0.0002
	2.65	0.001618	3.6×10^{-5}	-0.00023 +0.00023
	2.85	0.001743	3.5×10^{-5}	-0.00025 +0.00025
	3.04	0.001821	3.4×10^{-5}	-0.00026 +0.00026
1-2 GeV/c	-3.04	0.0006803	1.6×10^{-5}	-8.3×10^{-5} $+8.3 \times 10^{-5}$
	-2.85	0.0006625	1.6×10^{-5}	-7.9×10^{-5} $+7.9 \times 10^{-5}$
	-2.65	0.0006508	1.7×10^{-5}	-7×10^{-5} $+7 \times 10^{-5}$
	-2.45	0.0006412	1.8×10^{-5}	-6.1×10^{-5} $+6.1 \times 10^{-5}$
	-2.26	0.0006687	2×10^{-5}	-5.3×10^{-5} $+5.3 \times 10^{-5}$
	-2.06	0.000618	2.4×10^{-5}	-4.8×10^{-5} $+4.8 \times 10^{-5}$
	-1.87	0.0005237	2.8×10^{-5}	-4.5×10^{-5} $+4.5 \times 10^{-5}$
	-1.67	0.0003844	3.5×10^{-5}	-4.2×10^{-5} $+4.2 \times 10^{-5}$
	-1.47	0.000133	3.9×10^{-5}	-4×10^{-5} $+4 \times 10^{-5}$
	-1.28	0.0001253	2.8×10^{-5}	-3.9×10^{-5} $+3.9 \times 10^{-5}$
	-1.08	-4.838×10^{-6}	2.3×10^{-5}	-4×10^{-5} $+4 \times 10^{-5}$
	-0.88	6.558×10^{-5}	1.9×10^{-5}	-4.2×10^{-5} $+4.2 \times 10^{-5}$
	-0.69	0.000308	1.8×10^{-5}	-4.6×10^{-5} $+4.6 \times 10^{-5}$
	-0.49	0.0007615	1.7×10^{-5}	-5.4×10^{-5} $+5.4 \times 10^{-5}$
	-0.29	0.001395	1.6×10^{-5}	-6.7×10^{-5} $+6.7 \times 10^{-5}$
	-0.10	0.00193	1.7×10^{-5}	-7.8×10^{-5} $+7.8 \times 10^{-5}$
	0.10	0.001952	1.7×10^{-5}	-7.8×10^{-5} $+7.8 \times 10^{-5}$
	0.29	0.001393	1.6×10^{-5}	-6.7×10^{-5} $+6.7 \times 10^{-5}$
	0.49	0.0007949	1.7×10^{-5}	-5.4×10^{-5} $+5.4 \times 10^{-5}$
	0.69	0.0002928	1.8×10^{-5}	-4.6×10^{-5} $+4.6 \times 10^{-5}$

Table C.8 – (20-40% Au+Au, $p_{T,\mathrm{trig}}$: 3-5 GeV/c) continued from previous page

$p_{T,\mathrm{assoc}}$	$\Delta\phi$	$J(\Delta\phi_{ta})$	**Stat. Error**	**Syst. Error**
	0.88	6.476×10^{-5}	1.9×10^{-5}	-4.2×10^{-5} $+4.2 \times 10^{-5}$
	1.08	-2.435×10^{-6}	2.3×10^{-5}	-4×10^{-5} $+4 \times 10^{-5}$
	1.28	0.0001052	2.9×10^{-5}	-3.9×10^{-5} $+3.9 \times 10^{-5}$
	1.47	0.0003518	3.8×10^{-5}	-4×10^{-5} $+4 \times 10^{-5}$
	1.67	0.000413	3.5×10^{-5}	-4.2×10^{-5} $+4.2 \times 10^{-5}$
	1.87	0.0005836	2.8×10^{-5}	-4.5×10^{-5} $+4.5 \times 10^{-5}$
	2.06	0.000649	2.4×10^{-5}	-4.8×10^{-5} $+4.8 \times 10^{-5}$
	2.26	0.0006469	2×10^{-5}	-5.3×10^{-5} $+5.3 \times 10^{-5}$
	2.45	0.000675	1.8×10^{-5}	-6.1×10^{-5} $+6.1 \times 10^{-5}$
	2.65	0.0006268	1.7×10^{-5}	-7×10^{-5} $+7 \times 10^{-5}$
	2.85	0.0006414	1.6×10^{-5}	-7.9×10^{-5} $+7.9 \times 10^{-5}$
	3.04	0.0006656	1.6×10^{-5}	-8.3×10^{-5} $+8.3 \times 10^{-5}$
2-3 GeV/c	-3.04	8.248×10^{-5}	4.5×10^{-6}	-1×10^{-5} $+1 \times 10^{-5}$
	-2.85	6.939×10^{-5}	4.6×10^{-6}	-9.1×10^{-6} $+9.1 \times 10^{-6}$
	-2.65	6.95×10^{-5}	4.7×10^{-6}	-7.6×10^{-6} $+7.6 \times 10^{-6}$
	-2.45	7.659×10^{-5}	5.2×10^{-6}	-6.3×10^{-6} $+6.3 \times 10^{-6}$
	-2.26	7.934×10^{-5}	5.8×10^{-6}	-5.5×10^{-6} $+5.5 \times 10^{-6}$
	-2.06	7.557×10^{-5}	6.8×10^{-6}	-5.1×10^{-6} $+5.1 \times 10^{-6}$
	-1.87	6.437×10^{-5}	7.7×10^{-6}	-4.8×10^{-6} $+4.8 \times 10^{-6}$
	-1.67	5.134×10^{-5}	9.9×10^{-6}	-4.4×10^{-6} $+4.4 \times 10^{-6}$
	-1.47	2.99×10^{-5}	1.1×10^{-5}	-4.2×10^{-6} $+4.2 \times 10^{-6}$
	-1.28	4.778×10^{-6}	7.9×10^{-6}	-4×10^{-6} $+4 \times 10^{-6}$
	-1.08	8.564×10^{-6}	6.4×10^{-6}	-4×10^{-6} $+4 \times 10^{-6}$
	-0.88	7.557×10^{-6}	5.4×10^{-6}	-4.4×10^{-6} $+4.4 \times 10^{-6}$
	-0.69	6.204×10^{-5}	5.1×10^{-6}	-5.1×10^{-6} $+5.1 \times 10^{-6}$
	-0.49	0.000158	4.8×10^{-6}	-5.7×10^{-6} $+5.7 \times 10^{-6}$
	-0.29	0.0003115	4.5×10^{-6}	-7.7×10^{-6} $+7.7 \times 10^{-6}$

Table C.8 – (20-40% Au+Au, $p_{T,\mathrm{trig}}$: 3-5 GeV/c) continued from previous page

$p_{T,\mathrm{assoc}}$	$\Delta\phi$	$J(\Delta\phi_{ta})$	**Stat. Error**	**Syst. Error**
	-0.10	0.000527	4.7×10^{-6}	-1.1×10^{-5} $+1.1 \times 10^{-5}$
	0.10	0.0005328	4.7×10^{-6}	-1.1×10^{-5} $+1.1 \times 10^{-5}$
	0.29	0.00033	4.5×10^{-6}	-7.7×10^{-6} $+7.7 \times 10^{-6}$
	0.49	0.0001499	4.8×10^{-6}	-5.7×10^{-6} $+5.7 \times 10^{-6}$
	0.69	6.056×10^{-5}	5.2×10^{-6}	-5.1×10^{-6} $+5.1 \times 10^{-6}$
	0.88	1.297×10^{-5}	5.4×10^{-6}	-4.4×10^{-6} $+4.4 \times 10^{-6}$
	1.08	1.799×10^{-5}	6.5×10^{-6}	-4×10^{-6} $+4 \times 10^{-6}$
	1.28	1.036×10^{-5}	8×10^{-6}	-4×10^{-6} $+4 \times 10^{-6}$
	1.47	3.077×10^{-5}	1.1×10^{-5}	-4.2×10^{-6} $+4.2 \times 10^{-6}$
	1.67	6.56×10^{-5}	1×10^{-5}	-4.4×10^{-6} $+4.4 \times 10^{-6}$
	1.87	7.44×10^{-5}	7.7×10^{-6}	-4.8×10^{-6} $+4.8 \times 10^{-6}$
	2.06	6.863×10^{-5}	6.8×10^{-6}	-5.1×10^{-6} $+5.1 \times 10^{-6}$
	2.26	7.057×10^{-5}	5.7×10^{-6}	-5.5×10^{-6} $+5.5 \times 10^{-6}$
	2.45	7.052×10^{-5}	5.2×10^{-6}	-6.3×10^{-6} $+6.3 \times 10^{-6}$
	2.65	6.846×10^{-5}	4.7×10^{-6}	-7.6×10^{-6} $+7.6 \times 10^{-6}$
	2.85	7.877×10^{-5}	4.6×10^{-6}	-9.1×10^{-6} $+9.1 \times 10^{-6}$
	3.04	7.898×10^{-5}	4.5×10^{-6}	-1×10^{-5} $+1 \times 10^{-5}$
3-5 GeV/c	-3.04	2.099×10^{-5}	1.6×10^{-6}	-2.2×10^{-6} $+2.2 \times 10^{-6}$
	-2.85	1.268×10^{-5}	1.6×10^{-6}	-1.7×10^{-6} $+1.7 \times 10^{-6}$
	-2.65	1.619×10^{-5}	1.6×10^{-6}	-1.3×10^{-6} $+1.3 \times 10^{-6}$
	-2.45	9.13×10^{-6}	1.8×10^{-6}	-1.1×10^{-6} $+1.1 \times 10^{-6}$
	-2.26	1.054×10^{-5}	2×10^{-6}	-1×10^{-6} $+1 \times 10^{-6}$
	-2.06	1.005×10^{-5}	2.4×10^{-6}	-8.9×10^{-7} $+8.9 \times 10^{-7}$
	-1.87	8.532×10^{-6}	2.6×10^{-6}	-7.8×10^{-7} $+7.8 \times 10^{-7}$
	-1.67	6.371×10^{-6}	3.4×10^{-6}	-7.2×10^{-7} $+7.2 \times 10^{-7}$
	-1.47	6.258×10^{-6}	3.7×10^{-6}	-7×10^{-7} $+7 \times 10^{-7}$
	-1.28	2.841×10^{-6}	2.7×10^{-6}	-7×10^{-7} $+7 \times 10^{-7}$

Table C.8 – (20-40% Au+Au, $p_{T,\mathrm{trig}}$: 3-5 GeV/c) continued from previous page

$p_{T,\mathrm{assoc}}$	$\Delta\phi$	$J(\Delta\phi_{ta})$	**Stat. Error**	**Syst. Error**
	-1.08	8.109×10^{-7}	2.2×10^{-6}	-7×10^{-7} $+7 \times 10^{-7}$
	-0.88	2.571×10^{-6}	1.8×10^{-6}	-7×10^{-7} $+7 \times 10^{-7}$
	-0.69	8.066×10^{-6}	1.8×10^{-6}	-7.6×10^{-7} $+7.6 \times 10^{-7}$
	-0.49	2.592×10^{-5}	1.6×10^{-6}	-1.2×10^{-6} $+1.2 \times 10^{-6}$
	-0.29	7.288×10^{-5}	1.6×10^{-6}	-1.3×10^{-6} $+1.3 \times 10^{-6}$
	-0.10	0.0001761	1.8×10^{-6}	-2.7×10^{-6} $+2.7 \times 10^{-6}$
	0.10	0.000176	1.8×10^{-6}	-2.7×10^{-6} $+2.7 \times 10^{-6}$
	0.29	7.308×10^{-5}	1.6×10^{-6}	-1.3×10^{-6} $+1.3 \times 10^{-6}$
	0.49	2.562×10^{-5}	1.6×10^{-6}	-1.2×10^{-6} $+1.2 \times 10^{-6}$
	0.69	8.189×10^{-6}	1.8×10^{-6}	-7.6×10^{-7} $+7.6 \times 10^{-7}$
	0.88	2.692×10^{-6}	1.8×10^{-6}	-7×10^{-7} $+7 \times 10^{-7}$
	1.08	1.192×10^{-6}	2.2×10^{-6}	-7×10^{-7} $+7 \times 10^{-7}$
	1.28	3.117×10^{-6}	2.7×10^{-6}	-7×10^{-7} $+7 \times 10^{-7}$
	1.47	6.223×10^{-6}	3.7×10^{-6}	-7×10^{-7} $+7 \times 10^{-7}$
	1.67	6.282×10^{-6}	3.4×10^{-6}	-7.2×10^{-7} $+7.2 \times 10^{-7}$
	1.87	9.133×10^{-6}	2.6×10^{-6}	-7.8×10^{-7} $+7.8 \times 10^{-7}$
	2.06	9.153×10^{-6}	2.3×10^{-6}	-8.9×10^{-7} $+8.9 \times 10^{-7}$
	2.26	1.073×10^{-5}	2×10^{-6}	-1×10^{-6} $+1 \times 10^{-6}$
	2.45	8.755×10^{-6}	1.8×10^{-6}	-1.1×10^{-6} $+1.1 \times 10^{-6}$
	2.65	1.579×10^{-5}	1.6×10^{-6}	-1.3×10^{-6} $+1.3 \times 10^{-6}$
	2.85	1.331×10^{-5}	1.6×10^{-6}	-1.7×10^{-6} $+1.7 \times 10^{-6}$
	3.04	2.055×10^{-5}	1.6×10^{-6}	-2.2×10^{-6} $+2.2 \times 10^{-6}$

Table C.9: **Two-particle 40-60% Au+Au jet-induced correlation for $p_{T,\mathrm{trig}}$: 3-5 GeV/c.**

$p_{T,\mathrm{assoc}}$	$\Delta\phi$	$J(\Delta\phi_{ta})$	**Stat. Error**	**Syst. Error**
0.4-1 GeV/c	-3.04	0.002024	3.9×10^{-5}	-0.00026 +0.00026
	-2.85	0.002036	4×10^{-5}	-0.00025 +0.00025
	-2.65	0.00192	4.1×10^{-5}	-0.00022 +0.00022
	-2.45	0.001663	4.5×10^{-5}	-0.00019 +0.00019
	-2.26	0.001511	5.1×10^{-5}	-0.00017 +0.00017
	-2.06	0.001309	5.8×10^{-5}	-0.00015 +0.00015
	-1.87	0.0008204	7×10^{-5}	-0.00014 +0.00014
	-1.67	0.0004927	8.6×10^{-5}	-0.00014 +0.00014
	-1.47	0.0002593	9.3×10^{-5}	-0.00013 +0.00013
	-1.28	7.663×10^{-5}	7.2×10^{-5}	-0.00013 +0.00013
	-1.08	7.367×10^{-5}	5.6×10^{-5}	-0.00013 +0.00013
	-0.88	0.0002702	4.8×10^{-5}	-0.00014 +0.00014
	-0.69	0.0006617	4.3×10^{-5}	-0.00015 +0.00015
	-0.49	0.001357	4.1×10^{-5}	-0.00018 +0.00018
	-0.29	0.002288	3.8×10^{-5}	-0.00022 +0.00022
	-0.10	0.002831	4.1×10^{-5}	-0.00024 +0.00024
	0.10	0.002859	4.1×10^{-5}	-0.00024 +0.00024
	0.29	0.002206	3.8×10^{-5}	-0.00022 +0.00022
	0.49	0.001381	4.1×10^{-5}	-0.00018 +0.00018
	0.69	0.0006583	4.4×10^{-5}	-0.00015 +0.00015
	0.88	0.0002828	4.9×10^{-5}	-0.00014 +0.00014
	1.08	3.441×10^{-5}	5.7×10^{-5}	-0.00013 +0.00013
	1.28	4.492×10^{-5}	7.4×10^{-5}	-0.00013 +0.00013
	1.47	0.0005222	8.8×10^{-5}	-0.00013 +0.00013
	1.67	0.0005563	8.4×10^{-5}	-0.00014 +0.00014

Table C.9 – (40-60% Au+Au, $p_{T,\mathrm{trig}}$: 3-5 GeV/c) continued from previous page

$p_{T,\mathrm{assoc}}$	$\Delta\phi$	$J(\Delta\phi_{ta})$	**Stat. Error**	**Syst. Error**
	1.87	0.0009365	6.8×10^{-5}	-0.00014 +0.00014
	2.06	0.001227	5.8×10^{-5}	-0.00015 +0.00015
	2.26	0.001591	5×10^{-5}	-0.00017 +0.00017
	2.45	0.001687	4.5×10^{-5}	-0.00019 +0.00019
	2.65	0.001853	4.1×10^{-5}	-0.00022 +0.00022
	2.85	0.001924	3.9×10^{-5}	-0.00025 +0.00025
	3.04	0.002055	3.9×10^{-5}	-0.00026 +0.00026
1-2 GeV/c	-3.04	0.0008689	1.8×10^{-5}	-5.4×10^{-5} $+5.4 \times 10^{-5}$
	-2.85	0.0008395	1.8×10^{-5}	-5×10^{-5} $+5 \times 10^{-5}$
	-2.65	0.000793	1.9×10^{-5}	-4.3×10^{-5} $+4.3 \times 10^{-5}$
	-2.45	0.0007058	2×10^{-5}	-3.6×10^{-5} $+3.6 \times 10^{-5}$
	-2.26	0.0006203	2.3×10^{-5}	-3.1×10^{-5} $+3.1 \times 10^{-5}$
	-2.06	0.0005528	2.7×10^{-5}	-2.9×10^{-5} $+2.9 \times 10^{-5}$
	-1.87	0.0004264	3×10^{-5}	-2.7×10^{-5} $+2.7 \times 10^{-5}$
	-1.67	0.0003054	3.9×10^{-5}	-2.5×10^{-5} $+2.5 \times 10^{-5}$
	-1.47	0.0002564	4.3×10^{-5}	-2.4×10^{-5} $+2.4 \times 10^{-5}$
	-1.28	8.858×10^{-5}	3.1×10^{-5}	-2.3×10^{-5} $+2.3 \times 10^{-5}$
	-1.08	2.067×10^{-5}	2.5×10^{-5}	-2.4×10^{-5} $+2.4 \times 10^{-5}$
	-0.88	5.675×10^{-5}	2.1×10^{-5}	-2.6×10^{-5} $+2.6 \times 10^{-5}$
	-0.69	0.0002888	2×10^{-5}	-2.8×10^{-5} $+2.8 \times 10^{-5}$
	-0.49	0.0008208	1.9×10^{-5}	-3.3×10^{-5} $+3.3 \times 10^{-5}$
	-0.29	0.001458	1.8×10^{-5}	-4.4×10^{-5} $+4.4 \times 10^{-5}$
	-0.10	0.002025	1.9×10^{-5}	-5.5×10^{-5} $+5.5 \times 10^{-5}$
	0.10	0.002062	1.9×10^{-5}	-5.5×10^{-5} $+5.5 \times 10^{-5}$
	0.29	0.001433	1.8×10^{-5}	-4.4×10^{-5} $+4.4 \times 10^{-5}$
	0.49	0.0007788	1.9×10^{-5}	-3.3×10^{-5} $+3.3 \times 10^{-5}$
	0.69	0.000312	2×10^{-5}	-2.8×10^{-5} $+2.8 \times 10^{-5}$

Table C.9 – (40-60% Au+Au, $p_{T,\text{trig}}$: 3-5 GeV/c) continued from previous page

$p_{T,\text{assoc}}$	$\Delta\phi$	$J(\Delta\phi_{ta})$	**Stat. Error**	**Syst. Error**
	0.88	6.061×10^{-5}	2.1×10^{-5}	-2.6×10^{-5} $+2.6 \times 10^{-5}$
	1.08	7.536×10^{-6}	2.5×10^{-5}	-2.4×10^{-5} $+2.4 \times 10^{-5}$
	1.28	2.924×10^{-5}	3.2×10^{-5}	-2.3×10^{-5} $+2.3 \times 10^{-5}$
	1.47	0.0002042	4.2×10^{-5}	-2.4×10^{-5} $+2.4 \times 10^{-5}$
	1.67	0.0002857	3.9×10^{-5}	-2.5×10^{-5} $+2.5 \times 10^{-5}$
	1.87	0.0004389	3×10^{-5}	-2.7×10^{-5} $+2.7 \times 10^{-5}$
	2.06	0.0004993	2.7×10^{-5}	-2.9×10^{-5} $+2.9 \times 10^{-5}$
	2.26	0.0006532	2.3×10^{-5}	-3.1×10^{-5} $+3.1 \times 10^{-5}$
	2.45	0.0007306	2×10^{-5}	-3.6×10^{-5} $+3.6 \times 10^{-5}$
	2.65	0.0007809	1.9×10^{-5}	-4.3×10^{-5} $+4.3 \times 10^{-5}$
	2.85	0.000859	1.8×10^{-5}	-5×10^{-5} $+5 \times 10^{-5}$
	3.04	0.0008906	1.8×10^{-5}	-5.4×10^{-5} $+5.4 \times 10^{-5}$
2-3 GeV/c	-3.04	0.0001382	5.1×10^{-6}	-8.6×10^{-6} $+8.6 \times 10^{-6}$
	-2.85	0.0001389	5.2×10^{-6}	-7.5×10^{-6} $+7.5 \times 10^{-6}$
	-2.65	0.0001151	5.4×10^{-6}	-5.9×10^{-6} $+5.9 \times 10^{-6}$
	-2.45	8.885×10^{-5}	5.8×10^{-6}	-4.8×10^{-6} $+4.8 \times 10^{-6}$
	-2.26	9.091×10^{-5}	6.5×10^{-6}	-4.3×10^{-6} $+4.3 \times 10^{-6}$
	-2.06	7.249×10^{-5}	7.6×10^{-6}	-4×10^{-6} $+4 \times 10^{-6}$
	-1.87	5.839×10^{-5}	8.6×10^{-6}	-3.7×10^{-6} $+3.7 \times 10^{-6}$
	-1.67	1.047×10^{-5}	1.1×10^{-5}	-3.4×10^{-6} $+3.4 \times 10^{-6}$
	-1.47	2.45×10^{-5}	1.2×10^{-5}	-3.2×10^{-6} $+3.2 \times 10^{-6}$
	-1.28	-6.113×10^{-6}	8.8×10^{-6}	-3.1×10^{-6} $+3.1 \times 10^{-6}$
	-1.08	-4.02×10^{-6}	7.1×10^{-6}	-3×10^{-6} $+3 \times 10^{-6}$
	-0.88	3.143×10^{-6}	5.9×10^{-6}	-3.2×10^{-6} $+3.2 \times 10^{-6}$
	-0.69	5.896×10^{-5}	5.7×10^{-6}	-4×10^{-6} $+4 \times 10^{-6}$
	-0.49	0.0001405	5.4×10^{-6}	-4.8×10^{-6} $+4.8 \times 10^{-6}$
	-0.29	0.0003385	5.3×10^{-6}	-5.9×10^{-6} $+5.9 \times 10^{-6}$

Table C.9 – (40-60% Au+Au, $p_{T,\mathrm{trig}}$: 3-5 GeV/c) continued from previous page

$p_{T,\mathrm{assoc}}$	$\Delta\phi$	$J(\Delta\phi_{ta})$	**Stat. Error**	**Syst. Error**
	-0.10	0.0006067	5.7×10^{-6}	-9.8×10^{-6} $+9.8 \times 10^{-6}$
	0.10	0.0006042	5.7×10^{-6}	-9.8×10^{-6} $+9.8 \times 10^{-6}$
	0.29	0.0003328	5.3×10^{-6}	-5.9×10^{-6} $+5.9 \times 10^{-6}$
	0.49	0.0001516	5.4×10^{-6}	-4.8×10^{-6} $+4.8 \times 10^{-6}$
	0.69	4.159×10^{-5}	5.7×10^{-6}	-4×10^{-6} $+4 \times 10^{-6}$
	0.88	9.552×10^{-6}	6×10^{-6}	-3.2×10^{-6} $+3.2 \times 10^{-6}$
	1.08	8.779×10^{-6}	7.2×10^{-6}	-3×10^{-6} $+3 \times 10^{-6}$
	1.28	1.061×10^{-5}	8.9×10^{-6}	-3.1×10^{-6} $+3.1 \times 10^{-6}$
	1.47	2.231×10^{-5}	1.2×10^{-5}	-3.2×10^{-6} $+3.2 \times 10^{-6}$
	1.67	4.271×10^{-5}	1.1×10^{-5}	-3.4×10^{-6} $+3.4 \times 10^{-6}$
	1.87	5.126×10^{-5}	8.6×10^{-6}	-3.7×10^{-6} $+3.7 \times 10^{-6}$
	2.06	7.511×10^{-5}	7.6×10^{-6}	-4×10^{-6} $+4 \times 10^{-6}$
	2.26	8.594×10^{-5}	6.4×10^{-6}	-4.3×10^{-6} $+4.3 \times 10^{-6}$
	2.45	9.693×10^{-5}	5.8×10^{-6}	-4.8×10^{-6} $+4.8 \times 10^{-6}$
	2.65	0.0001066	5.3×10^{-6}	-5.9×10^{-6} $+5.9 \times 10^{-6}$
	2.85	0.0001259	5.2×10^{-6}	-7.5×10^{-6} $+7.5 \times 10^{-6}$
	3.04	0.0001445	5.1×10^{-6}	-8.6×10^{-6} $+8.6 \times 10^{-6}$
3-5 GeV/c	-3.04	4.237×10^{-5}	1.9×10^{-6}	-2.5×10^{-6} $+2.5 \times 10^{-6}$
	-2.85	3.131×10^{-5}	1.9×10^{-6}	-2×10^{-6} $+2 \times 10^{-6}$
	-2.65	2.532×10^{-5}	2×10^{-6}	-1.4×10^{-6} $+1.4 \times 10^{-6}$
	-2.45	1.857×10^{-5}	2.1×10^{-6}	-1.2×10^{-6} $+1.2 \times 10^{-6}$
	-2.26	1.381×10^{-5}	2.3×10^{-6}	-1.1×10^{-6} $+1.1 \times 10^{-6}$
	-2.06	7.258×10^{-6}	2.7×10^{-6}	-9.5×10^{-7} $+9.5 \times 10^{-7}$
	-1.87	8.2×10^{-6}	3.1×10^{-6}	-8.1×10^{-7} $+8.1 \times 10^{-7}$
	-1.67	1.188×10^{-6}	4×10^{-6}	-7.5×10^{-7} $+7.5 \times 10^{-7}$
	-1.47	4.642×10^{-6}	4.4×10^{-6}	-7.4×10^{-7} $+7.4 \times 10^{-7}$
	-1.28	3.828×10^{-6}	3.2×10^{-6}	-7.4×10^{-7} $+7.4 \times 10^{-7}$

Table C.9 – (40-60% Au+Au, $p_{T,\mathrm{trig}}$: 3-5 GeV/c) continued from previous page

$p_{T,\mathrm{assoc}}$	$\Delta\phi$	$J(\Delta\phi_{ta})$	**Stat. Error**	**Syst. Error**
	-1.08	-1.116×10^{-6}	2.5×10^{-6}	-7.4×10^{-7} $+7.4\times10^{-7}$
	-0.88	-3.198×10^{-6}	2.1×10^{-6}	-7.4×10^{-7} $+7.4\times10^{-7}$
	-0.69	6.388×10^{-6}	2×10^{-6}	-7.5×10^{-7} $+7.5\times10^{-7}$
	-0.49	2.31×10^{-5}	2×10^{-6}	-1.1×10^{-6} $+1.1\times10^{-6}$
	-0.29	8.45×10^{-5}	2.1×10^{-6}	-1.6×10^{-6} $+1.6\times10^{-6}$
	-0.10	0.0002344	2.6×10^{-6}	-3.1×10^{-6} $+3.1\times10^{-6}$
	0.10	0.0002343	2.6×10^{-6}	-3.1×10^{-6} $+3.1\times10^{-6}$
	0.29	8.503×10^{-5}	2.1×10^{-6}	-1.6×10^{-6} $+1.6\times10^{-6}$
	0.49	2.243×10^{-5}	2×10^{-6}	-1.1×10^{-6} $+1.1\times10^{-6}$
	0.69	6.552×10^{-6}	2×10^{-6}	-7.5×10^{-7} $+7.5\times10^{-7}$
	0.88	-2.976×10^{-6}	2.1×10^{-6}	-7.4×10^{-7} $+7.4\times10^{-7}$
	1.08	-8.188×10^{-7}	2.6×10^{-6}	-7.4×10^{-7} $+7.4\times10^{-7}$
	1.28	3.697×10^{-6}	3.2×10^{-6}	-7.4×10^{-7} $+7.4\times10^{-7}$
	1.47	4.468×10^{-6}	4.4×10^{-6}	-7.4×10^{-7} $+7.4\times10^{-7}$
	1.67	1.916×10^{-6}	4×10^{-6}	-7.5×10^{-7} $+7.5\times10^{-7}$
	1.87	8.347×10^{-6}	3.1×10^{-6}	-8.1×10^{-7} $+8.1\times10^{-7}$
	2.06	7.111×10^{-6}	2.7×10^{-6}	-9.5×10^{-7} $+9.5\times10^{-7}$
	2.26	1.398×10^{-5}	2.3×10^{-6}	-1.1×10^{-6} $+1.1\times10^{-6}$
	2.45	1.898×10^{-5}	2.1×10^{-6}	-1.2×10^{-6} $+1.2\times10^{-6}$
	2.65	2.528×10^{-5}	2×10^{-6}	-1.4×10^{-6} $+1.4\times10^{-6}$
	2.85	3.112×10^{-5}	1.9×10^{-6}	-2×10^{-6} $+2\times10^{-6}$
	3.04	4.289×10^{-5}	2×10^{-6}	-2.5×10^{-6} $+2.5\times10^{-6}$

Table C.10: **Two-particle 60-92% Au+Au jet-induced correlation for $p_{T,\mathrm{trig}}$: 3-5 GeV/c.**

$p_{T,\mathrm{assoc}}$	$\Delta\phi$	$J(\Delta\phi_{ta})$	**Stat. Error**	**Syst. Error**
0.4-1 GeV/c	-3.04	0.002143	4.4×10^{-5}	-0.00019 +0.00019
	-2.85	0.002087	4.5×10^{-5}	-0.00018 +0.00018
	-2.65	0.001811	4.7×10^{-5}	-0.00016 +0.00016
	-2.45	0.001623	5.1×10^{-5}	-0.00013 +0.00013
	-2.26	0.001241	5.8×10^{-5}	-0.00012 +0.00012
	-2.06	0.0009929	6.5×10^{-5}	-0.00011 +0.00011
	-1.87	0.0006371	8×10^{-5}	-9.8×10^{-5} $+9.8 \times 10^{-5}$
	-1.67	0.0003429	9.8×10^{-5}	-9.3×10^{-5} $+9.3 \times 10^{-5}$
	-1.47	0.0001779	0.00011	-8.9×10^{-5} $+8.9 \times 10^{-5}$
	-1.28	-3.031×10^{-5}	8×10^{-5}	-8.6×10^{-5} $+8.6 \times 10^{-5}$
	-1.08	0.0001229	6.3×10^{-5}	-8.7×10^{-5} $+8.7 \times 10^{-5}$
	-0.88	0.0002379	5.3×10^{-5}	-9.1×10^{-5} $+9.1 \times 10^{-5}$
	-0.69	0.0006289	4.8×10^{-5}	-9.9×10^{-5} $+9.9 \times 10^{-5}$
	-0.49	0.001396	4.6×10^{-5}	-0.00012 +0.00012
	-0.29	0.002053	4.3×10^{-5}	-0.00015 +0.00015
	-0.10	0.002715	4.6×10^{-5}	-0.00018 +0.00018
	0.10	0.002646	4.7×10^{-5}	-0.00018 +0.00018
	0.29	0.002081	4.4×10^{-5}	-0.00015 +0.00015
	0.49	0.001297	4.7×10^{-5}	-0.00012 +0.00012
	0.69	0.0006783	4.9×10^{-5}	-9.9×10^{-5} $+9.9 \times 10^{-5}$
	0.88	0.0002679	5.4×10^{-5}	-9.1×10^{-5} $+9.1 \times 10^{-5}$
	1.08	-1.926×10^{-5}	6.4×10^{-5}	-8.7×10^{-5} $+8.7 \times 10^{-5}$
	1.28	-0.0001573	8.3×10^{-5}	-8.6×10^{-5} $+8.6 \times 10^{-5}$
	1.47	0.0001035	9.9×10^{-5}	-8.9×10^{-5} $+8.9 \times 10^{-5}$
	1.67	0.0001309	9.5×10^{-5}	-9.3×10^{-5} $+9.3 \times 10^{-5}$

Table C.10 – (60-92% Au+Au, $p_{T,\text{trig}}$: 3-5 GeV/c) continued from previous page

$p_{T,\text{assoc}}$	$\Delta\phi$	$J(\Delta\phi_{ta})$	**Stat. Error**	**Syst. Error**
	1.87	0.0004437	7.7×10^{-5}	-9.8×10^{-5} $+9.8 \times 10^{-5}$
	2.06	0.0007993	6.5×10^{-5}	-0.00011 +0.00011
	2.26	0.001242	5.7×10^{-5}	-0.00012 +0.00012
	2.45	0.001592	5.1×10^{-5}	-0.00013 +0.00013
	2.65	0.001844	4.7×10^{-5}	-0.00016 +0.00016
	2.85	0.002032	4.5×10^{-5}	-0.00018 +0.00018
	3.04	0.002222	4.4×10^{-5}	-0.00019 +0.00019
1-2 GeV/c	-3.04	0.001033	2×10^{-5}	-3.9×10^{-5} $+3.9 \times 10^{-5}$
	-2.85	0.0009415	2×10^{-5}	-3.5×10^{-5} $+3.5 \times 10^{-5}$
	-2.65	0.0007812	2.1×10^{-5}	-2.9×10^{-5} $+2.9 \times 10^{-5}$
	-2.45	0.0006046	2.2×10^{-5}	-2.3×10^{-5} $+2.3 \times 10^{-5}$
	-2.26	0.0004535	2.5×10^{-5}	-2×10^{-5} $+2 \times 10^{-5}$
	-2.06	0.0003209	2.9×10^{-5}	-1.9×10^{-5} $+1.9 \times 10^{-5}$
	-1.87	0.0001738	3.3×10^{-5}	-1.8×10^{-5} $+1.8 \times 10^{-5}$
	-1.67	0.0001096	4.3×10^{-5}	-1.6×10^{-5} $+1.6 \times 10^{-5}$
	-1.47	7.513×10^{-5}	4.7×10^{-5}	-1.5×10^{-5} $+1.5 \times 10^{-5}$
	-1.28	2.842×10^{-5}	3.4×10^{-5}	-1.5×10^{-5} $+1.5 \times 10^{-5}$
	-1.08	-1.606×10^{-5}	2.7×10^{-5}	-1.4×10^{-5} $+1.4 \times 10^{-5}$
	-0.88	2.096×10^{-5}	2.2×10^{-5}	-1.6×10^{-5} $+1.6 \times 10^{-5}$
	-0.69	0.0002585	2.1×10^{-5}	-1.9×10^{-5} $+1.9 \times 10^{-5}$
	-0.49	0.0006677	2×10^{-5}	-2.1×10^{-5} $+2.1 \times 10^{-5}$
	-0.29	0.001295	2.1×10^{-5}	-2.8×10^{-5} $+2.8 \times 10^{-5}$
	-0.10	0.001893	2.2×10^{-5}	-4.1×10^{-5} $+4.1 \times 10^{-5}$
	0.10	0.001921	2.2×10^{-5}	-4.1×10^{-5} $+4.1 \times 10^{-5}$
	0.29	0.001279	2.1×10^{-5}	-2.8×10^{-5} $+2.8 \times 10^{-5}$
	0.49	0.0006794	2.1×10^{-5}	-2.1×10^{-5} $+2.1 \times 10^{-5}$
	0.69	0.0002207	2.2×10^{-5}	-1.9×10^{-5} $+1.9 \times 10^{-5}$

Table C.10 – (60-92% Au+Au, $p_{T,\text{trig}}$: 3-5 GeV/c) continued from previous page

$p_{T,\text{assoc}}$	$\Delta\phi$	$J(\Delta\phi_{ta})$	**Stat. Error**	**Syst. Error**
	0.88	3.092×10^{-5}	2.3×10^{-5}	-1.6×10^{-5} $+1.6 \times 10^{-5}$
	1.08	-2.473×10^{-5}	2.7×10^{-5}	-1.4×10^{-5} $+1.4 \times 10^{-5}$
	1.28	-4.835×10^{-5}	3.4×10^{-5}	-1.5×10^{-5} $+1.5 \times 10^{-5}$
	1.47	-7.528×10^{-5}	4.6×10^{-5}	-1.5×10^{-5} $+1.5 \times 10^{-5}$
	1.67	8.667×10^{-5}	4.3×10^{-5}	-1.6×10^{-5} $+1.6 \times 10^{-5}$
	1.87	0.0002159	3.3×10^{-5}	-1.8×10^{-5} $+1.8 \times 10^{-5}$
	2.06	0.0003716	2.9×10^{-5}	-1.9×10^{-5} $+1.9 \times 10^{-5}$
	2.26	0.0004576	2.5×10^{-5}	-2×10^{-5} $+2 \times 10^{-5}$
	2.45	0.0006314	2.2×10^{-5}	-2.3×10^{-5} $+2.3 \times 10^{-5}$
	2.65	0.0007779	2.1×10^{-5}	-2.9×10^{-5} $+2.9 \times 10^{-5}$
	2.85	0.0009321	2×10^{-5}	-3.5×10^{-5} $+3.5 \times 10^{-5}$
	3.04	0.0009695	2×10^{-5}	-3.9×10^{-5} $+3.9 \times 10^{-5}$
2-3 GeV/c	-3.04	0.0001937	6.2×10^{-6}	-8.5×10^{-6} $+8.5 \times 10^{-6}$
	-2.85	0.0001592	6.2×10^{-6}	-7×10^{-6} $+7 \times 10^{-6}$
	-2.65	0.0001209	6.3×10^{-6}	-5.2×10^{-6} $+5.2 \times 10^{-6}$
	-2.45	8.448×10^{-5}	6.7×10^{-6}	-4.2×10^{-6} $+4.2 \times 10^{-6}$
	-2.26	6.561×10^{-5}	7.3×10^{-6}	-4×10^{-6} $+4 \times 10^{-6}$
	-2.06	3.291×10^{-5}	8.5×10^{-6}	-3.6×10^{-6} $+3.6 \times 10^{-6}$
	-1.87	1.994×10^{-5}	9.5×10^{-6}	-3.2×10^{-6} $+3.2 \times 10^{-6}$
	-1.67	-1.796×10^{-5}	1.2×10^{-5}	-2.8×10^{-6} $+2.8 \times 10^{-6}$
	-1.47	1.847×10^{-5}	1.4×10^{-5}	-2.7×10^{-6} $+2.7 \times 10^{-6}$
	-1.28	-5.769×10^{-6}	9.7×10^{-6}	-2.6×10^{-6} $+2.6 \times 10^{-6}$
	-1.08	-9.831×10^{-6}	7.8×10^{-6}	-2.6×10^{-6} $+2.6 \times 10^{-6}$
	-0.88	4.007×10^{-6}	6.5×10^{-6}	-2.6×10^{-6} $+2.6 \times 10^{-6}$
	-0.69	2.78×10^{-5}	6.2×10^{-6}	-2.9×10^{-6} $+2.9 \times 10^{-6}$
	-0.49	0.0001032	6.1×10^{-6}	-4.3×10^{-6} $+4.3 \times 10^{-6}$
	-0.29	0.0003158	6.7×10^{-6}	-5×10^{-6} $+5 \times 10^{-6}$

Table C.10 – (60-92% Au+Au, $p_{T,\text{trig}}$: 3-5 GeV/c) continued from previous page

$p_{T,\text{assoc}}$	$\Delta\phi$	$J(\Delta\phi_{ta})$	**Stat. Error**	**Syst. Error**
	-0.10	0.0006441	8×10^{-6}	-9.9×10^{-6} $+9.9 \times 10^{-6}$
	0.10	0.0006462	8×10^{-6}	-9.9×10^{-6} $+9.9 \times 10^{-6}$
	0.29	0.0003266	6.7×10^{-6}	-5×10^{-6} $+5 \times 10^{-6}$
	0.49	9.507×10^{-5}	6.1×10^{-6}	-4.3×10^{-6} $+4.3 \times 10^{-6}$
	0.69	1.34×10^{-5}	6.2×10^{-6}	-2.9×10^{-6} $+2.9 \times 10^{-6}$
	0.88	-1.138×10^{-5}	6.4×10^{-6}	-2.6×10^{-6} $+2.6 \times 10^{-6}$
	1.08	-2.534×10^{-5}	7.6×10^{-6}	-2.6×10^{-6} $+2.6 \times 10^{-6}$
	1.28	-2.485×10^{-5}	9.6×10^{-6}	-2.6×10^{-6} $+2.6 \times 10^{-6}$
	1.47	-2.141×10^{-6}	1.3×10^{-5}	-2.7×10^{-6} $+2.7 \times 10^{-6}$
	1.67	5.622×10^{-6}	1.2×10^{-5}	-2.8×10^{-6} $+2.8 \times 10^{-6}$
	1.87	1.784×10^{-5}	9.5×10^{-6}	-3.2×10^{-6} $+3.2 \times 10^{-6}$
	2.06	3.574×10^{-5}	8.5×10^{-6}	-3.6×10^{-6} $+3.6 \times 10^{-6}$
	2.26	6.82×10^{-5}	7.3×10^{-6}	-4×10^{-6} $+4 \times 10^{-6}$
	2.45	9.412×10^{-5}	6.7×10^{-6}	-4.2×10^{-6} $+4.2 \times 10^{-6}$
	2.65	0.000125	6.3×10^{-6}	-5.2×10^{-6} $+5.2 \times 10^{-6}$
	2.85	0.0001641	6.3×10^{-6}	-7×10^{-6} $+7 \times 10^{-6}$
	3.04	0.0001907	6.2×10^{-6}	-8.5×10^{-6} $+8.5 \times 10^{-6}$
3-5 GeV/c	-3.04	7.131×10^{-5}	2.9×10^{-6}	-3.3×10^{-6} $+3.3 \times 10^{-6}$
	-2.85	5.463×10^{-5}	2.8×10^{-6}	-2.4×10^{-6} $+2.4 \times 10^{-6}$
	-2.65	3.771×10^{-5}	2.7×10^{-6}	-1.6×10^{-6} $+1.6 \times 10^{-6}$
	-2.45	2.174×10^{-5}	2.7×10^{-6}	-1.5×10^{-6} $+1.5 \times 10^{-6}$
	-2.26	1.413×10^{-5}	2.9×10^{-6}	-1.3×10^{-6} $+1.3 \times 10^{-6}$
	-2.06	6.975×10^{-6}	3.3×10^{-6}	-1×10^{-6} $+1 \times 10^{-6}$
	-1.87	-4.702×10^{-7}	3.6×10^{-6}	-8.7×10^{-7} $+8.7 \times 10^{-7}$
	-1.67	4.445×10^{-6}	4.9×10^{-6}	-8.3×10^{-7} $+8.3 \times 10^{-7}$
	-1.47	-7.985×10^{-6}	4.8×10^{-6}	-8.2×10^{-7} $+8.2 \times 10^{-7}$
	-1.28	-6.174×10^{-7}	3.7×10^{-6}	-8.2×10^{-7} $+8.2 \times 10^{-7}$

Table C.10 – (60-92% Au+Au, $p_{T,\text{trig}}$: 3-5 GeV/c) continued from previous page

$p_{T,\text{assoc}}$	$\Delta\phi$	$J(\Delta\phi_{ta})$	**Stat. Error**	**Syst. Error**
	-1.08	-3.528×10^{-6}	2.9×10^{-6}	-8.2×10^{-7} $+8.2\times10^{-7}$
	-0.88	-3.842×10^{-6}	2.4×10^{-6}	-8.2×10^{-7} $+8.2\times10^{-7}$
	-0.69	3.331×10^{-6}	2.4×10^{-6}	-8.3×10^{-7} $+8.3\times10^{-7}$
	-0.49	2.14×10^{-5}	2.4×10^{-6}	-1.2×10^{-6} $+1.2\times10^{-6}$
	-0.29	9.463×10^{-5}	3×10^{-6}	-2.2×10^{-6} $+2.2\times10^{-6}$
	-0.10	0.0002896	4.7×10^{-6}	-4.3×10^{-6} $+4.3\times10^{-6}$
	0.10	0.000289	4.7×10^{-6}	-4.3×10^{-6} $+4.3\times10^{-6}$
	0.29	9.502×10^{-5}	3.1×10^{-6}	-2.2×10^{-6} $+2.2\times10^{-6}$
	0.49	2.149×10^{-5}	2.4×10^{-6}	-1.2×10^{-6} $+1.2\times10^{-6}$
	0.69	3.573×10^{-6}	2.4×10^{-6}	-8.3×10^{-7} $+8.3\times10^{-7}$
	0.88	-4.575×10^{-6}	2.4×10^{-6}	-8.2×10^{-7} $+8.2\times10^{-7}$
	1.08	-3.673×10^{-6}	2.9×10^{-6}	-8.2×10^{-7} $+8.2\times10^{-7}$
	1.28	-1.241×10^{-7}	3.8×10^{-6}	-8.2×10^{-7} $+8.2\times10^{-7}$
	1.47	-6.702×10^{-6}	4.9×10^{-6}	-8.2×10^{-7} $+8.2\times10^{-7}$
	1.67	6.064×10^{-6}	5×10^{-6}	-8.3×10^{-7} $+8.3\times10^{-7}$
	1.87	-4.553×10^{-7}	3.6×10^{-6}	-8.7×10^{-7} $+8.7\times10^{-7}$
	2.06	6.248×10^{-6}	3.3×10^{-6}	-1×10^{-6} $+1\times10^{-6}$
	2.26	1.376×10^{-5}	2.9×10^{-6}	-1.3×10^{-6} $+1.3\times10^{-6}$
	2.45	2.275×10^{-5}	2.7×10^{-6}	-1.5×10^{-6} $+1.5\times10^{-6}$
	2.65	3.716×10^{-5}	2.7×10^{-6}	-1.6×10^{-6} $+1.6\times10^{-6}$
	2.85	5.606×10^{-5}	2.8×10^{-6}	-2.4×10^{-6} $+2.4\times10^{-6}$
	3.04	7.179×10^{-5}	2.9×10^{-6}	-3.3×10^{-6} $+3.3\times10^{-6}$

Table C.11: **Two-particle p+p jet-induced correlation for $p_{T,\mathrm{trig}}$: 5-10 GeV/c.**

$p_{T,\mathrm{assoc}}$	$\Delta\phi$	$J(\Delta\phi_{ta})$	**Stat. Error**	**Syst. Error**
0.4-1 GeV/c	-3.04	0.0004001	9×10^{-6}	-1.2×10^{-5} $+1.2 \times 10^{-5}$
	-2.85	0.0003785	9.2×10^{-6}	-1×10^{-5} $+1 \times 10^{-5}$
	-2.65	0.0003054	8.9×10^{-6}	-8×10^{-6} $+8 \times 10^{-6}$
	-2.45	0.0002231	8.3×10^{-6}	-6.4×10^{-6} $+6.4 \times 10^{-6}$
	-2.26	0.0001553	8.2×10^{-6}	-5.7×10^{-6} $+5.7 \times 10^{-6}$
	-2.06	0.000104	8.6×10^{-6}	-5.4×10^{-6} $+5.4 \times 10^{-6}$
	-1.87	4.711×10^{-5}	9×10^{-6}	-4.9×10^{-6} $+4.9 \times 10^{-6}$
	-1.67	1.471×10^{-5}	8.3×10^{-6}	-4.4×10^{-6} $+4.4 \times 10^{-6}$
	-1.47	2.178×10^{-6}	7.6×10^{-6}	-4×10^{-6} $+4 \times 10^{-6}$
	-1.28	-7.733×10^{-6}	7.6×10^{-6}	-3.9×10^{-6} $+3.9 \times 10^{-6}$
	-1.08	2.88×10^{-6}	7.9×10^{-6}	-3.9×10^{-6} $+3.9 \times 10^{-6}$
	-0.88	3.75×10^{-5}	7.4×10^{-6}	-4.6×10^{-6} $+4.6 \times 10^{-6}$
	-0.69	9.144×10^{-5}	6.9×10^{-6}	-5.6×10^{-6} $+5.6 \times 10^{-6}$
	-0.49	0.0001941	7.4×10^{-6}	-6.1×10^{-6} $+6.1 \times 10^{-6}$
	-0.29	0.0003441	8.6×10^{-6}	-8.4×10^{-6} $+8.4 \times 10^{-6}$
	-0.10	0.0004462	8.8×10^{-6}	-1.2×10^{-5} $+1.2 \times 10^{-5}$
	0.10	0.0004596	9×10^{-6}	-1.2×10^{-5} $+1.2 \times 10^{-5}$
	0.29	0.0003605	9×10^{-6}	-8.4×10^{-6} $+8.4 \times 10^{-6}$
	0.49	0.00018	7.8×10^{-6}	-6.1×10^{-6} $+6.1 \times 10^{-6}$
	0.69	9.834×10^{-5}	7.7×10^{-6}	-5.6×10^{-6} $+5.6 \times 10^{-6}$
	0.88	3.417×10^{-5}	8.4×10^{-6}	-4.6×10^{-6} $+4.6 \times 10^{-6}$
	1.08	1.486×10^{-5}	8.7×10^{-6}	-3.9×10^{-6} $+3.9 \times 10^{-6}$
	1.28	-7.521×10^{-7}	8.1×10^{-6}	-3.9×10^{-6} $+3.9 \times 10^{-6}$
	1.47	2.153×10^{-6}	8.2×10^{-6}	-4×10^{-6} $+4 \times 10^{-6}$
	1.67	1.953×10^{-5}	8.8×10^{-6}	-4.4×10^{-6} $+4.4 \times 10^{-6}$

Table C.11 – (p+p, $p_{T,\mathrm{trig}}$: 5-10 GeV/c) continued from previous page

$p_{T,\mathrm{assoc}}$	$\Delta\phi$	$J(\Delta\phi_{ta})$	**Stat. Error**	**Syst. Error**
	1.87	4.323×10^{-5}	9.2×10^{-6}	-4.9×10^{-6} $+4.9 \times 10^{-6}$
	2.06	8.553×10^{-5}	8.6×10^{-6}	-5.4×10^{-6} $+5.4 \times 10^{-6}$
	2.26	0.0001614	8.6×10^{-6}	-5.7×10^{-6} $+5.7 \times 10^{-6}$
	2.45	0.0002235	8.9×10^{-6}	-6.4×10^{-6} $+6.4 \times 10^{-6}$
	2.65	0.0003151	9.4×10^{-6}	-8×10^{-6} $+8 \times 10^{-6}$
	2.85	0.0003753	9.3×10^{-6}	-1×10^{-5} $+1 \times 10^{-5}$
	3.04	0.0004013	9×10^{-6}	-1.2×10^{-5} $+1.2 \times 10^{-5}$
1-2 GeV/c	-3.04	0.0002963	5.8×10^{-6}	-5.4×10^{-6} $+5.4 \times 10^{-6}$
	-2.85	0.000254	5.4×10^{-6}	-4.1×10^{-6} $+4.1 \times 10^{-6}$
	-2.65	0.0001713	4.8×10^{-6}	-2.7×10^{-6} $+2.7 \times 10^{-6}$
	-2.45	0.0001099	4.5×10^{-6}	-2.4×10^{-6} $+2.4 \times 10^{-6}$
	-2.26	6.946×10^{-5}	4.3×10^{-6}	-2.3×10^{-6} $+2.3 \times 10^{-6}$
	-2.06	4.3×10^{-5}	4.1×10^{-6}	-1.9×10^{-6} $+1.9 \times 10^{-6}$
	-1.87	1.993×10^{-5}	4.1×10^{-6}	-1.5×10^{-6} $+1.5 \times 10^{-6}$
	-1.67	8.006×10^{-6}	4.1×10^{-6}	-1.3×10^{-6} $+1.3 \times 10^{-6}$
	-1.47	-1.129×10^{-5}	3.9×10^{-6}	-1.3×10^{-6} $+1.3 \times 10^{-6}$
	-1.28	-5.511×10^{-6}	3.8×10^{-6}	-1.2×10^{-6} $+1.2 \times 10^{-6}$
	-1.08	-4.396×10^{-6}	3.3×10^{-6}	-1.2×10^{-6} $+1.2 \times 10^{-6}$
	-0.88	5.298×10^{-6}	3.2×10^{-6}	-1.3×10^{-6} $+1.3 \times 10^{-6}$
	-0.69	4.007×10^{-5}	3.4×10^{-6}	-1.9×10^{-6} $+1.9 \times 10^{-6}$
	-0.49	0.0001045	4.1×10^{-6}	-2.7×10^{-6} $+2.7 \times 10^{-6}$
	-0.29	0.0002717	5.1×10^{-6}	-3.1×10^{-6} $+3.1 \times 10^{-6}$
	-0.10	0.0004312	6.1×10^{-6}	-6.1×10^{-6} $+6.1 \times 10^{-6}$
	0.10	0.0004363	6.3×10^{-6}	-6.1×10^{-6} $+6.1 \times 10^{-6}$
	0.29	0.0002697	5.3×10^{-6}	-3.1×10^{-6} $+3.1 \times 10^{-6}$
	0.49	0.0001122	4.5×10^{-6}	-2.7×10^{-6} $+2.7 \times 10^{-6}$
	0.69	3.954×10^{-5}	3.9×10^{-6}	-1.9×10^{-6} $+1.9 \times 10^{-6}$

Table C.11 – (p+p, $p_{T,\text{trig}}$: 5-10 GeV/c) continued from previous page

$p_{T,\text{assoc}}$	$\Delta\phi$	$J(\Delta\phi_{ta})$	**Stat. Error**	**Syst. Error**
	0.88	1.484×10^{-5}	4×10^{-6}	-1.3×10^{-6} $+1.3 \times 10^{-6}$
	1.08	-5.984×10^{-6}	3.7×10^{-6}	-1.2×10^{-6} $+1.2 \times 10^{-6}$
	1.28	-1.144×10^{-5}	4×10^{-6}	-1.2×10^{-6} $+1.2 \times 10^{-6}$
	1.47	-3.429×10^{-6}	4.2×10^{-6}	-1.3×10^{-6} $+1.3 \times 10^{-6}$
	1.67	1.154×10^{-6}	4×10^{-6}	-1.3×10^{-6} $+1.3 \times 10^{-6}$
	1.87	2.031×10^{-5}	4.1×10^{-6}	-1.5×10^{-6} $+1.5 \times 10^{-6}$
	2.06	3.473×10^{-5}	4×10^{-6}	-1.9×10^{-6} $+1.9 \times 10^{-6}$
	2.26	6.586×10^{-5}	4.4×10^{-6}	-2.3×10^{-6} $+2.3 \times 10^{-6}$
	2.45	0.0001117	4.7×10^{-6}	-2.4×10^{-6} $+2.4 \times 10^{-6}$
	2.65	0.0001666	5.1×10^{-6}	-2.7×10^{-6} $+2.7 \times 10^{-6}$
	2.85	0.0002448	5.6×10^{-6}	-4.1×10^{-6} $+4.1 \times 10^{-6}$
	3.04	0.0002906	5.9×10^{-6}	-5.4×10^{-6} $+5.4 \times 10^{-6}$
2-3 GeV/c	-3.04	0.0001037	3.1×10^{-6}	-2.3×10^{-6} $+2.3 \times 10^{-6}$
	-2.85	7.345×10^{-5}	2.6×10^{-6}	-1.5×10^{-6} $+1.5 \times 10^{-6}$
	-2.65	4.854×10^{-5}	2.2×10^{-6}	-9.8×10^{-7} $+9.8 \times 10^{-7}$
	-2.45	2.534×10^{-5}	1.9×10^{-6}	-9.6×10^{-7} $+9.6 \times 10^{-7}$
	-2.26	1.578×10^{-5}	1.8×10^{-6}	-7.8×10^{-7} $+7.8 \times 10^{-7}$
	-2.06	6.691×10^{-6}	1.5×10^{-6}	-5.2×10^{-7} $+5.2 \times 10^{-7}$
	-1.87	2.135×10^{-6}	1.4×10^{-6}	-3.8×10^{-7} $+3.8 \times 10^{-7}$
	-1.67	3.67×10^{-7}	1.5×10^{-6}	-3.6×10^{-7} $+3.6 \times 10^{-7}$
	-1.47	-2.325×10^{-6}	1.4×10^{-6}	-3.5×10^{-7} $+3.5 \times 10^{-7}$
	-1.28	-2.411×10^{-6}	1.3×10^{-6}	-3.5×10^{-7} $+3.5 \times 10^{-7}$
	-1.08	-2.388×10^{-6}	1.1×10^{-6}	-3.5×10^{-7} $+3.5 \times 10^{-7}$
	-0.88	-6.181×10^{-9}	1.1×10^{-6}	-3.5×10^{-7} $+3.5 \times 10^{-7}$
	-0.69	4.818×10^{-6}	1.2×10^{-6}	-3.7×10^{-7} $+3.7 \times 10^{-7}$
	-0.49	2.002×10^{-5}	1.6×10^{-6}	-8.7×10^{-7} $+8.7 \times 10^{-7}$
	-0.29	8.506×10^{-5}	2.5×10^{-6}	-1.5×10^{-6} $+1.5 \times 10^{-6}$

Table C.11 – (p+p, $p_{T,\text{trig}}$: 5-10 GeV/c) continued from previous page

$p_{T,\text{assoc}}$	$\Delta\phi$	$J(\Delta\phi_{ta})$	**Stat. Error**	**Syst. Error**
	-0.10	0.0002198	3.8×10^{-6}	-3.1×10^{-6} $+3.1 \times 10^{-6}$
	0.10	0.0002295	3.9×10^{-6}	-3.1×10^{-6} $+3.1 \times 10^{-6}$
	0.29	8.352×10^{-5}	2.5×10^{-6}	-1.5×10^{-6} $+1.5 \times 10^{-6}$
	0.49	1.841×10^{-5}	1.7×10^{-6}	-8.7×10^{-7} $+8.7 \times 10^{-7}$
	0.69	5.354×10^{-6}	1.4×10^{-6}	-3.7×10^{-7} $+3.7 \times 10^{-7}$
	0.88	1.271×10^{-6}	1.3×10^{-6}	-3.5×10^{-7} $+3.5 \times 10^{-7}$
	1.08	-1.902×10^{-6}	1.3×10^{-6}	-3.5×10^{-7} $+3.5 \times 10^{-7}$
	1.28	-1.728×10^{-6}	1.4×10^{-6}	-3.5×10^{-7} $+3.5 \times 10^{-7}$
	1.47	-3.559×10^{-6}	1.3×10^{-6}	-3.5×10^{-7} $+3.5 \times 10^{-7}$
	1.67	-2.13×10^{-6}	1.3×10^{-6}	-3.6×10^{-7} $+3.6 \times 10^{-7}$
	1.87	7.994×10^{-7}	1.3×10^{-6}	-3.8×10^{-7} $+3.8 \times 10^{-7}$
	2.06	6.049×10^{-6}	1.5×10^{-6}	-5.2×10^{-7} $+5.2 \times 10^{-7}$
	2.26	1.184×10^{-5}	1.7×10^{-6}	-7.8×10^{-7} $+7.8 \times 10^{-7}$
	2.45	2.682×10^{-5}	2×10^{-6}	-9.6×10^{-7} $+9.6 \times 10^{-7}$
	2.65	4.868×10^{-5}	2.4×10^{-6}	-9.8×10^{-7} $+9.8 \times 10^{-7}$
	2.85	7.728×10^{-5}	2.8×10^{-6}	-1.5×10^{-6} $+1.5 \times 10^{-6}$
	3.04	0.0001054	3.2×10^{-6}	-2.3×10^{-6} $+2.3 \times 10^{-6}$
3-5 GeV/c	-3.04	6.751×10^{-5}	2.5×10^{-6}	-1.7×10^{-6} $+1.7 \times 10^{-6}$
	-2.85	4.22×10^{-5}	1.9×10^{-6}	-9.3×10^{-7} $+9.3 \times 10^{-7}$
	-2.65	2.345×10^{-5}	1.5×10^{-6}	-6.9×10^{-7} $+6.9 \times 10^{-7}$
	-2.45	1.034×10^{-5}	1.1×10^{-6}	-6.2×10^{-7} $+6.2 \times 10^{-7}$
	-2.26	5.597×10^{-6}	1×10^{-6}	-3.6×10^{-7} $+3.6 \times 10^{-7}$
	-2.06	2.512×10^{-6}	8.4×10^{-7}	-1.9×10^{-7} $+1.9 \times 10^{-7}$
	-1.87	6.926×10^{-7}	6.9×10^{-7}	-1.6×10^{-7} $+1.6 \times 10^{-7}$
	-1.67	1.321×10^{-6}	9.1×10^{-7}	-1.6×10^{-7} $+1.6 \times 10^{-7}$
	-1.47	-2.505×10^{-7}	8×10^{-7}	-1.6×10^{-7} $+1.6 \times 10^{-7}$
	-1.28	-1.406×10^{-6}	5.2×10^{-7}	-1.6×10^{-7} $+1.6 \times 10^{-7}$

Table C.11 – (p+p, $p_{T,\mathrm{trig}}$: 5-10 GeV/c) continued from previous page

$p_{T,\mathrm{assoc}}$	$\Delta\phi$	$J(\Delta\phi_{ta})$	**Stat. Error**	**Syst. Error**
	-1.08	-6.634×10^{-7}	5.4×10^{-7}	-1.6×10^{-7} $+1.6\times10^{-7}$
	-0.88	-7.62×10^{-7}	4.7×10^{-7}	-1.6×10^{-7} $+1.6\times10^{-7}$
	-0.69	-4.702×10^{-7}	4.9×10^{-7}	-1.6×10^{-7} $+1.6\times10^{-7}$
	-0.49	5.571×10^{-6}	8.1×10^{-7}	-2.5×10^{-7} $+2.5\times10^{-7}$
	-0.29	3.309×10^{-5}	1.5×10^{-6}	-1.1×10^{-6} $+1.1\times10^{-6}$
	-0.10	0.0001528	3.2×10^{-6}	-2.4×10^{-6} $+2.4\times10^{-6}$
	0.10	0.0001505	3.2×10^{-6}	-2.4×10^{-6} $+2.4\times10^{-6}$
	0.29	3.384×10^{-5}	1.6×10^{-6}	-1.1×10^{-6} $+1.1\times10^{-6}$
	0.49	6.988×10^{-6}	9.5×10^{-7}	-2.5×10^{-7} $+2.5\times10^{-7}$
	0.69	4.381×10^{-7}	6.5×10^{-7}	-1.6×10^{-7} $+1.6\times10^{-7}$
	0.88	-9.215×10^{-7}	5.2×10^{-7}	-1.6×10^{-7} $+1.6\times10^{-7}$
	1.08	-7.112×10^{-7}	6.1×10^{-7}	-1.6×10^{-7} $+1.6\times10^{-7}$
	1.28	-1.348×10^{-6}	6×10^{-7}	-1.6×10^{-7} $+1.6\times10^{-7}$
	1.47	-1.086×10^{-7}	7.8×10^{-7}	-1.6×10^{-7} $+1.6\times10^{-7}$
	1.67	-7.179×10^{-8}	7.3×10^{-7}	-1.6×10^{-7} $+1.6\times10^{-7}$
	1.87	1.943×10^{-7}	6.4×10^{-7}	-1.6×10^{-7} $+1.6\times10^{-7}$
	2.06	2.023×10^{-6}	8×10^{-7}	-1.9×10^{-7} $+1.9\times10^{-7}$
	2.26	7.443×10^{-6}	1.1×10^{-6}	-3.6×10^{-7} $+3.6\times10^{-7}$
	2.45	8.655×10^{-6}	1.1×10^{-6}	-6.2×10^{-7} $+6.2\times10^{-7}$
	2.65	2.274×10^{-5}	1.5×10^{-6}	-6.9×10^{-7} $+6.9\times10^{-7}$
	2.85	3.987×10^{-5}	1.9×10^{-6}	-9.3×10^{-7} $+9.3\times10^{-7}$
	3.04	6.992×10^{-5}	2.5×10^{-6}	-1.7×10^{-6} $+1.7\times10^{-6}$

Table C.12: **Two-particle 0-20% Au+Au jet-induced correlation for $p_{T,\mathrm{trig}}$: 5-10 GeV/c.**

$p_{T,\mathrm{assoc}}$	$\Delta\phi$	$J(\Delta\phi_{ta})$	**Stat. Error**	**Syst. Error**
0.4-1 GeV/c	-3.04	2.845×10^{-5}	3.6×10^{-6}	-4.3×10^{-5} $+4.3 \times 10^{-5}$
	-2.85	2.232×10^{-5}	3.6×10^{-6}	-4.2×10^{-5} $+4.2 \times 10^{-5}$
	-2.65	1.175×10^{-5}	3.8×10^{-6}	-3.9×10^{-5} $+3.9 \times 10^{-5}$
	-2.45	2.177×10^{-5}	4.1×10^{-6}	-3.6×10^{-5} $+3.6 \times 10^{-5}$
	-2.26	1.956×10^{-5}	4.7×10^{-6}	-3.3×10^{-5} $+3.3 \times 10^{-5}$
	-2.06	1.977×10^{-5}	5.3×10^{-6}	-3×10^{-5} $+3 \times 10^{-5}$
	-1.87	7.732×10^{-6}	6.3×10^{-6}	-2.7×10^{-5} $+2.7 \times 10^{-5}$
	-1.67	3.196×10^{-6}	7.6×10^{-6}	-2.6×10^{-5} $+2.6 \times 10^{-5}$
	-1.47	1.632×10^{-5}	8.1×10^{-6}	-2.4×10^{-5} $+2.4 \times 10^{-5}$
	-1.28	1.466×10^{-5}	6.3×10^{-6}	-2.3×10^{-5} $+2.3 \times 10^{-5}$
	-1.08	-1.695×10^{-5}	5×10^{-6}	-2.2×10^{-5} $+2.2 \times 10^{-5}$
	-0.88	9.683×10^{-7}	4.3×10^{-6}	-2.2×10^{-5} $+2.2 \times 10^{-5}$
	-0.69	7.095×10^{-6}	3.9×10^{-6}	-2.3×10^{-5} $+2.3 \times 10^{-5}$
	-0.49	7.069×10^{-6}	3.6×10^{-6}	-2.4×10^{-5} $+2.4 \times 10^{-5}$
	-0.29	1.991×10^{-5}	3.4×10^{-6}	-2.7×10^{-5} $+2.7 \times 10^{-5}$
	-0.10	2.209×10^{-5}	3.6×10^{-6}	-3×10^{-5} $+3 \times 10^{-5}$
	0.10	2.527×10^{-5}	3.7×10^{-6}	-3×10^{-5} $+3 \times 10^{-5}$
	0.29	2.015×10^{-5}	3.5×10^{-6}	-2.7×10^{-5} $+2.7 \times 10^{-5}$
	0.49	1.373×10^{-5}	3.8×10^{-6}	-2.4×10^{-5} $+2.4 \times 10^{-5}$
	0.69	-3.448×10^{-6}	4.1×10^{-6}	-2.3×10^{-5} $+2.3 \times 10^{-5}$
	0.88	5.948×10^{-6}	4.6×10^{-6}	-2.2×10^{-5} $+2.2 \times 10^{-5}$
	1.08	1.527×10^{-6}	5.5×10^{-6}	-2.2×10^{-5} $+2.2 \times 10^{-5}$
	1.28	9.652×10^{-6}	7×10^{-6}	-2.3×10^{-5} $+2.3 \times 10^{-5}$
	1.47	-1.76×10^{-6}	8.4×10^{-6}	-2.4×10^{-5} $+2.4 \times 10^{-5}$
	1.67	2.217×10^{-5}	8.2×10^{-6}	-2.6×10^{-5} $+2.6 \times 10^{-5}$

Table C.12 – (0-20% Au+Au, $p_{T,\mathrm{trig}}$: 5-10 GeV/c) continued from previous page

$p_{T,\mathrm{assoc}}$	$\Delta\phi$	$J(\Delta\phi_{ta})$	**Stat. Error**	**Syst. Error**
	1.87	1.091×10^{-5}	6.7×10^{-6}	-2.7×10^{-5} $+2.7 \times 10^{-5}$
	2.06	2.014×10^{-5}	5.6×10^{-6}	-3×10^{-5} $+3 \times 10^{-5}$
	2.26	1.662×10^{-5}	4.9×10^{-6}	-3.3×10^{-5} $+3.3 \times 10^{-5}$
	2.45	1.875×10^{-5}	4.2×10^{-6}	-3.6×10^{-5} $+3.6 \times 10^{-5}$
	2.65	2.648×10^{-5}	3.9×10^{-6}	-3.9×10^{-5} $+3.9 \times 10^{-5}$
	2.85	2.191×10^{-5}	3.7×10^{-6}	-4.2×10^{-5} $+4.2 \times 10^{-5}$
	3.04	2.184×10^{-5}	3.7×10^{-6}	-4.3×10^{-5} $+4.3 \times 10^{-5}$
1-2 GeV/c	-3.04	7.317×10^{-6}	1.7×10^{-6}	-8.7×10^{-6} $+8.7 \times 10^{-6}$
	-2.85	6.381×10^{-6}	1.7×10^{-6}	-8.4×10^{-6} $+8.4 \times 10^{-6}$
	-2.65	6.23×10^{-6}	1.7×10^{-6}	-7.8×10^{-6} $+7.8 \times 10^{-6}$
	-2.45	6.639×10^{-6}	1.9×10^{-6}	-7.1×10^{-6} $+7.1 \times 10^{-6}$
	-2.26	9.584×10^{-6}	2.2×10^{-6}	-6.3×10^{-6} $+6.3 \times 10^{-6}$
	-2.06	1.386×10^{-5}	2.5×10^{-6}	-5.7×10^{-6} $+5.7 \times 10^{-6}$
	-1.87	4.28×10^{-6}	2.8×10^{-6}	-5.2×10^{-6} $+5.2 \times 10^{-6}$
	-1.67	3.947×10^{-7}	3.6×10^{-6}	-4.8×10^{-6} $+4.8 \times 10^{-6}$
	-1.47	9.733×10^{-6}	3.9×10^{-6}	-4.6×10^{-6} $+4.6 \times 10^{-6}$
	-1.28	3.118×10^{-6}	2.9×10^{-6}	-4.4×10^{-6} $+4.4 \times 10^{-6}$
	-1.08	1.832×10^{-6}	2.3×10^{-6}	-4.2×10^{-6} $+4.2 \times 10^{-6}$
	-0.88	-2.122×10^{-7}	1.9×10^{-6}	-4.1×10^{-6} $+4.1 \times 10^{-6}$
	-0.69	3.486×10^{-7}	1.8×10^{-6}	-4.2×10^{-6} $+4.2 \times 10^{-6}$
	-0.49	8.006×10^{-6}	1.7×10^{-6}	-4.4×10^{-6} $+4.4 \times 10^{-6}$
	-0.29	1.844×10^{-5}	1.6×10^{-6}	-5.1×10^{-6} $+5.1 \times 10^{-6}$
	-0.10	2.302×10^{-5}	1.7×10^{-6}	-6.4×10^{-6} $+6.4 \times 10^{-6}$
	0.10	2.635×10^{-5}	1.7×10^{-6}	-6.4×10^{-6} $+6.4 \times 10^{-6}$
	0.29	1.412×10^{-5}	1.7×10^{-6}	-5.1×10^{-6} $+5.1 \times 10^{-6}$
	0.49	3.965×10^{-6}	1.7×10^{-6}	-4.4×10^{-6} $+4.4 \times 10^{-6}$
	0.69	3.179×10^{-6}	1.9×10^{-6}	-4.2×10^{-6} $+4.2 \times 10^{-6}$

Table C.12 – (0-20% Au+Au, $p_{T,\mathrm{trig}}$: 5-10 GeV/c) continued from previous page

$p_{T,\mathrm{assoc}}$	$\Delta\phi$	$J(\Delta\phi_{ta})$	**Stat. Error**	**Syst. Error**
	0.88	1.653×10^{-7}	2.1×10^{-6}	-4.1×10^{-6} $+4.1 \times 10^{-6}$
	1.08	3.241×10^{-7}	2.5×10^{-6}	-4.2×10^{-6} $+4.2 \times 10^{-6}$
	1.28	5.304×10^{-6}	3.1×10^{-6}	-4.4×10^{-6} $+4.4 \times 10^{-6}$
	1.47	1.594×10^{-6}	4.2×10^{-6}	-4.6×10^{-6} $+4.6 \times 10^{-6}$
	1.67	-1.066×10^{-6}	3.9×10^{-6}	-4.8×10^{-6} $+4.8 \times 10^{-6}$
	1.87	1.801×10^{-6}	3.1×10^{-6}	-5.2×10^{-6} $+5.2 \times 10^{-6}$
	2.06	7.86×10^{-6}	2.7×10^{-6}	-5.7×10^{-6} $+5.7 \times 10^{-6}$
	2.26	3.8×10^{-6}	2.2×10^{-6}	-6.3×10^{-6} $+6.3 \times 10^{-6}$
	2.45	7.873×10^{-6}	1.9×10^{-6}	-7.1×10^{-6} $+7.1 \times 10^{-6}$
	2.65	5.214×10^{-6}	1.8×10^{-6}	-7.8×10^{-6} $+7.8 \times 10^{-6}$
	2.85	3.74×10^{-6}	1.7×10^{-6}	-8.4×10^{-6} $+8.4 \times 10^{-6}$
	3.04	7.201×10^{-6}	1.7×10^{-6}	-8.7×10^{-6} $+8.7 \times 10^{-6}$
2-3 GeV/c	-3.04	5.041×10^{-7}	4.6×10^{-7}	-5.5×10^{-7} $+5.5 \times 10^{-7}$
	-2.85	1.511×10^{-6}	4.6×10^{-7}	-4×10^{-7} $+4 \times 10^{-7}$
	-2.65	9.612×10^{-8}	4.7×10^{-7}	-2.9×10^{-7} $+2.9 \times 10^{-7}$
	-2.45	1.587×10^{-8}	5.2×10^{-7}	-2.6×10^{-7} $+2.6 \times 10^{-7}$
	-2.26	2.084×10^{-7}	5.9×10^{-7}	-2.2×10^{-7} $+2.2 \times 10^{-7}$
	-2.06	-9.829×10^{-8}	6.9×10^{-7}	-1.9×10^{-7} $+1.9 \times 10^{-7}$
	-1.87	3.679×10^{-7}	7.8×10^{-7}	-1.8×10^{-7} $+1.8 \times 10^{-7}$
	-1.67	1.929×10^{-6}	1×10^{-6}	-1.8×10^{-7} $+1.8 \times 10^{-7}$
	-1.47	-1.304×10^{-7}	1.1×10^{-6}	-1.8×10^{-7} $+1.8 \times 10^{-7}$
	-1.28	-7.885×10^{-8}	7.9×10^{-7}	-1.8×10^{-7} $+1.8 \times 10^{-7}$
	-1.08	-6.328×10^{-8}	6.5×10^{-7}	-1.8×10^{-7} $+1.8 \times 10^{-7}$
	-0.88	7.209×10^{-7}	5.4×10^{-7}	-1.8×10^{-7} $+1.8 \times 10^{-7}$
	-0.69	-1.121×10^{-8}	5×10^{-7}	-1.8×10^{-7} $+1.8 \times 10^{-7}$
	-0.49	1.043×10^{-6}	4.6×10^{-7}	-2.7×10^{-7} $+2.7 \times 10^{-7}$
	-0.29	3.278×10^{-6}	4.4×10^{-7}	-3.4×10^{-7} $+3.4 \times 10^{-7}$

Table C.12 – (0-20% Au+Au, $p_{T,\mathrm{trig}}$: 5-10 GeV/c) continued from previous page

$p_{T,\mathrm{assoc}}$	$\Delta\phi$	$J(\Delta\phi_{ta})$	**Stat. Error**	**Syst. Error**
	-0.10	9.05×10^{-6}	4.7×10^{-7}	-6.9×10^{-7} $+6.9 \times 10^{-7}$
	0.10	9.196×10^{-6}	4.7×10^{-7}	-6.9×10^{-7} $+6.9 \times 10^{-7}$
	0.29	3.566×10^{-6}	4.5×10^{-7}	-3.4×10^{-7} $+3.4 \times 10^{-7}$
	0.49	1.318×10^{-6}	4.8×10^{-7}	-2.7×10^{-7} $+2.7 \times 10^{-7}$
	0.69	6.487×10^{-7}	5.3×10^{-7}	-1.8×10^{-7} $+1.8 \times 10^{-7}$
	0.88	-4.598×10^{-8}	5.7×10^{-7}	-1.8×10^{-7} $+1.8 \times 10^{-7}$
	1.08	4.173×10^{-7}	6.9×10^{-7}	-1.8×10^{-7} $+1.8 \times 10^{-7}$
	1.28	1.361×10^{-7}	8.6×10^{-7}	-1.8×10^{-7} $+1.8 \times 10^{-7}$
	1.47	7.831×10^{-7}	1.2×10^{-6}	-1.8×10^{-7} $+1.8 \times 10^{-7}$
	1.67	-1.305×10^{-6}	1.1×10^{-6}	-1.8×10^{-7} $+1.8 \times 10^{-7}$
	1.87	-2.717×10^{-7}	8.4×10^{-7}	-1.8×10^{-7} $+1.8 \times 10^{-7}$
	2.06	-3.342×10^{-7}	7.4×10^{-7}	-1.9×10^{-7} $+1.9 \times 10^{-7}$
	2.26	-2.691×10^{-7}	6×10^{-7}	-2.2×10^{-7} $+2.2 \times 10^{-7}$
	2.45	3.215×10^{-8}	5.3×10^{-7}	-2.6×10^{-7} $+2.6 \times 10^{-7}$
	2.65	1.694×10^{-7}	4.8×10^{-7}	-2.9×10^{-7} $+2.9 \times 10^{-7}$
	2.85	9.986×10^{-7}	4.8×10^{-7}	-4×10^{-7} $+4 \times 10^{-7}$
	3.04	4.487×10^{-7}	4.6×10^{-7}	-5.5×10^{-7} $+5.5 \times 10^{-7}$
3-5 GeV/c	-3.04	1.363×10^{-7}	1.5×10^{-7}	-1.8×10^{-7} $+1.8 \times 10^{-7}$
	-2.85	3.126×10^{-7}	1.5×10^{-7}	-1.1×10^{-7} $+1.1 \times 10^{-7}$
	-2.65	1.277×10^{-7}	1.6×10^{-7}	-8.3×10^{-8} $+8.3 \times 10^{-8}$
	-2.45	1.715×10^{-7}	1.7×10^{-7}	-7×10^{-8} $+7 \times 10^{-8}$
	-2.26	1.354×10^{-7}	2×10^{-7}	-5.4×10^{-8} $+5.4 \times 10^{-8}$
	-2.06	2.91×10^{-7}	2.4×10^{-7}	-5×10^{-8} $+5 \times 10^{-8}$
	-1.87	2.534×10^{-7}	2.6×10^{-7}	-5×10^{-8} $+5 \times 10^{-8}$
	-1.67	4.503×10^{-7}	3.5×10^{-7}	-5×10^{-8} $+5 \times 10^{-8}$
	-1.47	-1.606×10^{-7}	3.5×10^{-7}	-5×10^{-8} $+5 \times 10^{-8}$
	-1.28	8.809×10^{-8}	2.6×10^{-7}	-5×10^{-8} $+5 \times 10^{-8}$

Table C.12 – (0-20% Au+Au, $p_{T,\text{trig}}$: 5-10 GeV/c) continued from previous page

$p_{T,\text{assoc}}$	$\Delta\phi$	$J(\Delta\phi_{ta})$	**Stat. Error**	**Syst. Error**
	-1.08	-4.819×10^{-7}	2×10^{-7}	-5×10^{-8} $+5\times10^{-8}$
	-0.88	4.243×10^{-8}	1.8×10^{-7}	-5×10^{-8} $+5\times10^{-8}$
	-0.69	6.008×10^{-8}	1.7×10^{-7}	-5×10^{-8} $+5\times10^{-8}$
	-0.49	5.291×10^{-7}	1.6×10^{-7}	-5.5×10^{-8} $+5.5\times10^{-8}$
	-0.29	1.336×10^{-6}	1.6×10^{-7}	-1.2×10^{-7} $+1.2\times10^{-7}$
	-0.10	4.277×10^{-6}	1.9×10^{-7}	-2.2×10^{-7} $+2.2\times10^{-7}$
	0.10	4.834×10^{-6}	2×10^{-7}	-2.2×10^{-7} $+2.2\times10^{-7}$
	0.29	8.044×10^{-7}	1.5×10^{-7}	-1.2×10^{-7} $+1.2\times10^{-7}$
	0.49	8.26×10^{-8}	1.5×10^{-7}	-5.5×10^{-8} $+5.5\times10^{-8}$
	0.69	4.118×10^{-7}	1.8×10^{-7}	-5×10^{-8} $+5\times10^{-8}$
	0.88	2.929×10^{-8}	1.9×10^{-7}	-5×10^{-8} $+5\times10^{-8}$
	1.08	-4.823×10^{-7}	2.1×10^{-7}	-5×10^{-8} $+5\times10^{-8}$
	1.28	-1.93×10^{-8}	2.8×10^{-7}	-5×10^{-8} $+5\times10^{-8}$
	1.47	-5.397×10^{-7}	3.6×10^{-7}	-5×10^{-8} $+5\times10^{-8}$
	1.67	-2.454×10^{-7}	3.5×10^{-7}	-5×10^{-8} $+5\times10^{-8}$
	1.87	4.831×10^{-7}	2.9×10^{-7}	-5×10^{-8} $+5\times10^{-8}$
	2.06	-1.255×10^{-7}	2.4×10^{-7}	-5×10^{-8} $+5\times10^{-8}$
	2.26	-3.069×10^{-7}	1.9×10^{-7}	-5.4×10^{-8} $+5.4\times10^{-8}$
	2.45	-2.509×10^{-7}	1.7×10^{-7}	-7×10^{-8} $+7\times10^{-8}$
	2.65	2.259×10^{-7}	1.6×10^{-7}	-8.3×10^{-8} $+8.3\times10^{-8}$
	2.85	2.067×10^{-7}	1.6×10^{-7}	-1.1×10^{-7} $+1.1\times10^{-7}$
	3.04	5.637×10^{-7}	1.6×10^{-7}	-1.8×10^{-7} $+1.8\times10^{-7}$

Table C.13: **Two-particle 20-40% Au+Au jet-induced correlation for $p_{T,\mathrm{trig}}$: 5-10 GeV/c.**

$p_{T,\mathrm{assoc}}$	$\Delta\phi$	$J(\Delta\phi_{ta})$	**Stat. Error**	**Syst. Error**
0.4-1 GeV/c	-3.04	3.66×10^{-5}	3.9×10^{-6}	-3.1×10^{-5} $+3.1 \times 10^{-5}$
	-2.85	3.518×10^{-5}	4×10^{-6}	-3×10^{-5} $+3 \times 10^{-5}$
	-2.65	3.048×10^{-5}	4.1×10^{-6}	-2.7×10^{-5} $+2.7 \times 10^{-5}$
	-2.45	2.988×10^{-5}	4.5×10^{-6}	-2.4×10^{-5} $+2.4 \times 10^{-5}$
	-2.26	2.94×10^{-5}	5.1×10^{-6}	-2.1×10^{-5} $+2.1 \times 10^{-5}$
	-2.06	2.994×10^{-5}	5.7×10^{-6}	-1.9×10^{-5} $+1.9 \times 10^{-5}$
	-1.87	2.856×10^{-5}	6.8×10^{-6}	-1.8×10^{-5} $+1.8 \times 10^{-5}$
	-1.67	7.801×10^{-6}	8.2×10^{-6}	-1.7×10^{-5} $+1.7 \times 10^{-5}$
	-1.47	2.005×10^{-5}	8.9×10^{-6}	-1.6×10^{-5} $+1.6 \times 10^{-5}$
	-1.28	1.461×10^{-6}	6.8×10^{-6}	-1.5×10^{-5} $+1.5 \times 10^{-5}$
	-1.08	-1.991×10^{-7}	5.4×10^{-6}	-1.5×10^{-5} $+1.5 \times 10^{-5}$
	-0.88	1.615×10^{-6}	4.6×10^{-6}	-1.6×10^{-5} $+1.6 \times 10^{-5}$
	-0.69	1.092×10^{-5}	4.2×10^{-6}	-1.7×10^{-5} $+1.7 \times 10^{-5}$
	-0.49	8.282×10^{-6}	3.9×10^{-6}	-2×10^{-5} $+2 \times 10^{-5}$
	-0.29	2.285×10^{-5}	3.7×10^{-6}	-2.4×10^{-5} $+2.4 \times 10^{-5}$
	-0.10	3.554×10^{-5}	4×10^{-6}	-2.7×10^{-5} $+2.7 \times 10^{-5}$
	0.10	4.093×10^{-5}	4×10^{-6}	-2.7×10^{-5} $+2.7 \times 10^{-5}$
	0.29	2.976×10^{-5}	3.8×10^{-6}	-2.4×10^{-5} $+2.4 \times 10^{-5}$
	0.49	1.361×10^{-5}	4.1×10^{-6}	-2×10^{-5} $+2 \times 10^{-5}$
	0.69	5.344×10^{-6}	4.4×10^{-6}	-1.7×10^{-5} $+1.7 \times 10^{-5}$
	0.88	1.515×10^{-6}	4.9×10^{-6}	-1.6×10^{-5} $+1.6 \times 10^{-5}$
	1.08	2.877×10^{-6}	5.9×10^{-6}	-1.5×10^{-5} $+1.5 \times 10^{-5}$
	1.28	3.322×10^{-6}	7.5×10^{-6}	-1.5×10^{-5} $+1.5 \times 10^{-5}$
	1.47	1.268×10^{-5}	9.1×10^{-6}	-1.6×10^{-5} $+1.6 \times 10^{-5}$
	1.67	2.252×10^{-5}	8.7×10^{-6}	-1.7×10^{-5} $+1.7 \times 10^{-5}$

Table C.13 – (20-40% Au+Au, $p_{T,\text{trig}}$: 5-10 GeV/c) continued from previous page

$p_{T,\text{assoc}}$	$\Delta\phi$	$J(\Delta\phi_{ta})$	**Stat. Error**	**Syst. Error**
	1.87	2.77×10^{-5}	7.1×10^{-6}	-1.8×10^{-5} $+1.8 \times 10^{-5}$
	2.06	2.395×10^{-5}	6×10^{-6}	-1.9×10^{-5} $+1.9 \times 10^{-5}$
	2.26	3.507×10^{-5}	5.2×10^{-6}	-2.1×10^{-5} $+2.1 \times 10^{-5}$
	2.45	3.172×10^{-5}	4.6×10^{-6}	-2.4×10^{-5} $+2.4 \times 10^{-5}$
	2.65	3.803×10^{-5}	4.2×10^{-6}	-2.7×10^{-5} $+2.7 \times 10^{-5}$
	2.85	3.063×10^{-5}	4×10^{-6}	-3×10^{-5} $+3 \times 10^{-5}$
	3.04	2.769×10^{-5}	3.9×10^{-6}	-3.1×10^{-5} $+3.1 \times 10^{-5}$
1-2 GeV/c	-3.04	1.204×10^{-5}	1.8×10^{-6}	-6×10^{-6} $+6 \times 10^{-6}$
	-2.85	1.401×10^{-5}	1.8×10^{-6}	-5.5×10^{-6} $+5.5 \times 10^{-6}$
	-2.65	1.118×10^{-5}	1.9×10^{-6}	-4.9×10^{-6} $+4.9 \times 10^{-6}$
	-2.45	1.093×10^{-5}	2.1×10^{-6}	-4.2×10^{-6} $+4.2 \times 10^{-6}$
	-2.26	1.288×10^{-5}	2.3×10^{-6}	-3.6×10^{-6} $+3.6 \times 10^{-6}$
	-2.06	9.949×10^{-6}	2.7×10^{-6}	-3.2×10^{-6} $+3.2 \times 10^{-6}$
	-1.87	1.201×10^{-5}	3×10^{-6}	-3×10^{-6} $+3 \times 10^{-6}$
	-1.67	1.432×10^{-5}	3.9×10^{-6}	-2.9×10^{-6} $+2.9 \times 10^{-6}$
	-1.47	9.142×10^{-6}	4.3×10^{-6}	-2.7×10^{-6} $+2.7 \times 10^{-6}$
	-1.28	5.748×10^{-6}	3.1×10^{-6}	-2.6×10^{-6} $+2.6 \times 10^{-6}$
	-1.08	-1.282×10^{-6}	2.5×10^{-6}	-2.6×10^{-6} $+2.6 \times 10^{-6}$
	-0.88	1.828×10^{-6}	2.1×10^{-6}	-2.8×10^{-6} $+2.8 \times 10^{-6}$
	-0.69	3.638×10^{-6}	2×10^{-6}	-3×10^{-6} $+3 \times 10^{-6}$
	-0.49	1.174×10^{-5}	1.8×10^{-6}	-3.4×10^{-6} $+3.4 \times 10^{-6}$
	-0.29	2.346×10^{-5}	1.8×10^{-6}	-4.5×10^{-6} $+4.5 \times 10^{-6}$
	-0.10	3.768×10^{-5}	1.9×10^{-6}	-5.8×10^{-6} $+5.8 \times 10^{-6}$
	0.10	3.732×10^{-5}	1.9×10^{-6}	-5.8×10^{-6} $+5.8 \times 10^{-6}$
	0.29	2.204×10^{-5}	1.8×10^{-6}	-4.5×10^{-6} $+4.5 \times 10^{-6}$
	0.49	1.32×10^{-5}	1.9×10^{-6}	-3.4×10^{-6} $+3.4 \times 10^{-6}$
	0.69	6.25×10^{-6}	2.1×10^{-6}	-3×10^{-6} $+3 \times 10^{-6}$

Table C.13 – (20-40% Au+Au, $p_{T,\text{trig}}$: 5-10 GeV/c) continued from previous page

$p_{T,\text{assoc}}$	$\Delta\phi$	$J(\Delta\phi_{ta})$	**Stat. Error**	**Syst. Error**
	0.88	1.425×10^{-6}	2.2×10^{-6}	-2.8×10^{-6} $+2.8 \times 10^{-6}$
	1.08	-2.552×10^{-6}	2.6×10^{-6}	-2.6×10^{-6} $+2.6 \times 10^{-6}$
	1.28	6.965×10^{-6}	3.4×10^{-6}	-2.6×10^{-6} $+2.6 \times 10^{-6}$
	1.47	1.053×10^{-6}	4.5×10^{-6}	-2.7×10^{-6} $+2.7 \times 10^{-6}$
	1.67	4.141×10^{-9}	4.1×10^{-6}	-2.9×10^{-6} $+2.9 \times 10^{-6}$
	1.87	8.277×10^{-6}	3.2×10^{-6}	-3×10^{-6} $+3 \times 10^{-6}$
	2.06	7.772×10^{-6}	2.8×10^{-6}	-3.2×10^{-6} $+3.2 \times 10^{-6}$
	2.26	1.276×10^{-5}	2.4×10^{-6}	-3.6×10^{-6} $+3.6 \times 10^{-6}$
	2.45	1.522×10^{-5}	2.1×10^{-6}	-4.2×10^{-6} $+4.2 \times 10^{-6}$
	2.65	1.136×10^{-5}	1.9×10^{-6}	-4.9×10^{-6} $+4.9 \times 10^{-6}$
	2.85	1.073×10^{-5}	1.9×10^{-6}	-5.5×10^{-6} $+5.5 \times 10^{-6}$
	3.04	9.708×10^{-6}	1.8×10^{-6}	-6×10^{-6} $+6 \times 10^{-6}$
2-3 GeV/c	-3.04	1.915×10^{-6}	5.2×10^{-7}	-7.9×10^{-7} $+7.9 \times 10^{-7}$
	-2.85	7.35×10^{-7}	5.1×10^{-7}	-6.1×10^{-7} $+6.1 \times 10^{-7}$
	-2.65	1.02×10^{-6}	5.3×10^{-7}	-4.2×10^{-7} $+4.2 \times 10^{-7}$
	-2.45	1.492×10^{-6}	5.9×10^{-7}	-3.7×10^{-7} $+3.7 \times 10^{-7}$
	-2.26	1.587×10^{-6}	6.6×10^{-7}	-3.5×10^{-7} $+3.5 \times 10^{-7}$
	-2.06	-1.016×10^{-7}	7.5×10^{-7}	-2.9×10^{-7} $+2.9 \times 10^{-7}$
	-1.87	9.133×10^{-7}	8.5×10^{-7}	-2.5×10^{-7} $+2.5 \times 10^{-7}$
	-1.67	7.833×10^{-7}	1.1×10^{-6}	-2.3×10^{-7} $+2.3 \times 10^{-7}$
	-1.47	8.644×10^{-7}	1.2×10^{-6}	-2.3×10^{-7} $+2.3 \times 10^{-7}$
	-1.28	-2.665×10^{-7}	8.6×10^{-7}	-2.3×10^{-7} $+2.3 \times 10^{-7}$
	-1.08	9.241×10^{-7}	7.2×10^{-7}	-2.3×10^{-7} $+2.3 \times 10^{-7}$
	-0.88	1.227×10^{-6}	6×10^{-7}	-2.3×10^{-7} $+2.3 \times 10^{-7}$
	-0.69	7.906×10^{-7}	5.6×10^{-7}	-2.5×10^{-7} $+2.5 \times 10^{-7}$
	-0.49	1.633×10^{-6}	5.3×10^{-7}	-3.6×10^{-7} $+3.6 \times 10^{-7}$
	-0.29	5.339×10^{-6}	5.1×10^{-7}	-4.3×10^{-7} $+4.3 \times 10^{-7}$

Table C.13 – (20-40% Au+Au, $p_{T,\text{trig}}$: 5-10 GeV/c) continued from previous page

$p_{T,\text{assoc}}$	$\Delta\phi$	$J(\Delta\phi_{ta})$	**Stat. Error**	**Syst. Error**
	-0.10	1.292×10^{-5}	5.6×10^{-7}	-8.4×10^{-7} $+8.4 \times 10^{-7}$
	0.10	1.345×10^{-5}	5.7×10^{-7}	-8.4×10^{-7} $+8.4 \times 10^{-7}$
	0.29	5.185×10^{-6}	5.2×10^{-7}	-4.3×10^{-7} $+4.3 \times 10^{-7}$
	0.49	2.208×10^{-6}	5.4×10^{-7}	-3.6×10^{-7} $+3.6 \times 10^{-7}$
	0.69	-7.714×10^{-7}	5.8×10^{-7}	-2.5×10^{-7} $+2.5 \times 10^{-7}$
	0.88	8.433×10^{-8}	6.2×10^{-7}	-2.3×10^{-7} $+2.3 \times 10^{-7}$
	1.08	-7.251×10^{-7}	7.4×10^{-7}	-2.3×10^{-7} $+2.3 \times 10^{-7}$
	1.28	8.007×10^{-7}	9.4×10^{-7}	-2.3×10^{-7} $+2.3 \times 10^{-7}$
	1.47	1.557×10^{-6}	1.3×10^{-6}	-2.3×10^{-7} $+2.3 \times 10^{-7}$
	1.67	2.436×10^{-6}	1.2×10^{-6}	-2.3×10^{-7} $+2.3 \times 10^{-7}$
	1.87	2.499×10^{-6}	9.4×10^{-7}	-2.5×10^{-7} $+2.5 \times 10^{-7}$
	2.06	1.895×10^{-6}	8.2×10^{-7}	-2.9×10^{-7} $+2.9 \times 10^{-7}$
	2.26	4.922×10^{-7}	6.6×10^{-7}	-3.5×10^{-7} $+3.5 \times 10^{-7}$
	2.45	3.309×10^{-8}	5.9×10^{-7}	-3.7×10^{-7} $+3.7 \times 10^{-7}$
	2.65	1.654×10^{-6}	5.5×10^{-7}	-4.2×10^{-7} $+4.2 \times 10^{-7}$
	2.85	1.741×10^{-7}	5.3×10^{-7}	-6.1×10^{-7} $+6.1 \times 10^{-7}$
	3.04	2.539×10^{-6}	5.3×10^{-7}	-7.9×10^{-7} $+7.9 \times 10^{-7}$
3-5 GeV/c	-3.04	1.066×10^{-6}	1.9×10^{-7}	-2.4×10^{-7} $+2.4 \times 10^{-7}$
	-2.85	6.974×10^{-7}	1.9×10^{-7}	-1.9×10^{-7} $+1.9 \times 10^{-7}$
	-2.65	8.41×10^{-7}	2×10^{-7}	-1.3×10^{-7} $+1.3 \times 10^{-7}$
	-2.45	4.553×10^{-7}	2.1×10^{-7}	-1.1×10^{-7} $+1.1 \times 10^{-7}$
	-2.26	5.309×10^{-7}	2.4×10^{-7}	-1.1×10^{-7} $+1.1 \times 10^{-7}$
	-2.06	1.756×10^{-7}	2.6×10^{-7}	-9.4×10^{-8} $+9.4 \times 10^{-8}$
	-1.87	1.065×10^{-7}	2.9×10^{-7}	-7.9×10^{-8} $+7.9 \times 10^{-8}$
	-1.67	1.873×10^{-7}	3.9×10^{-7}	-7×10^{-8} $+7 \times 10^{-8}$
	-1.47	7.164×10^{-7}	4.5×10^{-7}	-6.8×10^{-8} $+6.8 \times 10^{-8}$
	-1.28	1.524×10^{-7}	3.1×10^{-7}	-6.7×10^{-8} $+6.7 \times 10^{-8}$

Table C.13 – (20-40% Au+Au, $p_{T,\text{trig}}$: 5-10 GeV/c) continued from previous page

$p_{T,\text{assoc}}$	$\Delta\phi$	$J(\Delta\phi_{ta})$	**Stat. Error**	**Syst. Error**
	-1.08	-7.384×10^{-9}	2.4×10^{-7}	-6.7×10^{-8} $+6.7\times10^{-8}$
	-0.88	-3.249×10^{-7}	1.9×10^{-7}	-6.7×10^{-8} $+6.7\times10^{-8}$
	-0.69	2.104×10^{-7}	2×10^{-7}	-6.7×10^{-8} $+6.7\times10^{-8}$
	-0.49	4.431×10^{-7}	1.9×10^{-7}	-7.3×10^{-8} $+7.3\times10^{-8}$
	-0.29	1.508×10^{-6}	1.9×10^{-7}	-1.5×10^{-7} $+1.5\times10^{-7}$
	-0.10	7.001×10^{-6}	2.8×10^{-7}	-2.9×10^{-7} $+2.9\times10^{-7}$
	0.10	7.359×10^{-6}	2.8×10^{-7}	-2.9×10^{-7} $+2.9\times10^{-7}$
	0.29	1.667×10^{-6}	2×10^{-7}	-1.5×10^{-7} $+1.5\times10^{-7}$
	0.49	2.041×10^{-7}	1.8×10^{-7}	-7.3×10^{-8} $+7.3\times10^{-8}$
	0.69	4.107×10^{-8}	2×10^{-7}	-6.7×10^{-8} $+6.7\times10^{-8}$
	0.88	-2.035×10^{-7}	2.1×10^{-7}	-6.7×10^{-8} $+6.7\times10^{-8}$
	1.08	4.175×10^{-7}	2.8×10^{-7}	-6.7×10^{-8} $+6.7\times10^{-8}$
	1.28	4.727×10^{-7}	3.4×10^{-7}	-6.7×10^{-8} $+6.7\times10^{-8}$
	1.47	-4.003×10^{-7}	4.1×10^{-7}	-6.8×10^{-8} $+6.8\times10^{-8}$
	1.67	-5.134×10^{-7}	3.8×10^{-7}	-7×10^{-8} $+7\times10^{-8}$
	1.87	5.42×10^{-7}	3.3×10^{-7}	-7.9×10^{-8} $+7.9\times10^{-8}$
	2.06	1.359×10^{-9}	2.7×10^{-7}	-9.4×10^{-8} $+9.4\times10^{-8}$
	2.26	3.641×10^{-7}	2.4×10^{-7}	-1.1×10^{-7} $+1.1\times10^{-7}$
	2.45	5.932×10^{-7}	2.2×10^{-7}	-1.1×10^{-7} $+1.1\times10^{-7}$
	2.65	4.401×10^{-7}	1.9×10^{-7}	-1.3×10^{-7} $+1.3\times10^{-7}$
	2.85	5.378×10^{-7}	1.9×10^{-7}	-1.9×10^{-7} $+1.9\times10^{-7}$
	3.04	1.053×10^{-6}	2×10^{-7}	-2.4×10^{-7} $+2.4\times10^{-7}$

Table C.14: **Two-particle 40-60% Au+Au jet-induced correlation for $p_{T,\mathrm{trig}}$: 5-10 GeV/c.**

$p_{T,\mathrm{assoc}}$	$\Delta\phi$	$J(\Delta\phi_{ta})$	**Stat. Error**	**Syst. Error**
0.4-1 GeV/c	-3.04	4.716×10^{-5}	4.7×10^{-6}	-2.2×10^{-5} $+2.2 \times 10^{-5}$
	-2.85	2.967×10^{-5}	4.7×10^{-6}	-2.1×10^{-5} $+2.1 \times 10^{-5}$
	-2.65	3.297×10^{-5}	4.9×10^{-6}	-1.9×10^{-5} $+1.9 \times 10^{-5}$
	-2.45	2.864×10^{-5}	5.3×10^{-6}	-1.6×10^{-5} $+1.6 \times 10^{-5}$
	-2.26	2.418×10^{-5}	6×10^{-6}	-1.4×10^{-5} $+1.4 \times 10^{-5}$
	-2.06	2.909×10^{-5}	6.8×10^{-6}	-1.3×10^{-5} $+1.3 \times 10^{-5}$
	-1.87	2.11×10^{-5}	8.1×10^{-6}	-1.2×10^{-5} $+1.2 \times 10^{-5}$
	-1.67	-4.484×10^{-7}	9.9×10^{-6}	-1.1×10^{-5} $+1.1 \times 10^{-5}$
	-1.47	1.403×10^{-5}	1.1×10^{-5}	-1.1×10^{-5} $+1.1 \times 10^{-5}$
	-1.28	-4.801×10^{-6}	8.1×10^{-6}	-1×10^{-5} $+1 \times 10^{-5}$
	-1.08	5.864×10^{-6}	6.4×10^{-6}	-1×10^{-5} $+1 \times 10^{-5}$
	-0.88	1.213×10^{-6}	5.5×10^{-6}	-1.1×10^{-5} $+1.1 \times 10^{-5}$
	-0.69	1.471×10^{-5}	5×10^{-6}	-1.2×10^{-5} $+1.2 \times 10^{-5}$
	-0.49	2.138×10^{-5}	4.7×10^{-6}	-1.4×10^{-5} $+1.4 \times 10^{-5}$
	-0.29	2.806×10^{-5}	4.4×10^{-6}	-1.7×10^{-5} $+1.7 \times 10^{-5}$
	-0.10	4.225×10^{-5}	4.7×10^{-6}	-2×10^{-5} $+2 \times 10^{-5}$
	0.10	4.121×10^{-5}	4.8×10^{-6}	-2×10^{-5} $+2 \times 10^{-5}$
	0.29	3.594×10^{-5}	4.5×10^{-6}	-1.7×10^{-5} $+1.7 \times 10^{-5}$
	0.49	2.006×10^{-5}	4.9×10^{-6}	-1.4×10^{-5} $+1.4 \times 10^{-5}$
	0.69	-4.633×10^{-6}	5.2×10^{-6}	-1.2×10^{-5} $+1.2 \times 10^{-5}$
	0.88	-9.935×10^{-7}	5.8×10^{-6}	-1.1×10^{-5} $+1.1 \times 10^{-5}$
	1.08	4.783×10^{-6}	6.9×10^{-6}	-1×10^{-5} $+1 \times 10^{-5}$
	1.28	-3.27×10^{-6}	8.9×10^{-6}	-1×10^{-5} $+1 \times 10^{-5}$
	1.47	1.422×10^{-5}	1.1×10^{-5}	-1.1×10^{-5} $+1.1 \times 10^{-5}$
	1.67	9.293×10^{-6}	1×10^{-5}	-1.1×10^{-5} $+1.1 \times 10^{-5}$

Table C.14 – (40-60% Au+Au, $p_{T,\mathrm{trig}}$: 5-10 GeV/c) continued from previous page

$p_{T,\mathrm{assoc}}$	$\Delta\phi$	$J(\Delta\phi_{ta})$	**Stat. Error**	**Syst. Error**
	1.87	2.533×10^{-5}	8.5×10^{-6}	-1.2×10^{-5} $+1.2 \times 10^{-5}$
	2.06	2.005×10^{-5}	7.1×10^{-6}	-1.3×10^{-5} $+1.3 \times 10^{-5}$
	2.26	2.606×10^{-5}	6.1×10^{-6}	-1.4×10^{-5} $+1.4 \times 10^{-5}$
	2.45	4.195×10^{-5}	5.4×10^{-6}	-1.6×10^{-5} $+1.6 \times 10^{-5}$
	2.65	3.212×10^{-5}	5×10^{-6}	-1.9×10^{-5} $+1.9 \times 10^{-5}$
	2.85	3.556×10^{-5}	4.7×10^{-6}	-2.1×10^{-5} $+2.1 \times 10^{-5}$
	3.04	3.919×10^{-5}	4.7×10^{-6}	-2.2×10^{-5} $+2.2 \times 10^{-5}$
1-2 GeV/c	-3.04	1.921×10^{-5}	2.1×10^{-6}	-6.2×10^{-6} $+6.2 \times 10^{-6}$
	-2.85	1.94×10^{-5}	2.1×10^{-6}	-5.7×10^{-6} $+5.7 \times 10^{-6}$
	-2.65	2.316×10^{-5}	2.2×10^{-6}	-4.9×10^{-6} $+4.9 \times 10^{-6}$
	-2.45	1.309×10^{-5}	2.4×10^{-6}	-4.1×10^{-6} $+4.1 \times 10^{-6}$
	-2.26	1.31×10^{-5}	2.7×10^{-6}	-3.5×10^{-6} $+3.5 \times 10^{-6}$
	-2.06	1.263×10^{-5}	3.1×10^{-6}	-3.2×10^{-6} $+3.2 \times 10^{-6}$
	-1.87	7.862×10^{-6}	3.5×10^{-6}	-3×10^{-6} $+3 \times 10^{-6}$
	-1.67	1.369×10^{-6}	4.5×10^{-6}	-2.9×10^{-6} $+2.9 \times 10^{-6}$
	-1.47	-2.674×10^{-6}	4.9×10^{-6}	-2.7×10^{-6} $+2.7 \times 10^{-6}$
	-1.28	4.505×10^{-6}	3.6×10^{-6}	-2.6×10^{-6} $+2.6 \times 10^{-6}$
	-1.08	-3.741×10^{-6}	2.9×10^{-6}	-2.6×10^{-6} $+2.6 \times 10^{-6}$
	-0.88	2.46×10^{-6}	2.4×10^{-6}	-2.8×10^{-6} $+2.8 \times 10^{-6}$
	-0.69	7.385×10^{-6}	2.3×10^{-6}	-3.1×10^{-6} $+3.1 \times 10^{-6}$
	-0.49	1.653×10^{-5}	2.2×10^{-6}	-3.6×10^{-6} $+3.6 \times 10^{-6}$
	-0.29	2.952×10^{-5}	2.1×10^{-6}	-4.8×10^{-6} $+4.8 \times 10^{-6}$
	-0.10	3.883×10^{-5}	2.2×10^{-6}	-6.2×10^{-6} $+6.2 \times 10^{-6}$
	0.10	3.896×10^{-5}	2.3×10^{-6}	-6.2×10^{-6} $+6.2 \times 10^{-6}$
	0.29	2.558×10^{-5}	2.2×10^{-6}	-4.8×10^{-6} $+4.8 \times 10^{-6}$
	0.49	1.188×10^{-5}	2.2×10^{-6}	-3.6×10^{-6} $+3.6 \times 10^{-6}$
	0.69	6.93×10^{-6}	2.4×10^{-6}	-3.1×10^{-6} $+3.1 \times 10^{-6}$

Table C.14 – (40-60% Au+Au, $p_{T,\text{trig}}$: 5-10 GeV/c) continued from previous page

$p_{T,\text{assoc}}$	$\Delta\phi$	$J(\Delta\phi_{ta})$	**Stat. Error**	**Syst. Error**
	0.88	1.554×10^{-6}	2.5×10^{-6}	-2.8×10^{-6} $+2.8 \times 10^{-6}$
	1.08	2.04×10^{-6}	3.1×10^{-6}	-2.6×10^{-6} $+2.6 \times 10^{-6}$
	1.28	2.177×10^{-6}	3.9×10^{-6}	-2.6×10^{-6} $+2.6 \times 10^{-6}$
	1.47	1.303×10^{-6}	5.3×10^{-6}	-2.7×10^{-6} $+2.7 \times 10^{-6}$
	1.67	1.884×10^{-7}	4.8×10^{-6}	-2.9×10^{-6} $+2.9 \times 10^{-6}$
	1.87	1.145×10^{-5}	3.8×10^{-6}	-3×10^{-6} $+3 \times 10^{-6}$
	2.06	8.81×10^{-6}	3.3×10^{-6}	-3.2×10^{-6} $+3.2 \times 10^{-6}$
	2.26	1.432×10^{-5}	2.8×10^{-6}	-3.5×10^{-6} $+3.5 \times 10^{-6}$
	2.45	1.325×10^{-5}	2.4×10^{-6}	-4.1×10^{-6} $+4.1 \times 10^{-6}$
	2.65	1.38×10^{-5}	2.2×10^{-6}	-4.9×10^{-6} $+4.9 \times 10^{-6}$
	2.85	1.73×10^{-5}	2.2×10^{-6}	-5.7×10^{-6} $+5.7 \times 10^{-6}$
	3.04	1.916×10^{-5}	2.1×10^{-6}	-6.2×10^{-6} $+6.2 \times 10^{-6}$
2-3 GeV/c	-3.04	4.613×10^{-6}	6.4×10^{-7}	-8.7×10^{-7} $+8.7 \times 10^{-7}$
	-2.85	4.62×10^{-6}	6.5×10^{-7}	-6.8×10^{-7} $+6.8 \times 10^{-7}$
	-2.65	2.863×10^{-6}	6.4×10^{-7}	-4.8×10^{-7} $+4.8 \times 10^{-7}$
	-2.45	1.826×10^{-6}	6.9×10^{-7}	-4.1×10^{-7} $+4.1 \times 10^{-7}$
	-2.26	8.573×10^{-7}	7.5×10^{-7}	-3.9×10^{-7} $+3.9 \times 10^{-7}$
	-2.06	-2.476×10^{-7}	8.5×10^{-7}	-3.4×10^{-7} $+3.4 \times 10^{-7}$
	-1.87	1.468×10^{-6}	1×10^{-6}	-2.9×10^{-7} $+2.9 \times 10^{-7}$
	-1.67	7.042×10^{-7}	1.3×10^{-6}	-2.7×10^{-7} $+2.7 \times 10^{-7}$
	-1.47	-6.384×10^{-7}	1.3×10^{-6}	-2.7×10^{-7} $+2.7 \times 10^{-7}$
	-1.28	-1.076×10^{-6}	9.8×10^{-7}	-2.7×10^{-7} $+2.7 \times 10^{-7}$
	-1.08	-1.587×10^{-6}	7.8×10^{-7}	-2.7×10^{-7} $+2.7 \times 10^{-7}$
	-0.88	8.881×10^{-7}	6.9×10^{-7}	-2.7×10^{-7} $+2.7 \times 10^{-7}$
	-0.69	2.185×10^{-6}	6.8×10^{-7}	-3×10^{-7} $+3 \times 10^{-7}$
	-0.49	1.542×10^{-6}	6.1×10^{-7}	-4.7×10^{-7} $+4.7 \times 10^{-7}$
	-0.29	7.82×10^{-6}	6.5×10^{-7}	-5.2×10^{-7} $+5.2 \times 10^{-7}$

Table C.14 – (40-60% Au+Au, $p_{T,\mathrm{trig}}$: 5-10 GeV/c) continued from previous page

$p_{T,\mathrm{assoc}}$	$\Delta\phi$	$J(\Delta\phi_{ta})$	**Stat. Error**	**Syst. Error**
	-0.10	1.852×10^{-5}	7.8×10^{-7}	-1.1×10^{-6} $+1.1 \times 10^{-6}$
	0.10	1.79×10^{-5}	7.7×10^{-7}	-1.1×10^{-6} $+1.1 \times 10^{-6}$
	0.29	8.38×10^{-6}	6.7×10^{-7}	-5.2×10^{-7} $+5.2 \times 10^{-7}$
	0.49	3.945×10^{-6}	6.6×10^{-7}	-4.7×10^{-7} $+4.7 \times 10^{-7}$
	0.69	1.611×10^{-6}	7×10^{-7}	-3×10^{-7} $+3 \times 10^{-7}$
	0.88	-3.617×10^{-7}	7×10^{-7}	-2.7×10^{-7} $+2.7 \times 10^{-7}$
	1.08	-5.579×10^{-7}	8.4×10^{-7}	-2.7×10^{-7} $+2.7 \times 10^{-7}$
	1.28	-1.696×10^{-6}	1×10^{-6}	-2.7×10^{-7} $+2.7 \times 10^{-7}$
	1.47	1.177×10^{-6}	1.5×10^{-6}	-2.7×10^{-7} $+2.7 \times 10^{-7}$
	1.67	-9.769×10^{-7}	1.3×10^{-6}	-2.7×10^{-7} $+2.7 \times 10^{-7}$
	1.87	1.03×10^{-8}	1×10^{-6}	-2.9×10^{-7} $+2.9 \times 10^{-7}$
	2.06	9.281×10^{-7}	9.4×10^{-7}	-3.4×10^{-7} $+3.4 \times 10^{-7}$
	2.26	1.576×10^{-6}	7.8×10^{-7}	-3.9×10^{-7} $+3.9 \times 10^{-7}$
	2.45	3.43×10^{-6}	7.3×10^{-7}	-4.1×10^{-7} $+4.1 \times 10^{-7}$
	2.65	2.882×10^{-6}	6.6×10^{-7}	-4.8×10^{-7} $+4.8 \times 10^{-7}$
	2.85	4.232×10^{-6}	6.6×10^{-7}	-6.8×10^{-7} $+6.8 \times 10^{-7}$
	3.04	5.788×10^{-6}	6.6×10^{-7}	-8.7×10^{-7} $+8.7 \times 10^{-7}$
3-5 GeV/c	-3.04	2.241×10^{-6}	2.9×10^{-7}	-3.5×10^{-7} $+3.5 \times 10^{-7}$
	-2.85	1.07×10^{-6}	2.6×10^{-7}	-2.1×10^{-7} $+2.1 \times 10^{-7}$
	-2.65	1.038×10^{-6}	2.7×10^{-7}	-1.5×10^{-7} $+1.5 \times 10^{-7}$
	-2.45	2.834×10^{-7}	2.6×10^{-7}	-1.4×10^{-7} $+1.4 \times 10^{-7}$
	-2.26	-4.415×10^{-10}	2.7×10^{-7}	-1×10^{-7} $+1 \times 10^{-7}$
	-2.06	4.719×10^{-7}	3.5×10^{-7}	-8×10^{-8} $+8 \times 10^{-8}$
	-1.87	-9.876×10^{-8}	3.6×10^{-7}	-7.7×10^{-8} $+7.7 \times 10^{-8}$
	-1.67	-1.08×10^{-6}	3.4×10^{-7}	-7.7×10^{-8} $+7.7 \times 10^{-8}$
	-1.47	-4.584×10^{-7}	5.1×10^{-7}	-7.7×10^{-8} $+7.7 \times 10^{-8}$

Table C.14 – (40-60% Au+Au, $p_{T,\text{trig}}$: 5-10 GeV/c) continued from previous page

$p_{T,\text{assoc}}$	$\Delta\phi$	$J(\Delta\phi_{ta})$	**Stat. Error**	**Syst. Error**
	-1.28	-1.556×10^{-7}	3.7×10^{-7}	-7.7×10^{-8} $+7.7\times10^{-8}$
	-1.08	4.161×10^{-7}	3.4×10^{-7}	-7.7×10^{-8} $+7.7\times10^{-8}$
	-0.88	-6.573×10^{-8}	2.5×10^{-7}	-7.7×10^{-8} $+7.7\times10^{-8}$
	-0.69	1.222×10^{-7}	2.4×10^{-7}	-7.7×10^{-8} $+7.7\times10^{-8}$
	-0.49	2.588×10^{-7}	2.3×10^{-7}	-8.7×10^{-8} $+8.7\times10^{-8}$
	-0.29	2.165×10^{-6}	2.8×10^{-7}	-2.2×10^{-7} $+2.2\times10^{-7}$
	-0.10	1.108×10^{-5}	4.9×10^{-7}	-4.3×10^{-7} $+4.3\times10^{-7}$
	0.10	1.013×10^{-5}	4.7×10^{-7}	-4.3×10^{-7} $+4.3\times10^{-7}$
	0.29	2.561×10^{-6}	2.9×10^{-7}	-2.2×10^{-7} $+2.2\times10^{-7}$
	0.49	8.126×10^{-7}	2.6×10^{-7}	-8.7×10^{-8} $+8.7\times10^{-8}$
	0.69	-7.607×10^{-8}	2.5×10^{-7}	-7.7×10^{-8} $+7.7\times10^{-8}$
	0.88	-4.436×10^{-7}	2.4×10^{-7}	-7.7×10^{-8} $+7.7\times10^{-8}$
	1.08	-3.927×10^{-7}	3.1×10^{-7}	-7.7×10^{-8} $+7.7\times10^{-8}$
	1.28	1.895×10^{-7}	4.2×10^{-7}	-7.7×10^{-8} $+7.7\times10^{-8}$
	1.47	-5.467×10^{-7}	5.2×10^{-7}	-7.7×10^{-8} $+7.7\times10^{-8}$
	1.67	3.863×10^{-8}	5.5×10^{-7}	-7.7×10^{-8} $+7.7\times10^{-8}$
	1.87	-2.221×10^{-7}	3.7×10^{-7}	-7.7×10^{-8} $+7.7\times10^{-8}$
	2.06	1.147×10^{-8}	3.4×10^{-7}	-8×10^{-8} $+8\times10^{-8}$
	2.26	4.544×10^{-7}	3×10^{-7}	-1×10^{-7} $+1\times10^{-7}$
	2.45	3.284×10^{-7}	2.7×10^{-7}	-1.4×10^{-7} $+1.4\times10^{-7}$
	2.65	7.523×10^{-7}	2.6×10^{-7}	-1.5×10^{-7} $+1.5\times10^{-7}$
	2.85	1.839×10^{-6}	2.9×10^{-7}	-2.1×10^{-7} $+2.1\times10^{-7}$
	3.04	2.479×10^{-6}	3×10^{-7}	-3.5×10^{-7} $+3.5\times10^{-7}$

Table C.15: **Two-particle 60-92% Au+Au jet-induced correlation for $p_{T,\mathrm{trig}}$: 5-10 GeV/c.**

$p_{T,\mathrm{assoc}}$	$\Delta\phi$	$J(\Delta\phi_{ta})$	**Stat. Error**	**Syst. Error**
0.4-1 GeV/c	-3.04	4.105×10^{-5}	5.5×10^{-6}	-3.7×10^{-5} $+3.7 \times 10^{-5}$
	-2.85	3.557×10^{-5}	5.6×10^{-6}	-3.6×10^{-5} $+3.6 \times 10^{-5}$
	-2.65	1.721×10^{-5}	5.7×10^{-6}	-3.3×10^{-5} $+3.3 \times 10^{-5}$
	-2.45	3.011×10^{-5}	6.3×10^{-6}	-3×10^{-5} $+3 \times 10^{-5}$
	-2.26	2.897×10^{-5}	7.1×10^{-6}	-2.7×10^{-5} $+2.7 \times 10^{-5}$
	-2.06	1.182×10^{-5}	7.9×10^{-6}	-2.4×10^{-5} $+2.4 \times 10^{-5}$
	-1.87	3.883×10^{-5}	9.9×10^{-6}	-2.2×10^{-5} $+2.2 \times 10^{-5}$
	-1.67	1.134×10^{-5}	1.2×10^{-5}	-2×10^{-5} $+2 \times 10^{-5}$
	-1.47	-6.665×10^{-6}	1.2×10^{-5}	-1.9×10^{-5} $+1.9 \times 10^{-5}$
	-1.28	-6.317×10^{-7}	9.6×10^{-6}	-1.9×10^{-5} $+1.9 \times 10^{-5}$
	-1.08	1.434×10^{-5}	7.7×10^{-6}	-1.8×10^{-5} $+1.8 \times 10^{-5}$
	-0.88	-3.105×10^{-6}	6.4×10^{-6}	-1.8×10^{-5} $+1.8 \times 10^{-5}$
	-0.69	1.318×10^{-5}	5.9×10^{-6}	-1.8×10^{-5} $+1.8 \times 10^{-5}$
	-0.49	2.041×10^{-5}	5.6×10^{-6}	-1.9×10^{-5} $+1.9 \times 10^{-5}$
	-0.29	3.086×10^{-5}	5.3×10^{-6}	-2.3×10^{-5} $+2.3 \times 10^{-5}$
	-0.10	4.643×10^{-5}	5.7×10^{-6}	-2.7×10^{-5} $+2.7 \times 10^{-5}$
	0.10	4.964×10^{-5}	5.8×10^{-6}	-2.7×10^{-5} $+2.7 \times 10^{-5}$
	0.29	4.034×10^{-5}	5.4×10^{-6}	-2.3×10^{-5} $+2.3 \times 10^{-5}$
	0.49	1.714×10^{-5}	5.7×10^{-6}	-1.9×10^{-5} $+1.9 \times 10^{-5}$
	0.69	3.805×10^{-6}	6×10^{-6}	-1.8×10^{-5} $+1.8 \times 10^{-5}$
	0.88	-8.196×10^{-6}	6.6×10^{-6}	-1.8×10^{-5} $+1.8 \times 10^{-5}$
	1.08	-5.3×10^{-6}	7.9×10^{-6}	-1.8×10^{-5} $+1.8 \times 10^{-5}$
	1.28	1.289×10^{-5}	1.1×10^{-5}	-1.9×10^{-5} $+1.9 \times 10^{-5}$
	1.47	7.331×10^{-6}	1.3×10^{-5}	-1.9×10^{-5} $+1.9 \times 10^{-5}$
	1.67	2.373×10^{-5}	1.3×10^{-5}	-2×10^{-5} $+2 \times 10^{-5}$

Table C.15 – (60-92% Au+Au, $p_{T,\mathrm{trig}}$: 5-10 GeV/c) continued from previous page

$p_{T,\mathrm{assoc}}$	$\Delta\phi$	$J(\Delta\phi_{ta})$	**Stat. Error**	**Syst. Error**
	1.87	2.208×10^{-5}	1×10^{-5}	-2.2×10^{-5} $+2.2 \times 10^{-5}$
	2.06	2.558×10^{-5}	8.5×10^{-6}	-2.4×10^{-5} $+2.4 \times 10^{-5}$
	2.26	2.323×10^{-5}	7.3×10^{-6}	-2.7×10^{-5} $+2.7 \times 10^{-5}$
	2.45	2.947×10^{-5}	6.4×10^{-6}	-3×10^{-5} $+3 \times 10^{-5}$
	2.65	3.481×10^{-5}	6×10^{-6}	-3.3×10^{-5} $+3.3 \times 10^{-5}$
	2.85	3.083×10^{-5}	5.6×10^{-6}	-3.6×10^{-5} $+3.6 \times 10^{-5}$
	3.04	3.48×10^{-5}	5.5×10^{-6}	-3.7×10^{-5} $+3.7 \times 10^{-5}$
1-2 GeV/c	-3.04	2.761×10^{-5}	2.6×10^{-6}	-4.1×10^{-6} $+4.1 \times 10^{-6}$
	-2.85	2.21×10^{-5}	2.6×10^{-6}	-3.4×10^{-6} $+3.4 \times 10^{-6}$
	-2.65	1.672×10^{-5}	2.6×10^{-6}	-2.6×10^{-6} $+2.6 \times 10^{-6}$
	-2.45	1.083×10^{-5}	2.8×10^{-6}	-2.1×10^{-6} $+2.1 \times 10^{-6}$
	-2.26	1×10^{-5}	3.1×10^{-6}	-1.9×10^{-6} $+1.9 \times 10^{-6}$
	-2.06	1.751×10^{-5}	3.8×10^{-6}	-1.8×10^{-6} $+1.8 \times 10^{-6}$
	-1.87	-4.401×10^{-6}	3.8×10^{-6}	-1.6×10^{-6} $+1.6 \times 10^{-6}$
	-1.67	6.046×10^{-6}	5.3×10^{-6}	-1.4×10^{-6} $+1.4 \times 10^{-6}$
	-1.47	-1.251×10^{-6}	5.6×10^{-6}	-1.4×10^{-6} $+1.4 \times 10^{-6}$
	-1.28	-5.086×10^{-8}	4.1×10^{-6}	-1.3×10^{-6} $+1.3 \times 10^{-6}$
	-1.08	-6.581×10^{-7}	3.3×10^{-6}	-1.3×10^{-6} $+1.3 \times 10^{-6}$
	-0.88	1.184×10^{-6}	2.7×10^{-6}	-1.4×10^{-6} $+1.4 \times 10^{-6}$
	-0.69	5.139×10^{-6}	2.6×10^{-6}	-1.7×10^{-6} $+1.7 \times 10^{-6}$
	-0.49	1.346×10^{-5}	2.5×10^{-6}	-2.2×10^{-6} $+2.2 \times 10^{-6}$
	-0.29	2.269×10^{-5}	2.5×10^{-6}	-2.6×10^{-6} $+2.6 \times 10^{-6}$
	-0.10	5.019×10^{-5}	3×10^{-6}	-4.7×10^{-6} $+4.7 \times 10^{-6}$
	0.10	4.602×10^{-5}	2.9×10^{-6}	-4.7×10^{-6} $+4.7 \times 10^{-6}$
	0.29	2.814×10^{-5}	2.7×10^{-6}	-2.6×10^{-6} $+2.6 \times 10^{-6}$
	0.49	1.106×10^{-5}	2.6×10^{-6}	-2.2×10^{-6} $+2.2 \times 10^{-6}$
	0.69	2.461×10^{-6}	2.7×10^{-6}	-1.7×10^{-6} $+1.7 \times 10^{-6}$

Table C.15 – (60-92% Au+Au, $p_{T,\text{trig}}$: 5-10 GeV/c) continued from previous page

$p_{T,\text{assoc}}$	$\Delta\phi$	$J(\Delta\phi_{ta})$	**Stat. Error**	**Syst. Error**
	0.88	5.1×10^{-6}	2.9×10^{-6}	-1.4×10^{-6} $+1.4 \times 10^{-6}$
	1.08	-4.12×10^{-6}	3.3×10^{-6}	-1.3×10^{-6} $+1.3 \times 10^{-6}$
	1.28	-3.727×10^{-6}	4.3×10^{-6}	-1.3×10^{-6} $+1.3 \times 10^{-6}$
	1.47	-6.614×10^{-6}	5.7×10^{-6}	-1.4×10^{-6} $+1.4 \times 10^{-6}$
	1.67	-6.468×10^{-6}	5.3×10^{-6}	-1.4×10^{-6} $+1.4 \times 10^{-6}$
	1.87	-4.995×10^{-6}	4.1×10^{-6}	-1.6×10^{-6} $+1.6 \times 10^{-6}$
	2.06	1.464×10^{-5}	4×10^{-6}	-1.8×10^{-6} $+1.8 \times 10^{-6}$
	2.26	5.593×10^{-6}	3.1×10^{-6}	-1.9×10^{-6} $+1.9 \times 10^{-6}$
	2.45	1.488×10^{-5}	2.9×10^{-6}	-2.1×10^{-6} $+2.1 \times 10^{-6}$
	2.65	1.675×10^{-5}	2.7×10^{-6}	-2.6×10^{-6} $+2.6 \times 10^{-6}$
	2.85	1.835×10^{-5}	2.6×10^{-6}	-3.4×10^{-6} $+3.4 \times 10^{-6}$
	3.04	2.852×10^{-5}	2.7×10^{-6}	-4.1×10^{-6} $+4.1 \times 10^{-6}$
2-3 GeV/c	-3.04	6.799×10^{-6}	9.3×10^{-7}	-1.1×10^{-6} $+1.1 \times 10^{-6}$
	-2.85	6.897×10^{-6}	9.5×10^{-7}	-7.3×10^{-7} $+7.3 \times 10^{-7}$
	-2.65	4.202×10^{-6}	8.8×10^{-7}	-5×10^{-7} $+5 \times 10^{-7}$
	-2.45	1.962×10^{-6}	8.7×10^{-7}	-4.7×10^{-7} $+4.7 \times 10^{-7}$
	-2.26	1.013×10^{-6}	9.2×10^{-7}	-3.9×10^{-7} $+3.9 \times 10^{-7}$
	-2.06	-7.439×10^{-7}	9.6×10^{-7}	-3.1×10^{-7} $+3.1 \times 10^{-7}$
	-1.87	-6.625×10^{-7}	1.1×10^{-6}	-2.8×10^{-7} $+2.8 \times 10^{-7}$
	-1.67	1.073×10^{-6}	1.7×10^{-6}	-2.8×10^{-7} $+2.8 \times 10^{-7}$
	-1.47	-2.248×10^{-7}	1.7×10^{-6}	-2.8×10^{-7} $+2.8 \times 10^{-7}$
	-1.28	-2.458×10^{-6}	9.4×10^{-7}	-2.8×10^{-7} $+2.8 \times 10^{-7}$
	-1.08	3.316×10^{-8}	9.7×10^{-7}	-2.8×10^{-7} $+2.8 \times 10^{-7}$
	-0.88	-2.172×10^{-7}	7.9×10^{-7}	-2.8×10^{-7} $+2.8 \times 10^{-7}$
	-0.69	2.904×10^{-7}	7.8×10^{-7}	-2.9×10^{-7} $+2.9 \times 10^{-7}$
	-0.49	2.345×10^{-6}	8×10^{-7}	-5×10^{-7} $+5 \times 10^{-7}$
	-0.29	8.078×10^{-6}	9.4×10^{-7}	-6.4×10^{-7} $+6.4 \times 10^{-7}$

Table C.15 – (60-92% Au+Au, $p_{T,\text{trig}}$: 5-10 GeV/c) continued from previous page

$p_{T,\text{assoc}}$	$\Delta\phi$	$J(\Delta\phi_{ta})$	**Stat. Error**	**Syst. Error**
	-0.10	2.112×10^{-5}	1.3×10^{-6}	-1.3×10^{-6} $+1.3 \times 10^{-6}$
	0.10	2.137×10^{-5}	1.3×10^{-6}	-1.3×10^{-6} $+1.3 \times 10^{-6}$
	0.29	9.74×10^{-6}	1×10^{-6}	-6.4×10^{-7} $+6.4 \times 10^{-7}$
	0.49	2.405×10^{-6}	8×10^{-7}	-5×10^{-7} $+5 \times 10^{-7}$
	0.69	8.482×10^{-7}	8.3×10^{-7}	-2.9×10^{-7} $+2.9 \times 10^{-7}$
	0.88	4.655×10^{-7}	8.6×10^{-7}	-2.8×10^{-7} $+2.8 \times 10^{-7}$
	1.08	6.789×10^{-7}	1×10^{-6}	-2.8×10^{-7} $+2.8 \times 10^{-7}$
	1.28	-5.3×10^{-7}	1.2×10^{-6}	-2.8×10^{-7} $+2.8 \times 10^{-7}$
	1.47	3.797×10^{-7}	1.9×10^{-6}	-2.8×10^{-7} $+2.8 \times 10^{-7}$
	1.67	-1.883×10^{-6}	1.5×10^{-6}	-2.8×10^{-7} $+2.8 \times 10^{-7}$
	1.87	-7.206×10^{-7}	1.2×10^{-6}	-2.8×10^{-7} $+2.8 \times 10^{-7}$
	2.06	2.837×10^{-6}	1.3×10^{-6}	-3.1×10^{-7} $+3.1 \times 10^{-7}$
	2.26	2.301×10^{-7}	9.1×10^{-7}	-3.9×10^{-7} $+3.9 \times 10^{-7}$
	2.45	1.826×10^{-6}	8.8×10^{-7}	-4.7×10^{-7} $+4.7 \times 10^{-7}$
	2.65	2.261×10^{-6}	8.2×10^{-7}	-5×10^{-7} $+5 \times 10^{-7}$
	2.85	6.434×10^{-6}	9.6×10^{-7}	-7.3×10^{-7} $+7.3 \times 10^{-7}$
	3.04	7.758×10^{-6}	9.8×10^{-7}	-1.1×10^{-6} $+1.1 \times 10^{-6}$
3-5 GeV/c	-3.04	4.25×10^{-6}	6.1×10^{-7}	-5.8×10^{-7} $+5.8 \times 10^{-7}$
	-2.85	2.789×10^{-6}	5.2×10^{-7}	-3×10^{-7} $+3 \times 10^{-7}$
	-2.65	9.545×10^{-7}	3.8×10^{-7}	-2.5×10^{-7} $+2.5 \times 10^{-7}$
	-2.45	3.934×10^{-7}	3.5×10^{-7}	-1.9×10^{-7} $+1.9 \times 10^{-7}$
	-2.26	-1.332×10^{-7}	3.1×10^{-7}	-1.1×10^{-7} $+1.1 \times 10^{-7}$
	-2.06	8.862×10^{-7}	6.4×10^{-7}	-9.5×10^{-8} $+9.5 \times 10^{-8}$
	-1.87	1.258×10^{-7}	4.9×10^{-7}	-9.4×10^{-8} $+9.4 \times 10^{-8}$
	-1.67	-6.127×10^{-7}	3.8×10^{-7}	-9.4×10^{-8} $+9.4 \times 10^{-8}$
	-1.47	-1.217×10^{-7}	6.6×10^{-7}	-9.4×10^{-8} $+9.4 \times 10^{-8}$
	-1.28	-9.006×10^{-8}	4.3×10^{-7}	-9.4×10^{-8} $+9.4 \times 10^{-8}$

Table C.15 – (60-92% Au+Au, $p_{T,\text{trig}}$: 5-10 GeV/c) continued from previous page

$p_{T,\text{assoc}}$	$\Delta\phi$	$J(\Delta\phi_{ta})$	**Stat. Error**	**Syst. Error**
	-1.08	-3.821×10^{-7}	2.9×10^{-7}	-9.4×10^{-8} $+9.4\times10^{-8}$
	-0.88	1.355×10^{-7}	3.4×10^{-7}	-9.4×10^{-8} $+9.4\times10^{-8}$
	-0.69	1.689×10^{-7}	3.3×10^{-7}	-9.4×10^{-8} $+9.4\times10^{-8}$
	-0.49	-2.179×10^{-7}	2.4×10^{-7}	-1×10^{-7} $+1\times10^{-7}$
	-0.29	2.842×10^{-6}	4.9×10^{-7}	-3.6×10^{-7} $+3.6\times10^{-7}$
	-0.10	1.415×10^{-5}	1.2×10^{-6}	-8.3×10^{-7} $+8.3\times10^{-7}$
	0.10	1.415×10^{-5}	1.1×10^{-6}	-8.3×10^{-7} $+8.3\times10^{-7}$
	0.29	2.632×10^{-6}	4.7×10^{-7}	-3.6×10^{-7} $+3.6\times10^{-7}$
	0.49	9.305×10^{-7}	4.1×10^{-7}	-1×10^{-7} $+1\times10^{-7}$
	0.69	8.151×10^{-7}	4.3×10^{-7}	-9.4×10^{-8} $+9.4\times10^{-8}$
	0.88	-3.409×10^{-7}	2.7×10^{-7}	-9.4×10^{-8} $+9.4\times10^{-8}$
	1.08	2.613×10^{-7}	4.9×10^{-7}	-9.4×10^{-8} $+9.4\times10^{-8}$
	1.28	2.544×10^{-7}	5.1×10^{-7}	-9.4×10^{-8} $+9.4\times10^{-8}$
	1.47	8.188×10^{-7}	1×10^{-6}	-9.4×10^{-8} $+9.4\times10^{-8}$
	1.67	1.593×10^{-7}	7.3×10^{-7}	-9.4×10^{-8} $+9.4\times10^{-8}$
	1.87	2.22×10^{-7}	5.9×10^{-7}	-9.4×10^{-8} $+9.4\times10^{-8}$
	2.06	6.576×10^{-7}	6.2×10^{-7}	-9.5×10^{-8} $+9.5\times10^{-8}$
	2.26	4.204×10^{-7}	4.2×10^{-7}	-1.1×10^{-7} $+1.1\times10^{-7}$
	2.45	1.067×10^{-6}	4.9×10^{-7}	-1.9×10^{-7} $+1.9\times10^{-7}$
	2.65	2.181×10^{-6}	5.5×10^{-7}	-2.5×10^{-7} $+2.5\times10^{-7}$
	2.85	3.809×10^{-6}	6.1×10^{-7}	-3×10^{-7} $+3\times10^{-7}$
	3.04	6.107×10^{-6}	7.8×10^{-7}	-5.8×10^{-7} $+5.8\times10^{-7}$

Appendix D

Correlation Yields Data Tables

Table D.1: 2+1 jet-induced near-side yield Y_{near} for $p_{T,\text{trig}} \otimes p_{T,\text{cond}} = 2-3 \otimes 2-3$ GeV

Centrality	$\langle p_{T,\text{assoc}} \rangle$	Y_{near}	**Stat. Error**	**Syst. error**
p+p	0.63	0.03135	0.00056	+0.0021 -0.0021
	1.3	0.02404	0.00033	+0.001 -0.001
	2.3	0.0113	0.00024	+0.00064 -0.00064
	3.5	0.00564	0.0002	+0.00053 -0.00053
0-20%	1	1.399×10^{-5}	2.2×10^{-7}	$+1.4\times10^{-6}$ -1.4×10^{-6}
	1.7	8.291×10^{-6}	1×10^{-7}	$+7.5\times10^{-7}$ -7.5×10^{-7}
	2.7	1.361×10^{-6}	2.8×10^{-8}	$+1.5\times10^{-7}$ -1.5×10^{-7}
	3.9	2.029×10^{-7}	9.2×10^{-9}	$+3.8\times10^{-8}$ -3.8×10^{-8}
20-40%	0.93	6.149×10^{-5}	2.8×10^{-6}	$+3.3\times10^{-5}$ -3.3×10^{-5}
	1.6	5.709×10^{-5}	1.3×10^{-6}	$+1.5\times10^{-5}$ -1.5×10^{-5}
	2.6	1.263×10^{-5}	3.6×10^{-7}	$+2.9\times10^{-6}$ -2.9×10^{-6}
	3.8	3.07×10^{-6}	1.3×10^{-7}	$+6.7\times10^{-7}$ -6.7×10^{-7}
40-60%	0.83	0.001383	4.6×10^{-5}	+0.00056 -0.00056
	1.5	0.0009445	2.1×10^{-5}	+0.00025 -0.00025
	2.5	0.0001909	6.1×10^{-6}	$+4 \times 10^{-5}$ -4×10^{-5}
	3.7	4.754×10^{-5}	2.2×10^{-6}	$+7.9\times10^{-6}$ -7.9×10^{-6}
60-92%	0.73	0.02574	0.0011	+0.028 -0.028
	1.4	0.009713	0.0005	+0.0023 -0.0023
	2.4	0.006919	0.00023	+0.0021 -0.0021
	3.6	0.00168	7.4×10^{-5}	+0.00021 -0.00021

Table D.2: 2+1 jet-induced near-side yield Y_{near} for $p_{T,\text{trig}} \otimes p_{T,\text{cond}} = 2-3 \otimes 3-5$ GeV

Centrality	$\langle p_{T,\text{assoc}} \rangle$	Y_{near}	**Stat. Error**	**Syst. error**
p+p	0.63	0.04298	0.00095	+0.0036 -0.0036
	1.3	0.03493	0.00071	+0.002 -0.002
	2.3	0.01652	0.00069	+0.0016 -0.0016
	3.5	0.0005897	9.9×10^{-5}	+0.00028 -0.00025
0-20%	1	2.016×10^{-5}	6.5×10^{-7}	$+5.1 \times 10^{-6}$ -5.1×10^{-6}
	1.7	9.46×10^{-6}	2.9×10^{-7}	$+2.2 \times 10^{-6}$ -2.2×10^{-6}
	2.7	1.368×10^{-6}	8.2×10^{-8}	$+4.7 \times 10^{-7}$ -4.7×10^{-7}
	3.9	2.167×10^{-7}	2.7×10^{-8}	$+9.8 \times 10^{-8}$ -9.8×10^{-8}
20-40%	0.93	0.0001457	7.8×10^{-6}	$+8.6 \times 10^{-5}$ -8.6×10^{-5}
	1.6	9.143×10^{-5}	3.6×10^{-6}	$+4 \times 10^{-5}$ -4×10^{-5}
	2.6	1.751×10^{-5}	1×10^{-6}	$+6.4 \times 10^{-6}$ -6.4×10^{-6}
	3.8	3.377×10^{-6}	3.6×10^{-7}	$+1.5 \times 10^{-6}$ -1.5×10^{-6}
40-60%	0.83	0.002377	0.00012	+0.0028 -0.0028
	1.5	0.001196	5.5×10^{-5}	+0.00057 -0.00057
	2.5	0.0002563	1.7×10^{-5}	+0.00011 -0.00011
	3.7	0.0001428	7.4×10^{-6}	$+5.5 \times 10^{-5}$ -5.5×10^{-5}
60-92%	0.73	0.0242	0.0026	+0.02 -0.02
	1.4	0.01441	0.0014	+0.0076 -0.0076
	2.4	0.008787	0.00044	+0.0014 -0.0014
	3.6	0.0001051	2.1×10^{-5}	+0.00014 -0.00013

Table D.3: 2+1 jet-induced near-side yield Y_{near} for $p_{T,\text{trig}} \otimes p_{T,\text{cond}} = 3-5 \otimes 2-3$ GeV

Centrality	$\langle p_{T,\text{assoc}} \rangle$	Y_{near}	**Stat. Error**	**Syst. error**
p+p	0.63	0.03687	0.00085	+0.0032 -0.0032
	1.3	0.02948	0.00056	+0.0016 -0.0016
	2.3	0.01887	0.0006	+0.0015 -0.0015
	3.5	0.003501	0.00031	+0.00064 -0.00061
0-20%	1	1.103×10^{-5}	6.5×10^{-7}	$+3.2\times10^{-6}$ -3.2×10^{-6}
	1.7	7.399×10^{-6}	2.9×10^{-7}	$+1.7\times10^{-6}$ -1.7×10^{-6}
	2.7	2.214×10^{-6}	8.3×10^{-8}	$+3.6\times10^{-7}$ -3.6×10^{-7}
	3.9	5.334×10^{-7}	2.7×10^{-8}	$+8.2\times10^{-8}$ -8.2×10^{-8}
20-40%	0.93	8.502×10^{-5}	7.8×10^{-6}	$+8.8\times10^{-5}$ -8.8×10^{-5}
	1.6	7.738×10^{-5}	3.5×10^{-6}	$+3.2\times10^{-5}$ -3.2×10^{-5}
	2.6	2.806×10^{-5}	1×10^{-6}	$+6.4\times10^{-6}$ -6.4×10^{-6}
	3.8	8.241×10^{-6}	3.6×10^{-7}	$+1.1\times10^{-6}$ -1.1×10^{-6}
40-60%	0.83	0.002041	0.00012	+0.002 -0.002
	1.5	0.001056	5.5×10^{-5}	+0.00038 -0.00038
	2.5	0.0003381	1.7×10^{-5}	$+6.4\times10^{-5}$ -6.4×10^{-5}
	3.7	0.0001287	7.3×10^{-6}	$+1.8\times10^{-5}$ -1.8×10^{-5}
60-92%	0.73	0.007882	0.0025	+0.012 -0.012
	1.4	0.01299	0.0012	+0.0059 -0.0059
	2.4	0.01059	0.00042	+0.0012 -0.0012
	3.6	0.0002298	4.1×10^{-5}	$+8.7 \times 10^{-5}$ -7×10^{-5}

Table D.4: 2+1 jet-induced near-side yield Y_{near} for $p_{T,\text{trig}} \otimes p_{T,\text{cond}} = 3-5 \otimes 3-5$ GeV

Centrality	$\langle p_{T,\text{assoc}} \rangle$	Y_{near}	**Stat. Error**	**Syst. error**
p+p	0.63	0.04875	0.0014	+0.0062 -0.0062
	1.3	0.04908	0.0013	+0.0034 -0.0034
	2.3	0.006265	0.00039	+0.0012 -0.0012
	3.5	0.000319	6.6×10^{-5}	+0.0002 -0.00017
0-20%	1	2.232×10^{-5}	1.9×10^{-6}	$+5.2\times10^{-5}$ -5.2×10^{-5}
	1.7	7.914×10^{-6}	8.6×10^{-7}	$+4.2\times10^{-6}$ -4.2×10^{-6}
	2.7	1.884×10^{-6}	2.4×10^{-7}	$+1 \times 10^{-6}$ -1×10^{-6}
	3.9	4.327×10^{-7}	8×10^{-8}	$+1.5\times10^{-7}$ -1.5×10^{-7}
20-40%	0.93	0.000118	2.2×10^{-5}	+0.00033 -0.00033
	1.6	0.0001738	9.9×10^{-6}	+0.00014 -0.00014
	2.6	3.337×10^{-5}	2.9×10^{-6}	$+3.8\times10^{-5}$ -3.8×10^{-5}
	3.8	1.03×10^{-5}	1.1×10^{-6}	$+2.6\times10^{-6}$ -2.6×10^{-6}
40-60%	0.83	0.00278	0.00031	+0.088 -0.088
	1.5	0.001367	0.00014	+0.00098 -0.00098
	2.5	0.0006327	5.1×10^{-5}	+0.0001 -0.0001
	3.7	0.0006108	2.9×10^{-5}	$+7.5\times10^{-5}$ -7.5×10^{-5}
60-92%	0.73	0.2082	0.0066	+6.6 -6.6
	1.4	0.1046	0.0036	+0.72 -0.72
	2.4	0.0008821	0.00017	+0.00039 -0.00039
	3.6	9.688×10^{-5}	1.2×10^{-5}	+0.0012 -0.0016

Table D.5: 2+1 jet-induced away-side yield Y_{away} for $p_{T,\text{trig}} \otimes p_{T,\text{cond}} = 2-3 \otimes 2-3$ GeV

Centrality	$\langle p_{T,\text{assoc}} \rangle$	Y_{away}	**Stat. Error**	**Syst. error**
p+p	0.63	0.03345	0.00057	+0.0021 -0.0021
	1.3	0.02586	0.00034	+0.001 -0.001
	2.3	0.01158	0.00026	+0.00071 -0.00071
	3.5	0.006172	0.00022	+0.00054 -0.00054
0-20%	1	1.536×10^{-5}	2.3×10^{-7}	$+1.4\times10^{-6}$ -1.4×10^{-6}
	1.7	8.394×10^{-6}	1.1×10^{-7}	$+7.3\times10^{-7}$ -7.3×10^{-7}
	2.7	1.369×10^{-6}	3×10^{-8}	$+1.4\times10^{-7}$ -1.4×10^{-7}
	3.9	2.306×10^{-7}	1×10^{-8}	$+3.8\times10^{-8}$ -3.8×10^{-8}
20-40%	0.93	7.514×10^{-5}	2.9×10^{-6}	$+3.2\times10^{-5}$ -3.2×10^{-5}
	1.6	5.867×10^{-5}	1.3×10^{-6}	$+1.5\times10^{-5}$ -1.5×10^{-5}
	2.6	1.347×10^{-5}	3.9×10^{-7}	$+2.8\times10^{-6}$ -2.8×10^{-6}
	3.8	3.017×10^{-6}	1.3×10^{-7}	$+6.5\times10^{-7}$ -6.5×10^{-7}
40-60%	0.83	0.00157	4.7×10^{-5}	+0.00054 -0.00054
	1.5	0.0009519	2.2×10^{-5}	+0.00024 -0.00024
	2.5	0.0001929	6.5×10^{-6}	$+3.8\times10^{-5}$ -3.8×10^{-5}
	3.7	5.06×10^{-5}	2.3×10^{-6}	$+8 \times 10^{-6}$ -8×10^{-6}
60-92%	0.73	0.02912	0.0011	+0.027 -0.027
	1.4	0.009003	0.00052	+0.0022 -0.0022
	2.4	0.006434	0.0002	+0.002 -0.002
	3.6	0.00157	6.6×10^{-5}	+0.00021 -0.00021

Table D.6: 2+1 jet-induced away-side yield Y_{away} for $p_{T,\text{trig}} \otimes p_{T,\text{cond}} = 2-3 \otimes 3-5$ GeV

Centrality	$\langle p_{T,\text{assoc}} \rangle$	Y_{away}	**Stat. Error**	**Syst. error**
p+p	0.63	0.03816	0.00091	+0.0035 -0.0035
	1.3	0.0335	0.00067	+0.0021 -0.0021
	2.3	0.01562	0.00063	+0.0016 -0.0016
	3.5	0.0008942	9.2×10^{-5}	+0.00037 -0.00034
0-20%	1	2.007×10^{-5}	6.8×10^{-7}	$+4.9\times10^{-6}$ -4.9×10^{-6}
	1.7	1.012×10^{-5}	3.2×10^{-7}	$+2.1\times10^{-6}$ -2.1×10^{-6}
	2.7	2.269×10^{-6}	8.9×10^{-8}	$+4.6\times10^{-7}$ -4.6×10^{-7}
	3.9	4.585×10^{-7}	2.9×10^{-8}	$+9.9\times10^{-8}$ -9.9×10^{-8}
20-40%	0.93	8.427×10^{-5}	8.1×10^{-6}	$+8.3\times10^{-5}$ -8.3×10^{-5}
	1.6	9.045×10^{-5}	3.8×10^{-6}	$+3.9\times10^{-5}$ -3.9×10^{-5}
	2.6	2.314×10^{-5}	1.1×10^{-6}	$+6.2\times10^{-6}$ -6.2×10^{-6}
	3.8	7.145×10^{-6}	3.8×10^{-7}	$+1.4\times10^{-6}$ -1.4×10^{-6}
40-60%	0.83	0.002184	0.00013	+0.0027 -0.0027
	1.5	0.001164	5.9×10^{-5}	+0.00055 -0.00055
	2.5	0.0003824	1.7×10^{-5}	+0.0001 -0.0001
	3.7	0.0001563	7.7×10^{-6}	$+5.2\times10^{-5}$ -5.2×10^{-5}
60-92%	0.73	0.02445	0.0027	+0.02 -0.02
	1.4	0.01219	0.0015	+0.0077 -0.0077
	2.4	0.008411	0.00041	+0.0014 -0.0014
	3.6	0.0001967	3.2×10^{-5}	+0.00022 -0.00021

Table D.7: 2+1 jet-induced away-side yield Y_{away} for $p_{T,\text{trig}} \otimes p_{T,\text{cond}} = 3-5 \otimes 2-3$ GeV

Centrality	$\langle p_{T,\text{assoc}} \rangle$	Y_{away}	**Stat. Error**	**Syst. error**
p+p	0.63	0.04702	0.00091	+0.0031 -0.0031
	1.3	0.03752	0.00061	+0.0017 -0.0017
	2.3	0.02345	0.00069	+0.0016 -0.0016
	3.5	0.003289	0.00018	+0.00087 -0.00079
0-20%	1	1.731×10^{-5}	6.8×10^{-7}	$+3.2\times10^{-6}$ -3.2×10^{-6}
	1.7	7.167×10^{-6}	3.2×10^{-7}	$+1.7\times10^{-6}$ -1.7×10^{-6}
	2.7	1.185×10^{-6}	8.8×10^{-8}	$+3.5\times10^{-7}$ -3.5×10^{-7}
	3.9	2.837×10^{-7}	2.9×10^{-8}	$+9.5\times10^{-8}$ -9.5×10^{-8}
20-40%	0.93	0.0001723	8.1×10^{-6}	$+8.5\times10^{-5}$ -8.5×10^{-5}
	1.6	8.407×10^{-5}	3.8×10^{-6}	$+3.1\times10^{-5}$ -3.1×10^{-5}
	2.6	2.267×10^{-5}	1.1×10^{-6}	$+6.3\times10^{-6}$ -6.3×10^{-6}
	3.8	4.833×10^{-6}	3.7×10^{-7}	$+1.3\times10^{-6}$ -1.3×10^{-6}
40-60%	0.83	0.002228	0.00013	+0.0019 -0.0019
	1.5	0.00121	5.9×10^{-5}	+0.00037 -0.00037
	2.5	0.0003186	1.7×10^{-5}	$+6.5\times10^{-5}$ -6.5×10^{-5}
	3.7	0.0001197	7.5×10^{-6}	$+2.5\times10^{-5}$ -2.5×10^{-5}
60-92%	0.73	0.01361	0.0026	+0.011 -0.011
	1.4	0.0201	0.0016	+0.006 -0.006
	2.4	0.009931	0.00045	+0.0012 -0.0012
	3.6	0.0001789	4.3×10^{-5}	+0.00023 -0.0002

Table D.8: 2+1 jet-induced away-side yield Y_{away} for $p_{T,\text{trig}} \otimes p_{T,\text{cond}} = 3-5 \otimes 3-5$ GeV

Centrality	$\langle p_{T,\text{assoc}} \rangle$	Y_{away}	**Stat. Error**	**Syst. error**
p+p	0.63	0.04978	0.0014	+0.0061 -0.0061
	1.3	0.05573	0.0014	+0.0034 -0.0034
	2.3	0.007825	0.0003	+0.0013 -0.0013
	3.5	0.0006645	0.00011	+0.00038 -0.00036
0-20%	1	2.513×10^{-5}	2×10^{-6}	$+5.1\times10^{-5}$ -5.1×10^{-5}
	1.7	8.017×10^{-6}	9.3×10^{-7}	$+4.1\times10^{-6}$ -4.1×10^{-6}
	2.7	1.859×10^{-6}	2.6×10^{-7}	$+1 \times 10^{-6}$ -1×10^{-6}
	3.9	6.679×10^{-7}	8.5×10^{-8}	$+3.1\times10^{-7}$ -3.1×10^{-7}
20-40%	0.93	0.0001362	2.3×10^{-5}	+0.00032 -0.00032
	1.6	0.0001747	1.1×10^{-5}	+0.00014 -0.00014
	2.6	3.387×10^{-5}	3.1×10^{-6}	$+3.7\times10^{-5}$ -3.7×10^{-5}
	3.8	1.189×10^{-5}	1.2×10^{-6}	$+3.5\times10^{-6}$ -3.5×10^{-6}
40-60%	0.83	0.002733	0.00032	+0.086 -0.086
	1.5	0.001591	0.00015	+0.00095 -0.00095
	2.5	0.0007129	5.4×10^{-5}	+0.00018 -0.00018
	3.7	0.000557	2.9×10^{-5}	$+7.2\times10^{-5}$ -7.2×10^{-5}
60-92%	0.73	0.194	0.0076	+6.5 -6.5
	1.4	0.08766	0.0029	+0.71 -0.71
	2.4	0.001379	0.00021	+0.00056 -0.00056
	3.6	0.000156	2.8×10^{-5}	+0.0012 -0.0016